Ruthenium(II) and -(III) Compounds With Biologically Relevant N-donor Heterocyclic Chelators: Synthesis, Structural Elucidation, Electrochemistry, ESR and Radical Scavenging Studies

by

Abimbola Augustine Adebisi

Submitted in the fulfillment of the requirements for the degree of

Doctor of Philosophy

in the School of Chemistry and Physics at the

University of KwaZulu-Natal

December 2015

Supervisor: Dr. Irvin N. Booysen

As the candidate's supervisor, I hereby approve this thesis for submission:

Signed: _____ Date: _____

Table of Contents

Chapter 3

Ruthenium(II) and -(III) complexes with Schiff base ligands containing Benz(othiazole/imidazole/oxazole) moieties: Structural, Electron Spin Resonance and Electrochemistry studies

Chapter 4

Formation, electrochemical and radical scavenging properties of novel ruthenium compounds with N, X-donor (X = O, N) heterocyclic chelators

Chapter 5

Coordination modes of Di- and Triimines towards Ruthenium(II) and -(III) centres: Structural, Electrochemical and Radical Scavenging studies

Chapter 6

The isolation of new Ruthenium complexes with Lumazine derivatives: Structural, Electrochemical, Computational and Radical Scavenging Studies

Chapter 7

Conclusion and Future Work

Abstract

The inclusion of biologically relevant ligands in coordination compounds of ruthenium is geared towards improving the biodistribution patterns of these metal complexes. In this research study, we investigate the coordination behaviours of N, X-donor (X = O, N or S) heterocyclic ligands incorporating various biologically active components (*viz.* benz(imidazole/othiazole/oxazole), chromone, tetrahydropyran, pyrrole or lumazine) towards ruthenium in its oxidation state of +II. The resultant ruthenium compounds were characterized *via* various spectroscopic techniques and structural elucidation was confirmed using single crystal X-ray diffraction analysis. The structural elucidation was complemented with electro-analytical, radical scavenging and DFT studies.

Novel ruthenium(II) and –(III) complexes of Schiff bases containing benzimidazole (bz), benzothiazole (bs) or benzoxazole (bo) moieties were formulated and characterized in chapter 3. The diamagnetic ruthenium complex, *cis*-[$Ru^{II}Cl_2(bzpy)(PPh_3)_2$] (**1**) was formed from the 1:1 molar reaction between *N*-((pyridine-2-*yl*)methylene)-1*H*-benzimidazole (bzpy) and metal precursor, *trans*-[$RuCl_2(PPh_3)_2$]. The same metal precursor, when reacted with the benzimidazole-derived Schiff bases [*N*-(2-hydroxybenzylidene)-benzothiazole (Hbsp) and *N*-(2-hydroxybenzylidene)-benzimidazole (Hbzp)], afforded the paramagnetic ruthenium (III) complexes [$RuCl(bsp)_2(PPh_3)$] (**2**) and *trans*-[$RuCl(bzp)(PPh_3)_2$] (**3**), respectively. *Trans*-[$RuCl_2(PPh_3)_2$] also gave a diamagnetic ruthenium(II) complex, *cis*-[$Ru^{II}Cl_2(bxth)(PPh_3)_2$] (**4**) when reacted with *N*-((thiophene-2-*yl*)methylene)-benzoxazole (bxth). These metal complexes were characterized *via* IR, mass and UV-Vis spectroscopy, elemental analysis, single crystal XRD analysis (for **1**-**3**) as well as conductivity measurements. Their redox properties were probed by voltammetry and accompanying UV-Vis spectroelectrochemistry (for **1**-**3**) experiments. Structural features of complex **1** and **4** were further investigated by multinuclear (^{1}H and ^{31}P)

NMR spectroscopy. The presence of the paramagnetic metal centres of **2** and **3** were confirmed by X-band ESR spectroscopy.

Chapter 4 describes the formation of novel ruthenium(II), -(III) and –(IV) compounds containing benzoxazole-amide, benzimidazole-amine and chromone- derived Schiff base ligands. A paramagnetic ruthenium(IV) complex, [RuCl(pho)(bzca)(PPh_3)] (**1**) (pho = 2-aminophenolate; bzca = 2-carboxylate-1*H*-benzimidazole) was isolated from the reaction of the ruthenium(II) precursor, *trans*-[$RuCl_2(PPh_3)_3$] and 2-((1*H*-benzimidazole)methylamino)phenol (Hbzap). The 1:1 molar reaction between the same metal precursor and *N*-(benzoxazole)-2-hydroxybenzamide (H_2bhb) led to the formation of *cis-Cl*, *trans-P*-[Ru^{III}(Hbhb)$Cl_2(PPh_3)_2$] (**2**). The dinuclear ruthenium compounds, (μ-Htba,Cl)$_2$[$Ru^{II}Cl(PPh_3)$]$_2$ (**3**) (Htba = *N*-(thiophene)methyl-benzoxazole-2-amine) and (μ-Cl)$_2$[Ru^{III}Cl(Hchpr)(PPh_3)]$_2$ (**4**) (H_2chpr = 2-amino-3-((tetrahydro-2*H*-pyran-4-ylimino)methyl)-4*H*-chromen-4-one) were formed from the equimolar ratio coordination reactions between *trans*-[$RuCl_2(PPh_3)_3$] and the respective free-ligands, Htba and H_2chpr. These metal complexes were characterized using IR-, NMR- and UV-Vis spectroscopy; molar conductivity measurements and structural elucidation was confirmed by single crystal X-ray analysis. The X-ray studies revealed that all the metallic compounds exhibited octahedral geometries and that the Hbzap free ligand have undergone a unique molecular transformation to afford the pho and bzca bidentate chelators in **1**. The electrochemical properties of the respective metal complexes were investigated by voltammetric analysis. The cyclic voltammograms (CVs) of **1**, **2**, **3** and **5** showed one redox couple each while within the CV of the dinuclear compound **4**, two redox couples are observed**.** The ligands and their metal complexes were also subjected to DPPH radical scavenging studies. The IC_{50} values showed that all the metallic compounds have higher radical scavenging activities than their corresponding free-ligands and the natural antioxidant, Vitamin C. A diamagnetic

[$Ru^{II}Cl_2$(Hbzpy)(PPh_3)$_2$] (**5**) was also formed using *N*-((pyridine-2-*yl*)methyl)-1*H*-benzimidazole (Hbzpy) ligand and aforementioned metal precursor.

Chapter 5 focuses on the coordination modes of di- and triimine chelators towards the ruthenium(II) and -(III) centres. The coordination reactions of 2,6-*bis*-((4-tetrahydropyranimino)methyl)pyridine (thppy), N^1,N^2-*bis*((3-chromone)methylene)-benzene-1,2-diamine (chb) and *tris*-((1*H*-pyrrol-2-ylmethylene)ethane)amine (H_3pym) with *trans*-[$Ru^{II}Cl_2$(PPh_3)$_3$] afforded the diamagnetic ruthenium(II) complex, *cis*-[$RuCl_2$(thppy)(PPh_3)] (**1**), the paramagnetic compounds (μ-chb)[*mer*-$RuCl_3$(PPh_3)]$_2$ (**2**) and [Ru(pym)] (**3**), respectively. The synthesized metal complexes were characterized *via* IR-, NMR- and UV-Vis spectroscopy; molar conductivity measurements as well as structural elucidation which were confirmed by single crystal X-ray diffraction. The redox properties of the metal complexes were probed *via* cyclic– and squarewave voltammetry. The radical scavenging capabilities of the metallic compounds towards the NO and DPPH radicals were investigated.

In chapter 6, new ruthenium(II) and -(III) complexes encompassing multidentate ligands derived from 6-acetyl-1,3,7-trimethyllumazine (almz) are described. The 1:1 molar coordination reactions of *trans*-[$RuCl_2$(PPh_3)$_3$] with *N*-1-[1,3,7-trimethyllumazine]benzohydride (bzlmz**)** and 6-(*N*-methyloxime)-1,3,7-trimethyllumazine (ohlmz**)** formed a diamagnetic ruthenium(II) complex, *cis*-[$RuCl_2$(bzlmz)(PPh_3)] (**1**) and a paramagnetic complex, *cis*-[$Ru^{III}Cl_2$(olmz)(PPh_3)] (**2**) [olmz = 6-(*N*-hydroxy-*N*'-methylamino)-1,3,7-trimethyllumazine], respectively. These ruthenium complexes were characterized *via* IR-, NMR-, UV-Vis and TOF-MS spectroscopy, elemental analysis, melting point and molar conductivity measurements. Structural elucidation of the metal complexes was confirmed using single crystal X-ray analysis. The redox properties of the metal complexes were investigated *via* cyclic voltammetry. ESR spectroscopy confirmed the presence of paramagnetic metal centres of **2** . The radical scavenging activities of the metal complexes were explored towards the DPPH and NO radicals. Computational

calculations at the DFT level provided insight in the interpretation of the experimental spectra of **1**.

Keywords: Ruthenium; Schiff base; Benz(imidazole/othiazole/oxazole); Lumazine; Amine; Amide; Heterocyclic; Crystal structure; Redox properties; Radical scavenging activity; Electron Spin Resonance; Electrochemistry; Simulated spectra.

Preface

The experimental work described in this thesis was carried out in the School of Chemistry and Physics at the University of KwaZulu-Natal, Pietermaritzburg, from February 2012 to December 2015, under the supervision of Dr. Irvin Noel Booysen.

These studies represent original work by the author and have not otherwise been submitted in any form for any degree or diploma to any tertiary institution. Where use has been made of the work of others, it is duly acknowledged in the text.

Declaration 1 – Plagiarism

I, Abimbola Augustine Adebisi, declare that:

1. The research reported in this thesis, except where otherwise indicated, is my original research.

2. This thesis has not been submitted for any degree or examination at any other university.

3. This thesis does not contain any other persons' data, pictures, graphs or other information, unless specifically acknowledged as being sourced from other persons'.

4. This thesis does not contain any other persons' writing, unless specifically acknowledged as being sourced from other researchers. Where other written sources have been quoted, then:
   a. Their words have been re-written but the general information attributed to them has been referenced.
   b. Where their exact words have been used, then their writing has been placed in italics and inside quotation marks, and referenced.

5. This thesis does not contain text, graphics or tables copied and pasted from the internet, unless specifically acknowledged, and the source being detailed in the thesis and in the references section.

Signed: _____

Declaration 2 – Publications

Manuscripts published:

- I.N. Booysen, A. Adebisi, O.Q. Munro, B. Xulu, "**Ruthenium(II) and -(III) complexes with Schiff base ligands containing Benz(othiazole/imidazole/oxazole) moieties: Structural, Electron Spin Resonance and Electrochemistry studies**", *Polyhedron*, 2014, **73**, 1.
- I.N. Booysen, A. Adebisi, M.P. Akerman, "**Formation, electrochemical and radical scavenging properties of novel ruthenium compounds with N, X-donor (X = O, N) heterocyclic chelators**", *Inorg. Chim. Acta*, 2015, **433**, 13.

Submitted for review:

- I.N. Booysen, A. Adebisi, M.P. Akerman, O.Q. Munro, B. Xulu, "**Coordination modes of Di- and Triimines towards the Ruthenium(II) and -(III) centres: Structural, Electrochemical and Radical Scavenging studies**", *J. Coord. Chem.*, 2015.

In preparation:

- A. Adebisi, I.N. Booysen, M.P. Akerman, E.Hosten, T.I.A. Gerber, B. Xulu, "**The isolation of new Ruthenium complexes with Lumazine derivatives: Structural, Electrochemical, Computational and Radical Scavenging Studies**", *Trans. Met. Chem.*, 2016.

The compounds involved in all the aforementioned manuscripts have been synthesized, characterized and analyzed by myself. Single crystal samples were run and solved by Dr. M. Akerman and Prof. O. Munro. The ESR spectrum was run by Dr. B. Xulu.

Acknowledgements

I would like to express my heartfelt gratitude to my supervisor, Dr. Irvin N. Booysen for his constant guidance, encouragement and constructive criticism throughout the project.

I would like to immensely thank Prof. Orde Munro and Dr. Matthew Akerman for their expertise with the crystallographic data collection. I would also like to thank Dr. B. Xulu for attaining the raw Electron Spin Resonance data.

My thanks are also extended to the members of my research group, M. Ismail, S. Maikoo, S. Chohan, I. Ebinumoliseh, B. Jadoo as well as other chemistry colleagues for their help, support, encouragement and friendship.

I am highly grateful to National Research Foundation (NRF) and UKZN College of Science and Agriculture for their financial support and to the Chemistry Department at the University of KwaZulu-Natal for providing laboratory space and equipment.

I would like to acknowledge all the academic and technical staff in the School of Chemistry and Physics, UKZN for their assistance and support. In particular, Mr Craig Grimmer for the training with regard to NMR analysis and Mrs Caryl J. Van Rensburg for her help with Mass Spectra and CHN analysis.

Finally, I would like to express my deepest appreciation to my family especially my parents and siblings for the unconditional love and unflinching support given to me all through my studies. Last but not least, to my better half, Evelyn, for the patience, understanding and encouragement.

Crystallographic Data

Supplementary data for all the crystal structures obtained during this study are stored on a compact disk that is attached to the inside back cover of this thesis.

This data includes the following:

- Final coordinates and equivalent isotropic displacement parameters of the non-hydrogen atoms;
- Final crystal data and details of the structure determinations;
- Isotropic displacement parameters;
- Hydrogen atom positions;
- Contact distances;
- Torsion angles;
- Hydrogen-bonds.

Chapter 1

Introduction

1.1 General Background

Ruthenium is a group 8 transition metal positioned in the second row of the periodic table. It belongs to a collection of metals classified as the Platinum Group Metals (PGMs) which also includes Osmium, Rhodium, Palladium, Iridium and Platinum. All these metals have closely associated physical and chemical properties. These metals typically occur together in the same mineral deposits [**1**]. Ruthenium is one of the rarest elements in the earth's crust being the 74th most abundant element on earth [**2**, **3**]. Naturally occurring ruthenium is made up of seven stable isotopes while several radioactive isotopes have been discovered with atomic weights ranging from 87 to 120. Among these radioisotopes, ^{106}Ru, ^{103}Ru and ^{97}Ru are the most stable with half-life of 373.59 days, 39.2 days and 2.9 days, respectively [**4**, **5**].

This transition metal possesses an electronic configuration of [Kr]4$d^7$5s^1 which confers its unique redox properties through its capability to exhibit a wide range of oxidation states. In fact, the variable valency is emphasized by the oxidation states of -II as in $Ru(CO)_4^{2-}$ and +VIII as in RuO_4 which corresponds to d^0 and d^{10} electronic configurations, respectively [**6**]. The +II, +III and +IV oxidation states are the most common, of which the +III state is substitutionally more inert, a feature which has proved useful for a number of single-electron transfer studies [**7**, **8**].

Ruthenium complexes exhibiting octahedral coordination geometry allows for the inclusion of specific ligands in a controlled manner to refine the photophysical, photochemical and electrochemical properties [**9**]. The coordination chemistry of

ruthenium is dictated by its affinity for nitrogen donor ligands such as in the $[Ru(bipy)]^{2+}$(bipy = bipyridine) core [**10**]. Furthermore, ruthenium complexes have received a lot of interest and are now studied extensively for their wide range of biological activities (*e.g.* anticancer, antimicrobial and antioxidant) [**11**]. This upsurge in research is attributed to the discovery of imidazolium-*trans*-imidazoledimethylsulfoxide-tetrachlororuthenate (III) (NAMI-A) and indazolium-*trans*-[tetrachloro-*bis* (1*H*-indazole) ruthenate(III)] (KP-1019) which have both entered clinical trials as ruthenium anticancer drugs [**12**, **13**].

1.2 Aim and Motivation

A current design strategy for discovering the next generation of ruthenium-based metallodrugs involves the incorporation of biologically relevant moieties into their chelators [**14**]. Hypothetically, these biologically active moieties should improve the biodistribution patterns of formulated ruthenium metallodrugs and possibly increase its solubility into the blood stream. In addition, the inclusion of a biologically active moiety can induced biocompatibility of the formulated ruthenium metallopharmaceuticals and also avoids the development of drug-resistant diseases [**15**]. Moreover, meticulous ligand design can ensure optimal DNA binding capability coupled with possibilities of ionic or direct covalent bonding interactions by the ruthenium metal centre to the DNA double helix [**16**]. Furthermore, the capability of ruthenium to imitate iron in binding to transferrin plays a huge part in the general low toxicity of ruthenium based metallodrugs [**17**]. Thus, within this study, our aim is to design ruthenium with multidentate N, X-donor (X = O, N, S) chelators incorporating various biologically relevant moieties. More specifically, biologically active moieties including benzimidazole (bz), benzothiazole (bs), benzoxazole (bo), chromone (chr), tetrahydropyran (thp), pyrrole (pyr) and lumazine (lmz) were considered within this research study, refer to Figure 1.1.

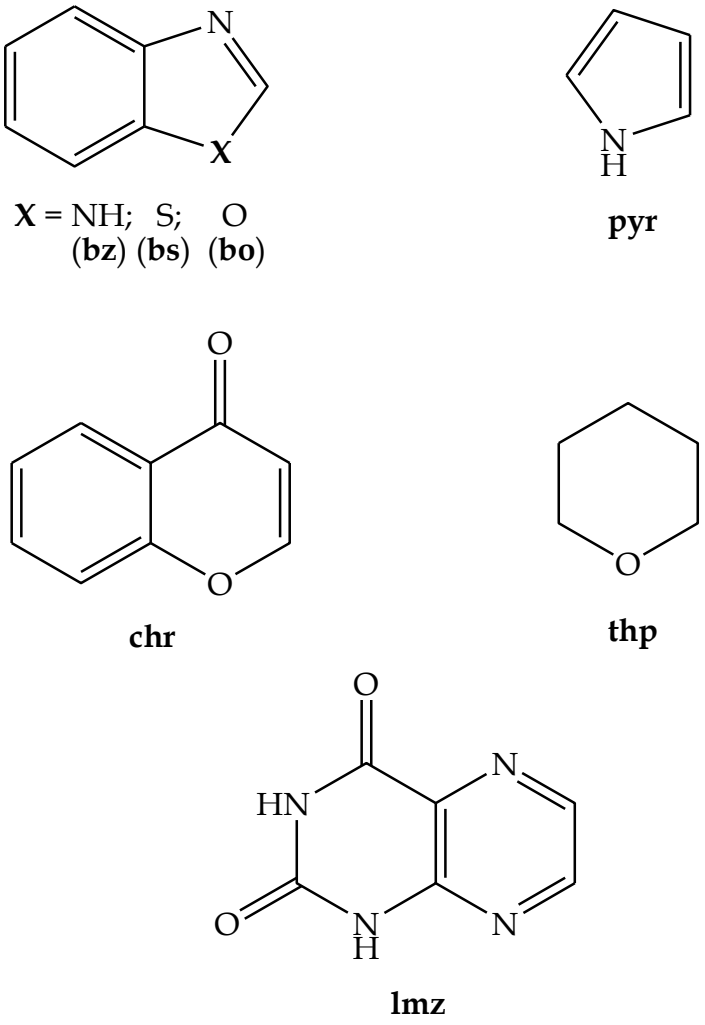

Figure 1.1: *Structures of the biologically active moieties considered within the study.*

Compounds containing benz(imidazole/othiazole/oxazole) moieties are building blocks for many compounds which have displayed different pharmacological activities [**18, 19**]. Like in the case of the *bis*-benzoxazole natural product analogue, [2,4'-bibenzoxazole]-4-carboxylicacid, 2'-(2-hydroxyphenyl) methyl ester (UK-1) which has shown potent anticancer activities against a wide spectrum of cell lines such as leukaemia and lymphoma [**20**], refer to Figure 1.2. Indicative to the aforementioned N-donor heterocyclic compounds, pyrroles and their derivatives exhibit a wide range of biological activities [**21-24**]. These pronounce biological activities are largely due to the

fact that pyrroles are found in many natural products such as porphyrins, chlorins, chlorophylls and corrins [**25, 26**]. For example, Astorvastatin, (Figure 1.3) contains a synthetic derivative of pyrrole: A drug used primarily for lowering blood cholesterol and for the prevention of events associated with cardiovascular disease [**27**].

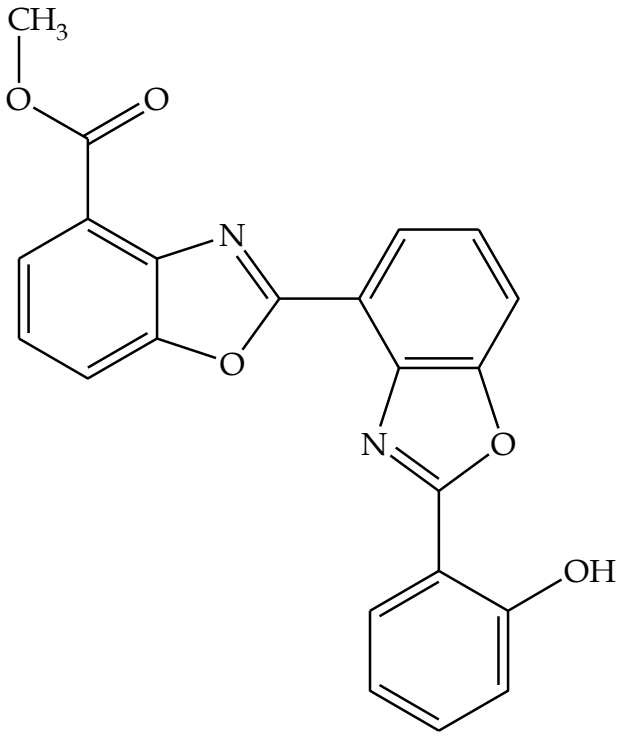

Figure 1.2: *Structure of UK-1.*

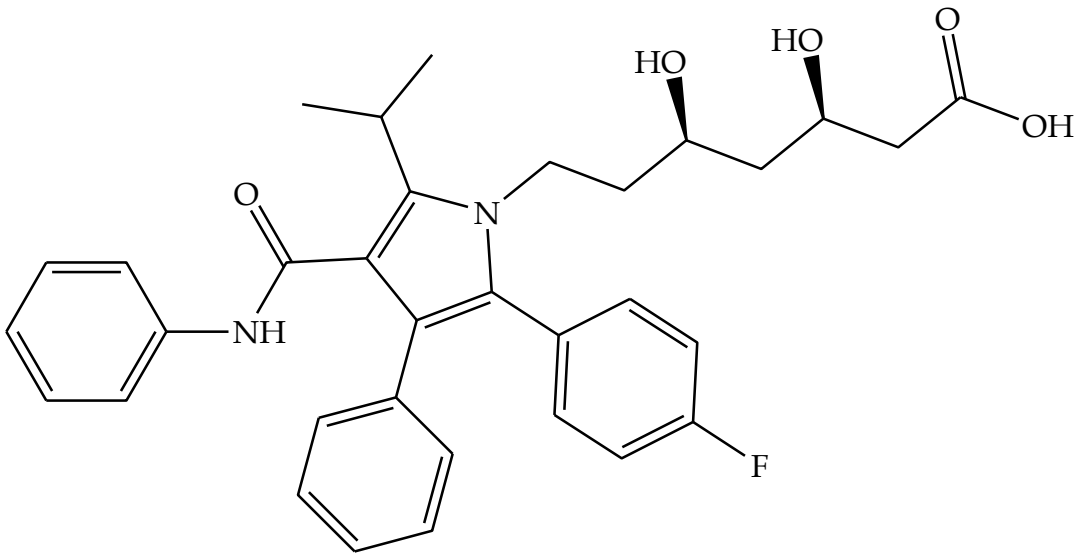

Figure 1.3: *Structure of Atorvastatin, a drug used for the treatment of cardiovascular diseases*.

Our choice in the consideration of chromone moiety rested on its biological relevance as a secondary metabolite and that transition metal complexes with Schiff base chelates bearing the chromone moiety are optimal DNA interchelators [**28**]. Our research study advanced further to the tetrahydropyran moiety as it has the same structural core of the carbohydrates. Synthetically, the tetrahydropyran moiety forms an integral constituent of the architectural setup of Phorboxazole, (Figure 1.4) isolated from an Indian Ocean sponge (genus *Phorbassp*.) which can inhibit the growth of tumour cells [**29-31**].

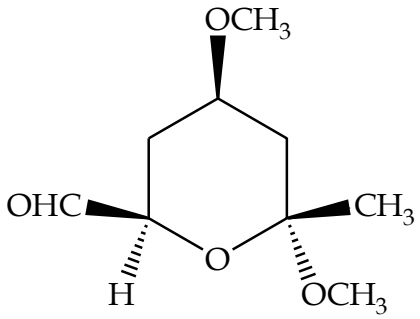

Figure 1.4: *Structure of the natural inhibiter of cancer cell lines, Phorboxazole.*

Lastly, lumazine acts as a substrate for the riboflavin synthase complex, an enzyme complex that catalyses the conversion of two molecules of lumazine into Riboflavin (vitamin B2) [**32, 33**], refer to Figure 1.5. Furthermore, one of the annealed ring systems of lumazine is a uracil which in turn is a constituent of well-established chemotherapeutic drugs, uramustine [Figure 1.6 (a)] and 5-fluoro-uracil [Figure 1.6(b)] [**34, 35**]. In fact, Booysen *et al.* have already demonstrated coordination susceptibility of Schiff bases derived from 5,6-diamino-1,3-dimethyluracil towards ruthenium in its oxidation state +II [**36**]. Therefore, the aforementioned research study allowed impetus to investigate the coordination reactions of *trans*-[$RuCl_2(PPh_3)_3$] and multidentate chelators derived from lumazine.

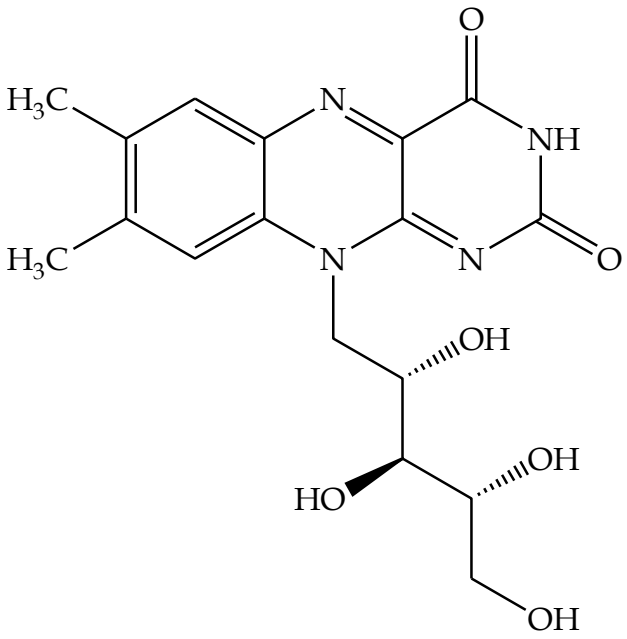

Figure 1.5: *Structure of vitamin B2, Riboflavin.*

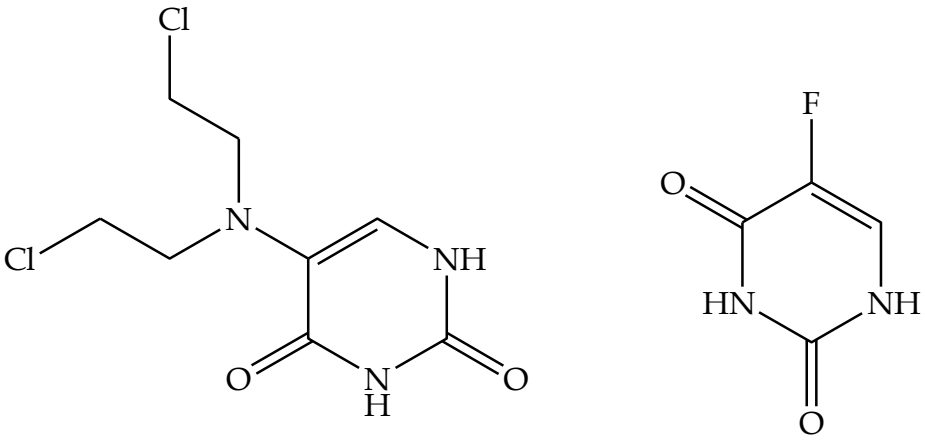

(a) (b)

Figure 1.6: *Structure of (a) uramustine and (b) 5-fluoro-uracil.*

The incorporation of biological active moieties (BAM) into multidentate chelators readily occurs through the formation of Schiff bases. The ruthenium centre generally has high coordination affinity to imino nitrogens and this class of ligands stabilizes ruthenium both in the low and high oxidation states. Another advantage includes the fact that numerous Schiff bases derived from biological active moieties has already been formed and subsequently coordinated to various transition metals. In fact, some transition metal complexes showed increased biological activities with regard to their free Schiff base ligands derived from BAMs [**37**]. However, some of the formulated Schiff bases within our research study have shown to be characteristically hydrolytically unstable and this phenomenon was combated by utilizing more robust ligand systems, amines and amides [**38**].

1.3 Schiff base metal complexes

Transition metal complexes containing Schiff base ligands possess the capability to stabilize different metals in various oxidation states [**39**]. This capability originates from the fact that numerous metal centres have affinity for the imino nitrogen and the coordination susceptibility for other metal ions can be tailored through the manipulation of other donor atoms which can be readily achieved by functionalization and derivatization of Schiff bases. In addition, the combination of hard and soft donor atoms (*viz.* nitrogen and oxygen) in Schiff bases incorporating benz(imidazole/othiazole) moieties have shown to be successful chelators to the acidic $[V^{IV}O]^{2+}$ and $[V^{V}O_2]^{+}$ cores, see Figure 1.7 [**40**]. Furthermore, multidentate Schiff bases are known to stabilize transition metals through chelation and even encapsulation (*i.e.* displacing all the original co-ligands of the metal precursor) [**41**].

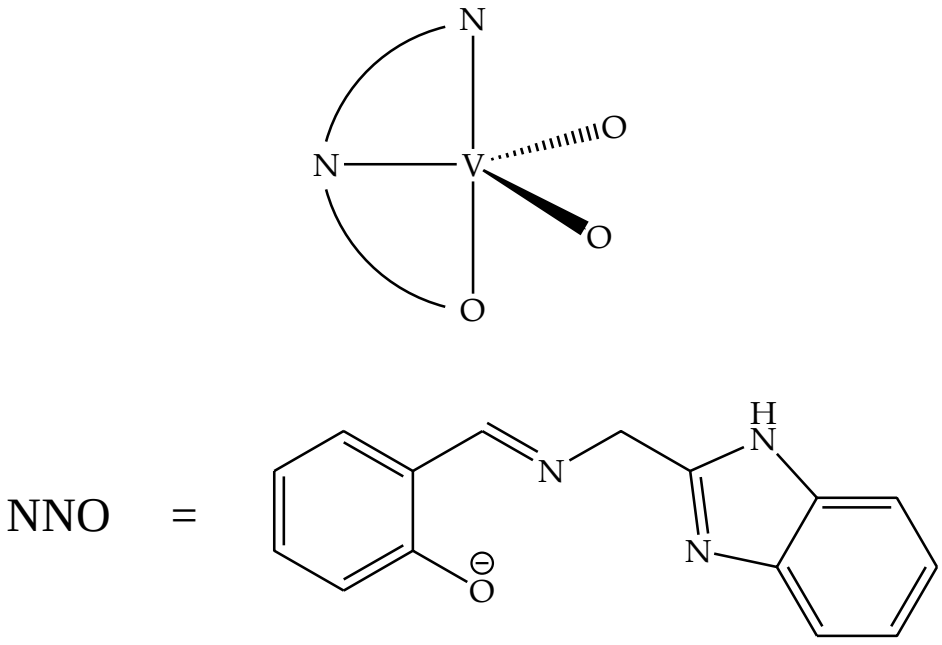

Figure 1.7: *A trigonal bipyrimidal dioxovanadium(V) complex bearing a monoanionic tridentate benzimidazole Schiff base chelator.*

More interestingly, the conformational effects imparted by the diimine chelators on d^6 metal centres have resulted in metal complexes with peculiar electronic properties. For example, diimine ruthenium (II) complexes typically show intense intraligand ($\pi^* \rightarrow \pi$) relaxations accompanied by more red-shifted $d_\pi(\text{Ru}) \rightarrow \pi^*$ MLCT relaxation with more longer lifetimes, ideally suited for applications in photocatalysis, photosensitization and photoelectrochemical sensing [**42**-**44**]. Also, altering the stereoelectronic properties of Schiff bases of *d*-block elements have induced significant influence on their redox and catalytic properties. More specifically, the series of paramagnetic ruthenium(III) complexes, *trans*-$[Ru(H_2O)_2(L_n)_2]Cl$ {*n* = OCH_3, CH_3, H, Cl or NO_2} where L is monoanionic bidentate chelators derived from 2-hydroxy-naphthaldehyde and the corresponding derivatized anilines; showed optimal catalytic activity towards the oxidation of benzoin, see Figure 1.8 [**45**]. The variable turn-over frequencies suggested that the nature of the para-substituent had significant influence on the efficiency of the molecular transformation to benzil.

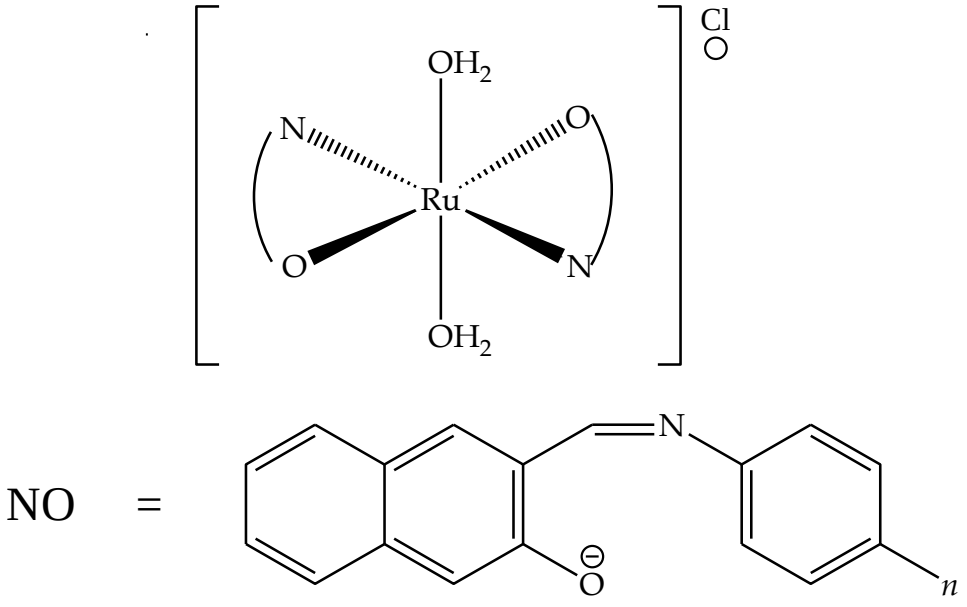

Figure 1.8: *The generic structure of the ruthenium (III) catalysts, trans-$[Ru(H_2O)_2(L_n)_2]Cl$ {n = OCH_3, CH_3, H, Cl or NO_2} in which the monoanionic L_n chelators coordinates in a '2+2' manner.*

Recently, researchers have also been showing interest in the nanofabrication of nanoconjugates of Schiff base metal complexes. For example, multi-walled carbon nanotubes (MWCNTs) covalently linked to a palladium(II) Schiff base metal complex afforded higher heterogeneous catalytic activity in comparison to when only the aforementioned Schiff base metal complex was used (see Figure 1.9) [**46**]. The rationale behind the use of carbon nanotubes is due to their high surface area and their network of sp^2-hybridised carbon atoms rendering excellent conductive properties. Furthermore, they are also thermally stable which aids in stabilizing Schiff bases which are traditionally prone to hydrolysis [**47-49**].

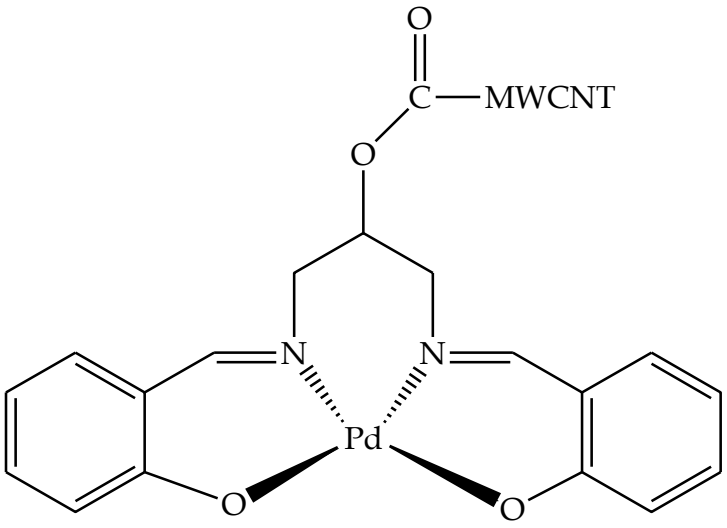

Figure 1.9: *Nanoconjugates comprising of a Pd(II) Schiff base complex and a MWCNT.*

1.4 Development of ruthenium metallopharmaceuticals

Following the discovery of the potent anticancer activity of Cisplatin, {*cis*-$[PtCl_2(NH_3)_2]$} [Figure 1.10(a)] in the 1960s, there has been growing interest to design other platinum-based metallo-drugs with fewer side effects [**50**]. Despite cisplatin being active against broad range of cancers, this anticancer drug has a tendency of targeting both cancer and

healthy cells leading to gastrointestinal tract degradation (*viz.* nausea, vomiting, diarrhoea and abdominal pain), hair loss, skin ailments, neuromuscular complications, renal tubular injury and ototoxicity [**50**, **51**]. To combat these side-effects, second generation platinum anticancer drugs (*e.g.* carboplatin [Figure 1.10(b)] and oxaliplatin [Figure 1.10(c)]) have been synthesized and found to be more stable and less neurotoxic than cisplatin [**52**, **53**]. However, regardless of the significant advances made in utilizing platinum-based drugs for cancer therapy, a new class of chemotherapeutic drugs are required that should target the different types of cancer cells specifically and ultimately lead to no or minimal side-effects as well as avoid the development of drug resistant cancers.

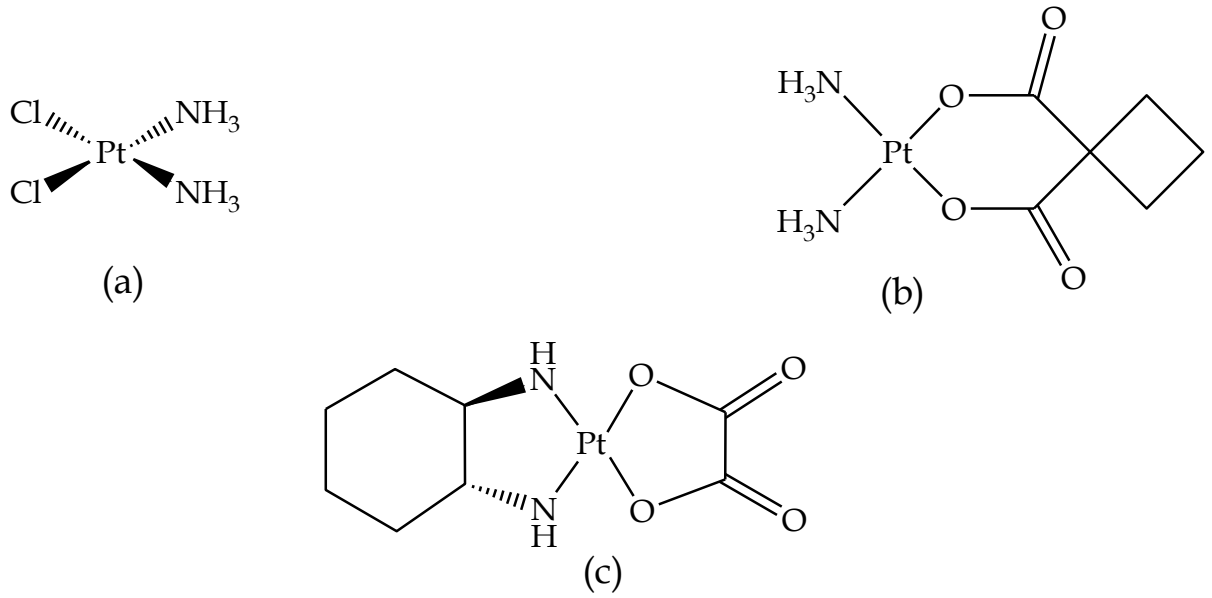

Figure 1.10: *Structures of (a) cisplatin (b) carboplatin and (c) oxaliplatin.*

Among the numerous metals considered for developing novel anticancer drugs, ruthenium share an essential attribute with platinum given by the fact that ruthenium (II) and -(III) complexes have substitution kinetics similar to platinum(II) complexes [**54**]. In addition, the ability of ruthenium to imitate iron in binding to numerous

biological molecules including serum proteins like transferrin and albumin, is a property believed to contribute to the general low toxicity of ruthenium drugs [**55**, **56**]. Furthermore, ruthenium exhibits optimal redox properties which have shown to be a significant contributing factor in the scavenging capabilities of free radicals associated with inducing cancer [**57**].

Consequently, numerous ruthenium based compounds in their oxidation states +II or +III have been isolated and their anti-tumour activities evaluated. Ruthenium red, $[(NH_3)_5Ru\text{-}O\text{-}Ru(NH_3)_4\text{-}O\text{-}Ru(NH_3)_5]^{6+}$, happened to be the first ruthenium compound to be used for biomedical purposes including as an electron microscopy stain and a blocking agent for Ca^{2+} ions [**58**, **59**]. The first reported anticancer activity of ruthenium compounds; *fac*-$[RuCl_3(NH_3)_3]$ and *cis*-$[RuCl_2(NH_3)_4]Cl$ were found toinduce filamentous growth of *E. coli* at concentrations comparable to those at which cisplatin generates similar effects. However, the main demerit of these metal complexes was their low solubility in physiological media [**60**, **61**].

Currently, *trans*-$[Ru^{III}Cl_4(DMSO)(Im)](ImH)$ {ImH = protonated imidazole} (NAMI-A) [Figure 1.11(a)] and *trans*-$[Ru^{III}(Ind)_2Cl_4][IndH]$ (Ind = protonated indazole) (KP-1019) [Figure 1.11(b)] are the first ruthenium-based drugs that have reached phase II clinical trials with both having similar structural features but surprisingly different biodistribution patterns. NAMI-A seems to minimize the metastatic potential of tumours, regardless of the absence of a notable reduction of the primary tumour growth [**62**]. Though NAMI-A can interchelate between the DNA base pairs, this doesn't appear to be the origin of its mechanism of activity. It rather appears to act as an anti-angiogenic and anti-invasive agent unlike KP1019 which has displayed direct cytotoxic activity against colorectal cancers by inducing apoptosis *via* anintrinsic mitochondrial pathway [**63-65**].

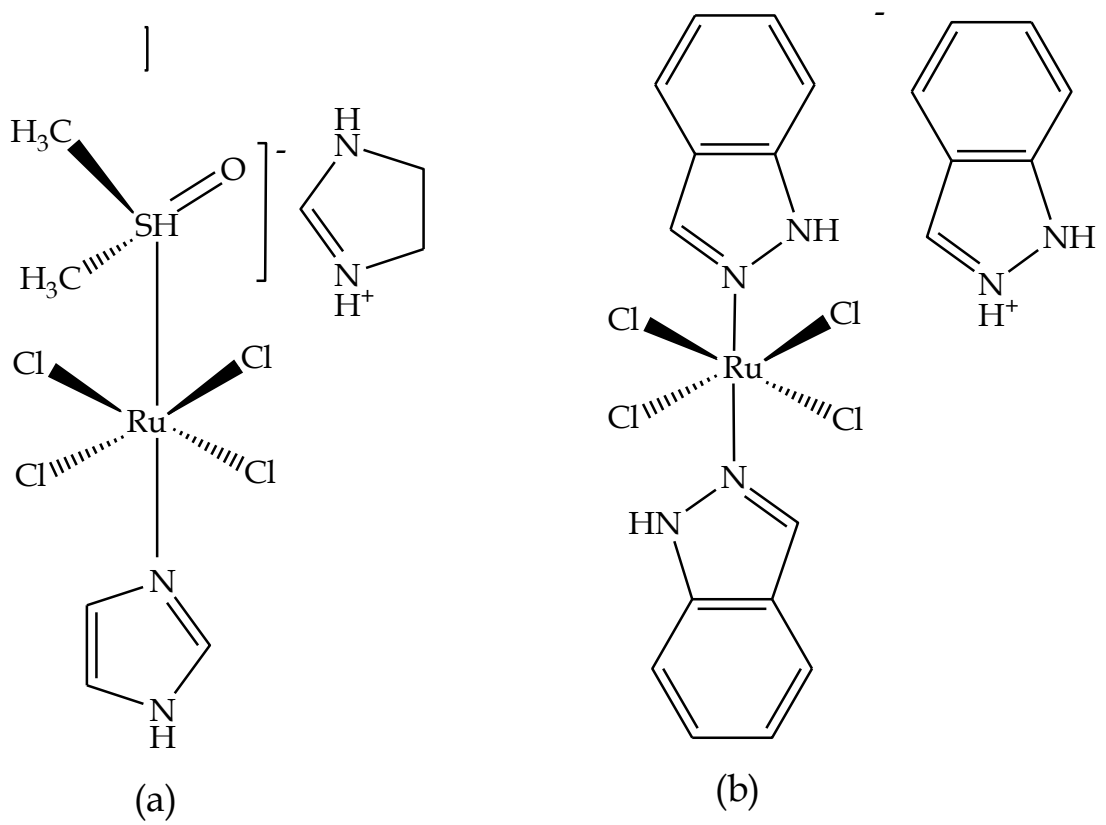

Figure 1.11: *The leading candidates for the ruthenium chemotherapeutic drugs: (a) NAMI-A and (b) KP1019.*

Furthermore, a number of organometallic ruthenium (II) arenes containing 1, 3, 5-triaza-7-phosphaadamantane (PTA) ligands, known as RAPTAs (refer to Figure 1.12) have been discovered and these metal complexes have shown to exhibit diverse biological activities [**66**]. These potential chemotherapeutic drugs are potent because of their high selectivity towards tumour cells accompanied with minor systemic toxicity to healthy cells. Unlike classical DNA interchelators which don't share a defined biodistribution pattern, this class of ruthenium compounds act as pro-drugs where they combine with proteins in a peculiar way and the resultant adduct is proposed to be the principal constituent under physiological conditions. Hence indicative to NAMI-A, these metal complexes show poor toxicity towards tumour *cells in vitro* but has

developed *in vivo* antimetastatic activity [**67**]. Especially, RAPTA-T has been proven to decrease *in vivo* lung metastases growth [**68**].

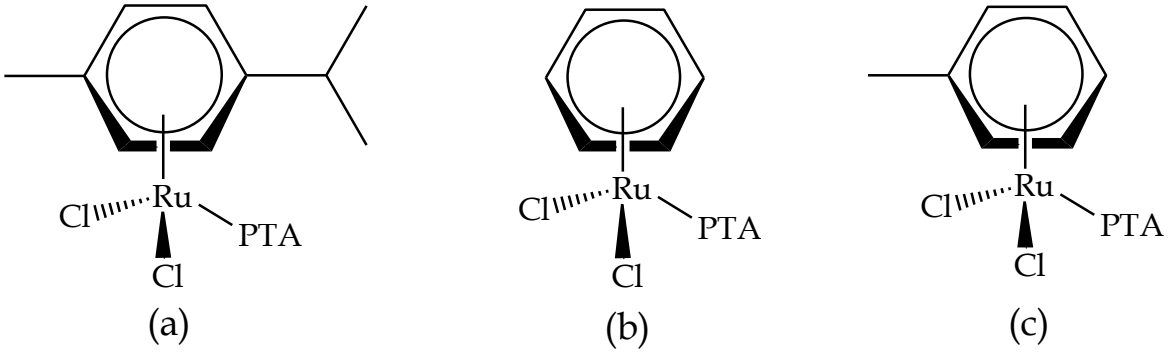

Figure 1.12: *Schematic representation of selected RAPTA-Ru(II)-arene analogues.*

1.5 General Chemistry of Ruthenium

1.5.1 Ligand Substitution

Low spin ruthenium (II) complexes are kinetically inert but ligand substitution can be boosted using metal precursors (*e.g. cis*-$[RuCl_2(bpy)_2]$, *trans*-$[RuCl_2(PPh_3)_3]$ and (μ-$Cl)_2[RuCl(p$-cymene)$]_2$)with labile co-ligands within the coordination environments of the ruthenium(II) metal precursors [**69**]. For example, the substitution reaction between the ruthenium(II) complex, $[Ru(terpy)bipy(H_2O)]^{2+}$ (terpy = 2, 2: 6′, 2″-terpyridine, bipy = 2, 2′-bipyridine) and biologically relevant sulphur donor nucleophile, thiourea is described in equation (**1**) [**70**].

$$[Ru(terpy)(bipy)(H_2O)]^{2+} + \text{thiourea} \rightarrow [Ru(terpy)(bipy)(\text{thiourea})]^{2+} + H_2O \qquad (\mathbf{1})$$

Interestingly, the substitution kinetics of $[Ru(terpy)(HPB)H_2O](PF_6)_2$ {HPB = 2-(2'-hydroxyphenylbenzoxale} indicated that it is ligand substitution by pyridine which occur *via* an initial reduction of the [Ru(III)-H_2O] complex to [Ru(II)-H_2O] complex before the substitution of the aqua ligand by pyridine occurs [**71**].

1.5.2 Redox reactions

Ruthenium compounds in its oxidation states of +II and +III are highly redox active and as a result, they are susceptible to ligand induced redox reactions. This can be seen in equation (**2**) whereby an organometallic ruthenium(III) complex,*trans*-P, *cis*-Cl-$[Ru^{III}(pch)Cl_2(PPh_3)_2]$ (pch = 4-((pyridine-2-ylimino)methylene)chromone) is formed from the diamagnetic metal precursor, [*trans*-$[Ru^{II}Cl_2(PPh_3)_3]$ [**72**].

$$[Ru^{II}Cl_2(PPh_3)_3] + pch \rightarrow [Ru^{III}(pch)Cl_2(PPh_3)_2] + PPh_3 \qquad (2)$$

A series of ruthenium(III) complexes have shown the tendency to be oxidized to Ru^{IV} or Ru^{V} species by various oxidants. An example is the reaction of *trans*-$[Ru^{II}Cl_2(PPh_3)_3]$ with H_3hdp ligand (H_3hdp = 5-(2-hydroxybenzylideneamino)-6-amino-1,3-dimethyluracil). The hydrolysis of H_3hdp occurred to form the ddd ligand (ddd = 5,6-diamino-1,3-dimethyluracil) and the resulting ddd ligand induced oxidation of the metal centre upon coordination to afford a ruthenium(IV) complex, *trans*-$[RuCl_2(ddd)(PPh_3)_2]$ [**73**].

1.5.3 *Disproportionation*

Extensive studies have been carried out on disproportionation reactions of ruthenium complexes owing to the relevance of the products (as oxidants and reductants) in DNA-oxidation studies and organometallic catalysis. In particular, ruthenium(III) complexes are known to disproportionate into Ru(II) and Ru(IV) species under basic conditions. Choi *et al.* reported the disproportionation of $[Ru^{III}(NH_3)_5(dGuo)]$ {d(Guo) = 2′-deoxyguanosine} under basic conditions which afforded $[Ru^{II}(NH_3)_5(dGuo)]^{2+}$ and$[Ru^{IV}(NH_3)_4(NH_2)(dGuo)]^{4+}$ [**74**], refer to equation(**3**):

$$2[Ru(NH_3)_5(dGuo)]^{3+} + OH^- \rightarrow [Ru(NH_3)_5(dGuo)]^{2+} + [Ru(NH_3)_4(NH_2)(dGuo)]^{4+} + H_2O \quad (\mathbf{3})$$

Ruthenium(II) complexes disproportionate seldom, but an unusual proton induced disproportionation of the metal complex, $Ru^{II}(NH_3)_2(bqdi)Cl_2$ (bqdi = *o*-benzoquinonediimine), have been studied. Kapovsky *et al.* reported that the complex $[Ru^{II}(NH_3)_2(bqdi)Cl_2]$ undergoes disproportionation when exposed to UV-Vis light, to generate two final ruthenium(III) species, refer to equation (**4**) and (**5**). At first, an intermediate, $[Ru^{IV}(NH_3)_2(opda)Cl_2]^{2+}$ (opda = 1,2-phenylenediamine) is formed bythe protonation of the diimine nitrogen donors of the bqdi group. The intermediate influences the oxidation of the residual molecules of $[Ru^{II}(NH_3)_2(bqdi)Cl_2]$ to produce the complex cations, $[Ru^{III}(NH_3)_2(opda)Cl_2]^+$ and $[Ru^{III}(NH_3)_2(bqdi)Cl_2]^+$ [**75**].

$$[Ru^{II}(NH_3)_2(bqdi)Cl_2] + 2H^+ \rightarrow [Ru^{IV}(NH_3)_2(opda)Cl_2]^{2+} \quad (\mathbf{4})$$

$$[Ru^{IV}(NH_3)_2(opda)Cl_2]^{2+} + [Ru^{II}(NH_3)_2(bqdi)Cl_2]^{2+} \rightarrow [Ru^{III}(NH_3)_2(opda)Cl_2]^+ + [Ru^{III}(NH_3)_2(bqdi)Cl_2]^+ \quad (\mathbf{5})$$

1.6 Coordination Chemistry of Ruthenium(II) and –(III)

1.6.1 Ruthenium complexes with N, N-donor ligands

Ruthenium displays a high affinity towards nitrogen donor atoms like pyridyl, imine and amine nitrogens [**76**]. For example, the reaction of a multidentate N-donor benzimidazole ligand, *tris*[benzimidazol-2-*yl*-methyl]amine (L^1) (see Figure1.13), with *trans*-[$RuCl_2(PPh_3)_3$] formed a distorted octahedral structure in which the Ru centre coordinate *via* $(N_3)_{benzimidazole}N_{amine}$ donor set of the neutral L^1 moiety while the chloro and PPh_3 co-ligands occupy the axial positions. DFT simulations indicate that in the HOMO and HOMO(-1) configurations, the frontier orbitals of the L^1 chelator are localized on the benzimidazole rings which facilitate the coordination to the metal centre [**77**].

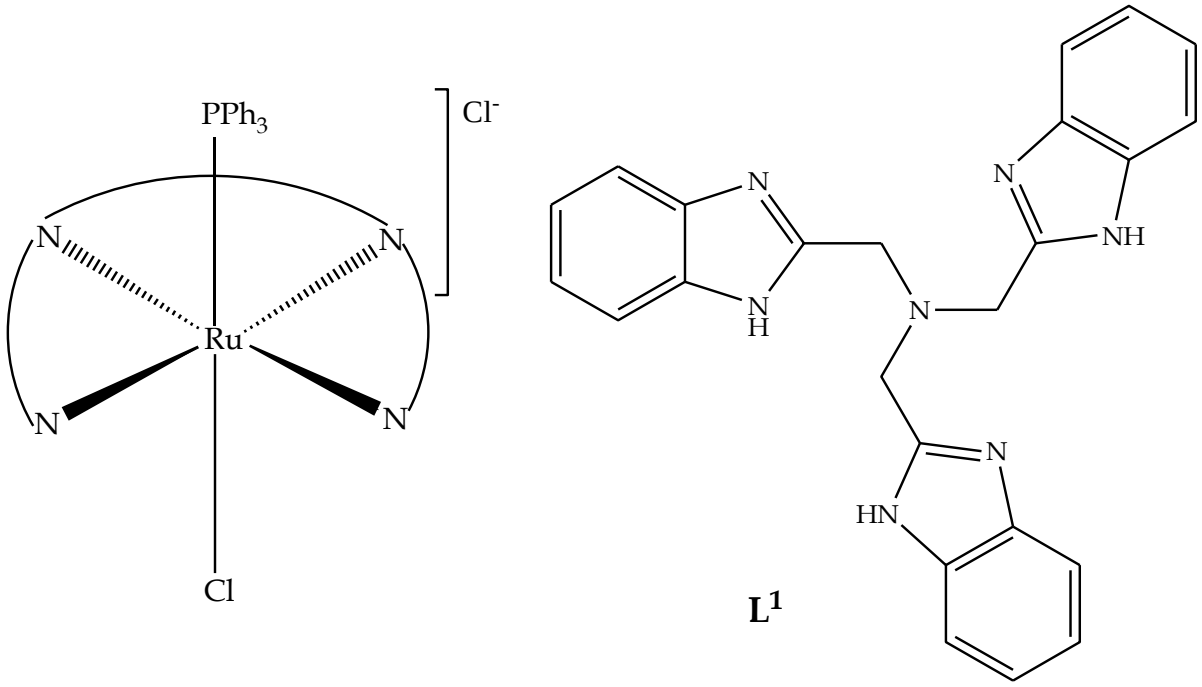

Figure 1.13: *Structures of the free L^1 ligand and its corresponding complex cation illustrating the neutral tetradentate moiety occupying the equatorial position.*

1.6.2 *Ruthenium complexes with N, O-donor ligands*

Numerous ruthenium complexes containing a combination of hard and soft donor atoms (nitrogen and oxygen) have been synthesized in literature due to their broad applications in the field of catalysis and other molecular transformations [**78**]. These donor atoms have been included in different classes of ligands ranging from Schiff bases to heterocyclic ligands which invariably alter the structural and electronic properties of these metal complexes [**79**]. Such as in the case of the diamagnetic ruthenium complex, *cis*-[$RuCl_2(L_3)(PPh_3)$] (L_3 = 2-[(2-pyridylmethoxy)methyl]quinolone) which have shown to be an effective catalyst in the transfer hydrogenation of various ketones [**80**].

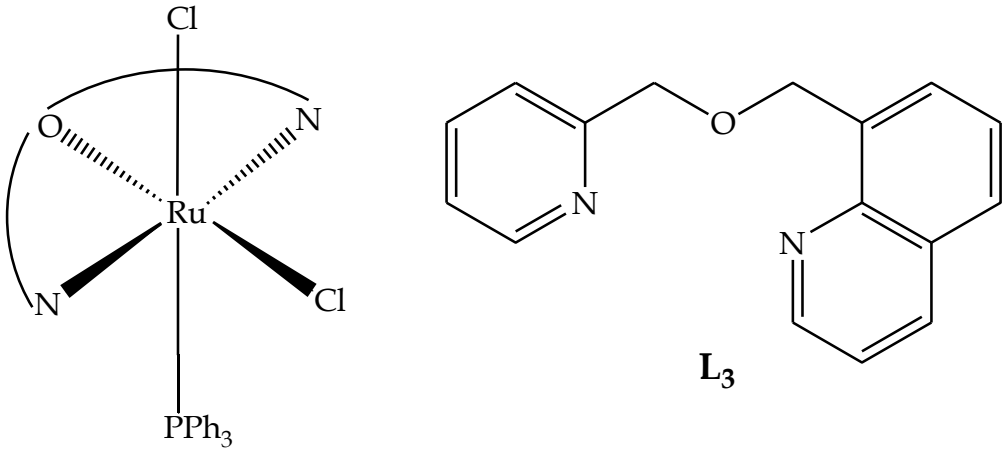

Figure 1.14: *Structure of the transfer hydrogenation catalyst, cis-*[$RuCl_2(L_3)(PPh_3)$].

1.6.3 *Ruthenium complexes with N, S-donor ligands*

Ruthenium complexes with multidentate ligands incorporating nitrogen and sulfur donors have been utilized in various applications owing to their diverse structural

features [**81**]. For example, in the ruthenium(II) carbonyl complex, *trans*-[RuH(CO)L_4(PPh_3)$_2$] (L_4 = 2-(3,4-dichlorobenzylidene)-*N*-ethylhydrazine carbothioamide), the L_4 ligand binds in a bidentate manner to the metal centre forming a four membered chelate ring [**82**] (see Figure 1.15). The emission spectra of this hydride complex afforded a single intra-ligand relaxation (at 411 nm) while two peak maxima (close to 415 and 460 nm) are observed in the chloride analogue, *trans*-[RuCl(CO)L_4(PPh_3)$_2$]. The electronic relaxations of the chloride complex was assigned to intra-ligand and metal-ligand-charge transfer electronic relaxations.

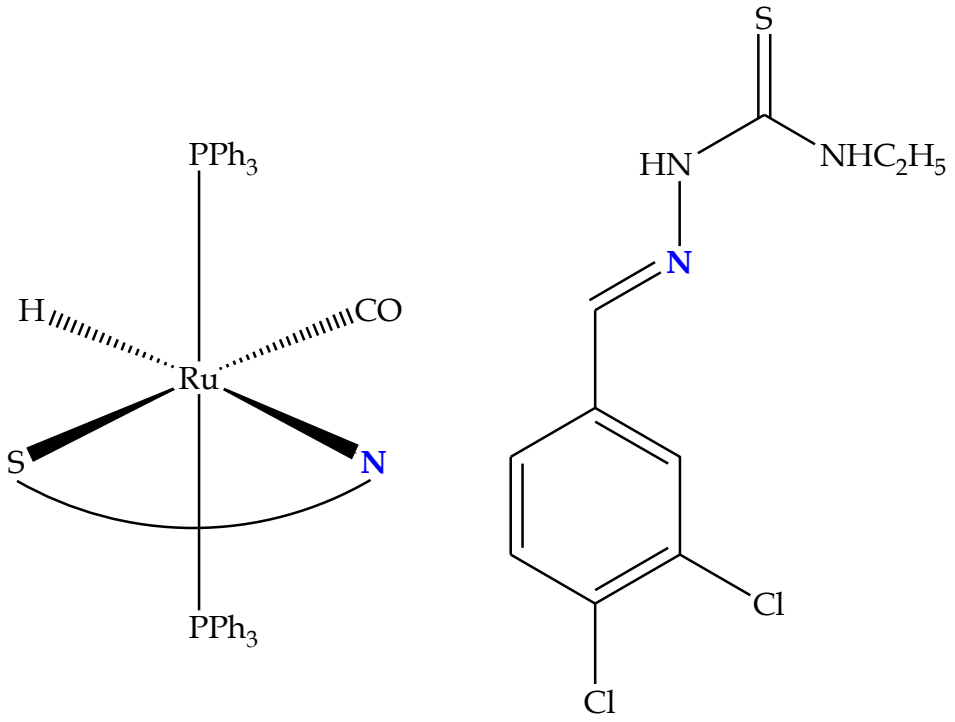

Figure 1.15: *Structures of trans-[RuH(CO)L_4(PPh_3)$_2$] and its free-ligand L_4. The coordinating nitrogen is shown in blue.*

1.7 References

1. W.P. Griffith, *Comprehensive Coordination Chemistry*, Vol.4, Pergamon Press, Oxford, 1987.
2. J. Emsley, *Nature's Building Block*, Oxford University Press, Oxford, 2001.
3. R.E. Krebs, *The History and Use of Our Earth's Chemical Elements*, 2nd ed., Greenwood Press, Westport, 2006.
4. J.W. Arblaster, *Platinum Metals Rev.,* 2011, **55**, 251.
5. G. Audi, O. Bersillon, J. Blachot, A.H. Wapstra, *Nuclear Physics A*., 2003, **729**, 3.
6. C. Bruneau, P.H. Dixneuf, *Ruthenium Catalyst and Fine Chemistry in*: Topics inOrganometallic Chemistry, Vol.11, 1st ed., Springer-Verlag, Berlin, 2004.
7. J.D. Hoeschele, J.E. Turner, M.W. England, *Sci. Total Environ*. 1991, **109/110**, 477.
8. M.L. Tobe, J. Burgess, *Inorganic Reaction Mechanisms,* 1st ed., Addison-Wesley Longman Inc., Essex, 1999.
9. J.G. Malecki, *Polyhedron*, 2010, **29**, 1237.
10. R.Prajapati, V.K. Yadav, S.K. Dubey, B. Durham, L. Mishra, *Ind. J.Chem*., **47A**, 1780.
11. C.E. Housecroft, *Comprehensive Coordination Chemistry II*, Vol.5, Elsevier, Oxford, 2004.
12. A. Levina, A. Mitra, P.A. Lay, *Metallomics*, 2009, **1,** 458.
13. P.J. Dyson, G. Sava, *Dalton Trans*., 2006, 1929.
14. M.J. Clarke, *Coord. Chem. Rev*., 2002, **232**, 69.
15. A. Levina, A. Mitra, P.A. Lay, *Metallomics*, 2009, **1**, 458
16. V. Brabec, O. Novakova, *Drug. Resist. Updat*., 2006, **9**, 111
17. C.S. Allardyce, P.J. Dyson, *Platin. Met. Rev*., 2001, **45**, 62.
18. L. Racane, V. Tralic-Kulenovic, L. Fiser-Jakic, D.W. Boykin, *Heterocycles*, 2001, **55**, 2085.

19. W. Ramanpreet, M.D. Hedaitullah, F.S. Naaz, K. Iqbal, H.S. Lamba, *IJRPC*, 2011, **1**, 565.

20. M.L. McKee, S.M. Kerwin, *Bioorg. Med. Chem*., 2008, **16**, 1775.

21. E. Bellur, I. Freifield, P. Langer, *Tetrahedron Lett*., 2005, **47**, 2151.

22. F.A. Davis, K. Bowen, H. Xu, V. Velvadapu, C. Ballard, *Tetrahedron*, 2008, **64**, 4174.

23. M. Reisser, G. Maas, *J. Org. Chem*., 2004, **69**, 4913.

24. D. Li, H. Zang, C. Wu, N.Q. Yu, *Ultrason. Sonochem*., 2013, **20**, 1144.

25. J.T. Gupton, *Top. Heterocycl. Chem*., 2006, **2**, 53.

26. H. Fan, J. Peng, M.T. Hamann, J.F. Hu, *Chem. Rev*., 2008, **108**, 264.

27. P. Mathew, C.V. Asokan, *Tetrahedron*, 2006**, 62**, 1708.

28. B. Wang, Z. Yang, M. Lu, J. Hai, Q. Wang, Z. Chen, *J. Organomet. Chem*., 2009, **694**, 4069.

29. F. Colobert, R. Mazery, G. Solladie, M.C. Carreno, *Org. Lett*., 2002, **4**, 1723.

30. T. Takeuchi, M. Matsuhashi, T. Nakata, *Tetrahedron Lett*., 2008, **49**, 6462.

31. C.J. Forsyth, F. Ahmed, R.D. Cink, C.S. Lee, *J. Am. Chem. Soc*., 1998, **120**, 5597.

32. M. Fischer, A. Bacher, *Biochem. Biophys*., 2008, **474**, 252.

33. X. Huang, H.M. Holden, F.M. Raushel, *Annu. Rev. Biochem*. 2001, **70**, 149.

34. M. Malet-Martino, P. Jolimaitre, R. Martino, *Curr. Med. Chem*., 2002, **2**, 267.

35. J. Wilkinson, M. Bourne, M. Isreals, *Br. Med. J*., 1963, **1**, 1563.

36. I.N. Booysen, S. Maikoo, M.P. Akerman, B. Xulu, *Polyhedron*, 2014, **79**, 250.

37. G.C. Mohamed, M.M. Omar, A.M. Hindy, *Turk. J. Chem*., 2006, **30**, 361.

38. L.L. Koh, J.O. Ranford, W.T. Robinson, J.O. Svensson, A.L. Choo Tan, D. Wu, *Inorg. Chem*., 1996, **35**, 6466.

39. A.M. Abu-Dief, I.M.A. Mohamed, *BJBAS,* 2015, **4**, 119.

40. R.M. Maurya, A. Kumar, M. Ebel, D. Rehder, *Inorg. Chem.*, 2006, **45**, 5924.

41. I. Booysen, T.I.A. Gerber, E. Hosten, P. Mayer, *Inorg. Chem. Commun.*, 2008, **11**, 33.

42. S. Fan, J. Shen, H. Wua, K. Wang, A. Zhang, *Chin. Chem. Lett.*, 2015, **26**, 580.

43. Q. Lam, M. Kato, L. Cheruzel, *Biochim. Biophys. Acta,* 2015, http://dx.doi.org/10.1016/j.bbabio.2015.09.004.

44. H. Sugihara, S. Sano, T. Yamaguchi, M. Yanagida, T. Sato, Y. Abe, Y. Nagao, H. Arakawa, *J. Photochem. Photobio. A*, 2004,**166**, 81.

45. A.F. Shoair, A.R. El-Shobaky, H.R. Abo-Yassin, *J. Mol. Liq.*, 2015, **211**, 217.

46. M. Navidi, B. Movassagh, S. Rayati, *Appl. Catal. A*, 2013, **452**, 24.

47. M. Salavati-Niasari, M. Bazarganipour, *J. Mol. Catal. A: Chem.*, 2007, **278**, 173.

48. C. Baleizão, B. Gigante, H. Garcia, A. Corma, *J. Catal.*, 2004, **221**, 77.

49. M. Bazarganipour, M. Salavati-Niasari, *Appl. Catal. A*, 2015, **502**, 57.

50. S. Medici, M. Peana, V.M. Nurchi, J. Izabela, G. Crisponi, M.A. Zoroddu, *Coord.Chem. Rev.*, 2015, **284**, 329.

51. F. Arnesano, A. Pannunzio, M. Coluccia, G. Natile, *Coord.Chem. Rev.*, 2015, **284**, 286.

52. S.R. Mcwhinney, R.M. Goldberg, H.L. Mcleod, *Mol. Cancer Ther.*, 2009, **8**, 10.

53. M.J. Mckeage, *Drug Saf.*, 1995, **13**, 228.

54. J. Reedijk, *Proc. Natl. Acad. Sci.*, 2003, **100**, 3611.

55. F. Kratz, L. Messori, *J. Inorg. Biochem.*, 1993, **49**, 79.

56. I. Bratsos, S. Jedner, T. Gianferrara, E. Alessio, *Chimia*, 2007, **61**, 692.

57. G. Prakash, R. Manikandan, P. Viswanathamurthi, K. Velmurugan, R. Nandhakumar, *J. Photochem. Photobio. B*, 2014, **138**, 63.

58. C.O. Malecot, V. Bito, J.A. Argibay, *Br. J. Pharmacol.*, 1998, **124**, 465.

59. R. Dierichs, *Histochemistry*, 1979, **64,** 171.

60. J.R. Durig, J. Danneman, W.D. Behnke, E.E. Mercer, *Chem. Biol. Interact.* 1976, **13**, 287.

61. E. Alessio, G. Mestroni, A. Bergamo, G. Sava, *Curr. Top. Med. Chem.*, 2004, **4**, 1525.

62. G. Sava, I. Capozzi, K. Clerici, G. Gagliardi, E. Alessio, G. Mestroni, *Clin. Exp. Metastasis,* 1998, **16**, 371.

63. G. Sava, S. Zorzet, C. Turrin, F. Vita, M. Soranzo, G. Zabucchi, M. Cocchietto, A. Bergamo, S. DiGiovine, G. Pezzoni, L. Sartor, S. Garbisa, *Clin. Cancer Res.* 2003, **9**, 1898.

64. A. Vacca, M. Bruno, A. Boccarelli, M. Coluccia, D. Ribatti, A. Bergamo, S. Garbisa, L. Sartor, G. Sava, *Br. J. Cancer,* 2002, **86**, 993.

65. S. Kapitza, M. Pongratz, M.A. Jakupec, P. Heffeter, W. Berger, L. Lackinger, B.K. Keppler, B. Marian, *J. Cancer. Res. Clin. Oncol.,* 2005, **131**, 101.

66. W.H. Ang, P.J. Dyson, *Eur. J. Inorg. Chem.*, 2006, **20**, 4003.

67. C. Scolaro, A. Bergamo, L. Brescacin, R. Delfino, M. Cocchietto, G. Laurenczy, T.J. Geldbach, G. Sava, P.J. Dyson, *J. Med. Chem.*, 2005, **48**, 4161.

68. A. Bergamo, A. Masi, P.J. Dyson, G. Sava, *Int. J. Oncol.,* 2008, **33**, 1281.

69. S. Chakraborty, P. Munshi, G.K. Lahiri, *Polyhedron*, 1999, **18**, 1437.

70. A. Mijatovic, B. Smit, A. Rilak, B. Petrovic, D. Canovic, *Inorg. Chim. Acta*, 2013, **394**, 552.

71. J.A. Moore, J.H. Acquaye, *Polyhedron*, 2009, **28**, 386.

72. I.N. Booysen, S. Maikoo, M.P. Akerman, B. Xulu, *Polyhedron*, 2014, **79**, 250.

73. I.N. Booysen, S. Maikoo, M.P. Akerman, B. Xulu, O. Munro, *J. Coord. Chem.*, 2013, **66**, 3673.

74. S. Choi, D. Ryu, J.G. DellaRocca, M.W. Wolf, J.A. Bogart, *Inorg. Chem.*, 2011, **50**, 6567.

75. M. Kapovsky, C. Dares, E.S. Dodsworth, R.A. Begum, V. Raco, A.B.P. Lever, *Inorg. Chem.*, 2013, **52**, 169.

76. N. Ljubijankic, A. Zahirovic, E. Turkusic, E. Kahrovic, *Croat. Chem. Acta.* 2013, **86**, 215.

77. J.G. Hernández, P. Thangarasu, H. Höpfl, J. Cruz, M. Serrano-Ruiz, A. Romerosa, *Inorg. Chim. Acta,* 2015, **431**, 258.

78. K.K. Raja, N.I. Gandhi, L. Lekha, D. Easwaramoorthy, G. Rajagopal, *J. Mol. Struct.* 2014, **1060**, 49.

79. T. Opstal, F. Verpoort, *Angew Chem. Int. Ed.*, 2003, **42**, 2876.

80. H. Xu, X. Lu, Y. Li, X. Chen, Z. Xue, *Inorg. Chim. Acta,* 2009, **362**, 4774.

81. A.K. Pramanik, T.K. Mondal, *Inorg. Chim. Acta,* 2014, **411**,106.

82. J.G. Małecki, A. Maron, M. Serda, J. Polanski, *Polyhedron*, 2013, **56**, 44.

Chapter 2

Materials and Methods

2.1 Handling of Ruthenium

Ruthenium tetroxide (RuO_4) is typically formed when acidic solutions containing ruthenium are oxidized rapidly by good oxidants like MnO_4^- or hot $HClO_4$ [**1**]. Alternatively, when ruthenium compounds are heated in air, this can potentially lead to the formation of RuO_4 which is poisonous, volatile and may cause damage to the eyes as well as the respiratory system [**2**]. On that account, special precautions were taken into consideration during the handling of all ruthenium compounds including the use of latex gloves, a nose mask as well as a fume cupboard in which all the coordination reactions were carried out.

2.2 Materials

2.2.1 Metal precursor

The metal precursor *trans*-$[RuCl_2(PPh_3)_3]$ (97% purity) was obtained from Sigma-Aldrich and no further purification was conducted on this chemical.

2.2.2 Commercially acquired chemicals

All solvents and common salts were obtained from Merck SA. Reagent grade toluene was dried over sodium wire while other solvents and chemicals that were purchased from Sigma-Aldrich were used without any further purification. Ultrapure water was produced from an Elga Purelab Ultra system.

Table 2.1: *List of chemicals attained from Sigma-Aldrich.*

Name	Purity
2-aminobenzothiazole	98%
2-aminobenzimidazole	97%
2-aminobenzoxazole	98%
Salicylaldehyde	98%
2-pyridylaldehyde	99%
2-thiophene-carboxaldehyde	98%
2-chloromethylbenzimidazole	98%
2-aminophenol	98%
2-amino-3-formylchromone	97%
Tetrahydro-2*H*-pyran-4-amine	97%
2,6-dicarboxaldehydepyridine	97%
1,2-diaminobenzene	99%
3-formylchromone	97%
Pyrrole-2-carboxaldehyde	98%
Tris-(2-aminoethyl)amine	96%
6-amino-1,3-dimethyl-5-nitrosouracil	98%
Acetylacetone	98%
Benzhydrazide	98%
Hydroxylamine hydrochloride	99%
Piperidine	98%
Sodium tetraborohydrate	98%
Tetrabutylammonium hexafluorophosphate	99%
2,2-di(4-tert-octylphenyl)-1-picrylhydrazyl (DPPH)	98%
Griess reagent	98%
Sodium nitroprusside	98%

2.3 Methods

The infrared spectra were recorded on a Perkin-Elmer Spectrum 100 in the 4000 – 350 cm^1 range. The ^1H and ^{31}P NMR spectra were obtained using a Bruker Avance 400 MHz spectrometer. All NMR spectra were recorded in DMSO-d_6. UV-visible spectra were recorded using a Perkin Elmer Lambda 25. The extinction coefficients (ε) are given in M^{-1} cm^{-1}. The X-band electron paramagnetic resonance (EPR) spectra were obtained at 298 K from a Bruker EMX Ultra X-band spectrometer. Melting points were determined using a Stuart SMP3 melting point apparatus. Mass spectral analysis of the complexes was done both in positive and negative modes *via* the direct injection of the respective samples into the Water Micromass LCT Premier instrument equipped with a Time-of-Flight (TOF) Mass spectrometer analyzer and an Electron Spray Ionization (ESI) source. Elemental composition of the complexes was determined using ThermoScientific Flash 2000 CHNS/O Analyser. The conductivity measurements were determined at 295 K on a Radiometer R21M127 CDM 230 conductivity and pH meter. A solution of 0.745 g KCl in 1 L of ultrapure water was used as the standard solution.

Voltammetry measurements were done using an Autolab potentiostat equipped with a three electrode system: a glassy carbon working electrode (GCWE), a pseudo Ag|AgCl reference electrode and an auxiliary Pt counter electrode. The Autolab Nova 1.7 software was utilized for the operation of the potentiostat and data analysis. The ruthenium complexes were made up in 2mM solutions along with tetrabutylammonium hexafluorophosphate (0.1 M) as a supporting electrolyte. Between each measurement, the GCWE electrode surface was polished with a slurry of ultrapure water and alumina on a Buehler felt pad followed by rinsing with excess ultrapure water and ultra-sonication in absolute ethanol. Spectroelectrochemical data were attained using a room temperature Specac optically transparent thin-layer electrochemical (OTTLE) cell purchased from the University of Reading which was connected to the Autolab potentiostat.

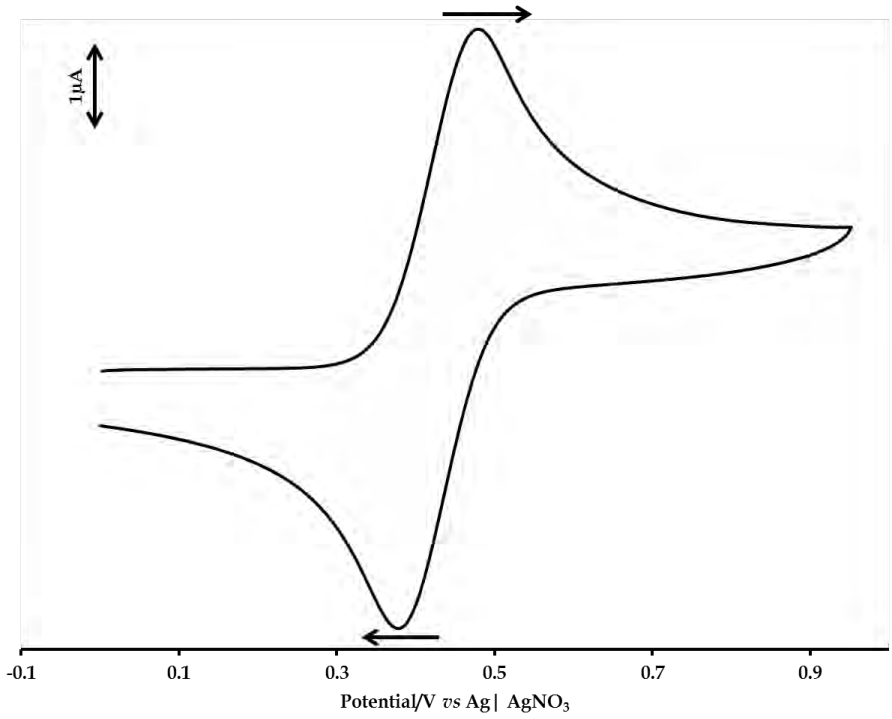

Figure 2.1: *Cyclic Voltammogram for the Ferrocene Standard at 100 mV/s with the arrows showing scan direction.*

The experimental procedures of the radical scavenging studies were adapted from literature methods [**3**, **4**]. All experiments were run in triplicate and the percentage radical scavenging activities were determined *via* the following equation:

% Radical scavenging activity = $[(A_c - A_f) / A_c] \times 100$

where A_c is the absorbance of the control (DPPH or NO radicals) and A_f is the absorbance upon addition of the ligand or metal complex to the control. In turn, the IC_{50} values of the respective ligands and their metal complexes were calculated from the individual percentage radical scavenging activities. Firstly, the UV-vis spectrum of the control (0.2 mM solution of DPPH) was measured and thereafter a 0.1 cm^3aliquot of the metal complex or the free ligand [30 μM] were added. The resultant solutions were

shaken vigorously, left to stand for 20 minutes in the dark and thereafter their respective UV-vis spectra were measured.

The NO radical assay was done using the following experimental procedure: A 5 mM solution of sodium nitroprusside was prepared in a phosphate buffered saline solution. After an incubation period of 3 hrs, the Griess reagent (0.5 cm^3) was added to 0.3 cm^3 of the nitroprusside solution. The UV-vis spectrum of this mixture was taken (which constitutes the "control"). The sample solutions were prepared by adding 0.3 cm^3 of sodium nitroprusside solution to 1 cm^3 of the metal complex or the free ligand (30 μM in DMSO) and allowing the resultant mixtures to incubate for 3 hrs at room temperature. After the incubation period, 0.5 cm^3 of the Griess reagent was added which was followed by analysis through UV-vis spectroscopic measurements.

The X-ray data for the metal complexes were recorded on a Bruker Apex Duo equippedwith an Oxford Instruments Cryojet operating at 100(2) K and an Incoatec microsource operating at 30W power. Data was collected with Mo Kα (λ = 0.71073 Å) radiation at a crystal-to-detector distance of 50 mm. The following conditions were used for data collection: omega and phi scans with exposures taken at 30 W X-ray power and 0.50° frame widths using APEX2 [**5**]. The data were reduced with the program SAINT [**5**] using outlier rejection, scan speed scaling, as well as standard Lorentz and polarization correction factors. A SADABS semi-empirical multi-scan absorption correction [**6**] was applied to the data. Direct methods, SHELX-2014 [**7**] and WinGX [**8**] were used to solve all structures.

Computational calculations were conducted using the Gaussian 09W software [**9**]. The geometry optimization of metal complexes **1** in Chapter 6 were accomplished at the DFT level using the B3LYP functional, with an accompanying hybrid basis set viz. the 6-

311G^{++} (*d, p*) basis set was applied to all the C, H, N, O, Cl and P atoms and the LANL2DZ basis set, which makes use of effective core potentials, applied to the metal center [**10**]. Prior to the calculation, the solvent molecules of recrystallization for **1** were omitted from the crystal structure and the resultant structure was used as the starting conformer. Good agreement was found between the optimized and geometrical parameters with the minor deviations attributed to the fact that gas phase optimized structures do not account for non-classical hydrogen bonding interactions or any short distance contacts. Using the optimized structure of the metal complex, the lack of any negative Eigen values in the frequency calculations confirmed that the structure is at a global minimum on the potential energy surface [**11**]. The simulated electronic spectrum of **1** was computed using Time Dependent (TD)-DFT calculations using the aforementioned functional and hybrid basis set.

2.4 References

1. M. Ullah, *Am. J. Pharmacol. Toxicol*., 2015, **10**, 13.
2. R. Hemmatzadeh, A. Mohammadi, *J. Theor. Appl. Phys.*, 2013, **7**, 57.
3. P. Krishnamoorthy, P. Sathyadevi, K. Senthilkumar, P. Thomas Muthiah, R. Ramesh, N. Dharmaraj, *Inorg. Chem. Commun.,* 2011, **14**, 1318.
4. R. Ramachandran, P. Viswanathamurthi, *Spectrochim. Acta A*, 2013, **103**, 53.
5. Bruker APEX2, SAINT and SADABS. Bruker AXS Inc., 2010, Madison, Wisconsin, USA.
6. R.H. Blessing, *Acta Crystallogr.,Sect. A: Found. Crystallogr.,* 1995, **A51**, 33.
7. G.M. Sheldrick, *Acta Crystallogr.,Sect. A: Found. Crystallogr.,* 2008, **A64**, 112.
8. L.J. Farrugia, *J. Appl. Cryst.,*2012, **45**, 849.

9. M.J. Frisch, G.W. Trucks, H.B. Schlegel, G.E. Scuseria, M.A. Robb, J.R. Cheeseman, G. Scalmani, V. Barone, B. Mennucci, G.A. Petersson, H. Nakatsuji, M. Caricato, X. Li, H.P. Hratchian, A.F. Izmaylov, J. Bloino, G. Zheng, J.L. Sonnenberg, M. Hada, M. Ehara, K. Toyota, R. Fukuda, J. Hasegawa, M. Ishida, T. Nakajima, Y. Honda, O. Kitao, H. Nakai, T. Vreven, J.A. Montgomery, J.E. Peralta, F. Ogliaro, M. Bearpark, J.J. Heyd, E. Brothers, K.N. Kudin, V.N. Staroverov, R. Kobayashi, J. Normand, K. Raghavachari, A. Rendell, J.C. Burant, S.S. Iyengar, J. Tomasi, M. Cossi,N. Rega, J.M. Millam, M. Klene, J.E. Knox, J.B. Cross, V. Bakken, C. Adamo, J. Jaramillo, R. Gomperts, R.E. Stratmann, O. Yazyev, A.J. Austin, R. Cammi, C. Pomelli, J.W. Ochterski, R.L. Martin, K. Morokuma, V.G. Zakrzewski, G.A. Voth, P. Salvador, J.J. Dannenberg, S. Dapprich, A.D. Daniels, Ö. Farkas, J.B. Foresman, J.V. Ortiz, J. Cioslowski, D.J. Fox, *Gaussian 09 (Revision A.01)*, 2009, Gaussian Inc., Wallingford CT.

10. A.O. Ogweno, S.O. Ojwach, M.P. Akerman, *Dalton Trans*., 2014, **43**, 1228.

11. K.C. Potgieter, T.I.A. Gerber, R. Betz, L. Rhyman, P. Ramasami. *Polyhedron*, 2013, **59**, 91.

Chapter 3

Ruthenium(II) and -(III) complexes with Schiff base ligands containing Benz(othiazole/imidazole/oxazole) moieties: Structural, Electron Spin Resonance and Electrochemistry studies

3.1 Introduction

The discovery of NAMI-A, *trans*-[$RuCl_4$(DMSO)(Im)](ImH) {ImH = imidazole} as a potential metallopharmaceutical for metastatic cancer, has led to a renewed interest into the medicinal inorganic chemistry of ruthenium [**1-7**]. In particular, ruthenium complexes with N-donor heterocyclic ligands have been widely investigated due to their diverse biological activities [**8-12**]. From a coordination chemistry perspective, this class of ligand systems afford ruthenium complexes with unique coordination environments, owing to the diverse donor atom combinations and resulting metal chelation [**13-16**].In addition, they can have variable stereo-electronic properties arising from their ability to form neutral or multivalent anionic N-donor chelators which inevitably allows for stabilization of the metal centre both in low and high oxidation states [**8-20**].

In this chapter, we report the reactions of *trans*-[$RuCl_2(PPh_3)_3$] with the Schiff bases derived from heterocyclic moieties [*N*-((pyridine-2-*yl*)methylene)-1*H*-benzimidazole (bzpy), *N*-(2-hydroxybenzylidene)-benzothiazole (Hbsp) , *N*-(2-hydroxybenzylidene)-benzimidazole (Hbzp) and *N*-((thiophene-2-*yl*)methylene)-benzoxazole (bxth)] (see

Figure 3.1) to afford the ruthenium complexes: *cis*-[$Ru^{II}Cl_2$(bzpy)(PPh_3)$_2$] (**1**), [RuCl(bsp)$_2$(PPh_3)] (**2**), *trans*-[RuCl(bzp)(PPh_3)$_2$] (**3**) and *cis*-[$Ru^{II}Cl_2$(bxth)(PPh_3)$_2$] (**4**), respectively. Despite the similar skeletal structures of the ligands, ruthenium complexes with diverse structural features were isolated. This diversity is also manifested in their redox and electronic properties.

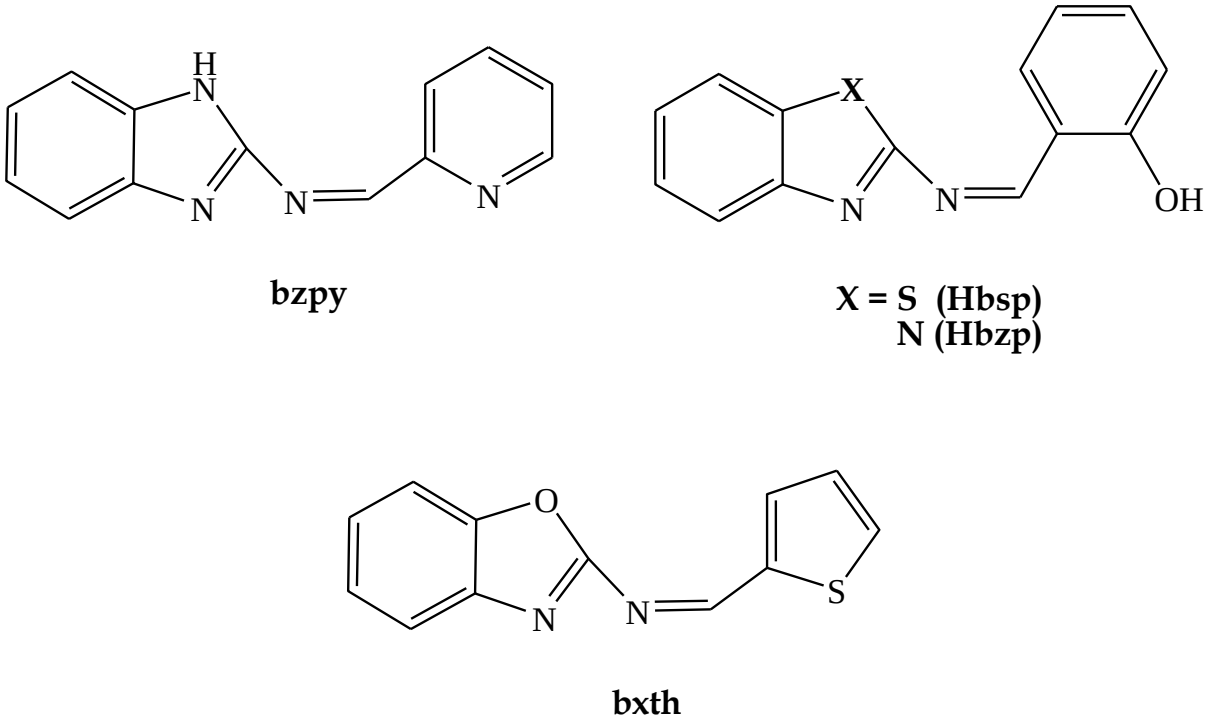

bzpy

X = S (Hbsp)
N (Hbzp)

bxth

Figure 3.1: *Structures and their corresponding abbreviations of the Schiff bases containing benz(othiazole/imidazole/oxazole) moieties.*

3.2 Experimental

3.2.1 Synthesis of ligands:

3.2.1.1 N-((pyridine-2-yl)methylene)-1H-benzimidazole (bzpy)

A mixture of 2-aminobenzimidazole (0.50 g; 3.76 mmol) and 2-pyridinecarboxaldehyde (0.40 g; 3.76 mmol) was heated at reflux temperature for 3 hours in methanol (20 cm^3),

along with 1 cm^3 of piperidine. The resulting yellow solution was allowed to cool to room temperature and concentrated under reduced pressure. Afterwards, dry toluene (40 cm^3) was added to the solution and heated to reflux for 6 hours with a Dean-Stark apparatus. A yellow precipitate was filtered and washed with cold anhydrous toluene. Yield = 75 %; M.P. 236 – 238 °C; IR (ν_{max}/cm^{-1}): ν(N-H) 3051 (w), ν(C=N) $_{Schiff\ base}$ 1612 (s), ν(C=N)$_{Heterocyclic}$ 1587 (s); ^{1}H NMR (295K/ppm/d^6-DMSO): 12.82 (br, s, 1H, N*H*), 9.36 (s, 1H, *H6*), 8.80 (d, 1H, *H1*), 8.03 (t, 1H, *H3*), 7.67 – 7.46 (m, 3H, *H2*, *H10*, *H11*), 7.24 – 7.17 (m, 2H, *H9*, *H12*);^{13}C NMR (295 K/ppm/d^6-DMSO): 165.50, 153.67, 150.71, 137.82, 127.01, 122.81, 122.16; UV–Vis (DCM, λ_{max}/nm (ε, $M^{-1}cm^{-1}$)): 255 (sh, 2300); 284 (1980); 360 (2480).

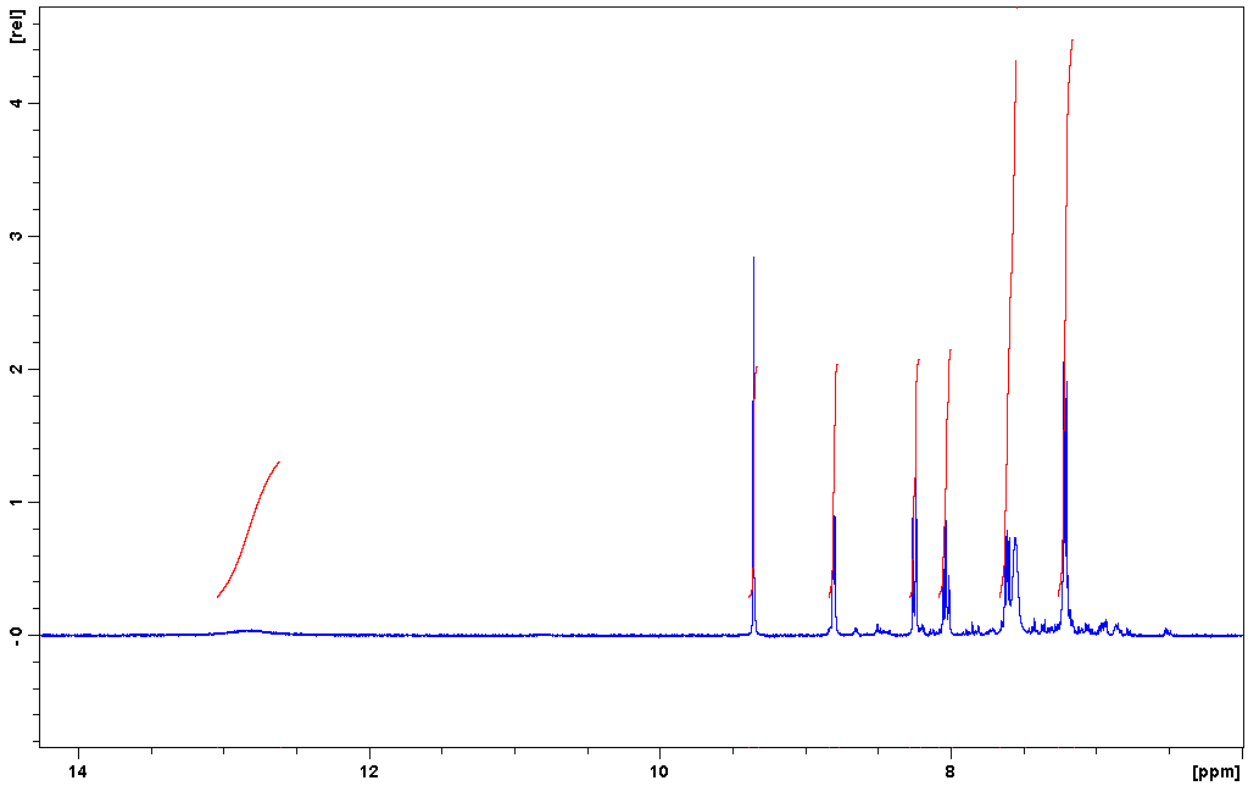

Figure 3.2: *^{1}H NMR spectrum of bzpy.*

3.2.1.2 *N-(2-hydroxybenzylidene)-benzothiazole (Hbsp) and N-(2-hydroxybenzylidene)-benzimidazole (Hbzp)*

The titled Schiff bases derived from salicylaldehyde were isolated from adapted experimental procedures attained from literature [**21, 22**].For Hbsp and Hbzp, the respective (1:1 molar ratio) condensation reactions of salicylaldehyde with 2-aminobenzothiazole and 2-aminobenzimidazole were conducted in dry toluene heated until reflux under a nitrogen atmosphere and in the presence of catalytic amounts of piperidine.

3.2.1.3 *N-((thiophene-2-yl)methylene)-benzoxazole (bxth)*

A reaction mixture of 2-aminobenzoxazole (0.50 g; 3.73 mmol) and 2-thiophenecarboxaldehyde (0.50 g; 4.47 mmol) was heated until reflux for 3 hours in methanol (20 cm^3), along with 1 cm^3 of piperidine. The resulting yellow solution was allowed to cool to room temperature and concentrated under reduced pressure. Afterwards, dry toluene (40 cm^3) was added to the solution and the latter was heated to reflux for 6 hours with a Dean-Stark apparatus. The yellow solution was cooled in an ice bath to give a yellow precipitate which was filtered and washed with petroleum ether. Yield = 72%; M.P. 134 - 137°C; IR (ν_{max}/cm^{-1}): ν(C=N) 1580 (vs), ν(thiophene)1503, 1450, 1416 (s);^{1}H NMR (295K/ppm/d^6-DMSO): 9.55 (s, 1H, *H1*), 8.08 – 8.14 (dd, 2H, *H2, H3*), 7.64 – 7.73 (m, 2H, *H4, H5*), 7.33 - 7.40(m, 3H, *H6, H7, H8*). UV–Vis (DCM, λ_{max}/nm (ε, $M^{-1}cm^{-1}$)): 286 (10191); 369 (1980); 360 (26439).

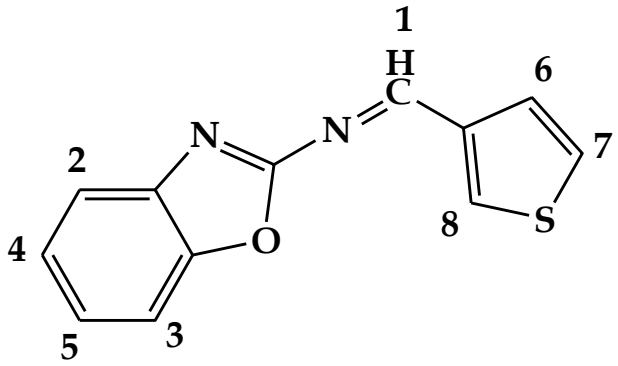

Figure 3.3: *Numbering scheme for bxth.*

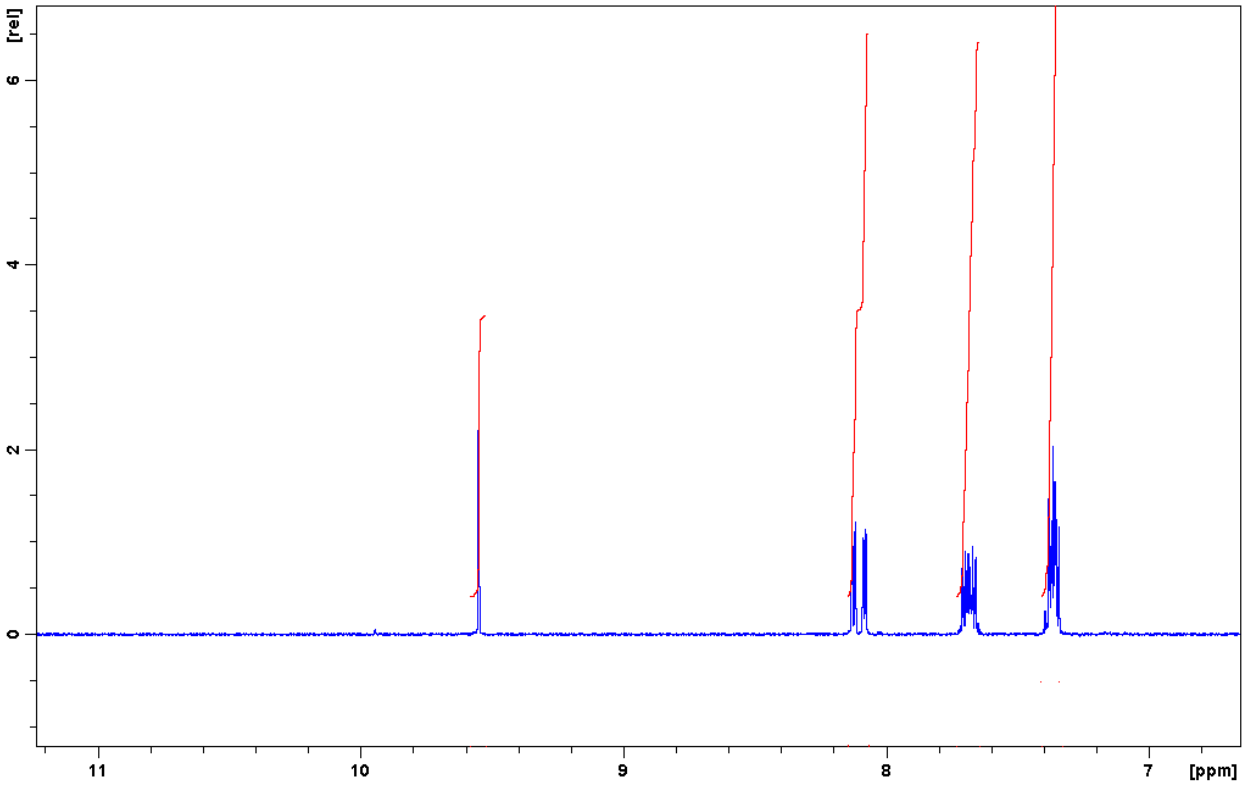

Figure 3.4: *^{1}H NMR spectrum of bxth.*

3.2.2 *Synthesis of metal complexes*

3.2.2.1 *Cis-Cl, trans-P [$RuCl_2(bzpy)(PPh_3)_2$] (**1**)*

A mixture of bzpy (0.0304 g; 0.1368 mmol) and *trans*-[$RuCl_2(PPh_3)_3$] (0.100 g; 0.1368 mmol) in dry toluene (20 cm^3) was heated to reflux under a nitrogen atmosphere for 6 hours (hrs). The volume of the resultant dark brown solution was reduced to half and then *n*-hexane was added dropwise to induce precipitation. In turn, the dark brown precipitate was recrystallized *via* slow diffusion in a dichloromethane and *n*-hexane [1:1 (*v*:*v*)] solution which resulted in the formation of dark brown XRD quality parallelograms. Yield = 63 %; M.P. > 350 °C; IR (ν_{max}/cm^{-1}): ν(N-H) 3067 (w), ν(C=N)$_{Heterocyclic}$ 1635 (s), ν(C=N)$_{Schiff\ base}$ 1606 (s), ν(Ru-[PPh_3]$_2$) 696 (s); ^{1}H NMR (295K/ppm/d^6-DMSO): 8.97 (s, 1H, *NH*), 8.47 (s, 1H, *H6*), 7.66 – 7.60 (m, 4H, *H1, H2, H3, H4*), 7.58 – 7.54 (m, 4H, *H9, H10, H11, H12*), 7.43 – 7.38 (m, 15H, PPh_3), 7.27 – 7.22 (m, 15H, PPh_3); ^{31}P NMR (295K/ppm/d^6-DMSO): 25.57; UV-Vis (DCM, (λ_{max}/nm (ε, $M^{-1}cm^{-1}$))): 301 (12800); 358 (sh, 10056); 410 (sh, 7620); 435 (sh, 5484); 576 (3218); Conductivity (DCM, 10^{-3} M): 15.51 $ohm^{-1}cm^{-2}mol^{-1}$; Calcd for $C_{49}H_{40}Cl_2N_4P_2Ru$: C, 64.05; H, 4.39; N, 6.10%. Found: C, 63.97; H, 4.01; N, 6.32; TOF-MS (*m/z*): Calcd: 918.11 [M]; Found: 848.16 [M-2Cl].

3.2.2.2 *[$RuCl(bsp)_2(PPh_3)$] (**2**)*

A two molar ratio of Hbsp (0.0695 g; 0.2736 mmol) with respect to the metal precursor, *trans*-[$RuCl_2(PPh_3)_3$] (0.100 g; 0.1368 mmol) were reacted together in refluxing toluene (20 cm^3) for 6 hrs. After the addition of 10 cm^3 acetonitrile to the mother liquor and from the slow evaporation of the resultant mixture, dark brown crystals were attained for X-ray analysis. Yield = 66 %; M.P. = 236 – 238 °C; IR (ν_{max}/cm^{-1}): ν(C=N)$_{Schiff\ Base}$ 1588 (m), ν(C=N)$_{Heterocyclic}$ 1531 (m), ν(C=C)1435 (s), ν(Ru-PPh_3) 693 (s); UV-Vis (DCM, (λ_{max}/nm (ε, $M^{-1}cm^{-1}$))): 279 (sh, 16198); 328 (sh, 10862); 524 (1789); 705 (795); Conductivity (DCM,

10^{-3} M): 19.38 $ohm^{-1}cm^{-2}mol^{-1}$; Calcd for $C_{46}H_{33}ClN_4O_2PRuS_2$: C, 61.02; H, 3.67; N, 6.19%. Found: C, 60.56; H, 4.01; N, 6.39%; TOF-MS (*m/z*): Calcd: 905.05 [M]; Found: 905.05 [M].

*3.2.2.3 Trans-[RuCl(bzp)(PPh_3)$_2$](**3**)*

The title compound was formed from the 1:1 molar ratio reaction of Hbzp (0.0324 g; 0.1368 mmol) and *trans*-[$RuCl_2(PPh_3)_3$] (0.1002 g; 0.1368 mmol) in (20 cm^3) toluene (after 6 hrs of refluxing). From the slow evaporation of the mother liquor, brown needle-like crystals suitable for X-ray analysis were obtained after 3 days. Yield = 71 %; M.P. = 256 – 258 °C; IR (ν_{max}/cm^{-1}): ν(N-H) 3062 (w), ν(C=N)$_{Schiff\ Base}$ 1679 (m), ν(C=N)$_{Heterocyclic}$ 1589 (m), ν(C=C)1433 (m), ν[Ru-(PPh_3)$_2$] 691; UV-Vis (DCM, (λ_{max}/nm (ε, $M^{-1}cm^{-1}$))): 270 (sh, 17891); 320 (sh, 10863); 385 (sh, 7029); 544 (sh, 1790); 692 (863); Conductivity (DCM, 10^{-3} M): 28.74 $ohm^{-1}cm^{-2}mol^{-1}$; Calcd for $C_{57}H_{47}P_2ClRuON_3$: C, 69.26; H, 4.79; N, 4.25%. Found: C, 68.87; H, 4.54; N, 4.75%; TOF-MS (*m/z*): Calcd: 896.13 [M]; Found: 895.14 [M-H].

*3.2.2.4 Cis-Cl, trans-P [$RuCl_2$(bxth)(PPh_3)$_2$](**4**)*

To a solution of bxth (0.0238 g; 0.104 mmol) in 10 cm^3 of toluene and *trans*-[$RuCl_2(PPh_3)_3$] (0.100 g; 0.1368 mmol) in toluene (10 cm^3) was heated until reflux for 6 hrs. After cooling to room temperature, the solution was filtered and allowed to evaporate slowly at room temperature. After 2 days, dark brown crystalline material was collected by filtration, washed with diethyl ether and dried under vacuum. Yield = 56%; M.P. = 232 – 235 °C; IR (ν_{max}/cm^{-1}): ν(C=N) 1536 (w), ν(thiophene)1481, 1432, 1392 (m), ν[Ru-(PPh_3)$_2$]692 (vs); ^{1}H NMR (295K/ppm/d^6-DMSO): 7.66 – 7.54 (m, 4H, *H2, H3, H4, H5*), 7.45 – 7.38 (m, 15H, PPh_3), 7.28 – 7.21 (m, 15H, PPh_3) 7.20 – 7.14 (m, 3H, *H6, H7, H8)*; ^{31}P NMR (295K/ppm/d^6-DMSO): 25.58; UV-Vis (DCM, (λ_{max}/nm (ε, $M^{-1}cm^{-1}$))): 286 (12612); 310 (11413); 362 (sh, 7994); 416 (sh, 2040); 476 (sh, 909); Conductivity (DCM, 10^{-}

^{3}M): 35.90 ohm^{-1}cm^{-2}mol^{-1}; Calcd for $C_{48}H_{38}Cl_2N_2OP_2RuS.C_7H_8$: C, 64.96; H, 4.56; N, 2.75%. Found: C, 64.60; H, 4.55; N, 2.51%; TOF-MS (*m/z*): Calcd: 924.82 [M]; Found: 591.04 [M-2Cl-1PPH$_3$].

3.3 X-ray diffraction

The X-ray data for the metal complexes **1-3** were recorded on a Bruker Apex Duo equipped with an Oxford Instruments Cryojet operating at 100(2) K and an Incoatec microsource operating at 30 W power. Crystal and structure refinement data are given in Table 3.3 while the selected bond lengths and angles are given in Tables 3.4, 3.5 and 3.6. In all three cases the data were collected with Mo Kα (λ = 0.71073 Å) radiation at a crystal-to-detector distance of 50 mm. The following conditions were used for the Bruker data collection: omega and phi scans with exposures taken at 30 W X-ray power and 0.50^{o} frame widths using APEX2 [**23**]. The data were reduced with the programme SAINT [**23**] using outlier rejection, scan speed scaling, as well as standard Lorentz and polarisation correction factors. A SADABS [**24**] semi-empirical multi-scan absorption correction was applied to the data [**25**].Direct methods, SHELXS-97 [**25**] and WinGX [**26**] were used to solve all three structures. All non-hydrogen atoms were located in the difference density map and refined anisotropically with SHELXL-97 [**25**]. All hydrogen atoms were included as idealised contributors in the least squares process. Their positions were calculated using a standard riding model with C-H$_{aromatic}$ distances of 0.93 Å and U_{iso} = 1.2 Ueq. The imidazolium N-H bonds of **1** and **2** as well as the toluene solvate C-H bonds of **3** were located in the difference density map, and refined isotropically. All hydrogen atoms of **1** and **2** were included as idealized contributors in the least squares process but for **3**, OLEX 2 was utilized where the hydrogen atoms were treated by a mixture of independent and constrained refinement [**27**].

3.4 Results and Discussion

*3.4.1 Synthesis and spectral characterization of **1**, **2** and **3***

The equimolar ratio reactions of bzpy and Hbzp with *trans*-[$RuCl_2(PPh_3)_3$] afforded a diamagnetic complex *cis-Cl, trans-P*-[$Ru^{II}Cl_2(bzpy)(PPh_3)_2$] (**1**) and a paramagnetic complex *trans*-[$Ru^{III}(bsp)Cl(PPh_3)_2$] (**3**), respectively. In addition, a '2+2' paramagnetic ruthenium (III) complex, [$RuCl(bsp)_2(PPh_3)$] (**2**) was attained from the 1:2 molar ratio reaction between *trans*-[$RuCl_2(PPh_3)_3$] and Hbsp. The isolated ruthenium(II) and -(III) complexes exhibits diverse structural features, despite the fact that similarly structured ligand systems were reacted with the same metal precursor. Both **1** and **3** are stabilized by the *trans axial*-[Ru^X-$(PPh_3)_2$] core {X = II (for **1**) and X = III (for **3**)}. In **1**, the bzpy chelator acts as a neutral bidentate chelator through the imino (N1) and pyridyl (N2) nitrogens, whereas in **3**, the coordinated bsp chelator acts as a dianionic tridentate chelator through the deprotonated imino carbon (C8) and phenolic oxygen (O1) as well as the neutral imidazolium nitrogen (N1) (see Figure 3.5).

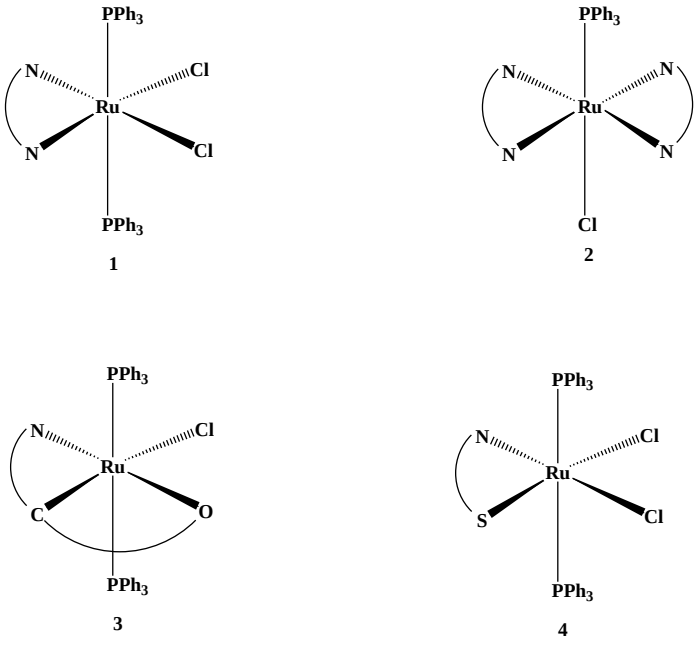

Figure 3.5: *Coordination modes of the Schiff base chelates.*

It is commonly found that multidentate Schiff base ligands stabilize the *trans*-$[Ru^{II}(PPh_3)_2]^{2+}$ core through their chelation and diverse donor capabilities. For example, the metal carbonyl complex *trans*-[RuH(cops)CO(PPh_3)$_2$] {Hcops = 2-chlorophenylsalicylaldimine}, where the cops Schiff base moiety acts as a monoanionic bidentate chelator, affords a stable 6-membered chelate ring through the deprotonated phenolic oxygen and imino nitrogen [**28**]. This is further exemplified, within the bicyclometalled complex, *trans*-[Ru(mbo)CO(PPh_3)$_2$] {H_2mbo = 2-mercaptophenylimino-4-bromophenol}, in which the mbo Schiff base chelates the metal centre *via* the SNO donor set thereby forming 5- as well as 6-membered chelate rings [**29**].In another study, efforts to isolate a ruthenium complex with the potentially tetradentate *bis*-Schiff base ligand H_2pmb, {1,2-*bis*(2′-pyridylmethyleneimino)benzene}, the ligand transformed when reacted with *trans*-[$RuCl_2(PPh_3)_3$] to afford the dicationic complex cation *trans*-[Ru(PPh_3)$_2$(pbz)$_2$](ClO)$_2$ {pbz = 2-pyridylbenzimidazole} [**30**].

The metal complexes **1**, **2** and **3** exhibit good solubility in most polar aprotic solvents but partial solubility in alcoholic media. The low molar conductivities of the respective complexes are typical of charge neutrality for ruthenium(II) and -(III) complexes [**31**].The ^{1}H NMR spectrum of **1** is dominated by the intense signals of the triphenylphosphine co-ligands which appear as two separate multiplets (at 7.43 – 7.38 ppm and 7.27 – 7.22 ppm) (see Figure3.6). More up-field, the aromatic signals of the pyridyl and benzimidazole moieties resonate as less intense multiplets [7.66 – 7.60 ppm and 7.58 – 7.54 ppm] respectively. Shifts in both the imidazolium [*NH* at 8.97 ppm] and imino [*H6* at 8.47 ppm] protons of **1** relative to the corresponding signals found within the free-ligand's ^{1}H NMR spectrum (Schiff base and imidazolium protons found at 12.82 and 9.36 ppm, respectively) affirms coordination of the bzpy chelator. Only one signal at 25.57 ppm is found for the two triphenylphosphine co-ligands which indicate that these co-ligands are in similar chemical environments (see Figure3.7).

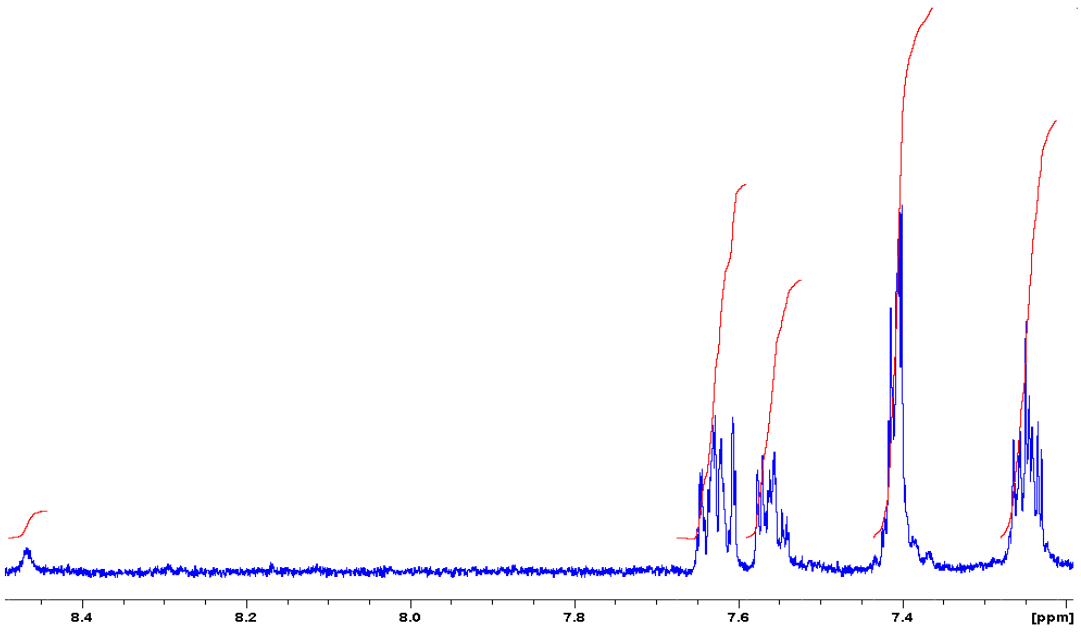

Figure 3.6: *^{1}H NMR spectrum of complex **1**.*

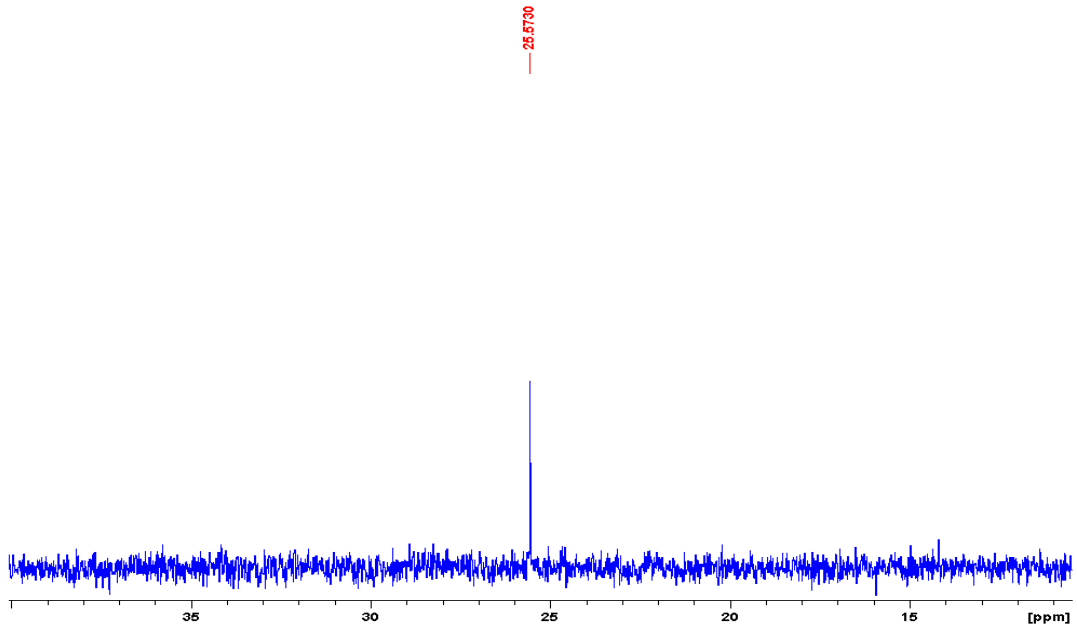

Figure 3.7: *^{31}P NMR spectrum of complex **1**.*

Within the IR spectra, the single Ru-P bond of **2** [693 cm^{-1}] shows a strong vibrational mode at nearly the same frequency as the *trans*-[$Ru(PPh_3)_2$] unit in **1** [696 cm^{-1}] and **3**[692 cm^{-1}] (see Figure 3.8 – 3.10). IR spectral analysis also confirmed coordination through the shifting of the C=N bands of the free–ligands in comparison to the corresponding bands found within the spectra of their complexes.

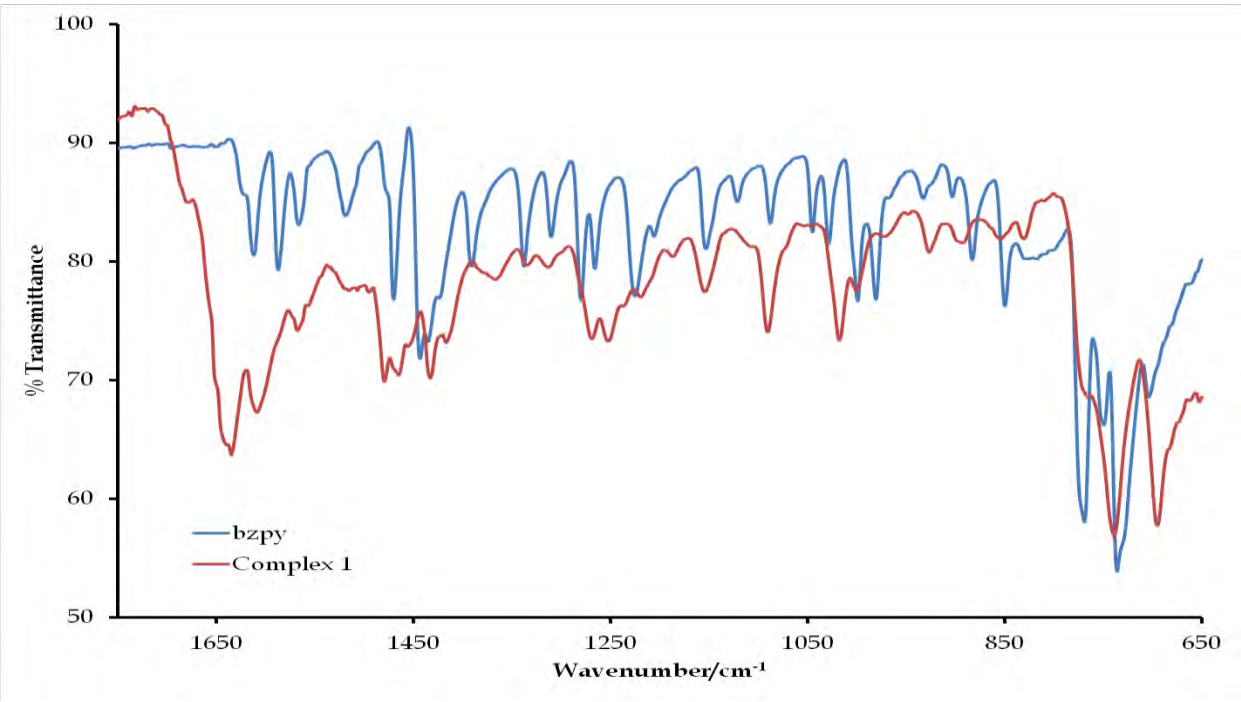

Figure 3.8: *Overlay IR spectra of complex **1** and its free ligand (bzpy) between 2000 and 650 cm^{-1}.*

For **1**, the C=N bands of heterocyclic [1635 cm^{-1}] and Schiff base [1606 cm^{-1}] moieties appear at higher frequency compared to the same bands found in the free ligand's [bzpy] IR spectrum [1612 cm^{-1} and 1587 cm^{-1}]. Similarly for **3**, the C=N [1679 cm^{-1} and 1589 cm^{-1}] bands are more red-shifted with respect to the bands of the free-ligand [1605 and 1589 cm^{-1}]. In contrast for **2**, the C=N [1588 and 1531 cm^{-1}] stretching modes appear

at low frequencies in comparison to analogous C=N stretches within in the Hbsp spectrum [1679 and 1573 cm^{-1}]. Weak intensity bands are found both in the IR spectra of **1** [3067 cm^{-1}] and **3** [3062 cm^{-1}] which are attributed to ν(N-H).

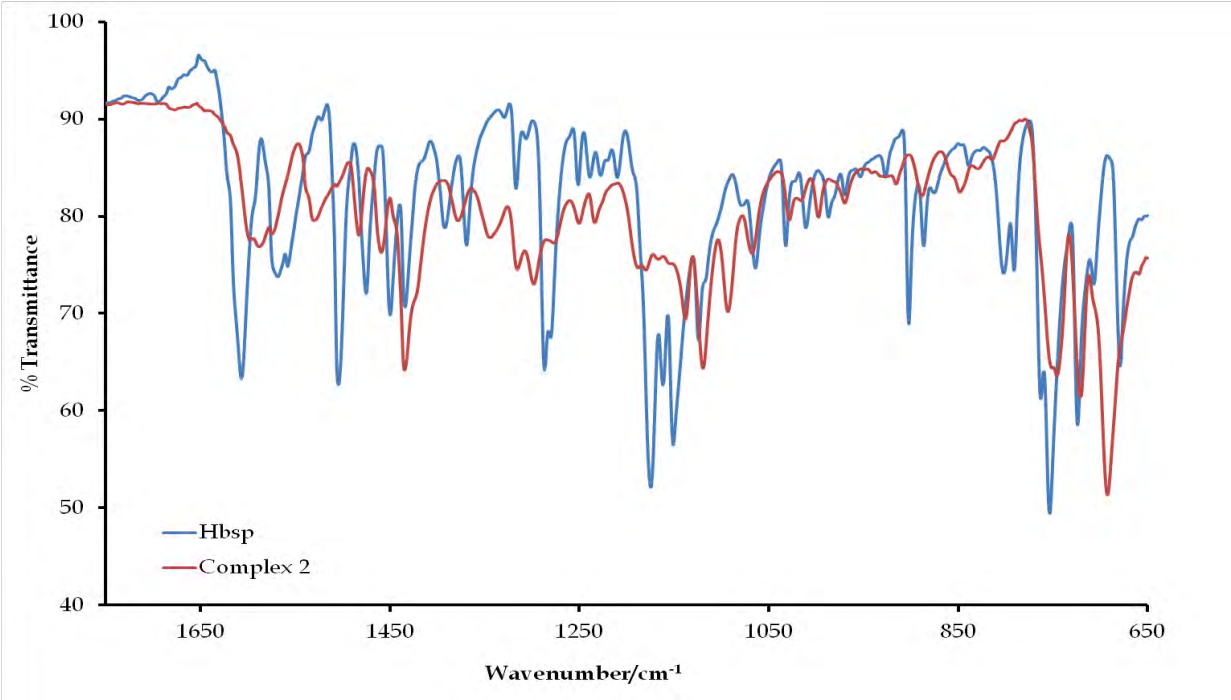

Figure 3.9: *Overlay IR spectra of complex **2** and its free ligand (Hbsp) between 2000 and 650 cm^{-1}.*

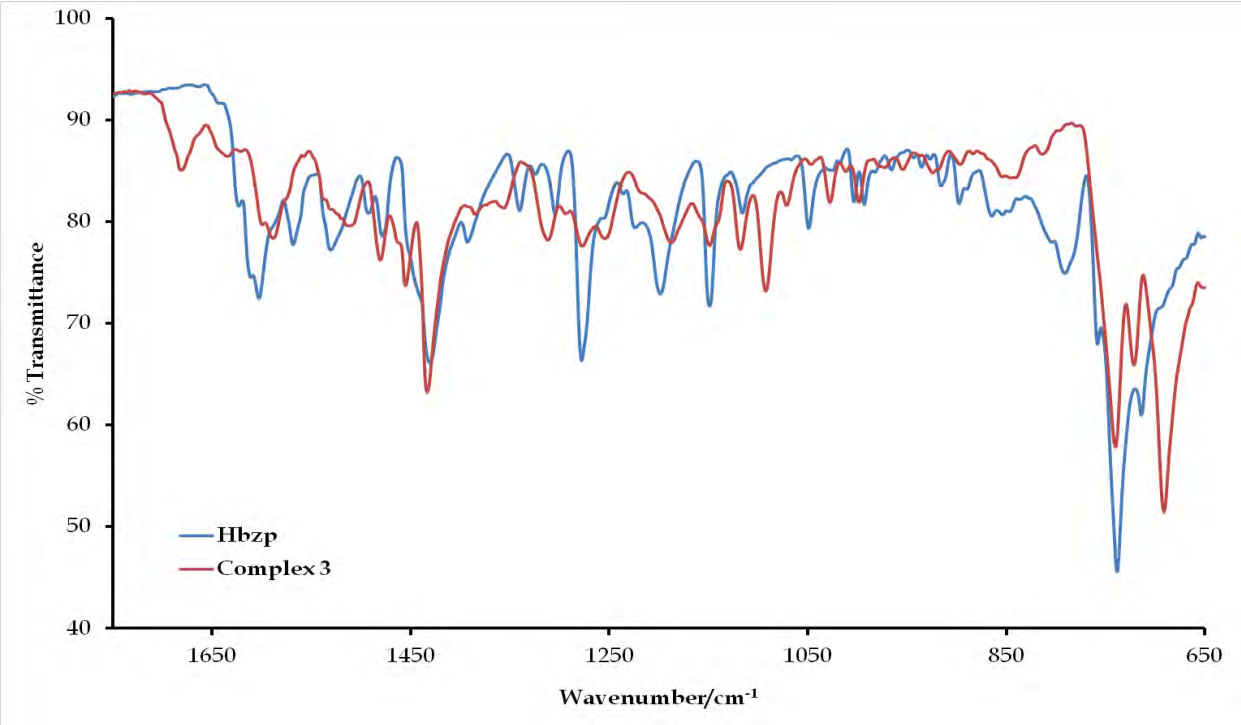

Figure 3.10: *Overlay IR spectra of complex **3** and its free ligand (Hbzp) between 2000 and 650 cm^{-1}.*

Although a soft-ionization technique was employed, the positive mode mass spectrum of **1** showed a peak corresponding to a fragment of the complex minus the chloro co-ligands (see Figure3.11). The peaks of **2** and **3** are detected at 905.049 *m/z* [M] and 895.142 *m/z* [M-H], respectively (see Figures3.12and 3.13).

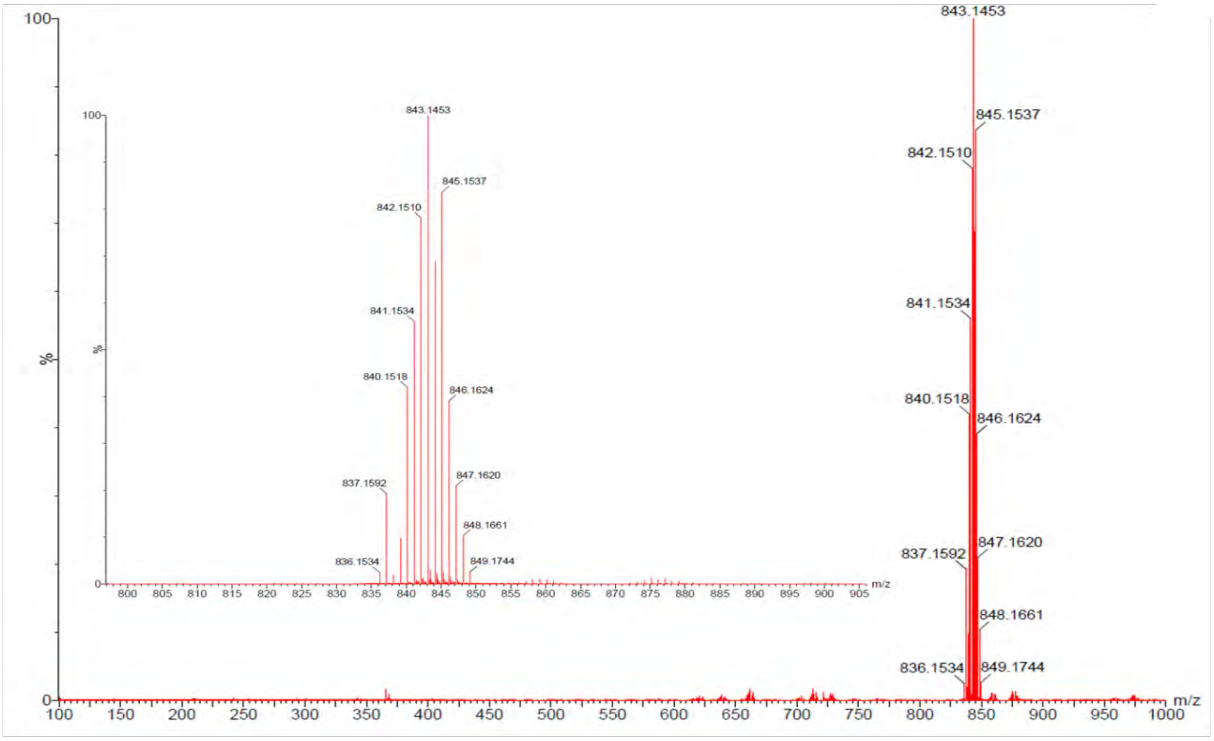

Figure 3.11: *ESI-TOF-Mass spectrum of* ***1****,with the inset showing an expanded region between 790 and 910 m/z.*

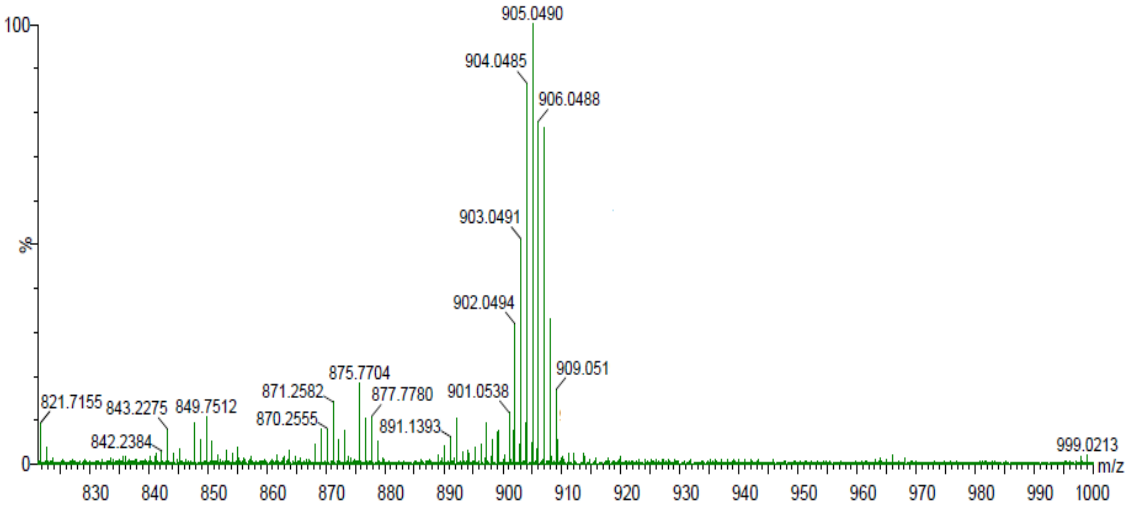

Figure 3.12: *ESI-TOF-Mass spectrum of* ***2****.*

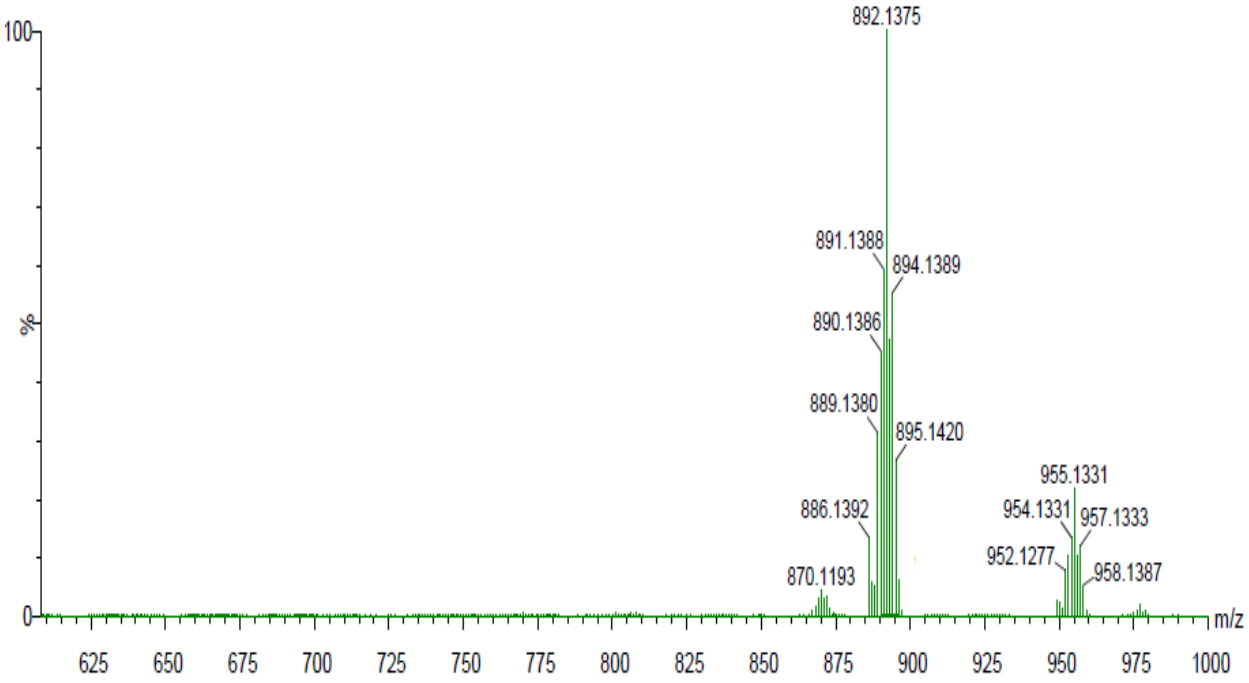

Figure 3.13: *ESI-TOF-Mass spectrum of* ***3.***

A series of intra-ligand π-π^* transitions [301, 358, 410 and 435 nm] are observed in the UV-Vis spectrum of **1** which were similar to that of the free ligand's electronic transitions (see Figure 3.14). A metal-to-ligand-charge transfer transition (MLCT) is observed at 576 nm while no d-d transition was found at longer wavelengths which are as expected for a low spin d^6 octahedral complex [**31**]. Characteristic of **1**, the highly delocalized chelators afford multiple π-π^* transitions below 400 nm in the UV-Vis spectra of both complexes **2** and **3** (see Figure 3.15). Above 400 nm, MLCT [524 (for **2**) and 544 (for **3**) nm] and *d-d* [705 (for **2**) and 692 (for **3**) nm] transitions are found with significantly lower extinction coefficients.

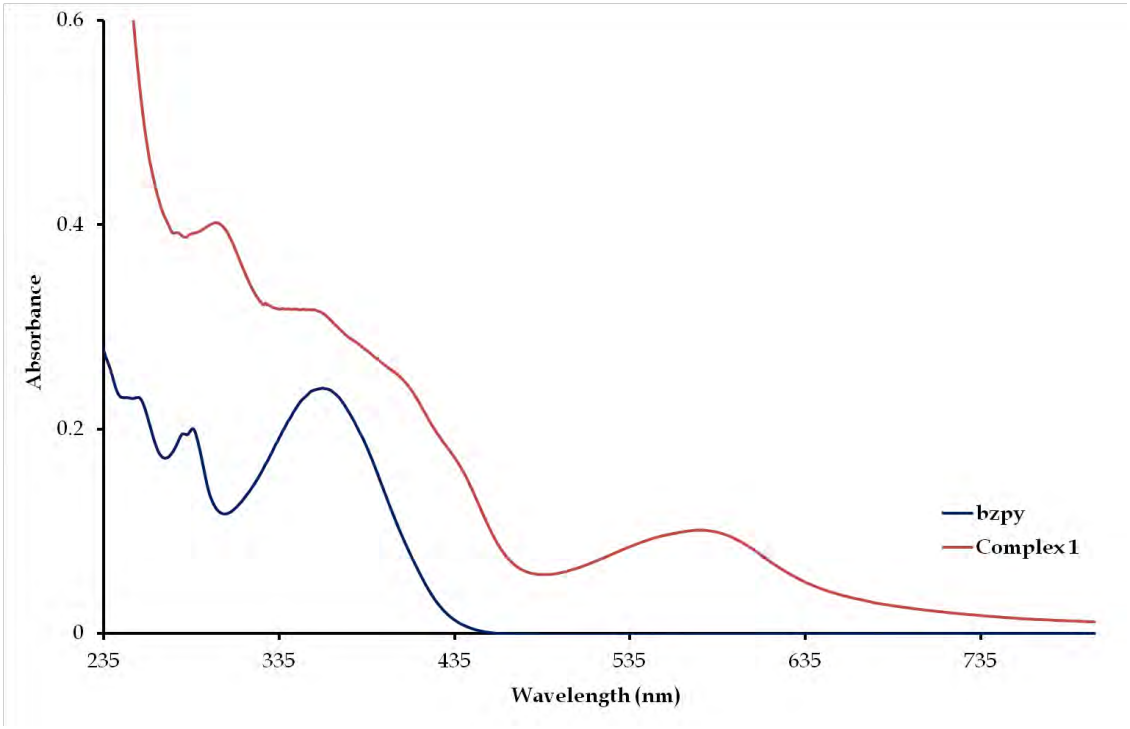

Figure 3.14: *Overlay UV-Vis spectra of complex **1** and its free ligand, bzpy.*

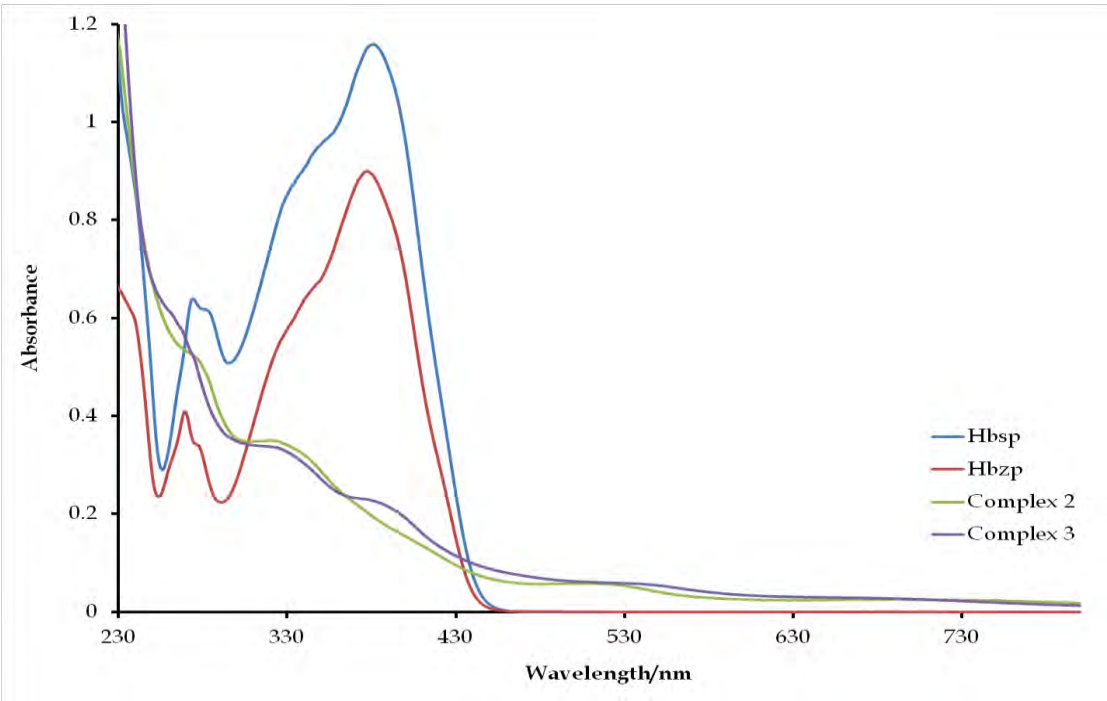

Figure 3.15: *Overlay UV/Vis spectra of complexes **2** and **3** as well as their respective free ligands, Hbsp and Hbzp.*

The paramagnetic centres of complexes **2** and **3** were confirmed by room temperature X-band ESR spectroscopy. The anisotropic solid state ESR spectrum of **2** is nearly identical to the classical rhombic ESR spectra attained for low-spin ruthenium(III) Schiff base complexes; see Figure 3.16 [**32, 33**].

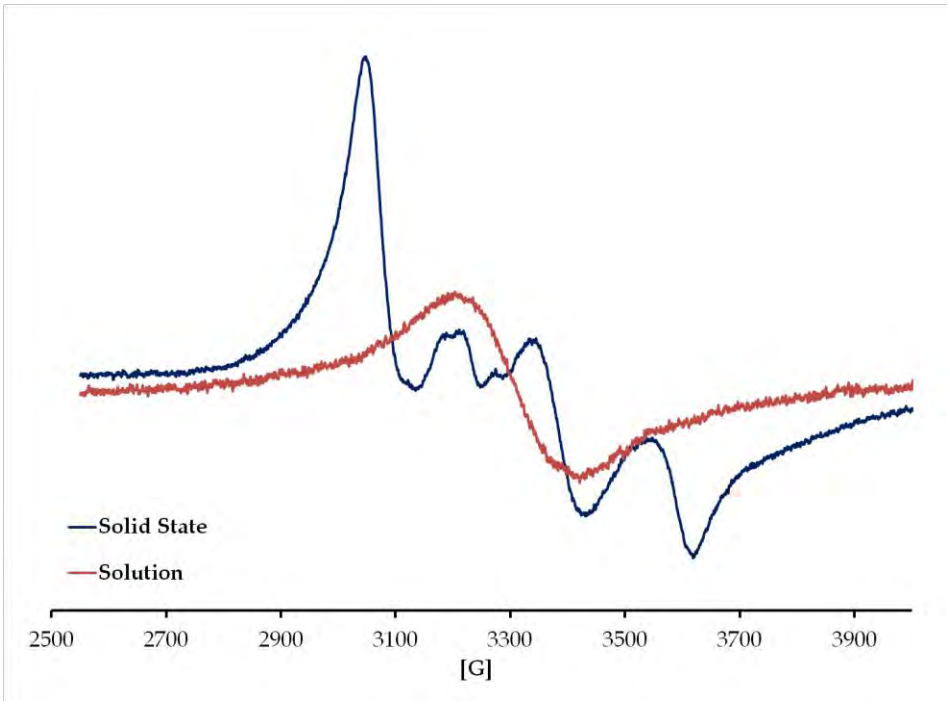

Figure 3.16: *Solid state and solution X-band ESR spectra of* **2** *at 298 K. Instrument settings: microwave bridge frequency, 9.8 GHz; microwave bridge attenuator, 20 dB; modulation frequency, 100 kHz; modulation amplitude, 5 G; centre field, 3500 G.*

The deviation (between 3130 and 3370 G) from the typical rhombic ESR spectrum reflects distortion of the octahedral geometry for **2** [**34**, **35**].The same phenomenon was observed within the poorly resolved solid state ESR spectrum of **3**, where only g_x- and g_y- values were observed, refer to Table 3.1 and Figure 3.17. In the case of the isotropic solution ESR spectra of **2** and **3** in dichloromethane: toluene (1:1), both compounds exhibit broad first derivative features devoid of additional fine structure with centralized g_{iso}-values of 2.113 and 2.111, respectively.

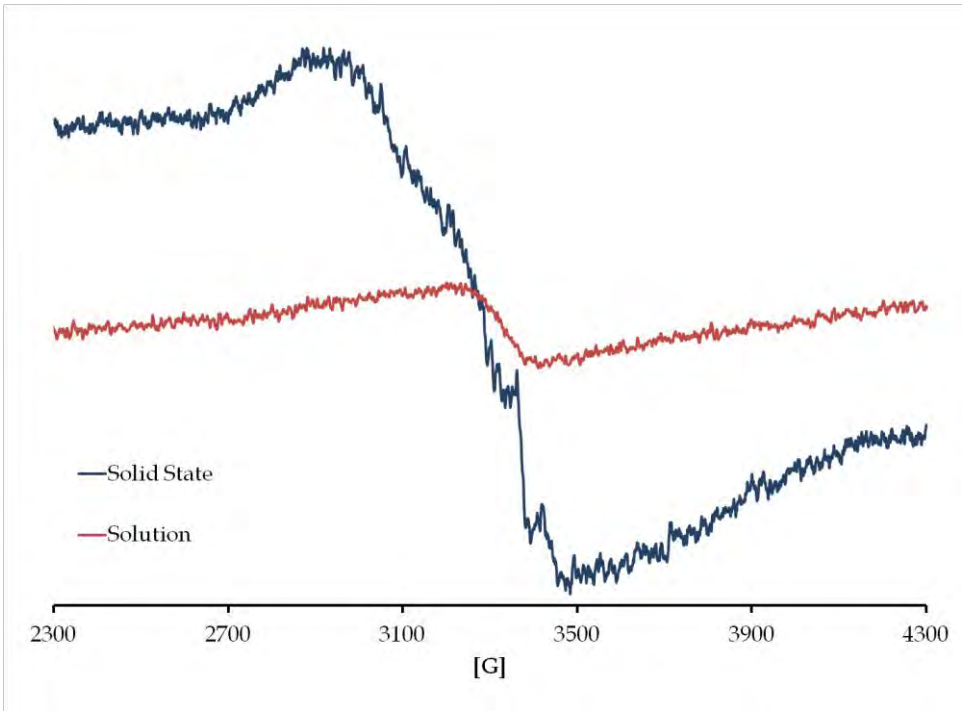

Figure 3.17: *Solid state and solution X-band ESR spectra of* ***3*** *at 298 K. Instrument settings: microwave bridge frequency, 9.8 GHz; microwave bridge attenuator, 20 dB; modulation frequency, 100 kHz; modulation amplitude, 5 G; centre field, 3500 G.*

Table 3.1: *G-values of the respective complexes in the solid state (**A**) and in solution (**B**).*

Spectrum	g_x	g_y	g_z	g_{iso}
2-A	2.198	2.090	1.910	-
2-B	-	-	-	2.113
3-A	2.309	2.018	-	-
3-B	-	-	-	2.1101

- *Not observed*

3.4.2 *Synthesis and spectral characterization of* **4**

The equimolar reaction of the ligand bxth and *trans*-[$RuCl_2(PPh_3)_3$] afforded the diamagnetic ruthenium(II) complex, *cis-Cl, trans-P*-[$Ru^{II}Cl_2$(bxth)$(PPh_3)_2$] (**4**) in moderate yield**.** Although this complexwas recrystallized from a 1:1 (*v:v*) dichloromethane: hexane solution using both slow and vapour diffusion methods, no X-ray quality crystals could be obtained. Compound **4** is non-electrolyte in DCM, moderately soluble in polar solvents such as methanol, ethanol and acetonitrile but readily soluble in DMSO and DMF.

This complex was characterized by infrared spectrometry, NMR (^{1}H and ^{31}P) spectroscopy, melting point measurements, elemental analysis and mass spectrometry. The IR spectrum of **4** confirms the presence of the*trans*-[$Ru(PPh_3)_2$] unit by the occurrence of an intense stretch at 692 cm^{-1} found within the IR spectrum(see Figure 3.18).Upon coordination of the bxth chelator to the metal centre, the acidic metal centre removes electron density from the imine double bond resulting in the weakening of the imine bond and hence the ν(C=N) appears as a weak intensity vibration band at 1536 cm^{-1} which is found at lower frequency when compared to the ν(C=N) [at 1580 cm^{-1}] of the free ligand bxth. Indicative to the aforementioned phenomena, when comparing the imine stretches of the free-ligand and chelator, significant shifts are also noticed in the thiophene vibrations (1503, 1450, 1416 cm^{-1}) associated with the free-ligand, bxth and analogous vibrational bands (1481, 1432 and 1392 cm^{-1}) of the bxth chelator. In turn, this IR spectral observation provides an indication that the thienyl sulfur is coordinated to the ruthenium centre [**36**]. Furthermore, the ^{1}H NMR spectrum for the diamagnetic complex of **4** is dominated by multiplets (7.45 – 7.21 ppm) due to the triphenylphosphine co-ligands which are well clearly confirmed by ^{31}P NMR spectrometry showing a single peak (see Figures 3.19 and 3.20).

The upfield shifts of the aromatic signals of the benzoxazole and thiophene moieties in **4** relative to those of the free ligand affirm coordination. In the UV-Vis spectrum of **4**, no *d-d* transition is observed at longer wavelength but a metal to ligand charge transfer transition (MLCT) at 476 nm with low extinction coefficient is seen (see Figure 3.21). The elemental analysis data and mass spectral analysis provided definitive insight into the structural elucidation. More specifically, the low resolution mass spectrum in the positive modeshowed a peak corresponding to a fragment of the complex minus the chloro co-ligands and one of triphenylphosphine co-ligands (see Figure 3.22). Thus taken into account the spectral characterization, the proposed structure of **4** is comprised of a *trans*-[$Ru(PPh_3)_2$] core with the equatorial plane being occupied by the $N_{imine}S_{thienyl}$-donor neutral bidentate bxth chelator and the *cis*-orientated chloro co-ligands.

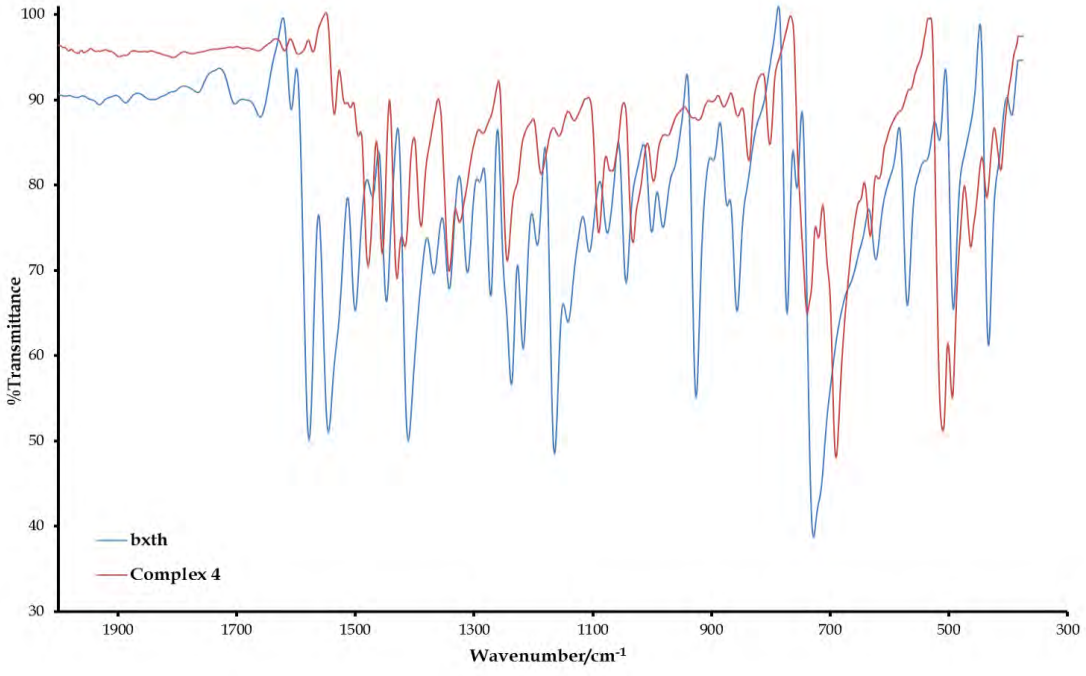

Figure 3.18: *Overlay IR spectra of complex* **4** *and its free ligand (bxth) between 2000 and 300* cm^{-1}.

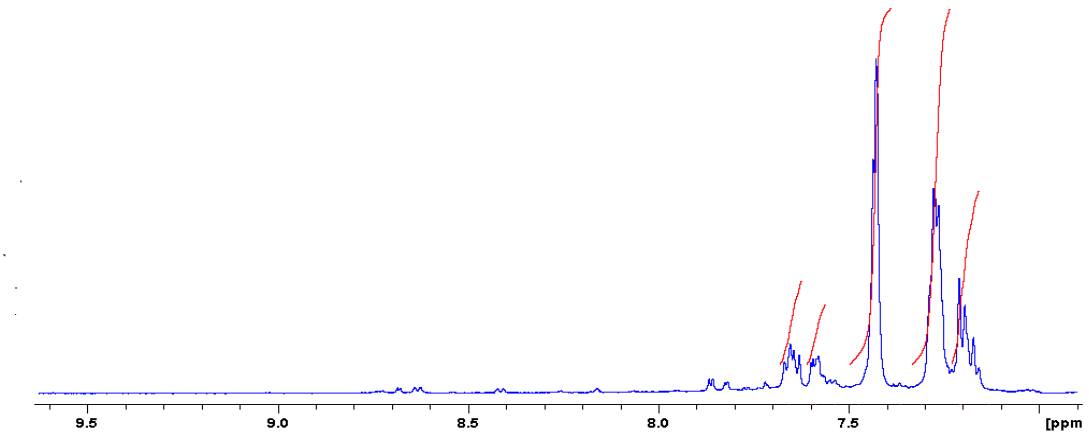

Figure 3.19: *^{1}H NMR spectrum of complex* ***4****.*

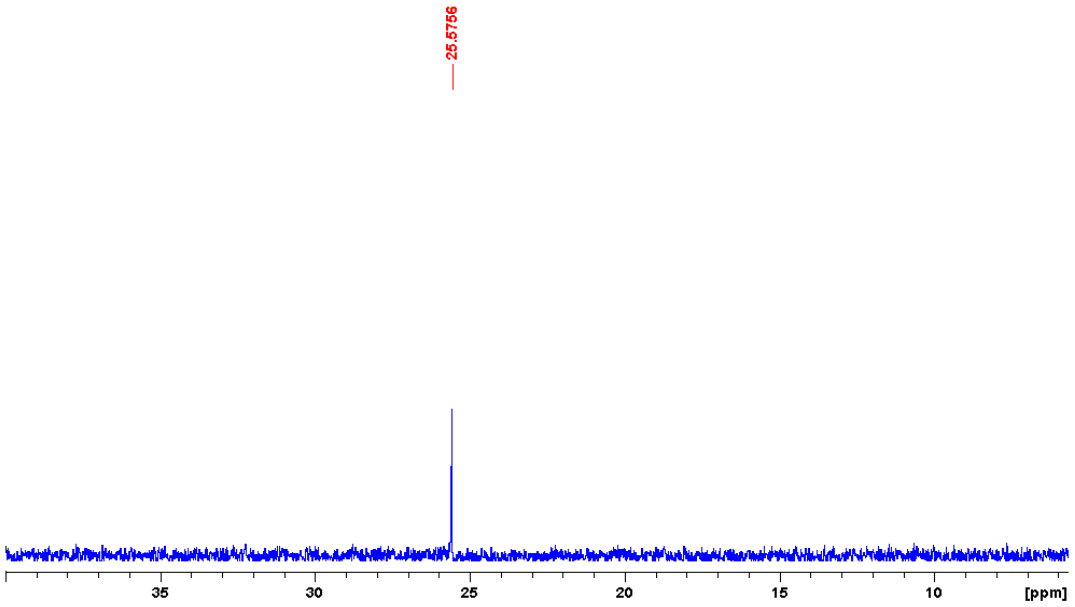

Figure 3.20: *^{31}P NMR spectrum of complex* ***4****.*

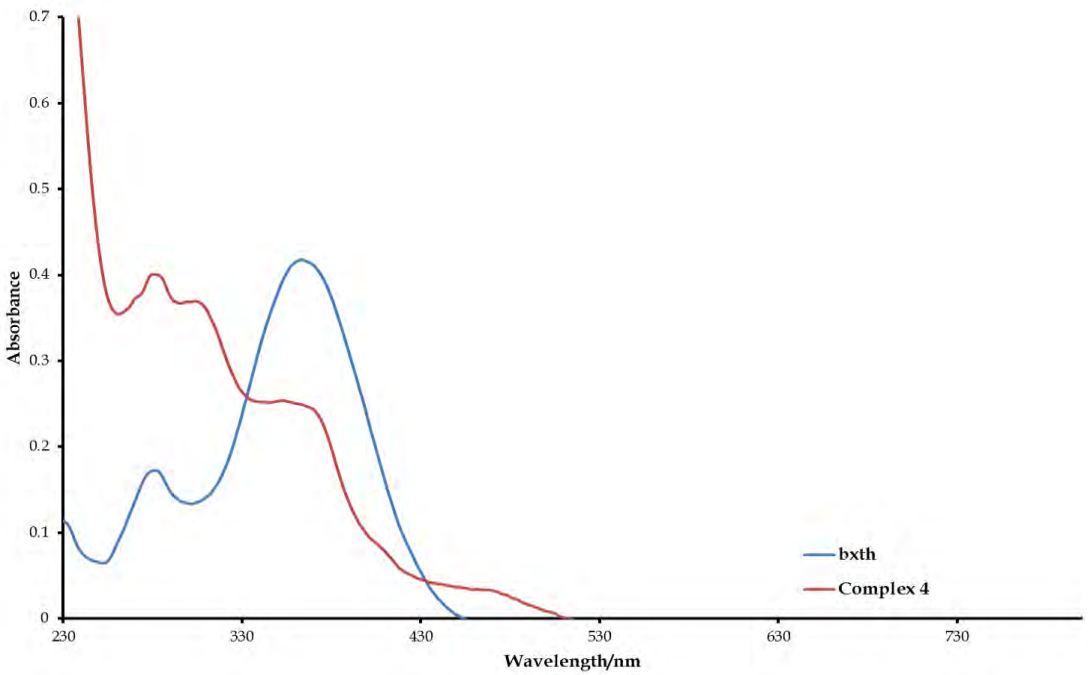

***Figure 3.21**: Overlay UV-Vis spectra of complex **4** and its free ligand, bxth.*

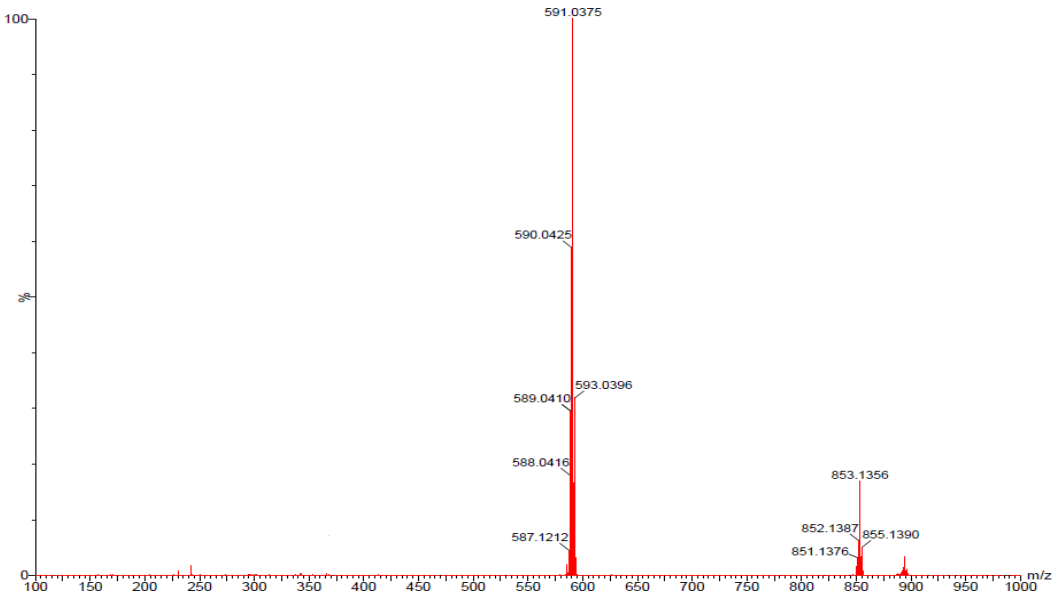

***Figure 3.22:** ESI-TOF-Mass spectrum of **4**.*

3.4.3 *Electrochemistry*

Selected cyclic voltammogram (CV) parameters of the metal complexes **1**-**4** are summarized in Table 3.3 and their respective CVs are shown in Figures 3.23–3.26. The CVs of **1** and **3** showed one redox couple each whereas the CVs of **2** and **4** showed two redox couples labelled **A** and **B**. For **2**, the peak potentials on the squarewave voltammogram (SWV, see Figure 3.27) are as expected equal to the calculated halfwave potentials. All the redox couples are quasi-reversible since their peak to peak separations (ΔE) are different from ferrocene (ΔE = 90 mV at 100 mV/s). In addition, all the redox couples showed diffusion controlled behaviour with increasing scan rates. This is illustrated by the overlay CVs of complex **3** for which scan rates ranged from 50 mV/s to 200 mV/s, at increments of 25 mV/s(see Figure 3.28). Peak current ratios approaching one, were observed for all the complexes which imply that the redox couples are for one electron redox processes.

The quasi-reversible redox processes of **1** and **3** were ascribed to the Ru(II/III) redox couples since they have similar halfwave potentials ($E_{½}$) found for other ruthenium(II/III) complexes in the literature. Like in the case of the ruthenium(II) complexes, *trans*-[Ru(H^{R}bmp)(PPh$_3$)$_2$(CO)(Cl)], 2-(benzylimino-methyl)-4-*R*—phenol (H^{R}bmp) in DCM (*vs* Ag|AgCl) with halfwave potentials ranging from 0.62 V to 1.16 V [**37**].Similarly, the paramagnetic *trans*-[Ru^{III}Cl(L)(PPh$_3$)$_2$] {Schiff base (H_2L) ligands derived from benzaldehyde and various functionalized acetic hydrazides} complexes exhibited comparable Ru(II/III) redox couples, under similar experimental conditions [**38**].

The two redox processes (**A** and **B**) of **2** were both assigned to be metal based redox processes as the CV of the free-ligand (*i.e.* Hbsp) indicated that the compound was not

redox active within the same potential window as **A** and **B**, respectively. These redox couples were assigned to the Ru(II/III) [for **A**] and Ru(III/IV) [for **B**] couples, consistent with analogous electrochemical behaviour as the ruthenium(III) bipyridine (bpy) complexes, $[Ru(bpy)Cl_3(X)]$ {X = MeOH, PPh_3, 4, 4'-bipyridine or CH_3CN} [**39**]. It has been noted, that the literature range of the halfwave potential differences ($\Delta E_{½}$) for mononuclear ruthenium complexes is 1.2 – 1.7 V. Within this study, a $\Delta E_{½}$ of 1.358 V for complex **2** was attained which supports the assignments of the respective couples.

Table 3.2: *Selected CV parameters (at 100 mV/s) for the complexes **1**, **2**, **3** and **4**.*

Complex	1	**2**		**3**	**4**	
		A	**B**		**A**	**B**
E_{pa}/V	0.896	-0.433	0.965	0.660	-0.022	0.767
E_{pc}/V	0.820	-0.497	0.899	0.739	-0.111	0.657
$E_{½}/V$	0.858	-0.465	0.932	0.700	-0.067	0.712
$\Delta E/mV$	76	64	66	79	89	110

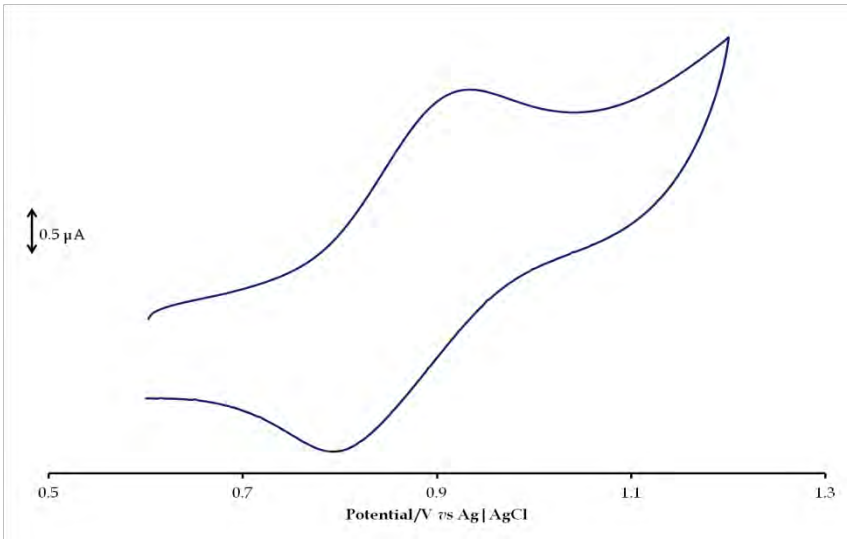

Figure 3.23: *CV of complex **1** at 100 mV/s between the potential window, 0.5 V and 1.3 V.*

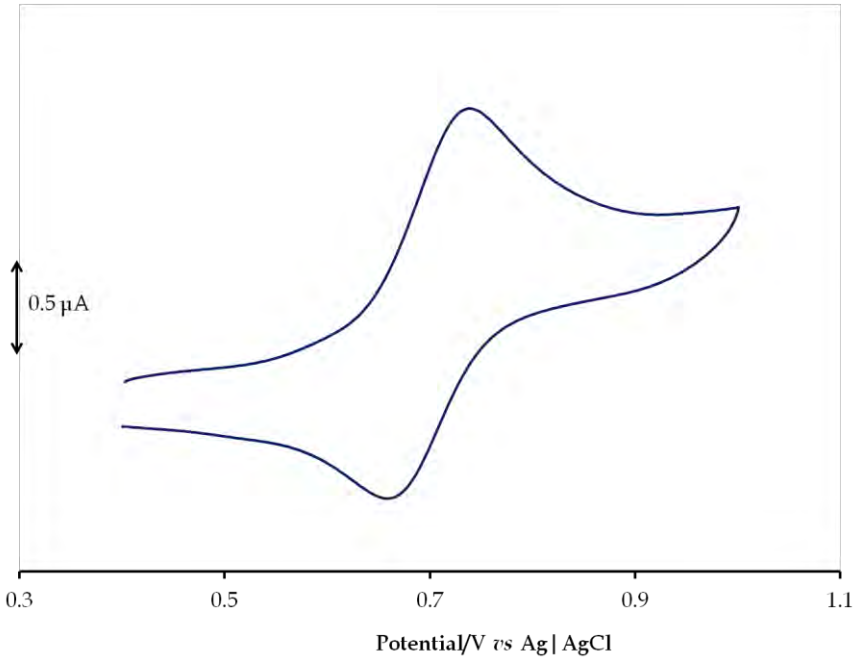

Figure 3.24*: CV of complex* ***3*** *at 100 mV/s between the potential range of 0.3 V and 1.1 V*

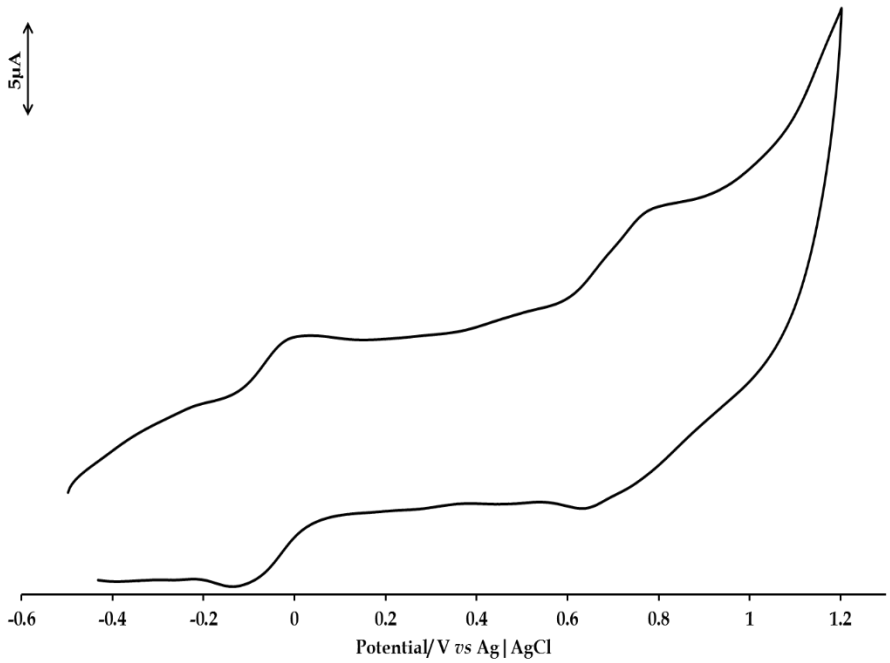

Figure 3.25: *CV of complex* ***4*** *at 100 mV/s between the potential window, -0.5 V and 1.2V.*

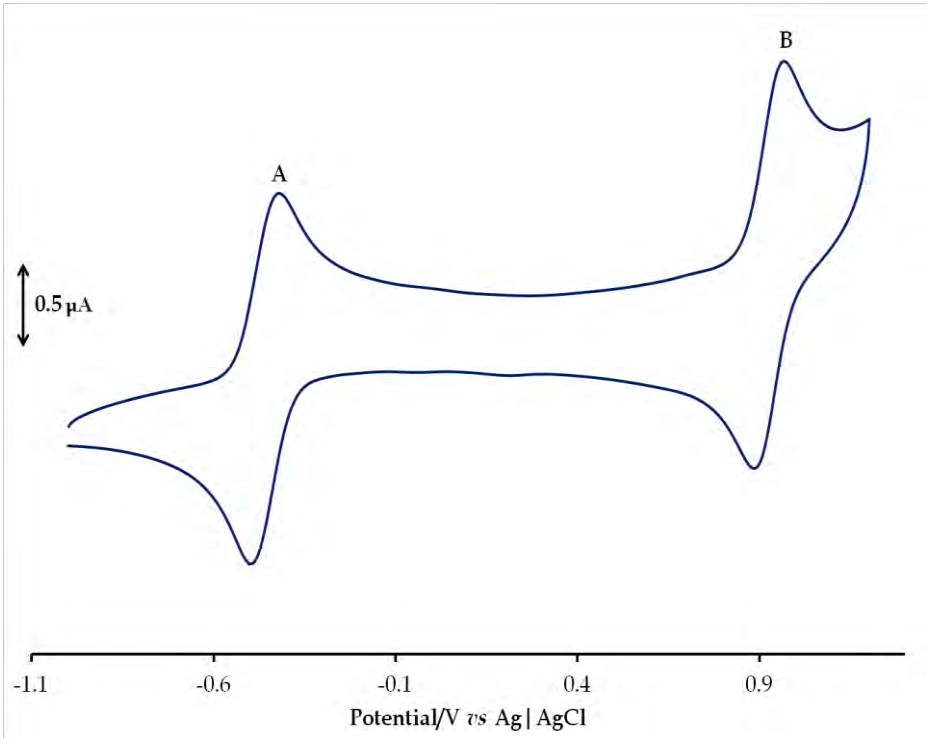

Figure 3.26: *CV of complex* **2** *at 100 mV/s between the potential range of -1.0 V and +1.2 V.*

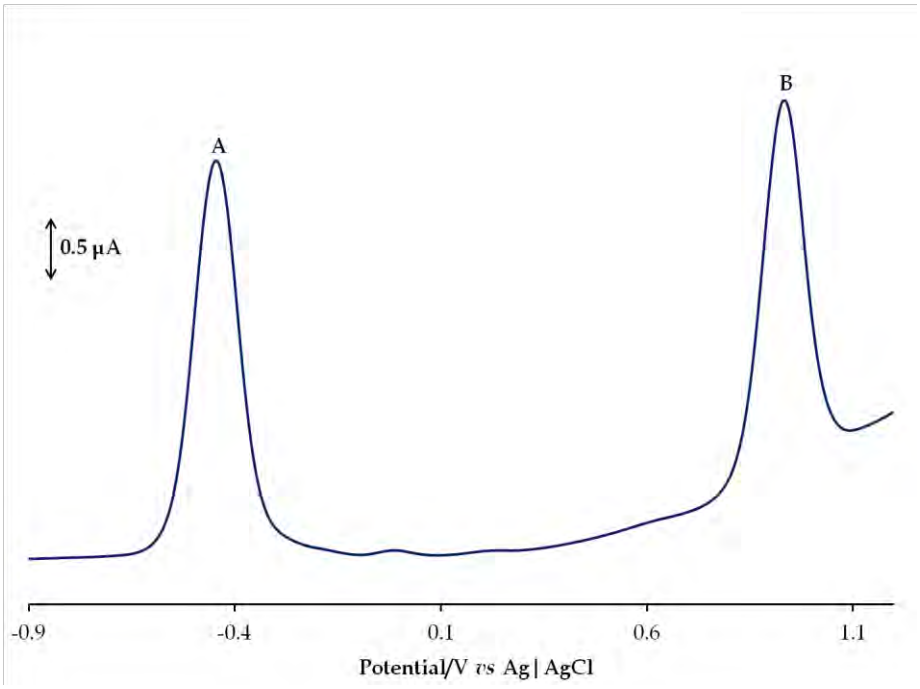

Figure 3.27: *SWV of complex* **2** *at 100 mV/s between the potential range of -0.9 V and +1.2V.*

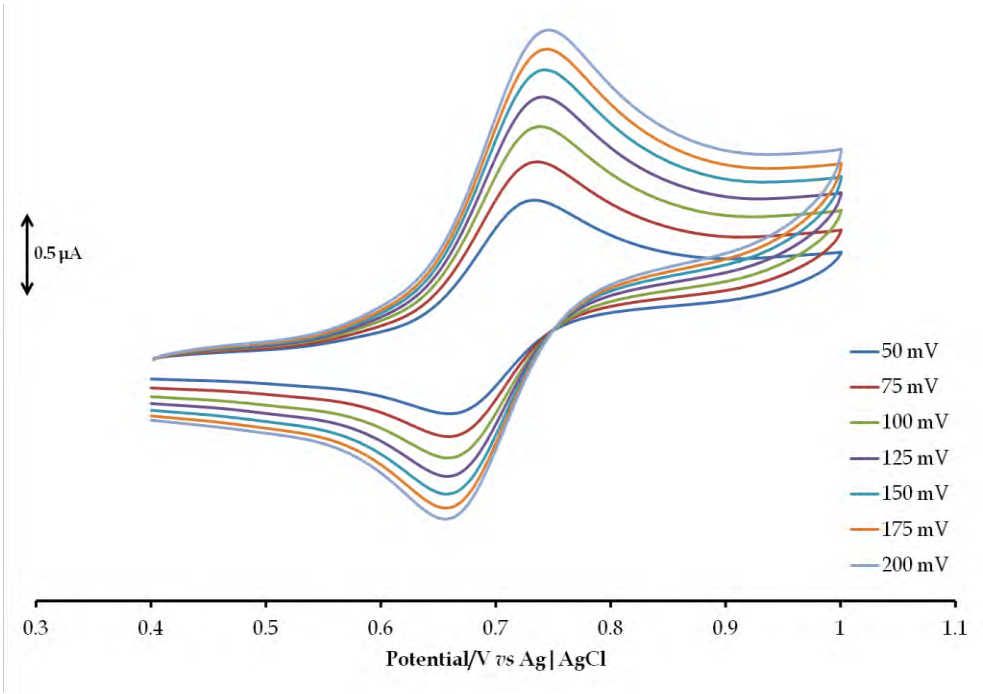

Figure 3.28: *Overlay voltammograms of complex **3** from 50 mV/s to 200 mV/s at 25 mV/s increments.*

The redox couples of the respective complexes were further investigated with spectroelectrochemistry to corroborate the voltammetric assignments. The overlay UV-Vis spectra of **1** showed a distinctive isosbetic point at 603 nm which is due to the appearance of a shoulder (at 681 nm) ascribed to a *d-d* electronic transition (see Figure 3.29). Occurrence of this metal-based electronic transition implies that the d^6 to d^5system conversion transpired, confirming the Ru(II/III) redox couple in the CV assignment [**40**]. A characteristic feature is the accompanying decrease in the MLCT (at 576 nm) and becomes progressively red-shifted until 585 nm [**41, 42**].

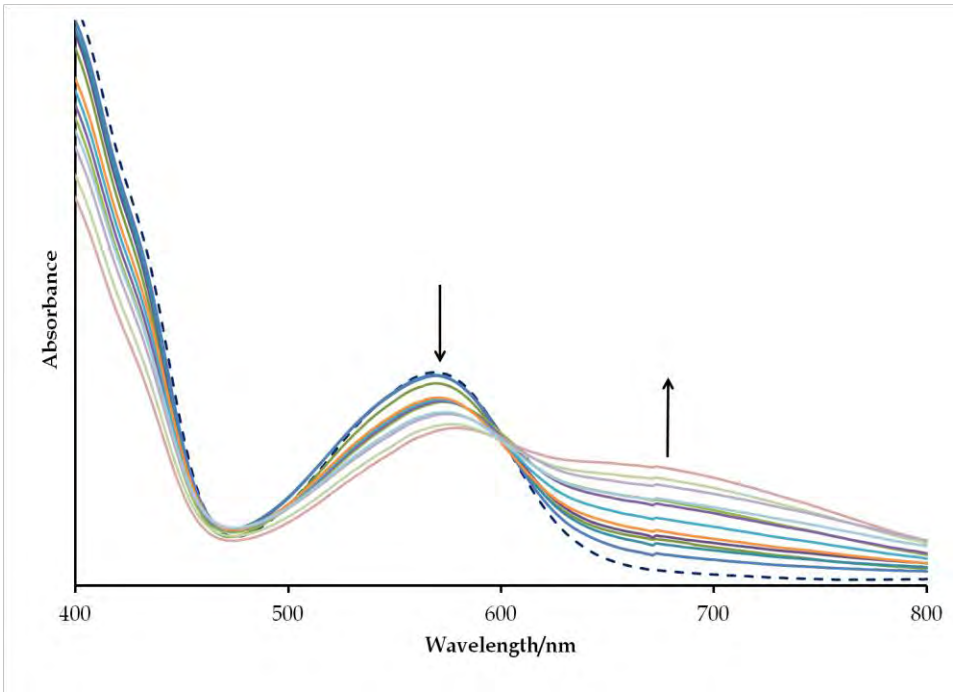

Figure 3.29: *UV-Vis spectral changes observed for reduction of complex **1** at an applied potential of -0.90 V. The initial spectrum is shown as a dashed blue line.*

Applying a controlled negative overpotential (at -0.55 V) for **2** while investigating the redox couple **A**, the reduction of the paramagnetic ruthenium(III) centre is confirmed by the disappearance of the *d-d* transition (at 705 nm) and the formation of a new MLCT band at 574 nm between the two defined isosbestic points (at 447 and 649 nm), see Figure 3.30. Another study of a ruthenium (III) complex, [Ru(H_2bpyp)(acac)] {H_2bpyp = 1, 2-benzyl-*bis*-(2-(pyrazol-4-*yl*)phenol)}, with similar CV traces as **2** showed that the reduction to the Ru(II) species also resulted in the formation of a new MLCT [**43**].

Nearly quantitative conversion back to **2** occurred when a zero potential was applied, leading to the regeneration of the *d-d* transition. At incrementing applied positive potentials, the characteristic feature of the redox couple **A**, is the intense π-π^* transitions

at 259 nm and 286 nm while a decrease in the rest of the bands were noted(see Figure 3.31), which could imply that ligand-induced oxidation of the metal centre took place [**44**, **45**]. These spectroelectrochemical observations of **2** confirm the CV and SWV assignments for redox couples **A** and **B**. Unfortunately for **3**, upon applying potentials between 0.865 V and 0.90 V, only diffuse isosbetic points were observed which is typical of the presence of two species within the solution.

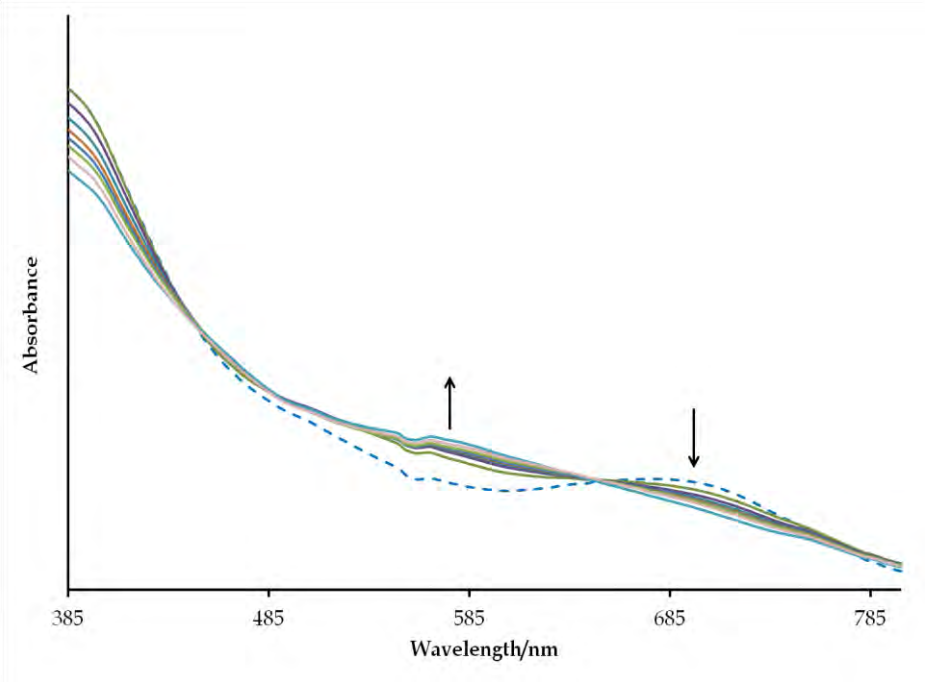

Figure 3.30: *UV-Vis spectral changes observed for reduction of complex* **2** *at potentials of redox couple* ***B****, at an applied potential -0.55 V. The initial spectrum is shown as a dashed blue line.*

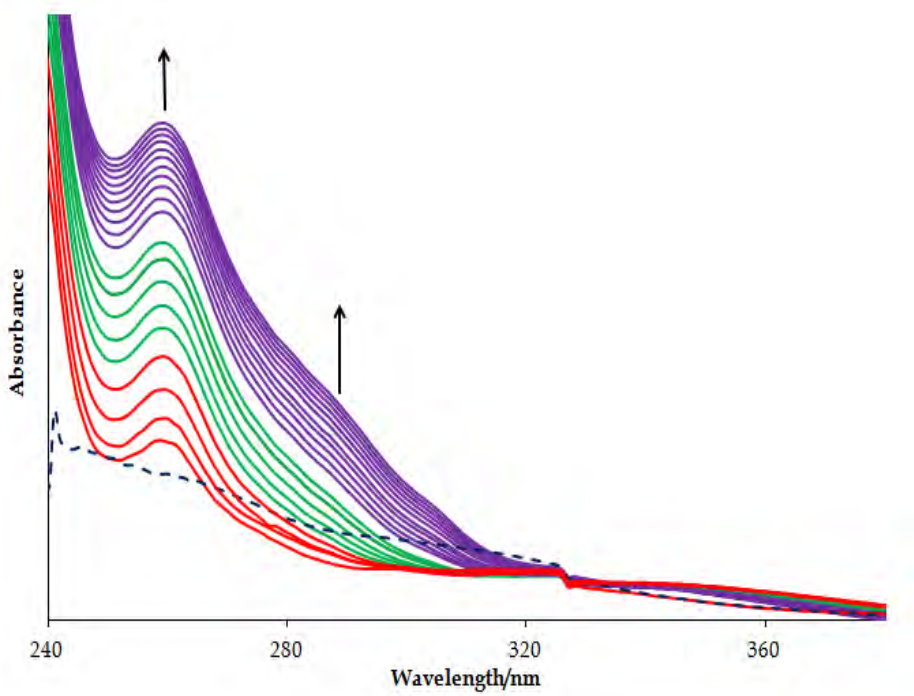

Figure 3.31: *UV-Vis spectral changes observed for reduction of complex* **2** *at potentials of redox couple* ***B****, at incrementing applied potentials. The initial spectrum is shown as a dashed blue line.*

3.4.4 Crystallographic Studies

Complexes **1** and **3**·C_7H_8 crystallize in the space group P-1, with two molecules of each occupying the respective triclinic unit cells (*i.e.* Z = 2) whereas four crystallographically identical molecules of **2** (*i.e.* Z = 4) are found within its monoclinic unit cell (see Figures 3.32–3.34). Similar crystal packing arrangements were observed for complexes **1** and **3**·C_7H_8: two mutual classical hydrogen bonds [N2-H2···N3 = 2.11294 Å] in **1** occur between two respective molecules resulting in a series of molecules aligned parallel with the [*c*]-axis; stabilization of the crystal lattice of **3** is rendered through non-classical hydrogen-bonding which allows the molecules to stack in columns along the [*c*]-axis. The molecules of **2** runs parallel with the [*a*]-axis due to a series of intermolecular interactions [3.87 Å] between the S1-benzothiazole moieties of adjacent molecules.

Crystallographic distortion of **1** was observed on one of the phenyl groups of the P(2)Ph_3 co-ligand. This distortion is ignored as it doesn't influence the coordination behaviour of the bzpy chelator.

The effects of cyclometallation are clearly evident from the distortion of the equatorial bond angles compared to the ideal octahedral values. For **1**, the constrained N1-Ru-N2 [78.45(5)^0] bite angle forces the Cl1-Ru-Cl2 [91.44(1)^0], Cl2-Ru-N2 [90.87(4)^0] and [Cl1-Ru-N1 = 99.24(4)^0] bond angles wider than the idealized 90^0 (see Figure 3.35). Similarly, the bicyclometalled complex **3** with its two 5-membered chelate rings [bite angles: N1-Ru1-C8 = 76.0(2)^0 and C8-Ru1-O1 = 80.8(1)^0] force the bond angles Cl-Ru1-C8 = 176.4(1)^0 and N1-Ru1-O1 = 155.8(1)^0 to deviate from linearity (see Figure 3.36). The same phenomenon was observed with complex **2**'s equatorial bond [Cl1-Ru1-N3 = 172.76(4)^0 and O1-Ru1-O2 = 177.69(5)^0] angles which were less than 180^0 as ascribed to the 6-membered chelate rings [N3-Ru1-O2 = 87.29(6)^0 and N1-Ru1-O1 = 90.51(6)^0] (see Figure 3.37).

In fact, the latter bond angles induces a P1-Ru-N1 [175.42(5)^0] axial bond angle which deviates from linearity. For **1**, non-linearity of its axial bond angle [P1-Ru-P2 = 174.37(1)^0] is ascribed to the interactions between selected phenyl rings of the PPh_3 co-ligands and the imidazolium/pyridyl moieties of the bzpy chelator, see Figure 3.38 {**I** = 3.748 Å, **II** = 3.553 Å and **III** = 3.575 Å}. Consequently, the respective non-coordinating heterocyclic moieties are found out of plane with the pyridyl (of **1**) and deprotonated phenolic (of **2**) rings. More specifically, the pyridyl moiety of **1** is slightly out of plane (by 11.07°) with respect to the benzimidazole moiety. Furthermore, the benzothiazole moieties of **2** are at different angles [54.72˚ with respect to the S1-benzothiazole ring and 11.53˚ with respect to the S2-benzothiazole ring] out of the plane of the deprotonated phenolic rings which are due to the combined effects of the inter- and intramolecular

steric interactions. Unlike **1** and **2**, no co-planar phenyl rings of the PPh_3 co-ligands were found with respect to the bzp chelator of **3** which lead to a straighter backbone [P1-Ru1-P2 = $178.55(4)^0$]. The axial linearity of **3** is also clearly evident from the Ru-P [Ru1-P1 = 2.386(1) Å and Ru1-P2 = 2.407(1) Å] bond distance being nearly equal.

The *cis*–chloro coordination bonds of **1** [Ru-Cl1 = 2.4369(3) Å and Ru-Cl2 = 2.4225(4) Å] are nearly equidistant which implies that the *trans*-influence on the N1 and N2 nitrogen atoms are approximately similar. The other coordination bonds, Ru-N1 [2.076(1) Å] and Ru-N2 [2.045(1) Å], are typical of a ruthenium(II) metal centre bonded to a pyridyl or Schiff base nitrogens, respectively. For example, the organoruthenium(II) complex, *trans-Cl, cis-CO*-$[Ru(CO)_2(spy)Cl_2]$ {spy = *N*-((pyridine-2-*yl*)methylene)-thiazole} has similar Ru-$N_{Schiff\ base}$ and Ru-$N_{pyridyl}$bond lengths of 2.169(4) Å and 2.091(5) Å, respectively [**46**].Comparatively, the stronger Lewis acidic character of the paramagnetic ruthenium(III) centres compared to the diamagnetic metal centre of **1**, afforded selected shorter analogous coordination sphere bonds for **2** [Ru1-P1 = 2.3536(5) Å, Ru1-N1 = 2.119(2) Å and Ru-N3 = 2.096(2) Å] and **3** [Ru-P1 = 2.386(1) Å, Ru-P2 = 2.407(1) Å and Ru1-N1 = 2.069(4) Å]. However, the metal to chloride bond distances for **2** [2.3634(5) Å] and **3** [2.436(1) Å] were different, which is largely due to the difference in the *trans*-influence experience by the various chloride ions. In addition, similar deprotonated phenolic oxygens to ruthenium (III) bond lengths were found for **2** [Ru1-O1 = 1.975(1) and Ru1-O2 = 2.004(1)Å] and **3** [Ru1-O1 = 2.060(3) Å]. The difference in the imino coordination bonds of **2** are ascribed to the varied *trans*-influence on the imino nitrogens.

The rare metal carbene [Ru1-C8 = 1.981(5) Å] bond distance (complex **3**) were shorter than the analogous bond [Ru-$C_{Schiff\ base}$= 2.048(7) Å] found in the ruthenium(II) complex, *trans*-$[Ru(cmp)(CO)Cl(PPh_3)_2]$ {cmp = methyl-4-((5-chloropyridin-2-*yl*-

imino)methyl)benzoate} which is expected since the latter complex has a lower oxidation state [**47**]. Nitrogen heterocyclic carbene (NHC) ruthenium complexes have been widely researched due to their optimal catalytic properties, like in hydroformylation, olefin metathesis as well as hydrogen-transfer reactions [**40, 41**]. More recently, the first ruthenium chemotherapeutic drug, NAMI-A, *trans*-[$RuCl_4$(DMSO)(Im)](ImH) {Im = imidazole} has recently entered Phase II clinical trials due to its optimal antimetastatic cancer activity which is accompanied with fewer significant side effects than platinum-based metallopharmaceuticals [**48**]. This has led to an interest in exploring the biological activities of NHC ruthenium complexes, *e.g.*, the NHC ruthenium(II) complexes, *cis*-[Ru(η^6-cymene)Cl_2(2R-bz)] {where R can be methyl, ethyl, isopropanol or benzyl subsitituents on the nitrogen atoms of the bz moiety} have shown to exhibit various biological activities ranging from DNA intercalation to protease inhibitor capabilities [**49**].

Similar bond lengths were attained for the individual $\{C=N\}_{Schiff\ base}$ [C6-N1 = 1.311(2) Å (for **1**) and C8-N3 = 1.326(6) Å] (for **3**)] and $\{C=N\}_{Heterocyclic}$ [C7-N4 = 1.325(2) Å (for **1**) and C7-N1 = 1.333(6) Å (for **3**)] bond distances as the nitrogen atoms are sp^2 hydridized nitrogens; but the aforementioned C=N bonds were still shorter than the carbon to sp^3hybridized nitrogen bonds within their individual heterocyclic moieties [C7-N3 = 1.357(2) Å (for **1**) and N2-C7 = 1.360(6) Å (for **3**)]. Within the bsp chelators (of **2**), the imino bond [N3-C21 = 1.310(2) Å and N1-C7 = 1.296(2) Å] distances were typical for ruthenium(III) complexes with Schiff base chelates [**50**]; while the C=N bond [C8-N2 = 1.297(2) Å and C22-N4 = 1.287(2) Å] (within the benzothiazole rings) lengths were shorter despite having the same bond order, but were comparable to transition metal complexes with non-coordinating benzothiazole moieties [**51**, **52**].

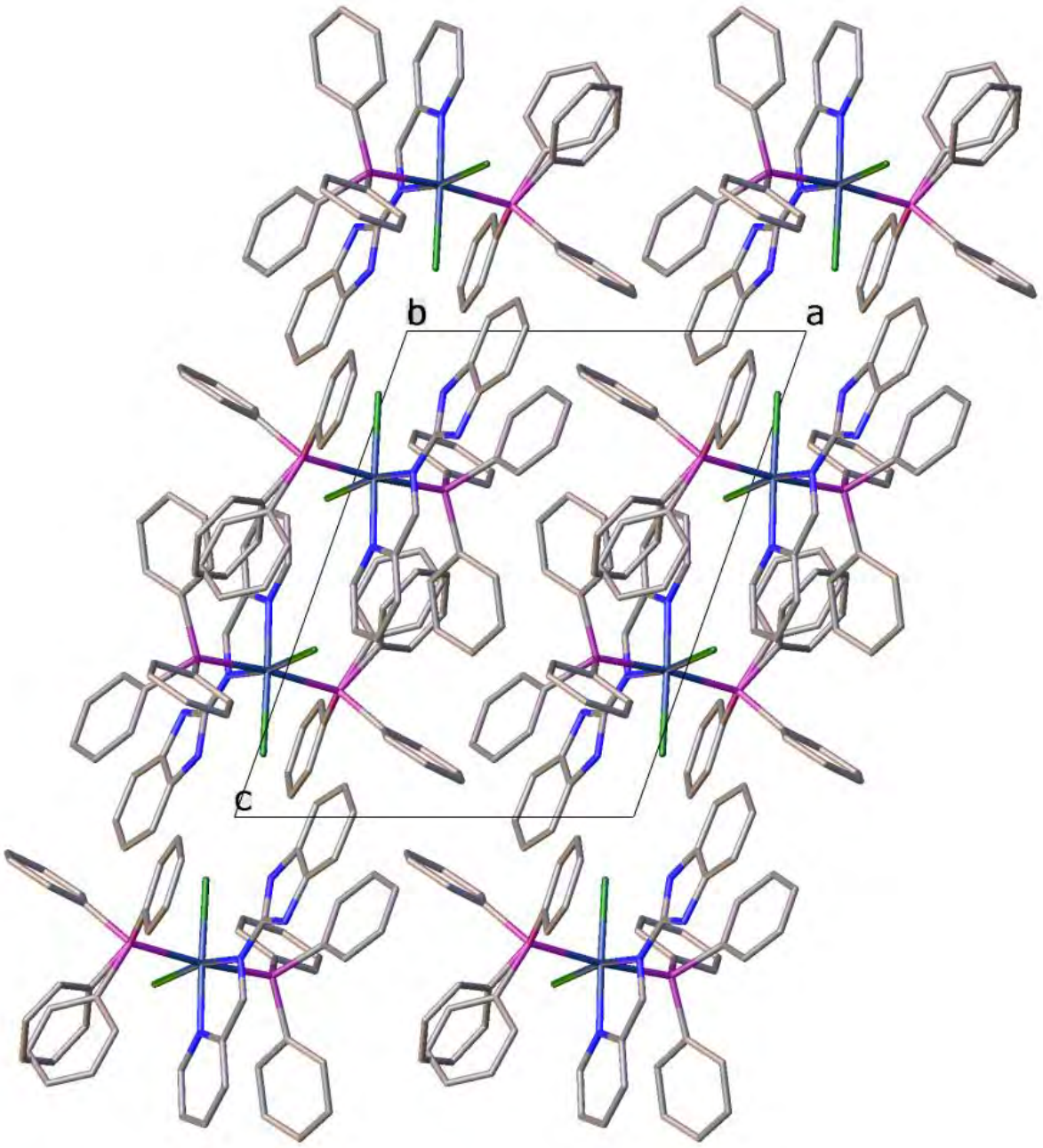

Figure 3.32: *Unit cell packing diagram for* ***1****. Hydrogen atoms have been omitted for clarity.*

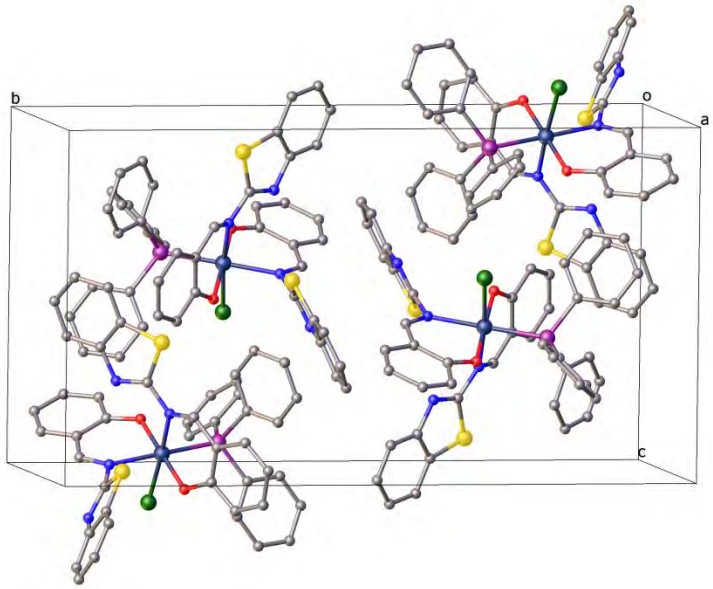

Figure 3.33: *Unit cell packing diagram for* **2**; *Hydrogen atoms have been omitted for clarity.*

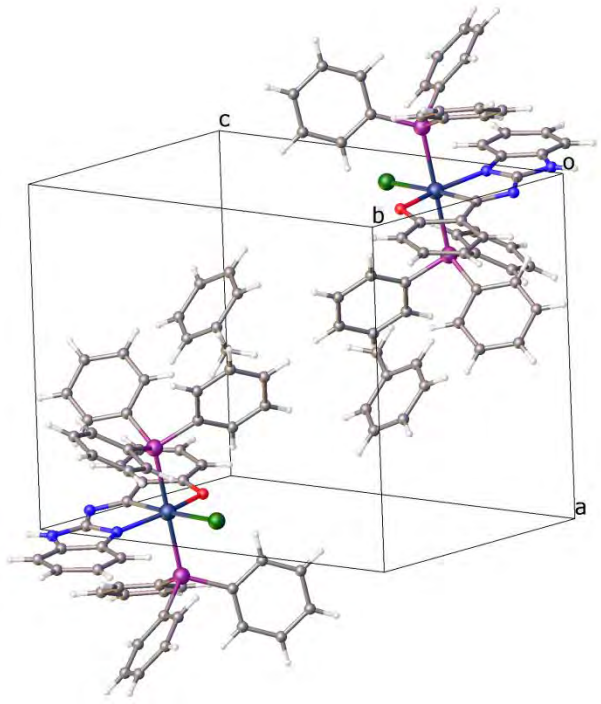

Figure 3.34: *A perspective view of two molecules of* **3** *occupying its triclinic unit cell.*

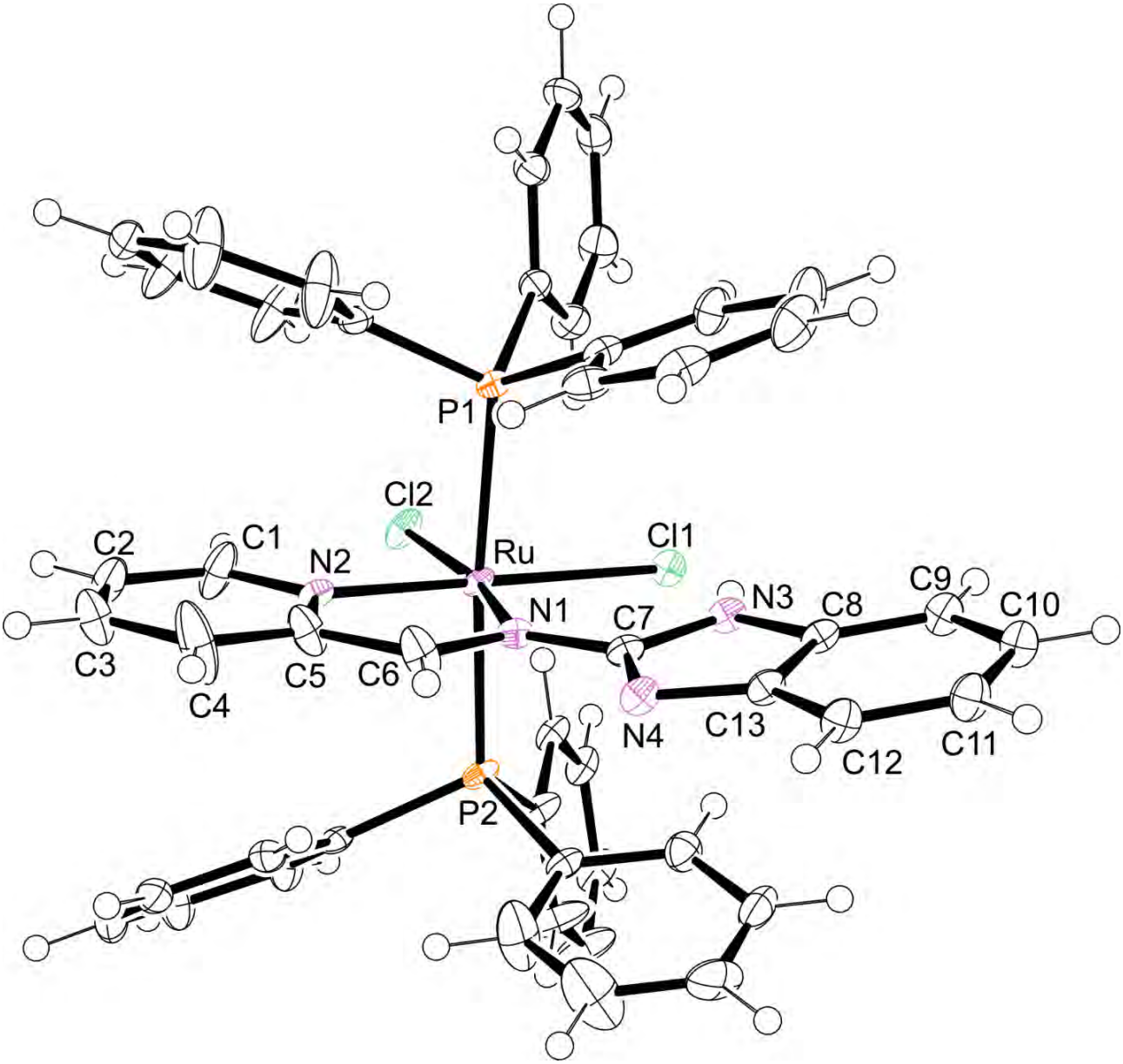

Figure 3.35: *An ORTEP view of complex **1** showing 50 % probability displacement ellipsoids and the atom labelling.*

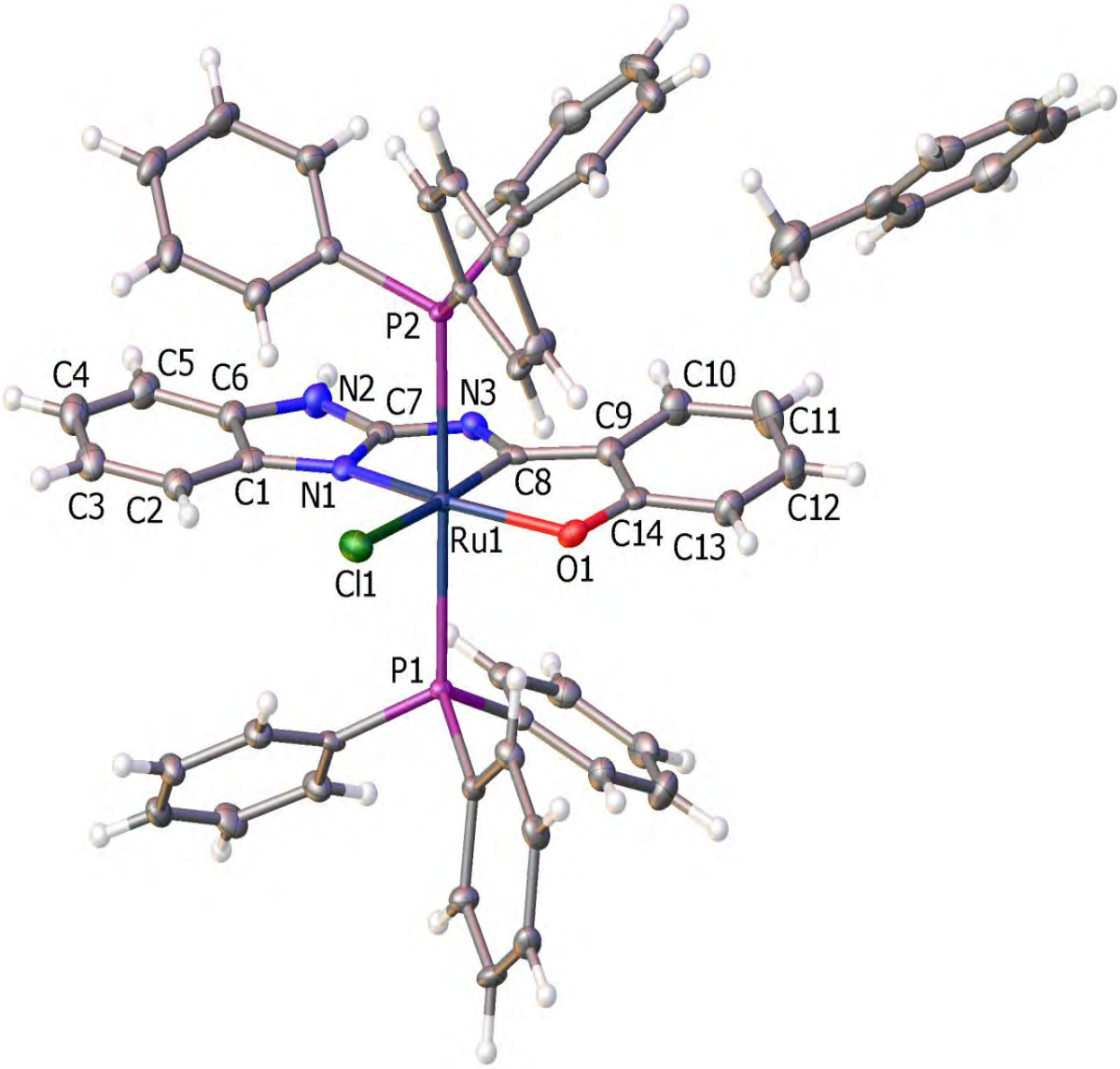

Figure 3.36: *An ORTEP view of complex* **3** *·C_7H_8 showing 50 % probability displacement ellipsoids and the atom labelling.*

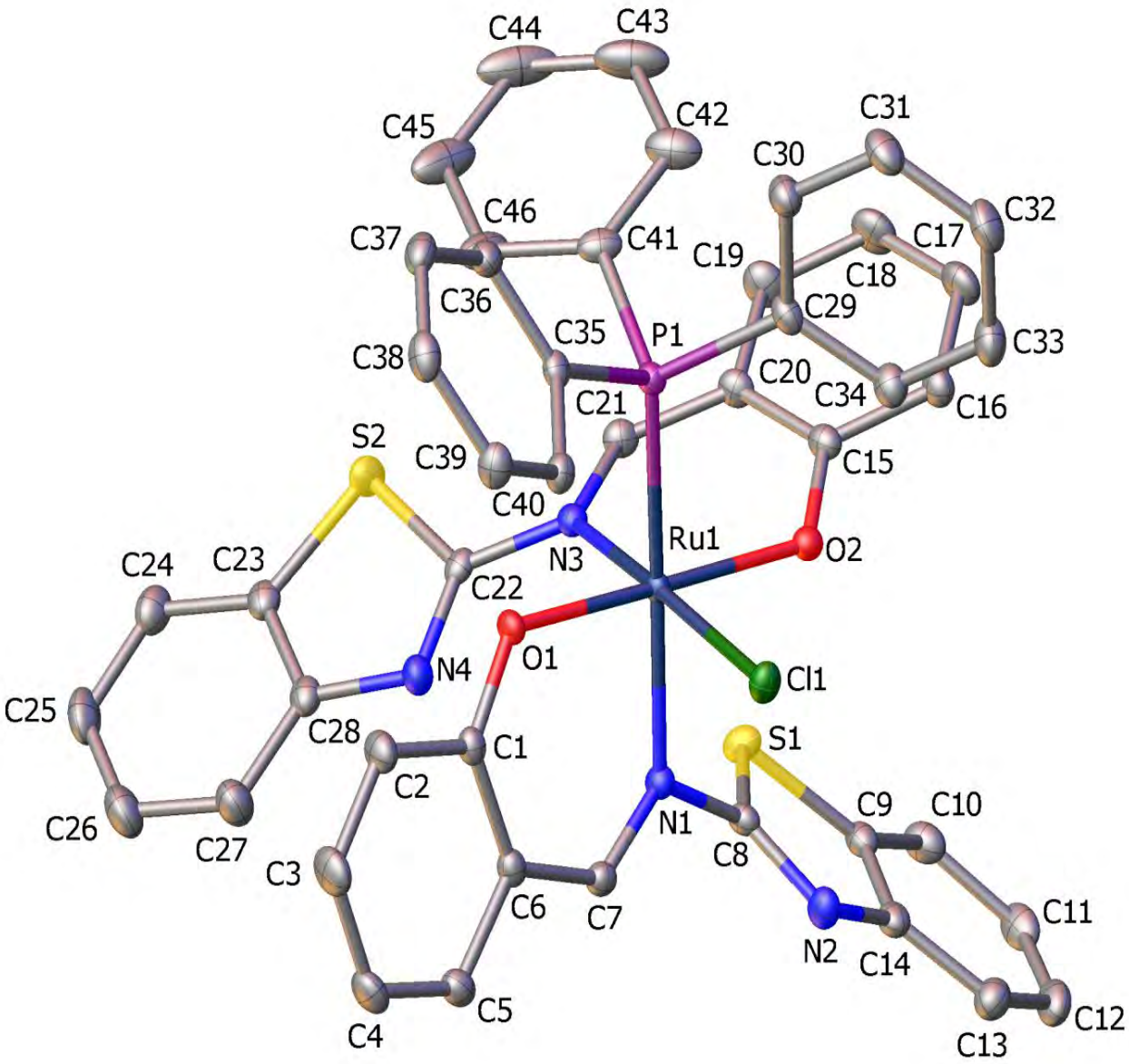

Figure 3.37: *An ORTEP view of complex* **2** *showing 50 % probability displacement ellipsoids and the atom labelling. Hydrogen atoms have been omitted for clarity.*

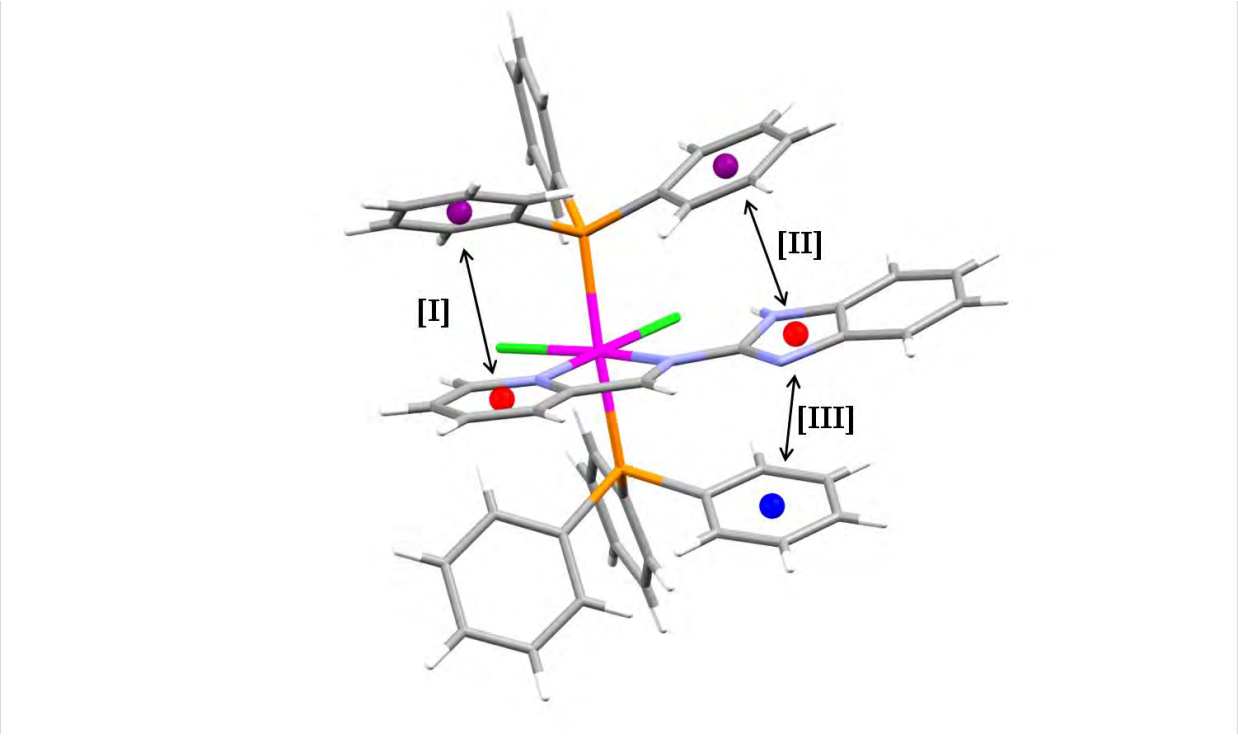

Figure 3.38: *Demonstration of the intramolecular π-π stacking interactions occurring in complex **1**; given as **I** = 3.748 Å, **II** = 3.553 Å and **III** = 3.575 Å.*

Table 3.3: *Crystal data and structure refinement data for **1**, **2** and **3**·C_7H_8.*

	1	**2**	**3**·C_7H_8
Chemical formula	$C_{49}H_{40}Cl_2N_4P_2Ru$	$C_{46}H_{33}ClN_4O_2PRuS_2$	$C_{57}H_{47}P_2ClRuON_3$
Formula weight	918.76	905.4	988.44
Temperature(K)	100(2)	100(2)	100(2)
Crystal system	Triclinic	Monoclinic	Triclinic
Space group	P-1	P_12_1/n	P-1
Unit cell dimensions (Å, °)	*a* = 12.2629(6) *b* = 13.4789(6) *c* = 14.8725(7) α= 104.012(2) β = 101.332(2) γ = 114.289(2)	*a* = 12.6611(5) *b* = 23.4989(8) *c* = 13.1178(5) α = 90.00 β = 91.807(2) γ = 90.00	*a* = 11.9756(10) *b* = 12.7076(11) *c* = 15.1112(13) α= 97.670(4) β = 91.750(4) γ = 90.061(4)
Crystal size (mm)	0.35 x 0.10 x 0.08	0.17 x 0.12 x 0.01	0.20 x 0.15 x 0.08
V(Å^3)	2048.54(17)	3900.89(4)	2278.0(3)
Z	2	4	2
Density (calc.) (Mg/m^3)	1.490	1.54	1.441
Absorption coefficient (mm^{-1})	0.63	0.665	0.519
F(000)	940.00	1843.7	1018.0
θ range for data collection (deg)	1.5; 30.53	1.7; 29.3	1.6; 27.08
Index ranges	-17 ≤ *h* ≤ 17 -19 ≤ *k* < 19 -21 ≤ ℓ ≤ 21	-17 ≤ *h* ≤ 17 -27 ≤ *k* < 32 -18 ≤ ℓ ≤ 18	-15 ≤ *h* ≤ 15 -15 ≤ *k* < 16 -18 ≤ ℓ ≤ 17
Reflections measured	46486	42006	21774
Observed reflections [*I*>2σ(*I*)]	12336	8949	7569
Independent reflections	11489	10638	8917
Data/Restraints/parameters	11489/0/582	10638/0/509	8917/0/587
Goodness of fit on F^2	1.044	1.036	1.117
Observed *R*, wR^2	0.0262; 0.066	0.031; 0.067	0.0564; 0.1404
R_{int}	0.020	0.019	0.0362

Table 3.4: *Selected bond lengths [Å] and bond angles [°] for* ***1****.*

Ru-P1	2.3785(5)
Ru-Cl1	2.4369(3)
Ru-N1	2.076(1)
C6-N1	1.311(2)
C7-N3	1.357(2)
Cl1-Ru-Cl2	91.44(1)
Cl1-Ru-N1	99.24(4)
Ru-P2	2.3964(4)
Ru-Cl2	2.4225(4)
Ru-N2	2.045(1)
C7-N4	1.325(2)
N1-Ru-N2	78.45(5)
Cl2-Ru-N2	90.87(4)
P1-Ru-P2	174.37(1)

Table 3.5: *Selected bond lengths [Å] and bond angles [°] for* ***2****.*

Ru1-Cl1	2.3634(5)
Ru1-N1	2.119(2)
Ru1-O1	1.975(1)
N3-C21	1.310(2)
N2-C8	1.297(2)
Cl1-Ru1-N3	172.76(4)
P1-Ru1-N1	175.42(5)
N1-Ru1-O1	90.51(6)
Ru1-P1	2.3536(5)
Ru1-N3	2.096(2)
Ru1-O2	2.004(1)
N1-C7	1.296(2)
N4-C22	1.287(2)
O1-Ru1-O2	177.69(5)
N3-Ru1-O2	87.29(6)

Table 3.6: *Selected bond lengths [Å] and bond angles [°] for* ***3****.*

Ru1-P1	2.386(1)
Ru1-C8	1.981(5)
Ru1-N1	2.069(4)
N3-C8	1.326(6)
N2-C7	1.360(6)
O1-Ru1-C8	80.8(1)
P1-Ru1-P2	178.55(4)
Ru1-P2	2.407(1)
Ru1-Cl1	2.436(1)
Ru1-O1	2.060(3)
N1-C7	1.333(6)
N1-Ru1-C8	76.0(2)
Cl1-Ru1-O1	99.79(8)
O1-Ru1-N1	155.8(1)

3.5 References

1. M. Groessl, E. Reisner, C.G. Hartinger, R.Eichinger, O. Semenova, A.R. Timerbaev, M.A. Jakupec, V.B. Arion, B.K. Keppler, *J. Med. Chem.,* 2007, **50**, 2185.

2. M.A. Sgambellone, A. David, R.N. Garner, K.R. Dunbar, C. Turro, *J. Am. Chem. Soc.*, 2013, **135**, 11274.

3. C. Ming Che, F. Siu, *Curr. Opin. Chem. Biol*., 2010, **14**, 255.

4. M.J. Clarke*, Coord. Chem. Rev.,* 2002, **232**, 69.

5. P. Heffeter, B. Atil, K. Kryeziu, D. Groza, G. Koellensperger, W. Körner, U. Jungwirth, T. Mohr, B.K. Keppler, W. Berger, *Eur.J.Cancer*, 2013, **49**, 3375.

6. M. Ravera, E. Gabano, S. Baracco, M. Sardi, D. Osella, *Inorg. Chim. Acta*, 2008, **361**, 2879.

7. S. Kapitza, M.A. Jakupec, M. Uhl, B.K. Keppler, B. Marian, *Cancer Lett*., 2005, **226**, 115.

8. M.P. Chelopo, S.A. Pawar, M.K. Sokhela, T. Govender, H.G. Kruger, G.E.M. Maguire, *Eur. J. Med. Chem*., 2013, **66**, 407.

9. Y. Chen, M. Qin, L. Wang, H. Chao, L. Ji, A. Xu, *Biochimie*, 2013, **95**, 2050.

10. S. David, R.S. Perkins, F.R. Fronczek, S. Kasiri, S.S. Mandal, R.S. Srivastava, *J. Inorg. Biochem.,* 2012**, 111,**33.

11. F. Dosio, B. Stella, A. Ferrero, C. Garino, D. Zonari, S. Arpicco, L. Cattel, S. Giordano, R. Gobetto, *Int. J. Pharm*., 2013, **440**, 221.

12. F.R. Pavan, G.V. Poelhsitz, M.I.F. Barbosa, S.R.A. Leite, A.A. Batista, J. Ellena, L.S. Sato, S.G. Franzblau, V. Moreno, D. Gambino, C.Q.F. Leite, *Eur. J. Med. Chem*., 2011, **46**, 5099.

13. J. DePasquale, N.J. White, E.J. Ennis, M. Zeller, J.P. Foley, E.T. Papish, *Polyhedron*, 2013, **58**, 162.

14. A. Grigoratos, N. Katsaros, *Inorg. Chim. Acta*, 1985, **108**, 41.

15. S.O. Pinheiro, J.R. de Sousa, M.O. Santiago, I.M.M. Carvalho, A.L.R. Silva, A.A. Batista, E.E. Castellano, J. Ellena, Í.S. Moreira, I.C.N. Diógenes, *Inorg. Chim. Acta*, 2006,**359**, 391.

16. F.E. Fernández, M. Puerta, P. Valerga, *Inorg. Chem*., 2013, **25**, 6502.

17. J.G. Małecki, A. Maron, *Polyhedron*, 2012, **40**, 125.

18. H. Sharma, H.J. Guadalupe, J. Narayanan, H. Hofeld, T. Pandiyan, N. Singh, *Anal. Methods*, 2013, **5**, 3880.

19. L. Oehninger, M. Stefanopoulou, H. Alborzinia, J. Schur, S. Ludewig, K. Namikawa, A. Muñoz-Castro, R.W. Köster, K. Baumann, S. Wölfl, W.S. Sheldrick Ingo Ott, *Dalton Trans.,* 2013, **42**, 1657.

20. A. Singh, B. Chetia, S.M. Mobi, G. Das, P.K. Iyer, B. Mondal, *Polyhedron,* 2008, **27**, 1983.

21. G.G. Mohamed, Z.H. Abd El-Wahab, *J. Therm. Anal. Calorim.,* 2003, **73**, 347.

22. Z.M. Zaki, *Spectrosc. Lett*., 1998, **31**, 757.

23. R.H. Blessing, *Acta Crystallogr.,Sect. A: Found. Crystallogr.*, 1995, **A51**, 33.

24. Bruker APEX2, SAINT and SADABS. Bruker AXS Inc., 2010, Madison, Wisconsin, USA.

25. G.M. Sheldrick, *Acta Crystallogr.,Sect. A: Found. Crystallogr.,* 2008, **A64**, 112.

26. L.J. Farrugia, *J. Appl. Cryst.*, 2012, **45**, 849.

27. O.V. Dolomanov, L.J. Bourhis, R.J. Gildea, J.A.K. Howard, H. Puschmann, *J. Appl. Cryst.*, 2009, **42**, 339.

28. J.D.E.T. Wilton-Ely, M. Wang, S.J. Honarkhah, D.A. Tocher, *Inorg. Chim. Acta*, 2005, **358**, 3218.

29. M.M. Tamizh, K. Mereiter, K. Kirchner, R. Karvembu, *J. Organomet. Chem.*, 2012, **700**, 194.

30. D. Mishra, S. Naskar, R.J. Butcher, S.K. Chattopadhyay, *Inorg. Chim. Acta,* 2005, **358**, 3115.

31. N.G. Tsierkezos, A.I. Philippopoulos, *Inorg. Chim. Acta*., 2009, **362**, 3079.

32. A.K. Das, R. Hübner, B. Sarkar, J. Fiedler, S. Záliš, G.K. Lahiric, W. Kaim, *Dalton Trans.,* 2012, **41**, 8913.

33. K. Nagaraju, S. Pal, *J. Organomet. Chem.,* 2013, **737**, 7.

34. C.P. Matos, A. Valente, F. Marques, P. Adão, M.P. Robalo, R.F.M. de Almeida, J.C. Pessoa, I. Santos, M.H. Garcia, A.I. Tomaz, *Inorg. Chim. Acta*, 2013, **394**, 616.

35. K. Nagaraju, R. Raveendran, S. Pal, S. Pal, *Polyhedron*, 2012, **33**, 52.

36. I.N. Booysen, S. Maikoo, M.P. Akerman, B. Xulu, O.Q. Munro *J. Coord. Chem.*, 2013, **66**, 3673.

37. R. Raveendran, S. Pal, *J. Organomet. Chem*., 2010, **695**, 630.

38. R. Raveendran, S. Pal, *J. Organomet. Chem*., 2007, **692**, 824.

39. E. Eskelinen, P. Da Costa, M. Haukka, *J. Electroanal. Chem*., 2005, **579**, 257.

40. T. Hamaguchi, Y. Kurashige, I. Ando, *Inorg. Chim. Acta,* 2013, **405**, 410.

41. V.R. de Souza, G.S. Nunes, R.C. Rocha, H.E. Toma, *Inorg. Chim. Acta*, 2003, **348**, 50.

42. R.M. Berger, *Inorg. Chem*., 1990, **29**, 1920.

43. G.F. Frey, Z.R. Bell, J.C. Jeffery, M.D. Ward, *Polyhedron*, 2001, **20**, 3231.

44. R. Jana, B. Schwederski, J. Fiedler, W. Kaim, *Polyhedron*, 2012, **44**, 174.

45. L. Giovagnini,S. Sitran,I. Castagliuolo,P. Brun,M. Corsini,P. Zanello, A. Zoleo,A. Maniero,B. Biondi, D. Fregona, *Dalton Trans*., 2008, 6699.

46. S. Kundu, D. Sarkar, M.S. Jana, A.K. Pramanik, S. Jana, T.K. Mondal, *J. Mol Struct*., 2013, **1035**, 277.

47. S. Mandal, D.K. Seth, P. Gupta, *Inorg. Chim. Acta*, 2013, **397**, 10.

48. M.J. Clarke, *Coord. Chem. Rev*., 2003, **236**, 209.

49. L. Oehninger, M. Stefanopoulou, H. Alborzinia, J. Schur, S. Ludewig, K. Namikawa, A. Muñoz-Castro, R.W. Köster, K. Baumann, S. Wölfl, W.S. Sheldrick, I. Otta, *Dalton Trans*., 2013, **42**, 1657.

50. R. Raveendran, S. Pal, *Polyhedron*, 2008, **27**, 655.

51. K.C. Potgieter, T.I.A. Gerber, E. Hosten, *Inorg. Chem. Commun*., 2012, **24**,231.

52. H. Yu, X. Fang, K. Zhang, M. Lin, D. Gao, M. Huanga, J. Wanga, *Cryst. Eng. Commun*., 2013, **15**, 343.

Chapter 4

Formation, electrochemical and radical scavenging properties of novel ruthenium compounds with N, X-donor (X = O, N) heterocyclic chelators

4.1 Introduction

The concerted efforts in the isolation of new analogues of NAMI-A, *trans*-[$RuCl_4$(DMSO)(Im)](ImH) {ImH = imidazole} are due to its potent anti-metastatic cancer activity [**1, 2**]. Our interest is the utilization of heterocyclic-derived ligands incorporating benz(imidazole/othiazole/oxazole) moieties due to their multitude of biological activities [**3-5**]. In addition, the secondary metabolite, chromone and its organic and inorganic compounds have proven to exhibit potent anticancer activities against a wide range of cancer cell lines [**6-9**]. Most recently, we have also designed Schiff bases containing the tetrahydro-2*H*-pyrane moiety which shares the same backbone structure as the sugar derivative, mannose. Their structural similarities' can potentially enforce the target specific binding of the tetrahydro-2*H*-pyrane-derived Schiff bases and their metal complexes to the mannose receptors in the Sentinel Lymph Node (SLN) [**10**].

This chapter details the formation of novel ruthenium compounds containing benzoxazole-amide, benzimidazole-amines and chromone-derived Schiff base ligands. The metal complexes: [RuCl(pho)(bzca)(PPh_3)] (**1**) (pho = 2-aminophenolate; bzca = 2-carboxylate-1*H*-benzimidazole), *cis-Cl*, *trans-P*-[Ru^{III}(Hbhb)Cl_2(PPh_3)$_2$] (**2**), (μ-Htba,Cl)$_2$[$Ru^{II}Cl(PPh_3)]_2$ (**3**) and (μ-Cl)$_2$[$Ru^{III}Cl$(Hchpr)(PPh_3)]$_2$ (**4**) were synthesized

from the reactions of *trans*-[$RuCl_2(PPh_3)_3$] with 2-((1*H*-benzimidazole)methylamino)phenol (Hbzap), *N*-(benzoxazole)-2-hydroxybenzamide (H_2bhb), *N*-(thiophene)methyl-benzoxazole-2-amine (Htba) and 2-amino-3-((tetrahydro-2*H*-pyran-4-ylimino)methyl)-4*H*-chromen-4-one (H_2chpr), respectively (see Figure 4.1). Under similar experimental conditions, a diamagnetic complex, [$Ru^{II}Cl_2$(Hbzpy)$(PPh_3)_2$] (**5**) was also formed using *N*-((pyridine-2-*yl*)methyl)-1*H*-benzimidazole (Hbzpy) with the same metal precursor. In addition, the redox properties of the metallic compounds **1**-**5** investigated *via* voltammetric analysis were comparable to other ruthenium compounds found within the literature [**11**]. The metallic complexes **1**-**4** exhibit higher DPPH radical scavenging activities than their corresponding free-ligands.

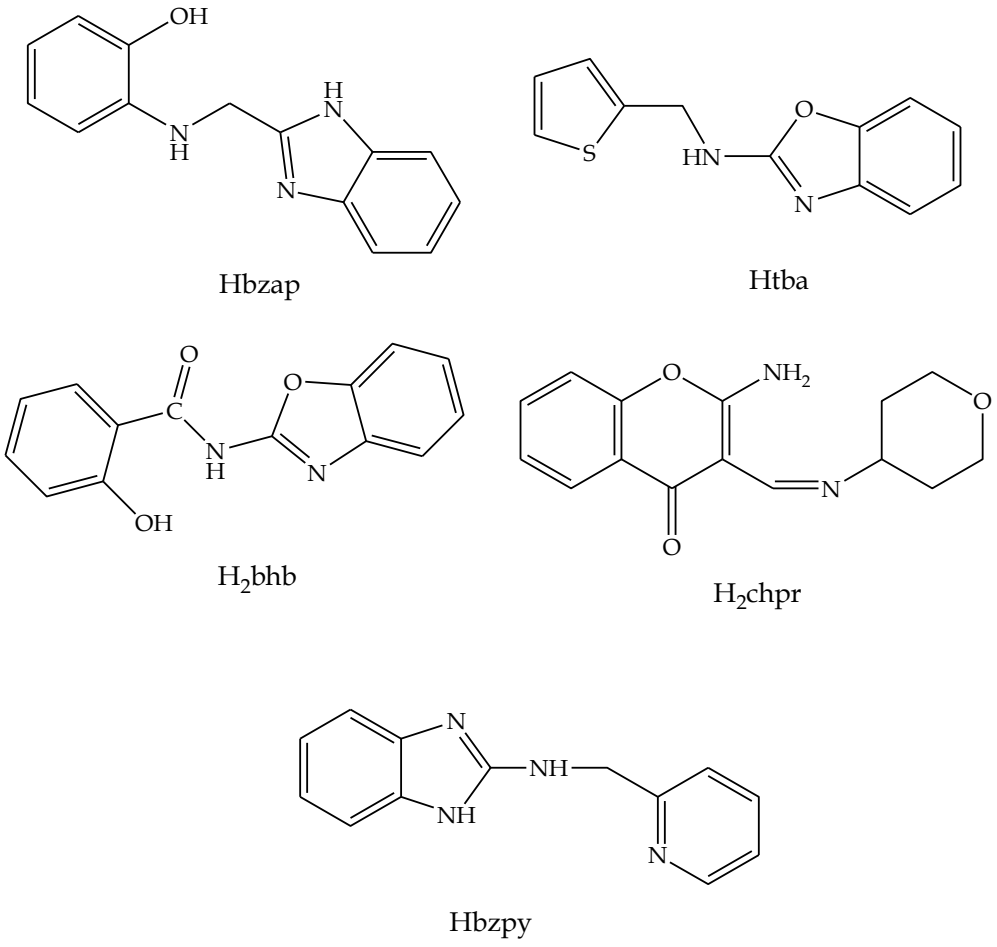

Figure 4.1: *Structures and abbreviations of synthesized ligands.*

4.2 Experimental

4.2.1 Synthesis of ligands:

4.2.1.1 2-((1H-benzimidazole)methylamino)phenol (Hbzap)

A reaction mixture of 2-chloromethylbenzimidazole (2.50 g; 15 mmol), 2-aminophenol (1.64 g; 15 mmol) and KI (2.50 g; 15 mmol) in 75 cm^3 of absolute ethanol was heated under reflux. After 6 hrs, a catalytic amount of KOH (0.84 g; 15 mmol) in 7.5 cm^3 of distilled water was added drop wise with continuous stirring for 2 hours. Thereafter, the reaction mixture was allowed to cool down to room temperature and then poured into crushed ice water. Instantaneously, a brown precipitate formed which was recrystallized from ethanol to afford brown needle-like crystals. Yield = 92%; M.P. = 210 – 212 °C; IR (ν_{max}/cm^{-1}): ν(N-H) 3043 (bz, m), 3003 (amine, w), ν(O-H) 2556 (w), ν(C=N) 1517 (s), ν(C-N) 1239 (s); ^{1}H NMR (295K/ppm /d^6-DMSO): 12.32 (br, s, 1H, *NH*)$_{bz}$, 9.40 (s, 1H, *NH*)$_{amine}$, 7.55-7.47 (m, 2H, *H1, H4*), 7.17 – 7.11 (m, 2H, *H2, H3*), 6.69 (d, 1H, *H10*), 6.58 (t, 1H, *H9*), 6.51 – 6.42 (m, 2H, *H7, H8*), 4.49 (s, 2H, *H5, H6*), 3.33 (br, s, 1H, *OH*). UV-Vis (DMF, (λ_{max} (ε, $M^{-1}cm^{-1}$))): 239 nm (sh, 28849); 282 nm (22435); 332 nm (27317); 352 nm (29035); 385 nm (34243).

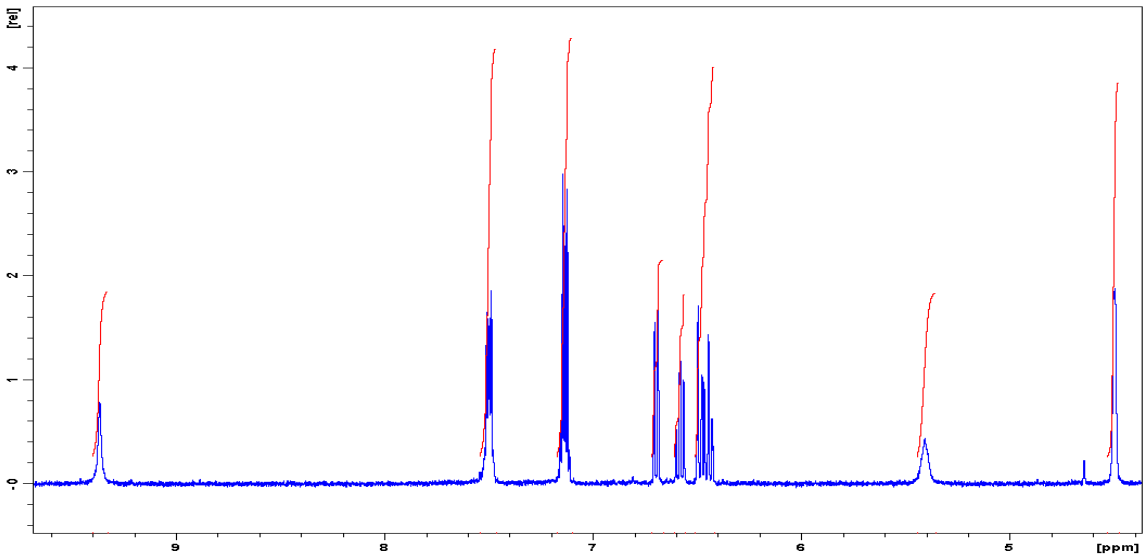

Figure 4.2: *^{1}H NMR spectrum of Hbzap.*

4.2.1.2 *N-(benzoxazole)-2-hydroxybenzamide (Hbhb)*

The reaction mixture of 2-aminobenzoxazole (0.25 g; 1.86 mmol) and salicylaldehyde (0.230 g; 1.86 mmol) dissolved in 40 cm^3 of dry toluene containing 3 drops of piperidine was heated at reflux temperature for 6 hrs under nitrogen. The initial yellow solution of the reaction mixture turned orange and was allowed to cool down to room temperature after the reflux period and thereafter left overnight in the fridge in order to induce precipitation. The resultant yellow precipitate was filtered and washed with cold anhydrous toluene and petroleum ether. Yield = 80%; M.P. = 136 – 138 °C; IR (ν_{max}/cm^{-1}): ν(N-H) 3339, ν(O-H) 3056 (w), ν(C=O) 1706 (m), ν(C=N) 1601 (vs), ν(C-N) 1244 (s); ^{1}H NMR (295K/ppm/d^6-DMSO): 9.68 (s, 1H, N*H*), 7.98 (d, 1H, *H5*), 7.75 – 7.67 (m, 2H, *H2, H3*), 7.54 (t, 1H, *H4*), 7.43 – 7.35 (m, 2H, *H10, H11*), 7.07 – 6.98 (m, 2H, *H9, H12*), 3.36 (br, s, 1H, OH); UV-Vis (DMF, (λ_{max} (ε, $M^{-1}cm^{-1}$))): 241 nm (10974); 282 nm (8712); 330 nm (15707); 351 nm (16979); 383 nm (20673).

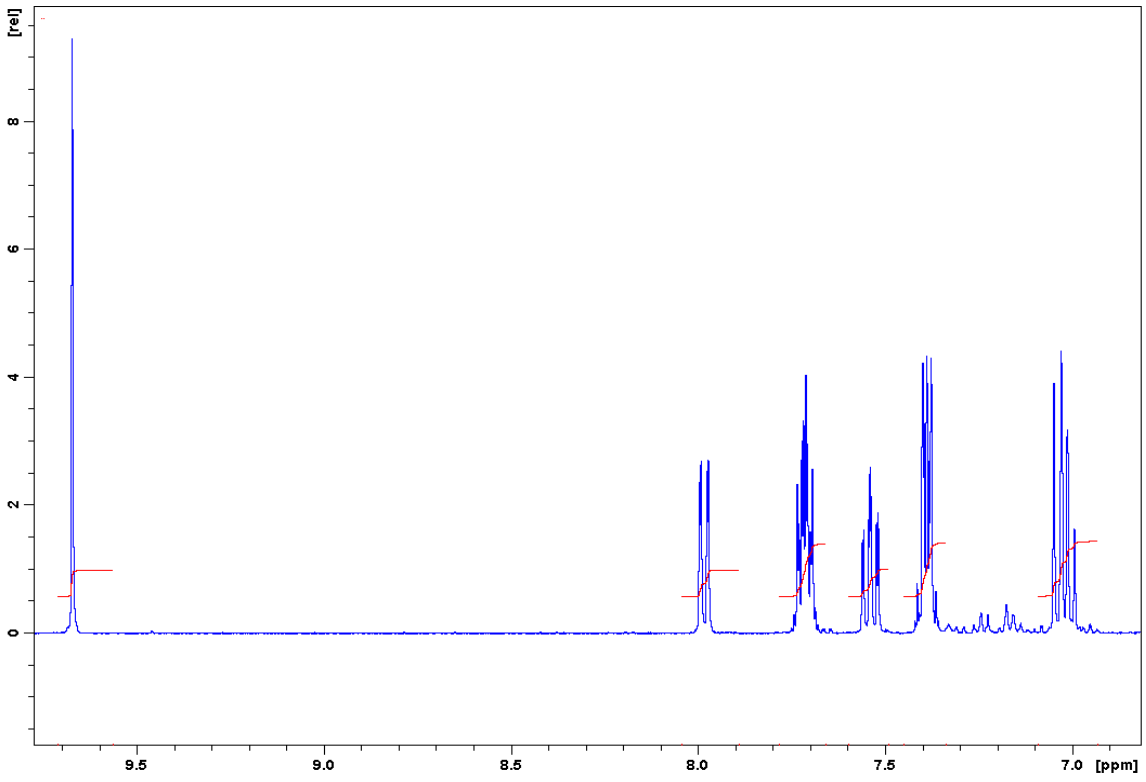

Figure 4.3: *^{1}H NMR spectrum of Hbhb between 9.77 and 6.82 ppm.*

4.2.1.3 *N-(thiophene)methyl-benzoxazole-2-amine (Htba)*

The Schiff base, *N*-((thiophen-2-yl)methyleneimino)benzoxazole (Htbi) was isolated as an orange crystalline substance from the equimolar condensation reaction between 2-aminobenzoxazole (0.250 g; 1.86 mmol) and 2-thiophenecarboxaldehyde (0.209; 1.86 mmol). The reaction was conducted in 40 cm^3 of dry toluene and in the presence 3 drops of piperidine, under nitrogen for 6 hrs followed by reducing the reaction mixture to 5 cm^3 and cooling it in an ice-bath to induce crystallization. The reducing agent, sodium borohydride (0.025 g, 0.66 mmol) in ethanol (10 cm^3) was added dropwise to a stirring solution of ethanol (20 cm^3) containing 0.15 g of Htbi (0.66 mmol) at room temperature. The reaction mixture was then refluxed for an hour and thereafter cooled to room temperature by adding an equal volume of cold distilled water. A white precipitate instantaneously formed which was collected, washed with distilled water and dried under vacuum.Yield = 88%; M.P. = 126 – 128 °C; IR (ν_{max}/cm^{-1}): ν(N-H) 3046 (w), ν(thiophene) 1459, 1439 sh, 1354, 1321 (s), ν(C-N) 1246 (s); ^{1}H NMR (295K/ppm/d^6-DMSO): 8.50 (s, 1H, N*H*), 7.40 (d, 1H, *H9*), 7.35 (t, 1H, *H8*), 7.27 (d, 1H, *H7*), 7.15 – 7.06 (m, 2H, *H3*, *H4*), 7.02 – 6.96 (m, 2H, *H1*, *H2*), 4.68 (s, 2H, *H5*, *H6*); UV-Vis (DMF, (λ_{max} (ε, $M^{-1}cm^{-1}$))): 245 nm (19632); 282 nm (8372); 288 nm (sh, 6995).

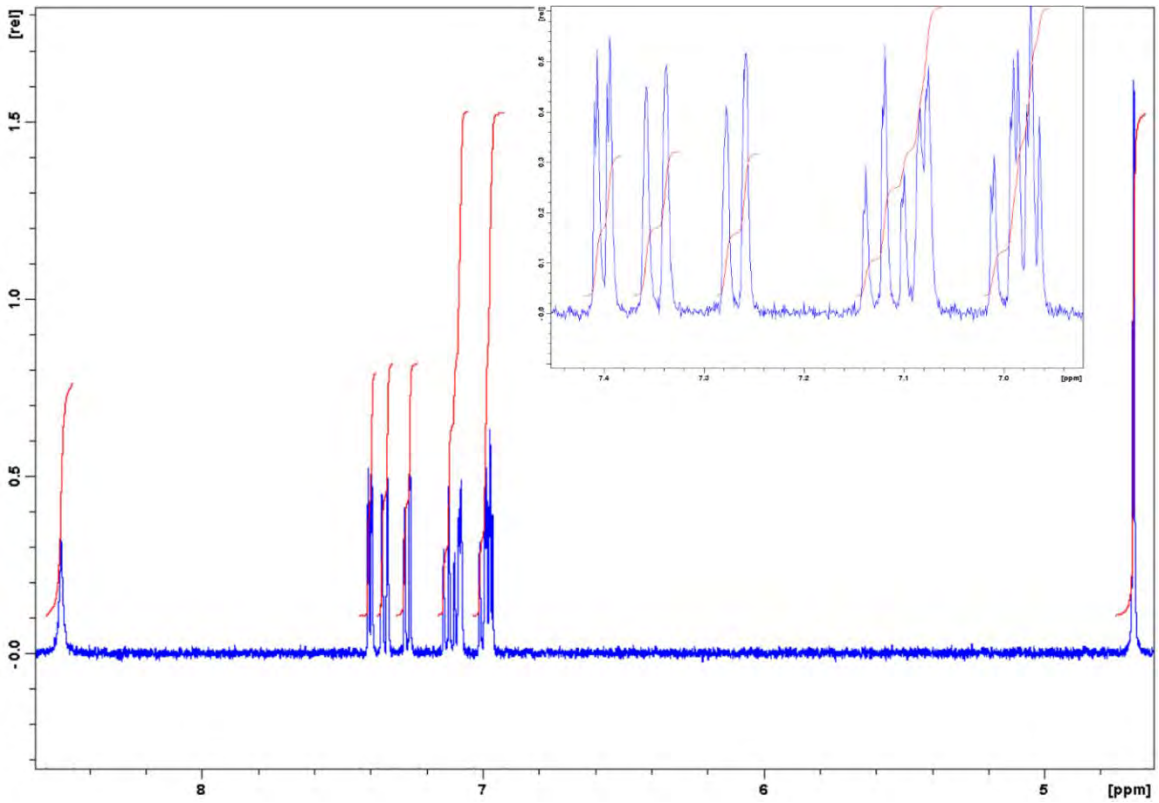

Figure 4.4: *^{1}H NMR spectrum of Htba and inset showing the signals for the aromatic protons.*

4.2.1.4 2-amino-3-((tetrahydro-2H-pyran-4-ylimino)methyl)-4H-chromen-4-one (H_2chpr)

A solution of tetrahydro-2*H*-pyran-4-amine (0.20 g; 1.98 mmol) in 20 cm^3 of methanol was added dropwise to a stirring methanolic solution (20 cm^3) of 2-amino-3-formylchromone (0.37 g; 1.98 mmol). The resultant reaction mixture was refluxed for 3 hrs and then reduced down to 5 cm^3 and cooled in an ice bath which resulted in the formation of yellow crystals of the titled compound. These crystals was washed with anhydrous petroleum ether and dried under vacuum. Yield = 86%; M.P. = 165 – 167 °C; IR (ν_{max}/cm^{-1}): ν(N-H) 3074 (m), ν(C=O) 1661 (s), ν(C=N) 1602 (vs), ν(C-O-C)$_{chromone}$ 1566, 1490 (s), ν(C-O-C)$_{tetrahydropyran}$ 1139 (s); ^{1}H NMR (295K/ppm/d^6-DMSO): 8.93 (br, s, 2H, NH_2), 8.76 (s, 1H, *H10*), 8.00 (d, 1H, *H3*), 7.67 (t, 1H, *H4*), 7.42 – 7.35 (m, 2H, *H5*, *H6*), 3.92

– 3.84 (m, 2H, *H12*, *H12'*), 3.39 – 3.53 (m, 2H, *H15*, *H15'*), 1.77 – 1.56 (m, 4H, *H13*, *H13'*, *H14*, *H14'*); UV-Vis (DMF, (λ_{max} (ε, $M^{-1}cm^{-1}$))): 236 nm (19312); 267 nm (sh, 12843); 301 nm (sh, 9134); 334 nm (7979); 350 nm (9253); 364 nm (sh, 7890).

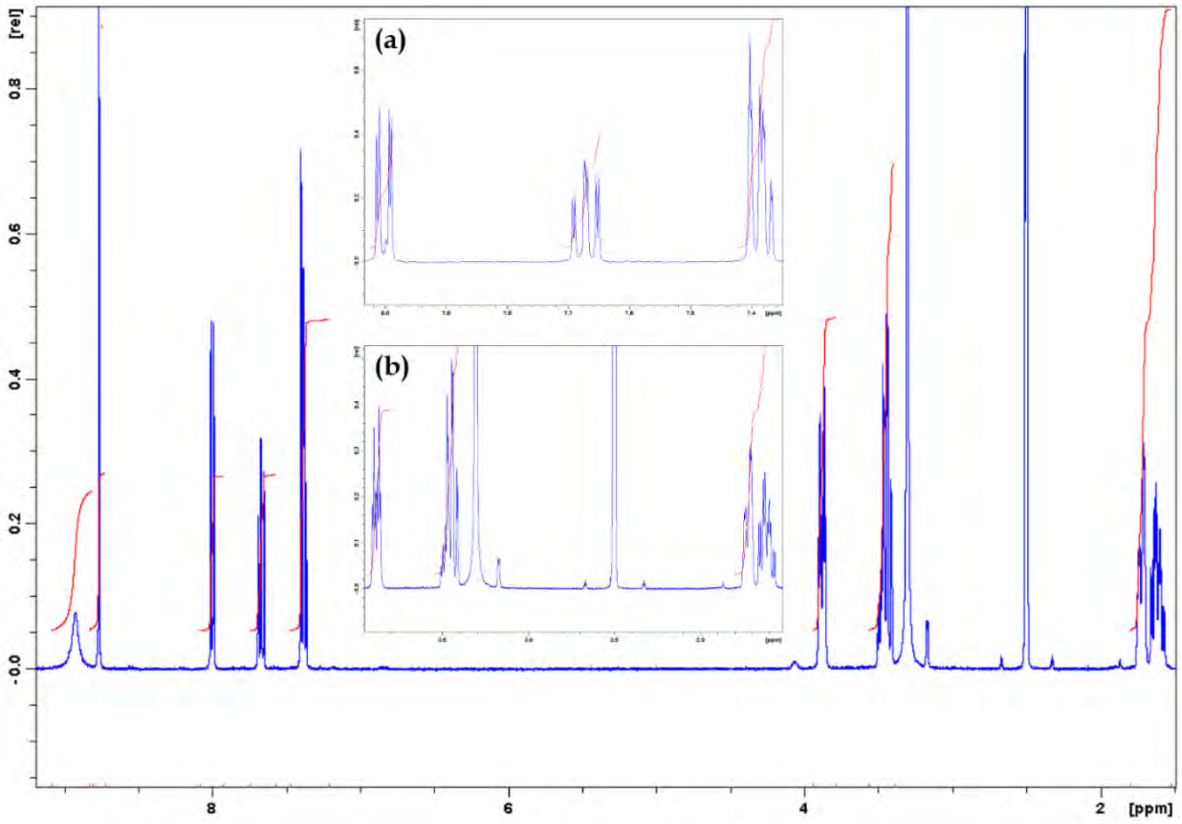

Figure 4.5: *^{1}H NMR spectrum of H_2chpr. Inset (a) showing the signals for the chromone protons. Inset (b) showing the signals for the tetrahydropyran aromatic protons.*

4.2.1.5 N-((pyridine-2-yl)methyl)-1H-benzimidazole (Hbzpy)

An equimolar amount of sodium borohydride was added dropwise to a stirring solution of the Schiff base, *N*-((pyridine-2-yl)methylene)-1*H*-benzimidazole (bzpy) (0.15 g; 0.68 mmol) in ethanol (20 cm^3) at room temperature for over 24 hrs. Afterwards the reaction mixture was refluxed for 1 hr and cooled to room temperature. Thereafter, this reaction mixture was added to an equal volume of cold distilled water and heated for 30

minutes. A white precipitate was formed which was filtered, washed with distilled water and dried under vacuum.Yield = 89%; M.P. = 218 – 220 °C; IR (ν_{max}/cm^{-1}):ν(N-H) 3242 (w), 3049 (w), ν(C-N) 1240 (s); ^{1}H NMR (295K/ppm/d^6-DMSO): 10.84 (s, 1H, *NH*), 8.53 (d, 1H, *H10*), 7.74 (t, 1H, *H9*), 7.38 (d, 1H, *H7*), 7.26 (t, 1H, *H8*), 7.15 – 7.06 (m, 3H, *H1, H4, NH*), 6.92 – 6.79 (m, 2H, *H2, H3*), 4.61 (d, 2H, *H5*, *H6*); UV-Vis (DCM, (λ_{max} (ε, M^{-1}cm^{-1}))): 254 nm (10048); 290 nm (9492).

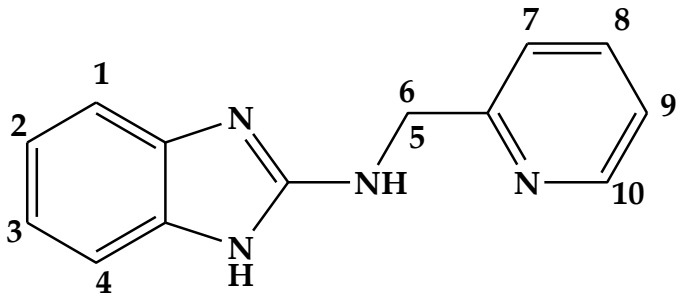

Figure 4.6: *Numbering scheme for Hbzpy.*

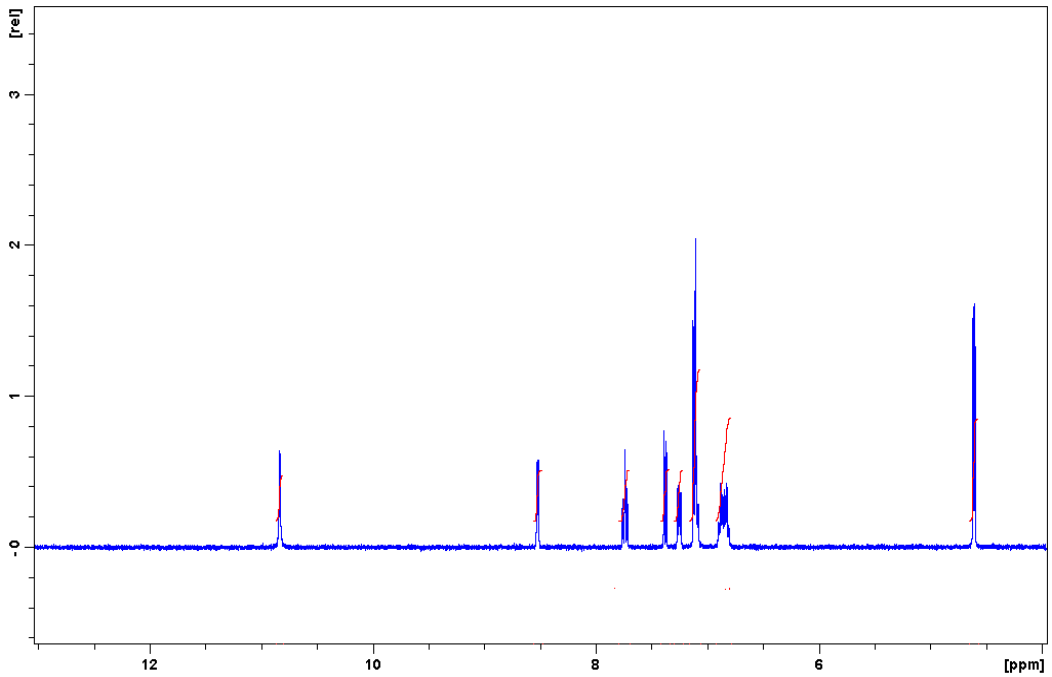

Figure 4.7: *^{1}H NMR spectrum of Hbzpy.*

4.2.2 Synthesis of metal complexes

*4.2.2.1 [RuCl(pho)(bzca)(PPh_3)] (**1**)*

A reaction mixture of Hbzap (0.0250 g; 0.104 mmol) and *trans*-[$RuCl_2(PPh_3)_3$] (0.1004 g; 0.104 mmol) in toluene (20 cm^3) was heated to reflux under a nitrogen atmosphere for 6 hrs. A dark brown precipitate was collected *via* filtration, washed with anhydrous di-ethyl ether and dried under vacuum. This precipitate was recrystallized *via* the slow diffusion of dichloromethane into a methanolic solution which yielded XRD quality dark brown crystals. Yield = 55%; M.P. = 250 – 252 °C; IR (ν_{max}/cm^{-1}): υ(N-H) 3050, 3025 sh (m), υ(O-H) 2552 (w), υ(C=O) 1588 (m), υ(C=N) 1531, 1514 (vs), υ(Ru-PPh_3) 693 (vs), υ(Ru-O, N)$_{phenolate}$ 466, 430 (s), υ(Ru-O, N)$_{benzimidazole}$ 541 (s), 511 (vs);UV-Vis (DCM, (λ_{max} (ε, $M^{-1}cm^{-1}$))): 232 nm (sh, 31968); 272 nm (sh, 14474); 359 nm (sh, 9806); 435 nm (sh, 6511); 470 nm (5848); 703 (sh, 1977).Conductivity (DCM, 10^{-3} M): 21.94$ohm^{-1}cm^{-2}mol^{-1}$; Anal. Calc. for $C_{33}H_{29}ClN_3O_4PRu$ (%): C, 56.69; H, 4.18; N, 6.01. Found: C, 56.74; H, 4.13; N, 6.16.

*4.2.2.2 cis-Cl, trans-P-[Ru(Hbhb)$Cl_2(PPh_3)_2$] (**2**)*

The equimolar amounts of H_2bhb (0.0249 g; 0.104 mmol) and *trans*-[$RuCl_2(PPh_3)_3$] (0.1004 g; 0. 104 mmol) in dichloromethane (20 cm^3) was allowed to stir for 24 hrs in an open atmosphere. A dark brown solution was obtained after which the volume was reduced and the product was precipitated by addition of *n*-hexane. The complex was recrystallized *via* slow diffusion of dichloromethane into a methanolic solution which resulted in the formation of brown crystals. Yield = 78%; M.P. = 255 – 257 ^oC; IR (ν_{max}/cm^{-1}): υ(O-H) 3051 (w), υ(C=N) 1547 (s), υ(C-N) 1238 (s), υ[Ru-(PPh_3)$_2$] 691 (vs), υ(Ru-N) 451 (s), υ(Ru-O) 433 (m).^{1}H NMR (295K/ppm): 7.68 – 7.52 (m, 30H, 2 x *PPh_3*), 7.43 – 7.38 (m, 4H, *H10*, *H11*, *H12*, *H13*), 7.27 – 7.21 (m, 4H, *H2*, *H3*, *H4*, *H5*), 5.09 (br, s, 1H, *OH*); ^{31}P NMR (295K/ppm): 25.38; UV-Vis (DCM, (λ_{max} (ε, $M^{-1}cm^{-1}$))): 274 nm (sh,

51784); 311 nm (37235); 351 nm (25117); 436 nm (8927); Conductivity (DCM, 10^{-3} M): 26.89 $ohm^{-1}cm^{-2}mol^{-1}$;Anal. Calc. for $C_{50}H_{39}Cl_2N_2O_3P_2Ru$ (%): C, 63.23; H, 4.14; N, 2.95. Found: C, 62.55; H, 4.07; N, 3.22.

*4.2.2.3 $(\mu$-Htba,Cl)$_2[Ru^{II}Cl(PPh_3)]_2$ (**3**)*

Compound **3** was isolated from the reaction of Htba (0.0240g; 0.104 mmol) and *trans*-$[RuCl_2(PPh_3)_3]$ (0.1004 g; 0.104 mmol) in hot benzene (20 cm^3) at reflux under a nitrogen atmosphere for 6 hrs. The volume was reduced to 5 cm^3 and the product precipitated by the addition of *n*-hexane. Recrystallization of the precipitate was achieved from the slow evaporation of a dichloromethane: methanol (1:1, *v:v*) solution giving solid dark brown cubic crystals. Yield = 63%; M.P. = 165 –167 °C; IR (ν_{max}/cm^{-1}): υ(N-H) 3052 (w), υ(C=N) 1649 (s), υ(thiophene, C=C) 1465, 1436 (s), 1366, 1339 (w), υ(C-N) 1246 (m), υ(Ru-PPh_3) 694 (vs), υ(Ru-N)$_{benzimidazole}$ 539 (vs), υ(Ru-N)$_{amine}$ 515 (vs);^{1}H NMR (295K/ppm): 8.84 (br, s, 2H, *NH, NH'*), 8.53 (t, 2H, *H3, H3'*), 7.84 (t, 2H, *H2, H2'*), 7.68 – 7.51 (m, 15H, *PPh_3*), 7.45 – 7.32 (m, 15H, *PPh_3*), 7.31 – 7.20 (m, 10H, *Ar, Ar' Toluene*), 7.15 – 7.06 (m, 4H, *H1, H1', H4, H4'*), 7.02 – 6.96 (m, 6H, *H7, H7', H8, H8', H9, H9'*), 4.68 (d, 4H, *H5, H5', H6, H6'*), 2.08 (s, 6H, *CH_3, CH_3'* of toluene); ^{31}P NMR (295K/ppm): 25.55; UV-Vis (DCM, (λ_{max} (ε, $M^{-1}cm^{-1}$))): 275 nm (sh, 67628); 404 nm (sh, 14805); 573 nm (9621). Conductivity (DCM, 10^{-3} M): 27.55 $ohm^{-1}cm^{-2}mol^{-1}$; Anal. Calc. for $C_{60}H_{52}Cl_4N_6P_2Ru_2S_2$ (%):C, 54.30; H, 3.95; N, 6.33. Found: C, 54.49; H, 3.60; N, 6.57.

*4.2.2.4 $(\mu$-Cl)$_2[Ru^{III}Cl(Hchpr)(PPh_3)]_2$ (**4**)*

The metal precursor, *trans*-$[RuCl_2(PPh_3)_3]$ (0.1004 g; 0.104 mmol), when reacted with H_2chpr (0.0284 g; 0.104 mmol) dissolved in hot anhydrous toluene (20 cm^3) at reflux temperature for 5 hrs under an open atmosphere, afforded a green mother liquor. From the slow evaporation of this green mother liquor, dark green crystals suitable for X-ray

analysis were obtained after several days. Yield = 72%, M.P. = 262 – 264 °C. IR (ν_{max}/cm^{-1}): υ(N-H) 3053 (w), υ(C=O) 1639 (m), υ(C=N) 1564 (vs), υ(C-O-C)$_{chromone}$ 1437 sh, 1433 (s), υ(C-O-C)$_{tetrahydropyran}$ 1136 (m), υ(Ru-PPh$_3$) 692 (vs), υ(Ru-N)$_{imino}$ 513 (vs), υ(Ru-N)$_{amindo}$ 488 (s). UV-Vis (DCM, (λ_{max} (ε, M^{-1}cm^{-1}))): 257 nm (sh, 28589); 280 nm (sh, 17664); 305 nm (sh, 13147); 355 nm (9632); 465 nm (sh, 4315); 688 nm (sh, 2334); Conductivity (DCM, 10^{-3} M): 22.73 ohm^{-1}cm^{-2}mol^{-1};Anal. Calc. for $C_{80}H_{76}Cl_4N_4O_6P_2Ru_2$ (%):C, 60.23; H, 4.80; N, 3.51. Found: C, 60.19; H, 4.78; N, 3.72.

*4.2.2.5 cis-[RuCl$_2$(Hbzpy)(PPh$_3$)$_2$] (**5**)*

A solution of Hbzpy (0.0234 g; 0.104 mmol) and *trans*-[RuCl$_2$(PPh$_3$)$_3$] (0.1004 g; 0.104 mmol) in toluene (20 cm^3) was heated at reflux temperature under a nitrogen atmosphere for 6 hrs. The volume was reduced to 5 cm^3 and the product precipitated by addition of *n*-hexane. The complex was recrystallized from dichloromethane/*n*-hexane solution to give dark brown crystals. Yield = 60%; M.P. = 253 – 255 °C; IR (ν_{max}/cm^{-1}): υ(N-H) 3055 (w), υ(C-N) 1227 (m), υ(Ru-PPh$_3$) 694 (vs), υ(Ru-N)$_{amine}$ 515 (vs);^{1}H NMR (295K/ppm): 7.48 (t, 1H, *H9*), 7.72 (t, 1H, *H8*), 7.42 – 7.35 (m, 15H, *PPh$_3$*), 7.28 – 7.20 (m, 15H, *PPh$_3$*), 7.18 – 7.12 (m, 3H, *H1, H4, NH*), 7.05 – 6.93 (m, 2H, *H2, H3*), 4.06 (d, 2H, *H5, H6*);^{31}P NMR (295K/ppm): 28.92; UV-Vis (DCM, (λ_{max} (ε, M^{-1}cm^{-1}))): 403 nm (5708); 582 nm (1620); Conductivity (DCM, 10^{-3} M): 27.33 ohm^{-1}cm^{-2}mol^{-1}; Anal. Calc. for $C_{49}H_{41}Cl_2N_4P_2Ru$ (%):C, 63.98; H, 4.49; N, 6.09. Found: C, 63.66; H, 4.10; N, 6.32.

4.3 X-ray diffraction

Crystal and structure refinement data are given in Table 4.3. Selected bond lengths and angles are given in Tables 4.4, 4.5 and 4.6 for **1**, **2** and **4**, respectively. Only a low resolution structure of **3** could be attained. In addition, one disordered toluene molecule was removed from the crystal lattice of compound **4** using Platon Squeeze [**13**]. In all

three cases the data were collected with Mo Kα (λ = 0.71073 Å) radiation at a crystal-to-detector distance of 50 mm. The following conditions were used for data collection: omega and phi scans with exposures taken at 30 W X-ray power and 0.50° frame widths using APEX2 [**14**]. The data were reduced with the programme SAINT [**14**] using outlier rejection, scan speed scaling, as well as standard Lorentz and polarization correction factors. A SADABS semi-empirical multi-scan absorption correction [**15**] was applied to the data. Direct methods, SHELX-2014 [**16**] and WinGX [**17**] were used to solve all three structures. All non-hydrogen atoms were located in the difference density map and refined anisotropically with SHELX-2014 [**16**]. All hydrogen atoms were included as idealised contributors in the least squares process. Their positions were calculated using a standard riding model with C-$H_{aromatic}$ distances of 0.93 Å and U_{iso} = 1.2 U_{eq}, C-$H_{methylene}$ distances of 0.99 Å and U_{iso} = 1.2 Ueq and C–H_{methyl}distances of 0.98 Å and U_{iso} = 1.5 U_{eq}. The amine N-H and hydroxyl O–H were located in the difference density map and refined isotropically.

4.4 Results and Discussion

*4.4.1 Synthesis and spectral characterization of **1**, **2**, **3** and **4***

The respective free ligands were attained in good yields and spectroscopic characterizations provided definitive insight into their individual molecular structures, see Figures 4.3–4.7 above. The metallic compounds exhibit remarkably good solubility in all chlorinated solvents and selected high boiling point aprotic solvents including dimethylformamide and dimethylsulfoxide but poor solubility in alcoholic media. The low molar conductivity values of the metallic compounds **1**-**4** are testimony to their electrical neutrality and these values were similar to other neutral ruthenium (II), – (III) and – (IV) compounds found within the literature [**11**, **18**].

A proposed route to the formation of **1** is illustrated in Scheme 4.1. The first step entails the equimolar ratio reaction between the metal precursor and ligand, Hbzap which afforded the ruthenium (II) intermediate, $[RuCl(bzap)L_2]$ ($L = PPh_3$). Despite the use of an inert nitrogen atmosphere, dimolecular oxygen diffused into the refluxing toluene solution. In turn, the dimolecular oxygen in the presence of H^+ ions and the ruthenium(II) intermediate afforded molecular hydrogen peroxide in the reaction mixture. This is supported by the patent of Diamond *et. al.*, in which their study have shown that hydrogen peroxide can be generated by the oxidation of their formulated ruthenium(II) compounds to analogous ruthenium(III) compounds in the presence of dimolecular oxygen and H^+ ions [**19**]. This is followed by C-N amine bond cleavage induced by hydrogen peroxide [**20**]. The residual hydrogen peroxide acts as co-catalyst with the ruthenium(III) intermediate, $[RuCl(bzca)L_2]^+$ which oxidizes the 2-methyl-1*H*-benzimidazole carbo-anion to 2-carboxylate-1*H*-benzimidazole (bzca) [**21**, **22**]. Then the bzca moiety coordinates to the ruthenium which oxidizes the metal centre to its +IV oxidation state. This ultimately led to the paramagnetic ruthenium (IV) centre of **1** being surrounded by the two bidentate chelators (*viz.* monoanionic bzca and dianionic pho), (see section 4.4.5.1, Figure 4.28**)**.

The Hbhb chelator of complex **2** acts as monoanionic bidentate chelator through the amide oxygen (O2) and benzoxazole nitrogen (N1) (see section 4.4.5.2, Figure 4.30**)**. Furthermore, this mononuclear ruthenium complex **2** is stabilized by the *trans*-$[Ru(PPh_3)_2]$ core. The metal centres of the dinuclear compounds **3** and **4** are bridged by chloro ligands while the former is reinforced by the bidentate coordination of the neutral Htba chelators through the benzimidazole and amine nitrogens to the respective metal centres (see section 4.4.5.3, Figures4.32 and 4.34). For compound **4**, each monoanionic Hchpr chelator coordinates in a bidentate manner through their singly deprotonated amino groups and neutral imino nitrogens. Furthermore, the octahedral

coordination spheres for each metal centre in **3** and **4** are completed by mono-triphenylphosphine and chloro co-ligands.

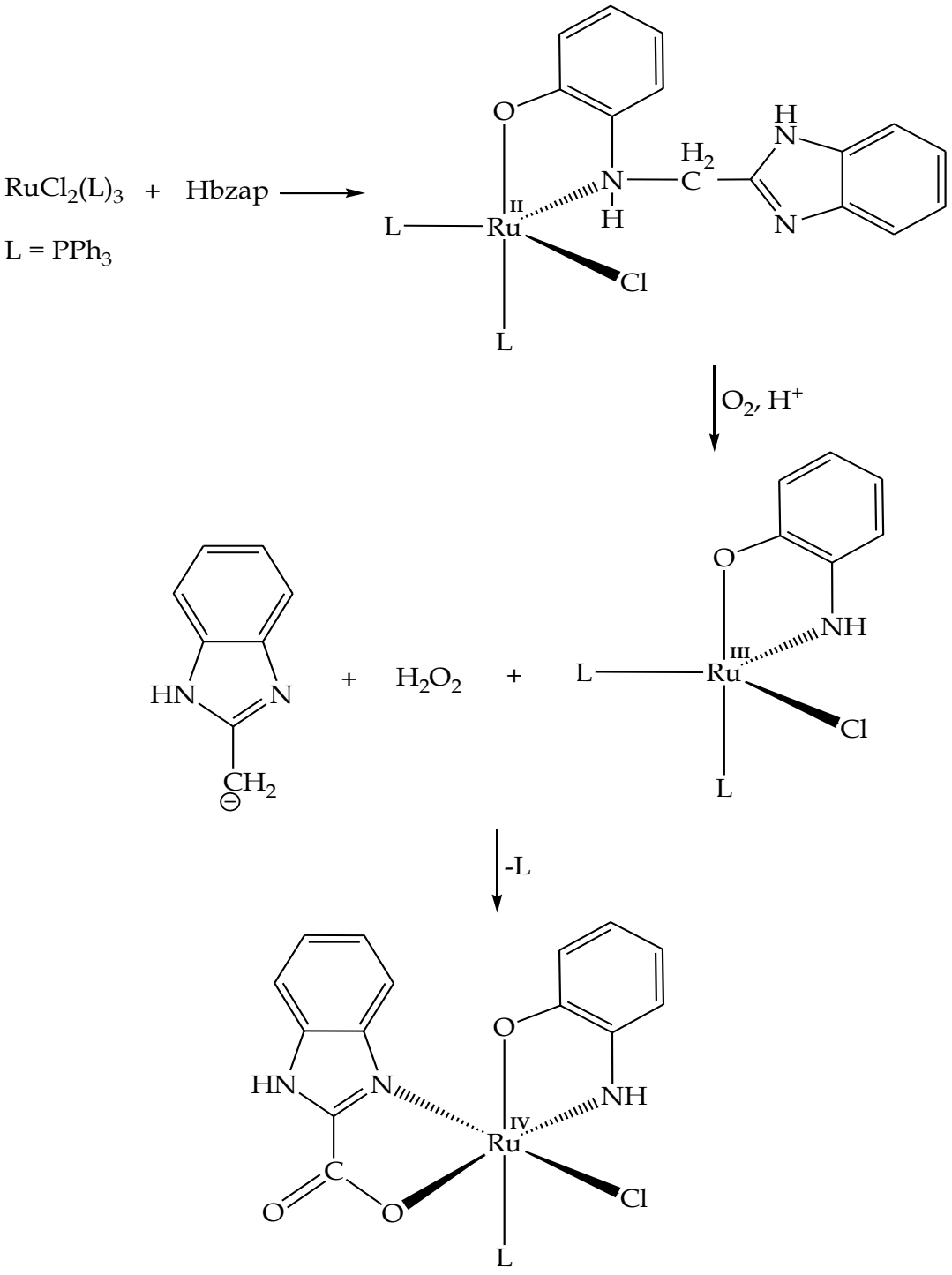

Scheme 4.1: *Proposed formation route of [RuCl(pho)(bzca)(PPh3)] (**1**).*

Mutual intense stretches are observed in the IR spectra of all the metallic compounds [at 693 cm^{-1} (for **1**), 691 cm^{-1} (for **2**), 694 cm^{-1} (for **3**) and 692 cm^{-1} (for **4**)] ascribed to the υ(Ru-PPh_3) vibrations, (see Figures 4.8–4.11). In addition, in the IR spectra of the respective metallic compounds, distinctive low intensity vibrations are also found below 600 cm^{-1} due to the Ru-N and Ru-O coordination bonds. The absence of the C-N stretch (at 1277 cm^{-1} for Hbzap) in the IR spectrum of **1** indicated that the Hbzap ligand has cleaved into bzca and pho moieties. Furthermore, the coordination of the bzca moiety is affirmed by the ν(C=N) vibration appearing as two splitted stretches compared to that of the free-ligand which is found at 1513 cm^{-1} as a broad single vibrational band. For complex **2**, the heterocyclic C=N vibrational band appears at a lower frequency (at 1547 cm^{-1}) in comparison to the corresponding vibrational band of its free ligand occurring at 1601 cm^{-1}. Similarly for the dinuclear ruthenium compound **4**, evidence of coordination of its chelators, are given by the C=N vibrational band of **4** shifting to lower frequencies [1564 cm^{-1} for **4** and 1602 cm^{-1} for H_2chpr]. For complex **3**, the C-N amine vibration is at a common frequency (at 1246 cm^{-1}) with respect to the analogous band of its free ligand, Htba.

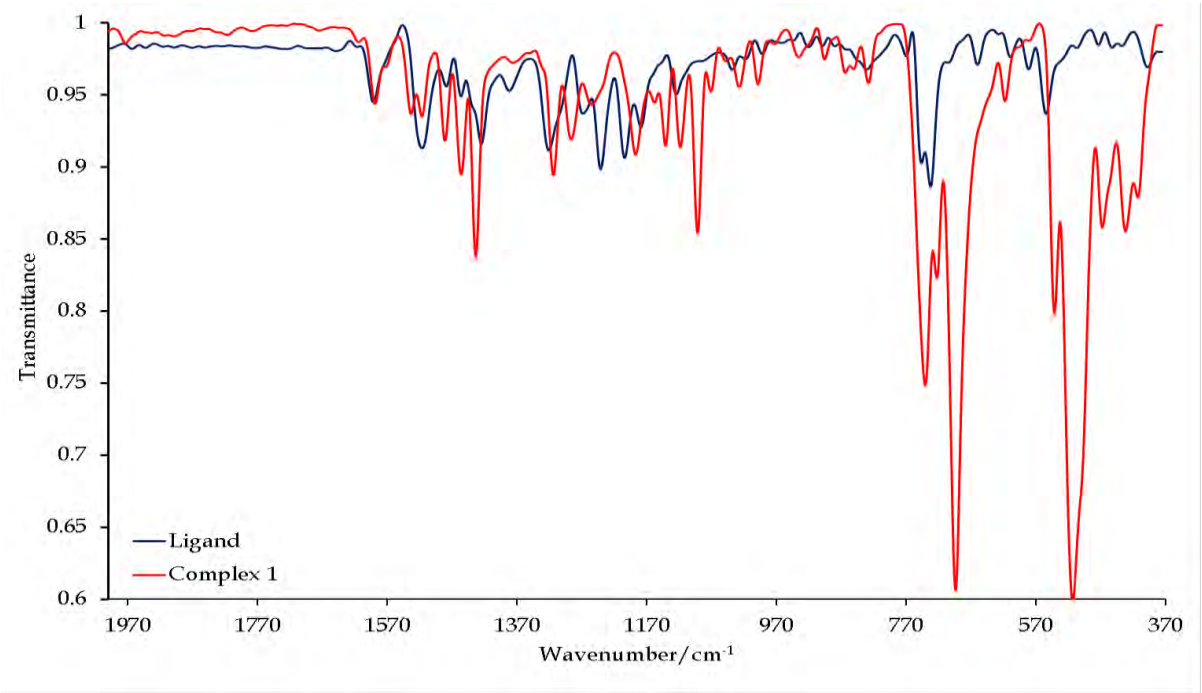

Figure 4.8: *Overlay IR spectra of complex **1** and its free ligand, bzap between 2000 and 370 cm^{-1}.*

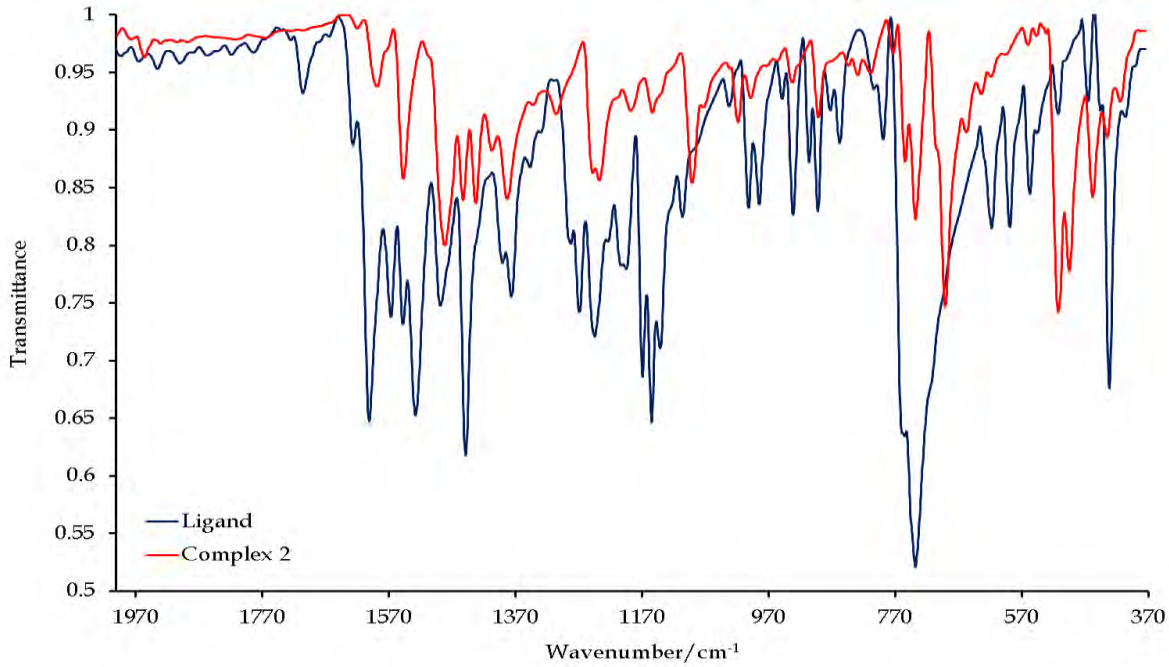

Figure 4.9: *Overlay IR spectra of complex **2** and its free ligand, H_2bhb between 2000 and 370 cm^{-1}.*

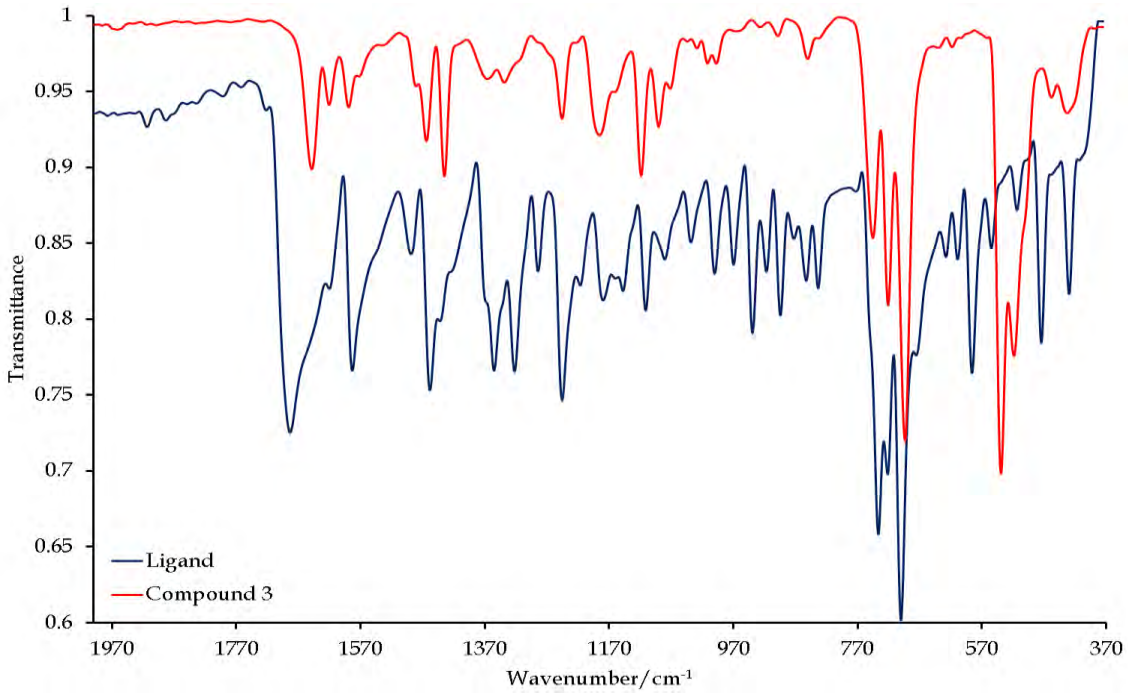

Figure 4.10: *Overlay IR spectra of compound* **3** *and its free ligand, Htba between 2000 and 370 cm-1.*

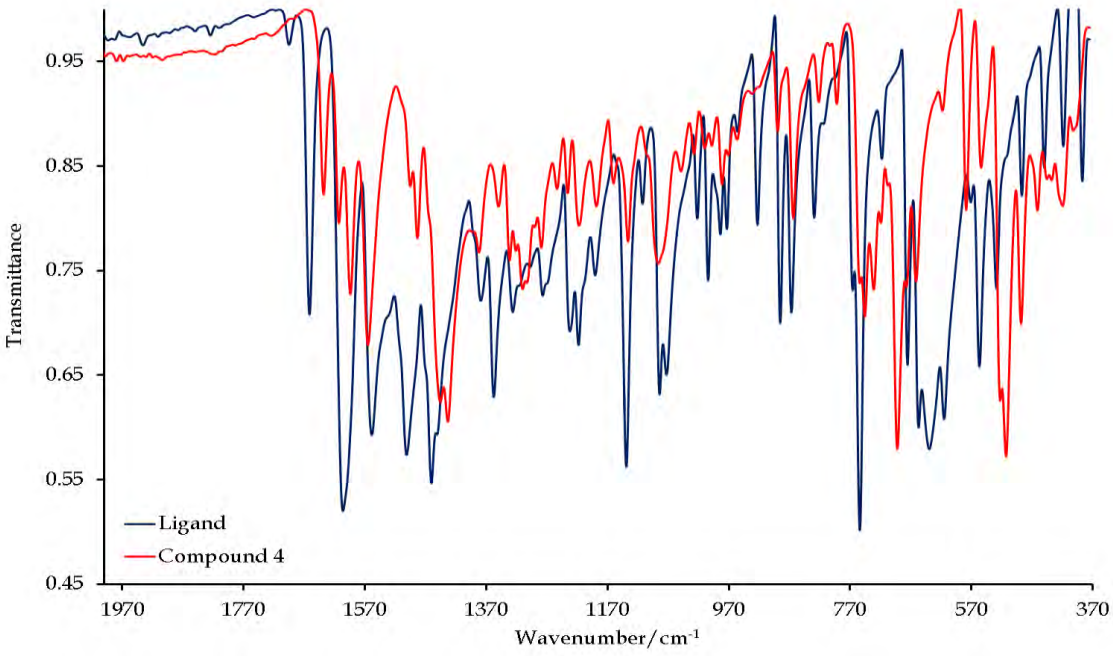

Figure 4.11: *Overlay IR spectra of compound* **4** *and its free ligand, H_2chpr between 2000 and 370 cm-1.*

Proof of chelation can also be attained from NMR spectral analysis of the diamagnetic compound **3**. The Htba ligands exhibit magnetic equivalence given by the fact that the signals resonate at the same position and that each signal integrates to double of that what is expected for one Htba chelator, (see Figure 4.12). For example, a broad singlet is observed at 8.84 ppm for the amine protons (for *NH* and *NH'*) whereas for the free-ligand, Htba a broad singlet integrating to one is found at 8.50 ppm for the amine proton. For **3**, the signal of the respective triphenylphosphine co-ligands does not coalesce but rather appear as two intense multiplets each integrating to 15 protons. Despite the trend observed with respect to the triphenylphosphine co-ligands in the proton NMR spectrum of **3**, the phosphorous signals of **3** (at 25.55 ppm) appear as a single peak indicating magnetic equivalence.

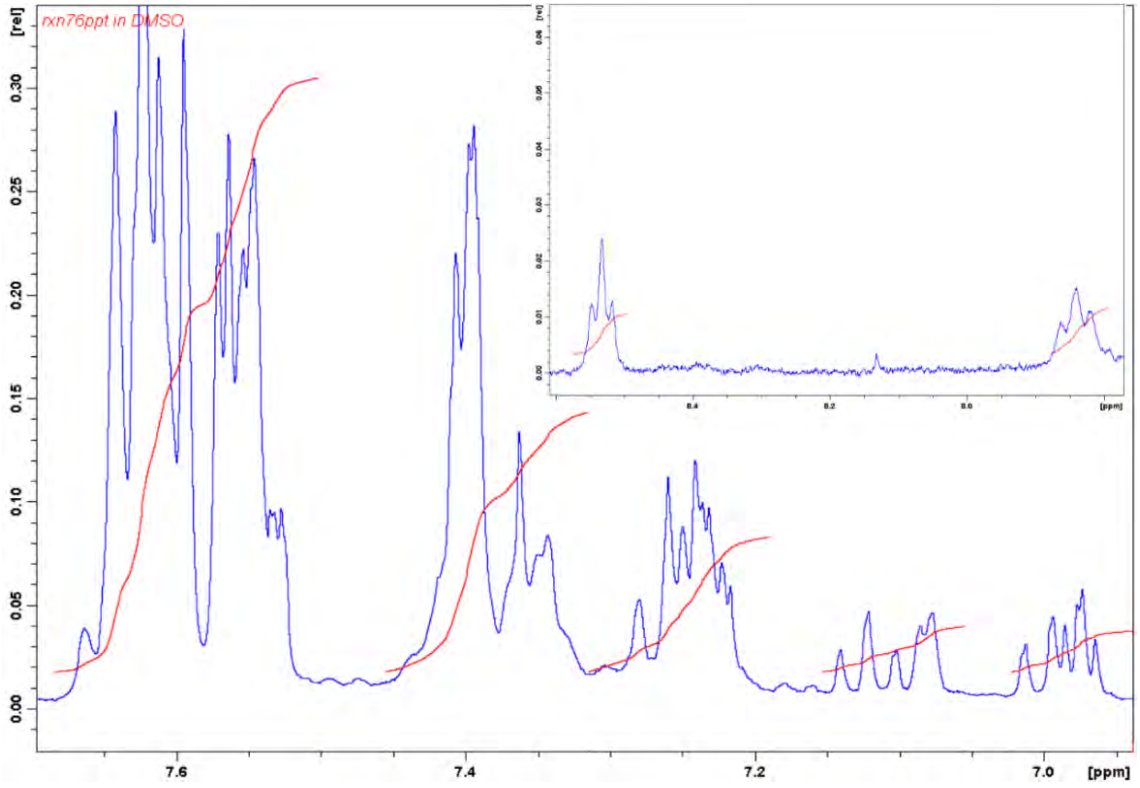

Figure 4.12: *^{1}H NMR spectrum of compound* ***3*** *between 7.65 and 6.94 ppm. Inset: The low intensity triplets of the H2, H2'and H3, H3' aromatic protons.*

Several common π-π^* intraligand transitions are observed below 400 nm in the overlay UV-Vis spectra of the free ligands and their metallic compounds **1**-**4**, (see Figures 4.13-4.16). In addition, at red-shifted wavelengths between 400 and 600 nm, Ligand-to-Metal-Charge-Transfer (LMCT) bands are found. As expected, the low spin d^6 metallic compound **3** has no metal-based electronic transitions while for the paramagnetic ruthenium(III) compounds **1** and **4**: a distinctive *d-d* transition for compound **4** (at 688 nm) and a shoulder with a low extinction coefficient for complex **1** (at 703 nm) is observed. However, for the d^5 complex **2**, no *d-d* transition was observed which could be due to higher band-gap energy and thus the metal-based electronic transition is unfavourable.

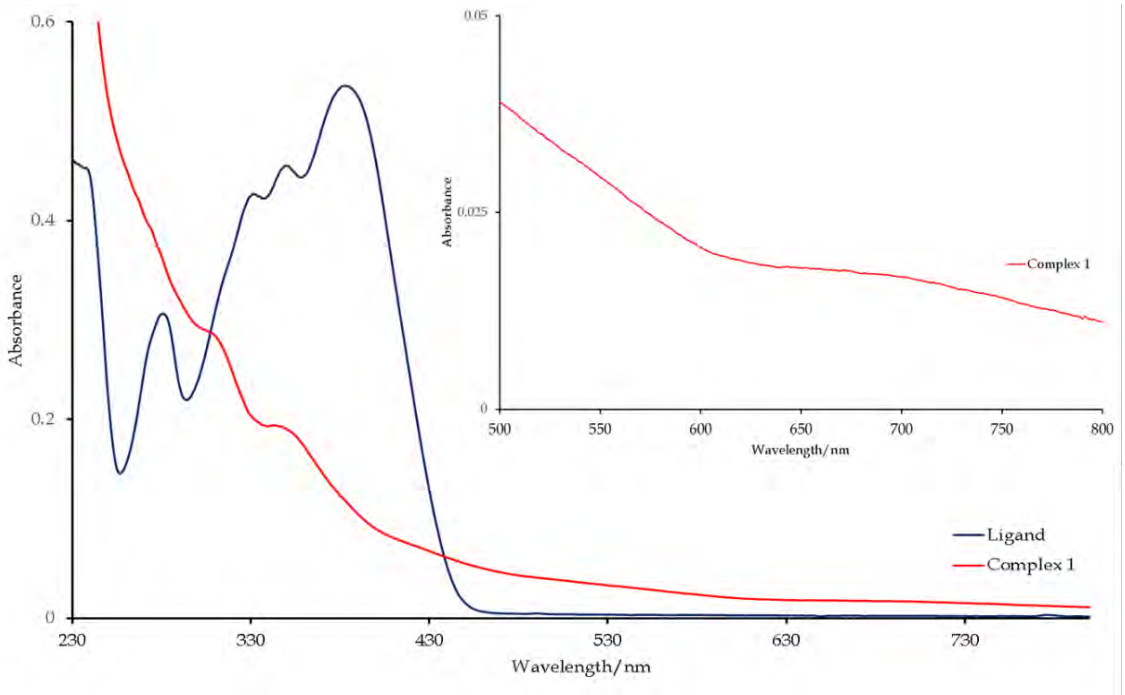

Figure 4.13: *Overlay UV/Vis spectra of complex* ***1*** *and its free-ligand, bzap. Inset: The d-d transition of the metal complex.*

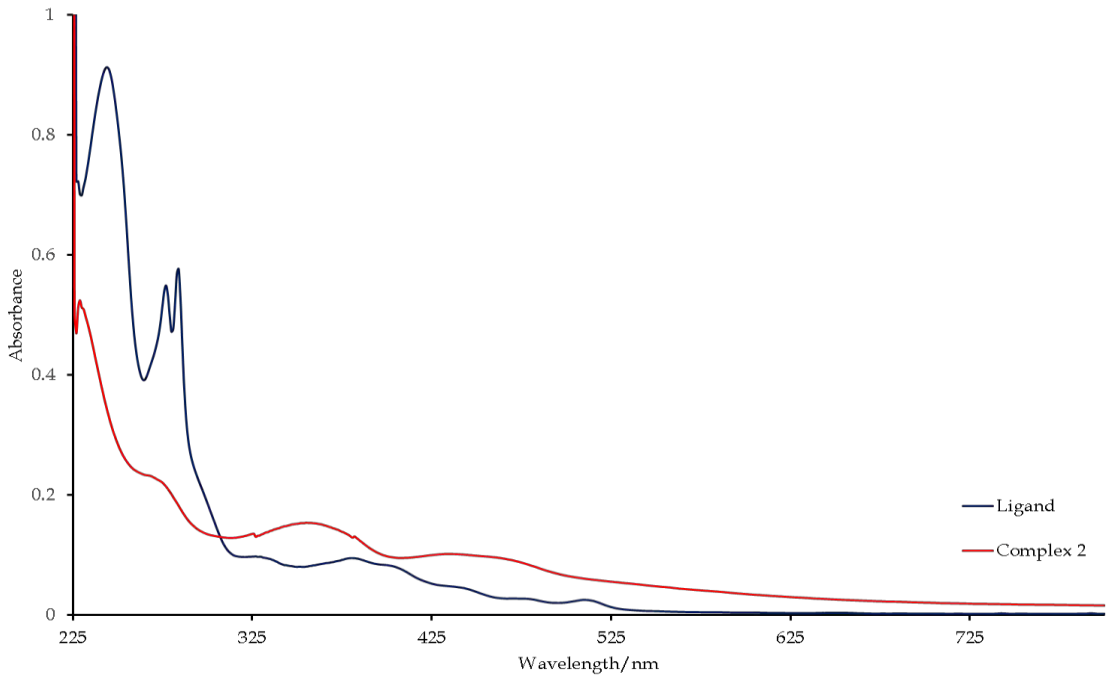

Figure 4.14: *Overlay UV/Vis spectra of complex* **2** *and its free-ligand, Hbhb.*

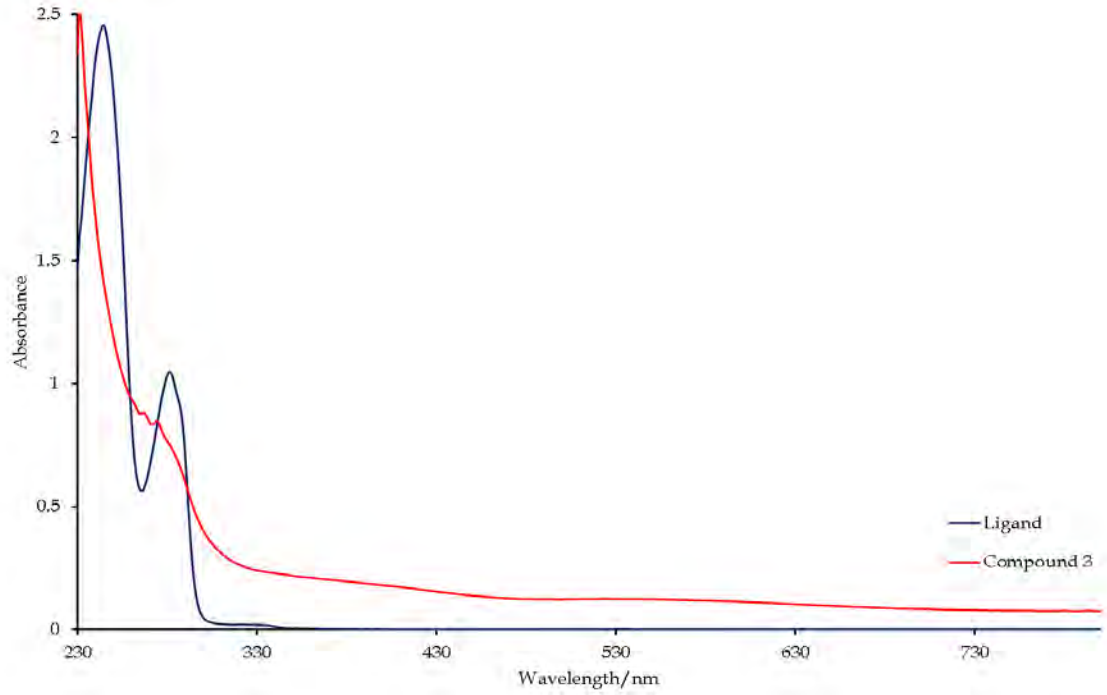

Figure 4.15: *Overlay UV/Vis spectra of compound* **3** *and its free-ligand, Htba.*

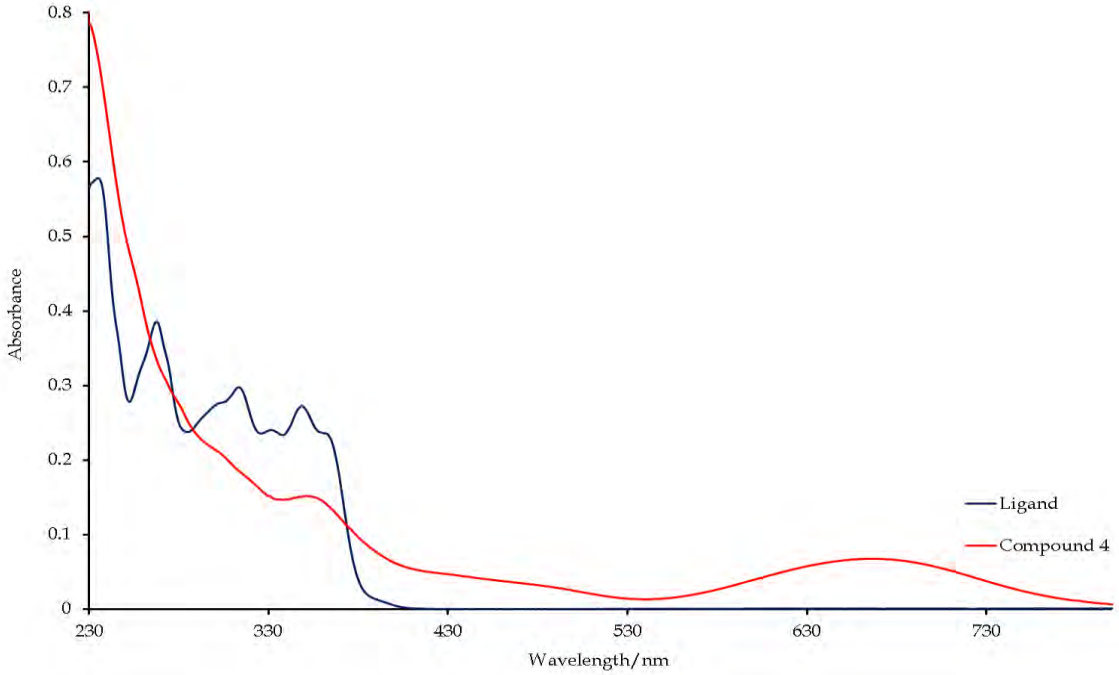

Figure 4.16: *Overlay UV/Vis spectra of compound* **4** *and its free-ligand, H_2pchr.*

4.4.2 Synthesis and spectral characterization of **5**

Complex **5** was synthesized from the 1:1 molar ratio reaction between *trans*-[$RuCl_2(PPh_3)_3$] and Hbzpy to give a diamagnetic ruthenium complex, *cis*-[$Ru^{II}Cl_2$(Hbzpy)$(PPh_3)_2$]. However, an X-ray crystal structure analysis of the metal complex could not be attained as the cubic crystal of **5** did not diffract using single crystal X-ray diffractometry. This metal complex is a non-electrolyte complex in DCM and it is soluble in a variety of polar solvents including chlorinated solvents. Indicative to what is observed in the IR spectra of metal complexes **1–4**, the presence of the*trans*-[$Ru(PPh_3)_2$] unit is seen at 694 cm^{-1} in the IR spectrum of **5.** In addition, an intense stretch at 515 cm^{-1} is ascribed to a vibration associated with the Ru-N coordination bonds of **5**. Furthermore, the ν(C-N) amine observed at 1240cm^{-1} in the free ligand's IR spectrum (Hbzpy) shifted to a lower frequency of 1227 cm^{-1} in the IR spectrum of **5** upon coordination (see Figure 4.17).

The ^{1}H NMR spectrum of **5** shows signals of the triphenylphosphine co-ligands emerging as two separate multiplets (7.42 – 7.35 ppm and 7.28 – 7.20 ppm) (see Figure 4.18). Confirmation of coordination is clearly observed by a shift in the $-CH_2$ protons for the free ligand at 4.61 ppm compared to 4.06 ppm as seen in **5**. In the ^{31}P NMR spectrum, a single peak observed at 28.92 ppm confirms the presence of the phosphorous atoms in **5** indicating magnetic equivalence of these atoms (see Figure 4.19). Broad Metal-to-Ligand Charge Transfer (MLCT) band appears for complex **5** at 582 nm.No *d-d* transition is found for the diamagnetic complex, which is due to its low-spin d^6 electron configuration (see Figure 4.20). The deductions from the spectral characterization implies that the proposed structure of **5** is comprised of a *trans*-$[Ru(PPh_3)_2]$ core with the equatorial plane being occupied by the neutral bidentate $N_{bz}N_{py}$ chelator and the *cis*-orientated chloro co-ligands (see Figure 4.21).

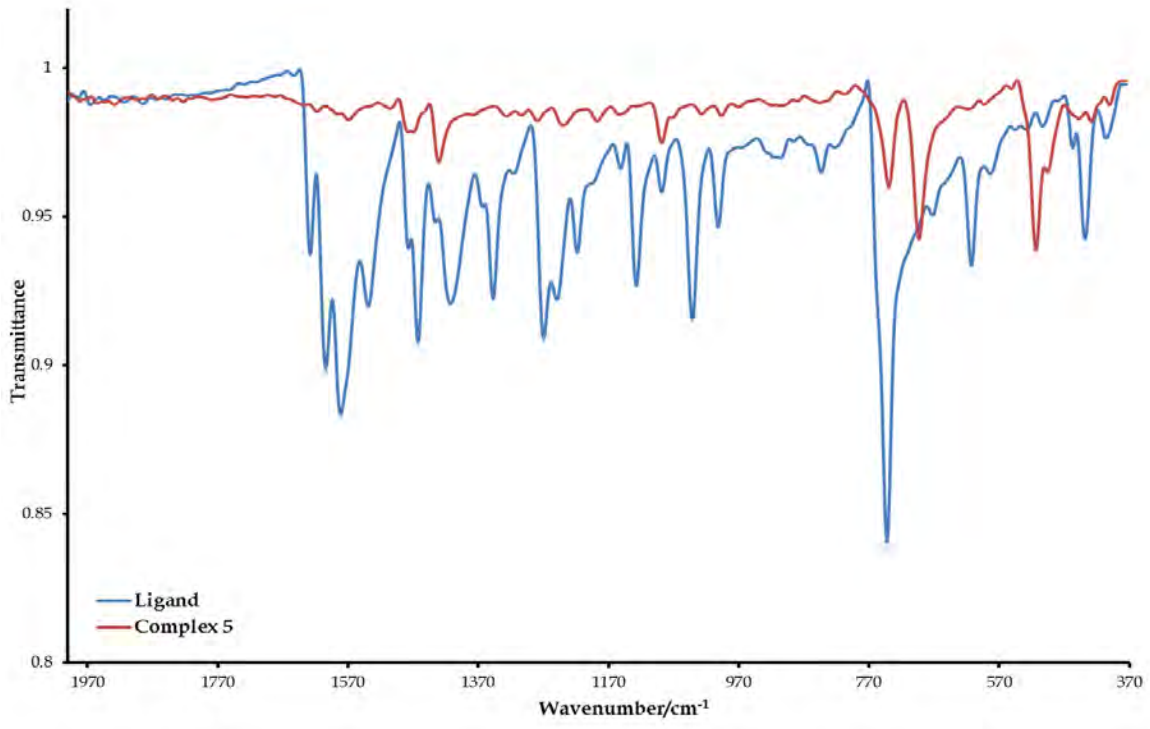

Figure 4.17: *Overlay IR spectra of complex* **5** *and its free ligand, Hbzpy between 2000 and 370* cm^{-1}.

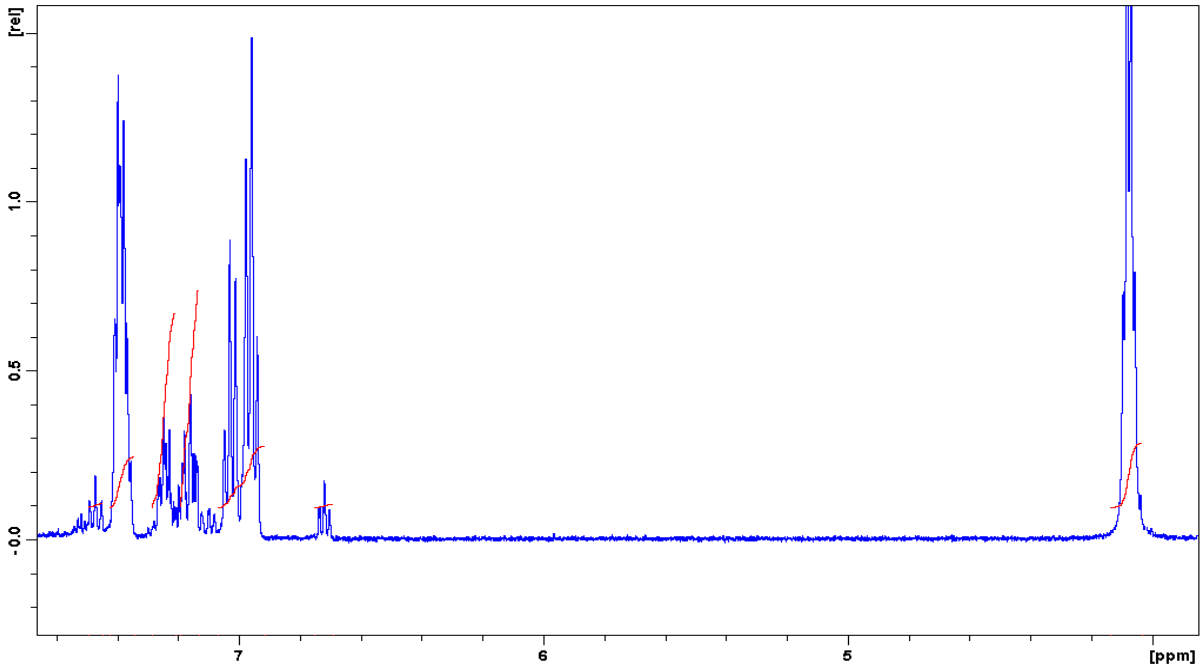

Figure 4.18: *^{1}H NMR spectrum of complex* **5**.

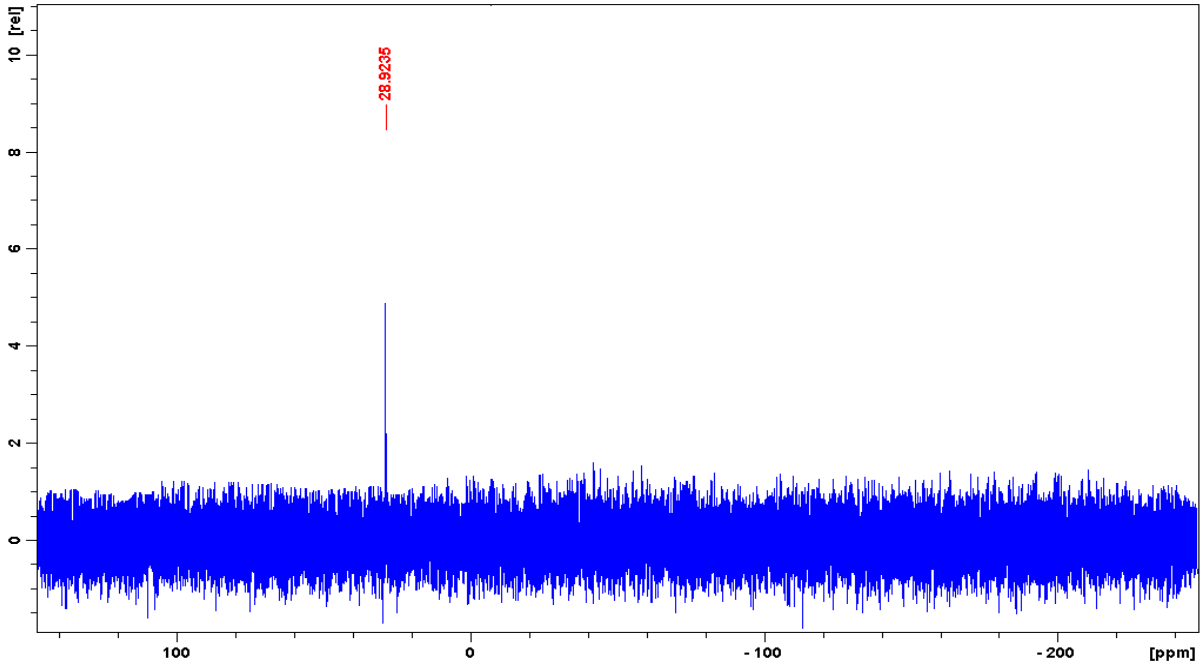

Figure 4.19: *^{31}P NMR spectrum of complex* **5**.

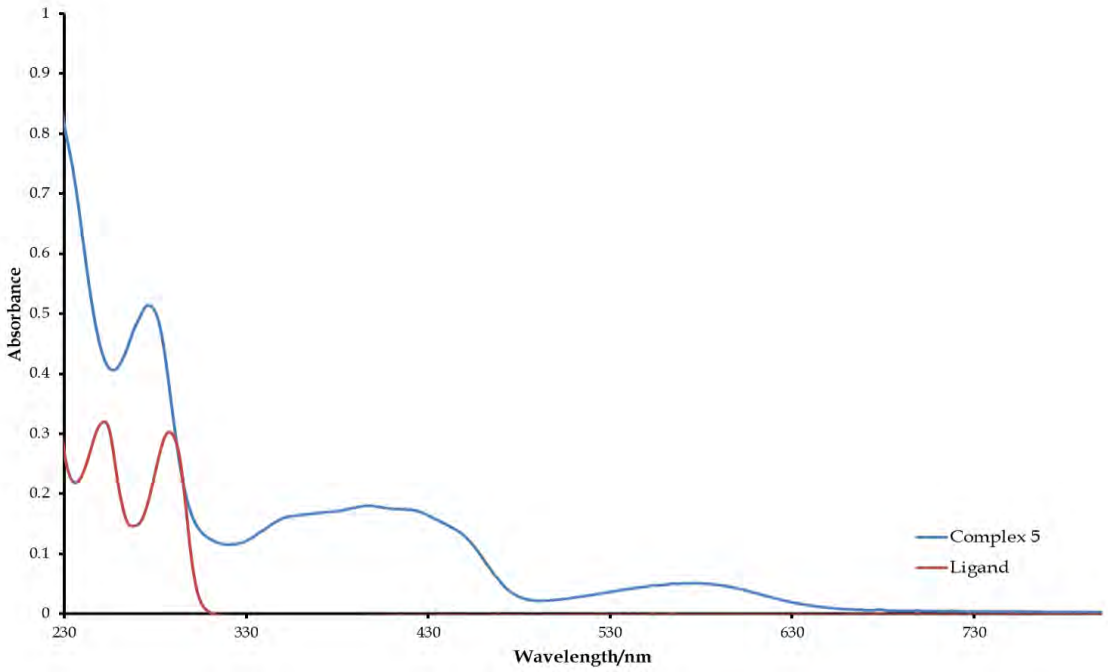

Figure 4.20: *Overlay UV/Vis spectra of complex* **5** *and its free-ligand, Hbzpy.*

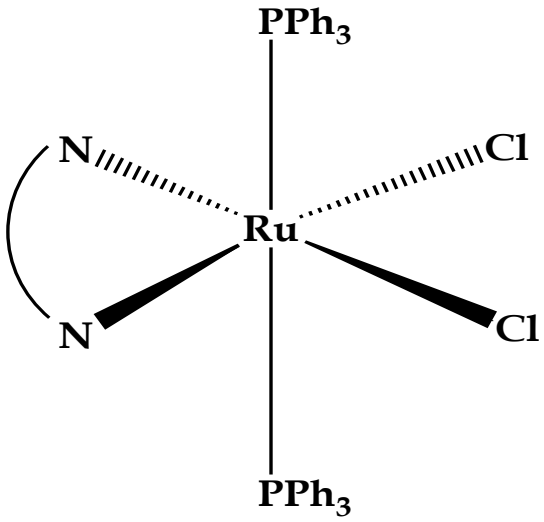

Figure 4.21: *Coordination mode of the neutral Hbzpy chelator of* **5.**

4.4.3 *Electrochemistry studies*

The cyclic voltammograms (CVs) of **1**, **2**, **3** and **5** showed one redox couple while within the CV of the dinuclear compound **4**, two redox couples labelled **A** and **B** can be found (see Figures 4.22 – 4.25). All the redox couples exhibits diffusion controlled behaviour at increasing scan rates (see Figure 4.26) for the overlay CVs of compound **4** at incrementing scan rates. Furthermore, the redox couples correspond to one electron redox processes indicated by their respective peak current ratios (I_{pa}/I_{pc}) which approach one. In addition, all these metallic compounds exhibit quasi-reversible behaviour indicated by their peak to peak separations which are different to the standard, ferrocene (90 *mV* at 100 *mV/s*), refer to Table4.1. More specifically, the redox couples of the metallic compounds **1- 3** exhibit slower electron transfer kinetics compared to compound **4**'s redox couples **A** and **B**. The halfwave potential of complex **1** is assigned to the Ru(III/IV) redox couple as it was found at a slightly lower potential than the paramagnetic diamido ruthenium(IV) complex, *trans-P, cis-Cl*-$[RuCl_2(ddd)(PPh_3)_2]$ (H_2ddd = 5, 6-diamino-1,3-dimethyluracil) [**11**]. For compounds **2**, **3** and **5**, the halfwave potentials are ascribed to the Ru(II/III) redox couple as they have comparable redox behaviour as other ruthenium compounds reported in the literature [**11**, **19**]. Similarly, the dinuclear ruthenium (III) compound **4** had analogous redox behaviour (redox couples **A** and **B** assigned to the Ru(II/III) and Ru(III/IV) process, respectively) as the paramagnetic ruthenium(III) complex, $[RuCl(bsp)_2(PPh_3)]$ {Hbsp = *N*-(2-hydroxybenzylidene)-benzothiazole} [**23**]. Noticeably, using the more sensitive square wave voltammetry technique, at lower potentials relative to each redox process (*viz.***A** and **B**), two smaller peaks are observed, see Figure 4.27. These peaks indicated by the arrows are due to the second metal centre undergoing analogous redox processes.

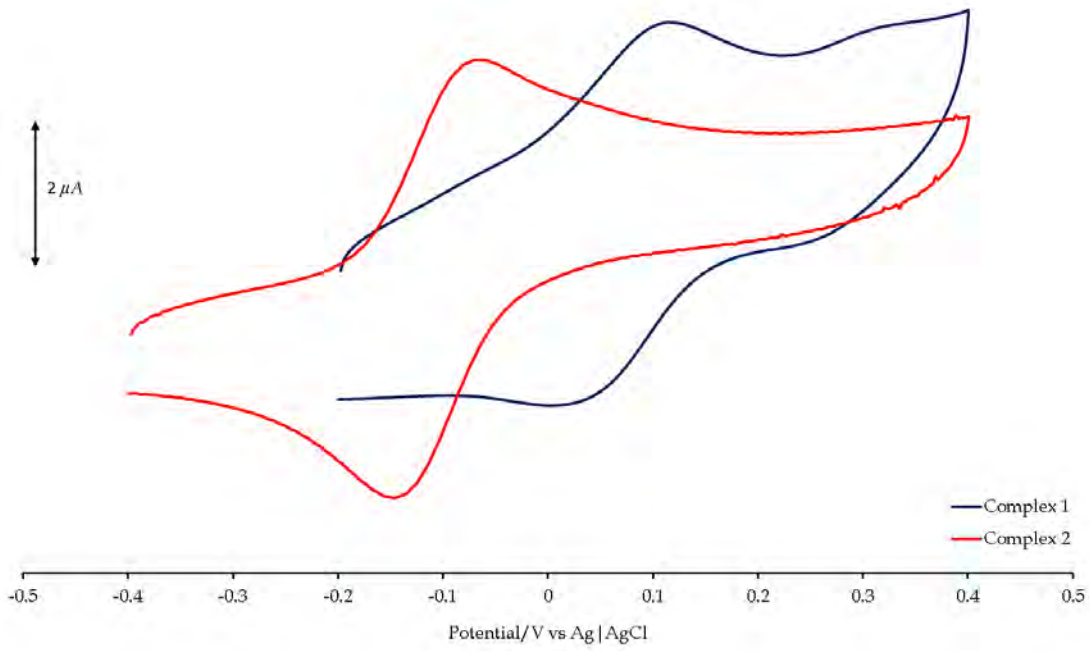

Figure 4.22: *Overlay CVs of complexes **1** and **2** at 100 mV/s.*

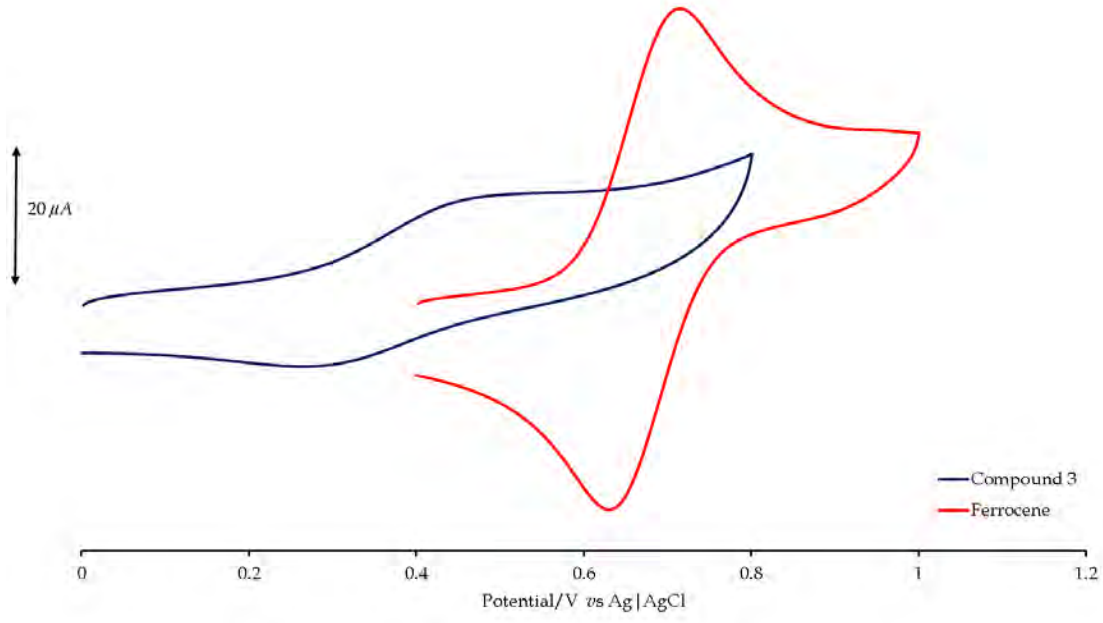

Figure 4.23: *Overlay CV of compound **3** and ferrocene at 100 mV/s.*

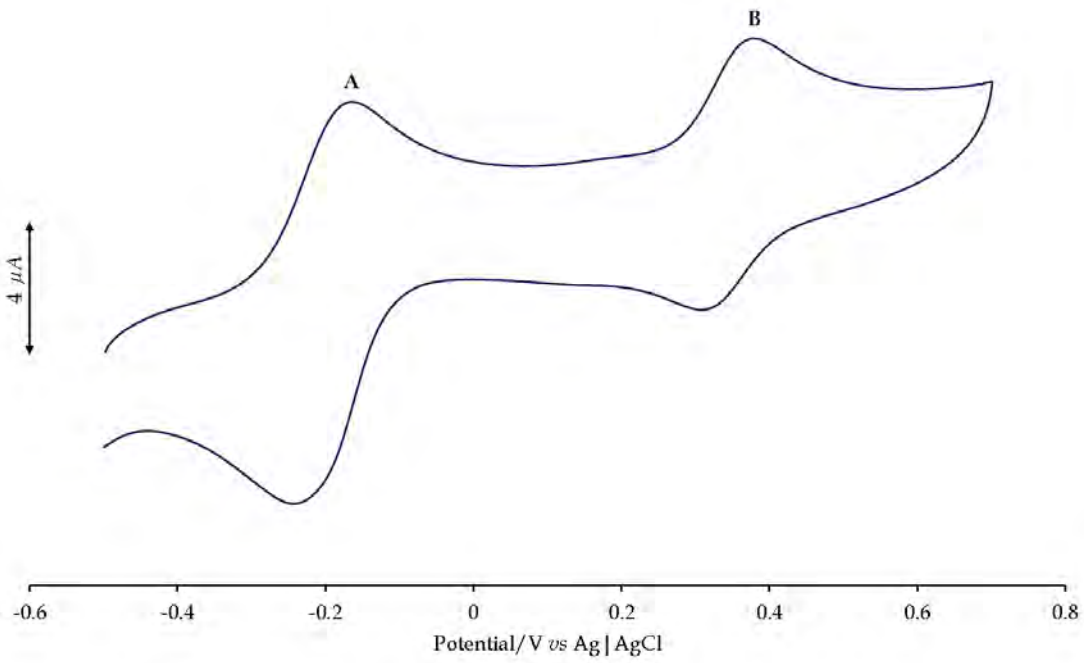

Figure 4.24: *CV of compound* **4** *at 100 mV/s.*

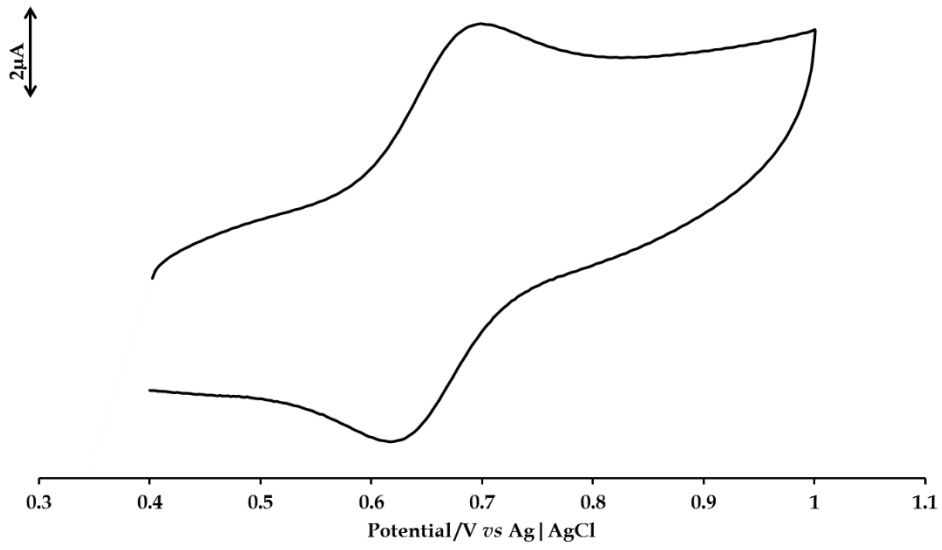

Figure 4.25: *Cyclic voltammogram of complex* **5** *at 100 mV/s.*

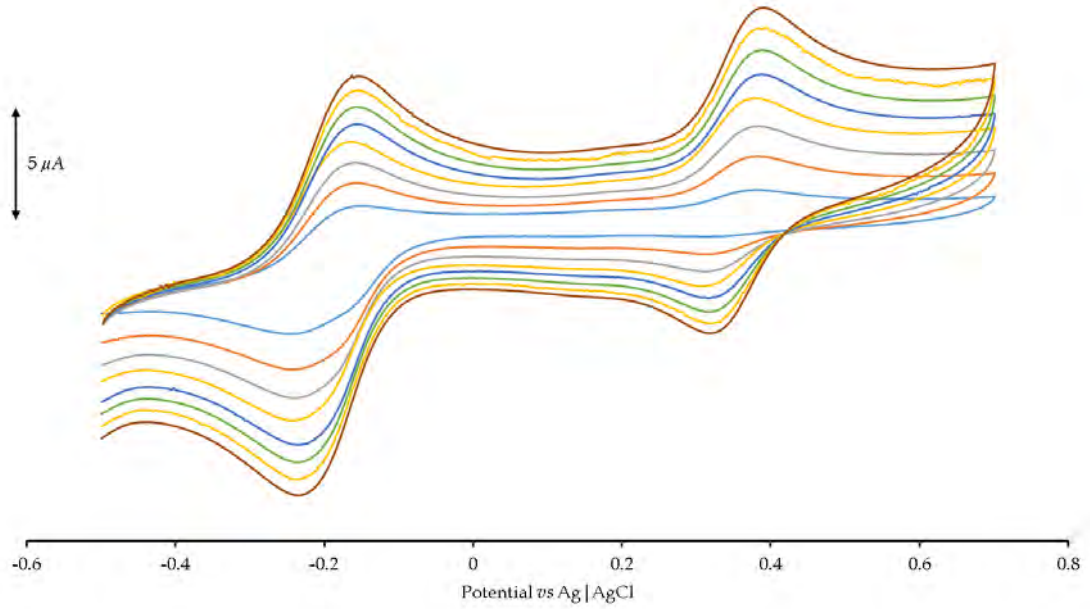

Figure 4.26: *Overlay CVs of compound* **4** *at incrementing scan rates between 25 mV/s and 200 mV/s.*

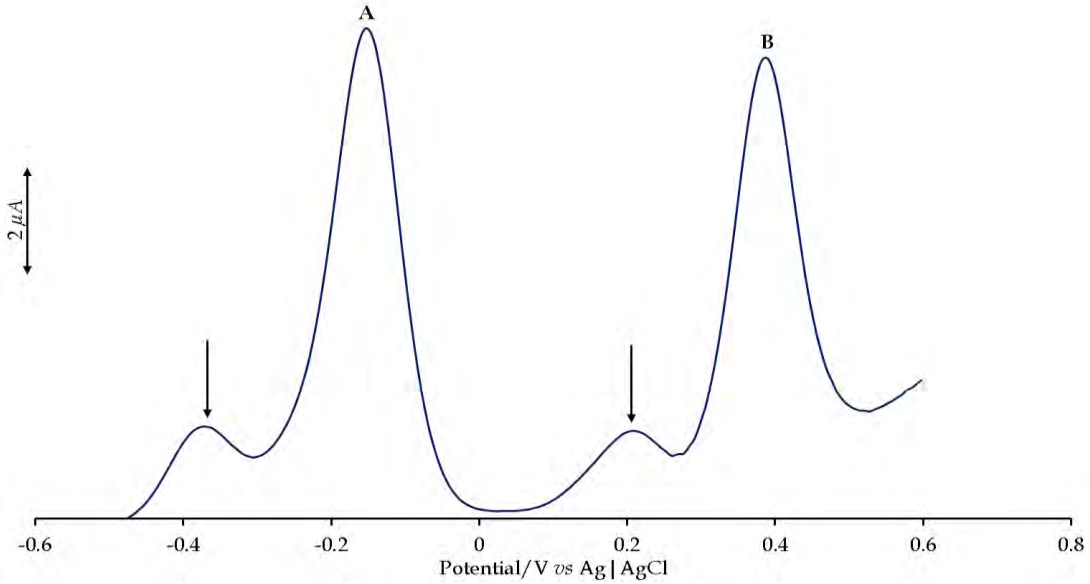

Figure 4.27: *Squarewave voltammogram (SWV) of compound* **4** *at 100 mV/s.*

Table 4.1: *Electrochemical parameters of the respective metal complexes at 100 mV/s.*

Compound	1	2	3	4		5
				A	B	
E_{pa}/V	0.025	-0.063	0.471	-0.241	0.384	0.691
E_{pc}/V	0.120	-0.146	0.280	-0.163	0.313	0.627
$E_{½}/V$	0.073	-0.105	0.376	-0.202	0.349	0.659
$\Delta E/mV$	95	83	191	78	71	64

4.4.4 Radical Scavenging studies

An increase of radicals within the human body can have detrimental effects on human health by inducing numerous diseases like cancer, arthritis, Parkinson's or Alzheimer's diseases [**24-26**]. Thus, there is an upsurge in discovering novel antioxidants which may offer higher radical scavenging capabilities than common natural antioxidants, *e.g.* vitamin C. Transition metal complexes with redox active metal centres have shown to exhibit optimal radical scavenging capabilities for a wide range of radicals by donating an electron to quench the radical specie [**27**, **28**]. Alternatively, transition metal complexes with aromatic hydrocarbon ligands can also act as proton donors to neutralize radicals [**29**]. In our study, the formulated metal complexes **1**-**4** were subjected to DPPH radical scavenging activities. The IC_{50} values showed that all the metallic compounds [89.98 µM (for **1**), 61.50 µM (for **2**), 96.40 µM (for **3**) and 66.31 µM (for **4**)] have higher radical scavenging activities than their corresponding free-ligands [112.53 µM (for Hbzap), 87.87 µM (for H_2bhb), negligible (for Htba) and 300 µM (for H_2chpr)]. Despite the negligible radical scavenging activity of the free ligand, Htba, the presence of the two metal centres in compound **3** induced an optimal activity. In fact, the unpaired *d*-electron configurations of the ruthenium (III) metal centres promoted the highest DPPH radical scavenging activity judged by its lower IC_{50} value.

Furthermore, all the metal complexes had considerable higher radical scavenging capabilities that the natural antioxidant, vitamin C (IC_{50} value = 147 μM). The observations are well in agreement with other ruthenium (II) and – (III) compounds found within the literature [**30-32**].

4.4.5 Crystal structures

*4.4.5.1 Crystal structure of [RuCl(pho)(bzca)(PPh_3)] (**1**)*

Complex **1** exhibits a distorted octahedral geometry which is imposed on by the O1-Ru-N1 (79.5(1)˚) and O2-Ru-N2 (76.94(9)˚) bite angles which are significantly narrower than the ideal octahedral angle of 90˚ (see Figure 4.28). Furthermore, the crystal lattice is stabilized by *π-π* stacking (interplanar spacing of 3.405Å) between the nearly co-planar C10-C15 phenyl group and the imidazole ring of the bzca chelator.

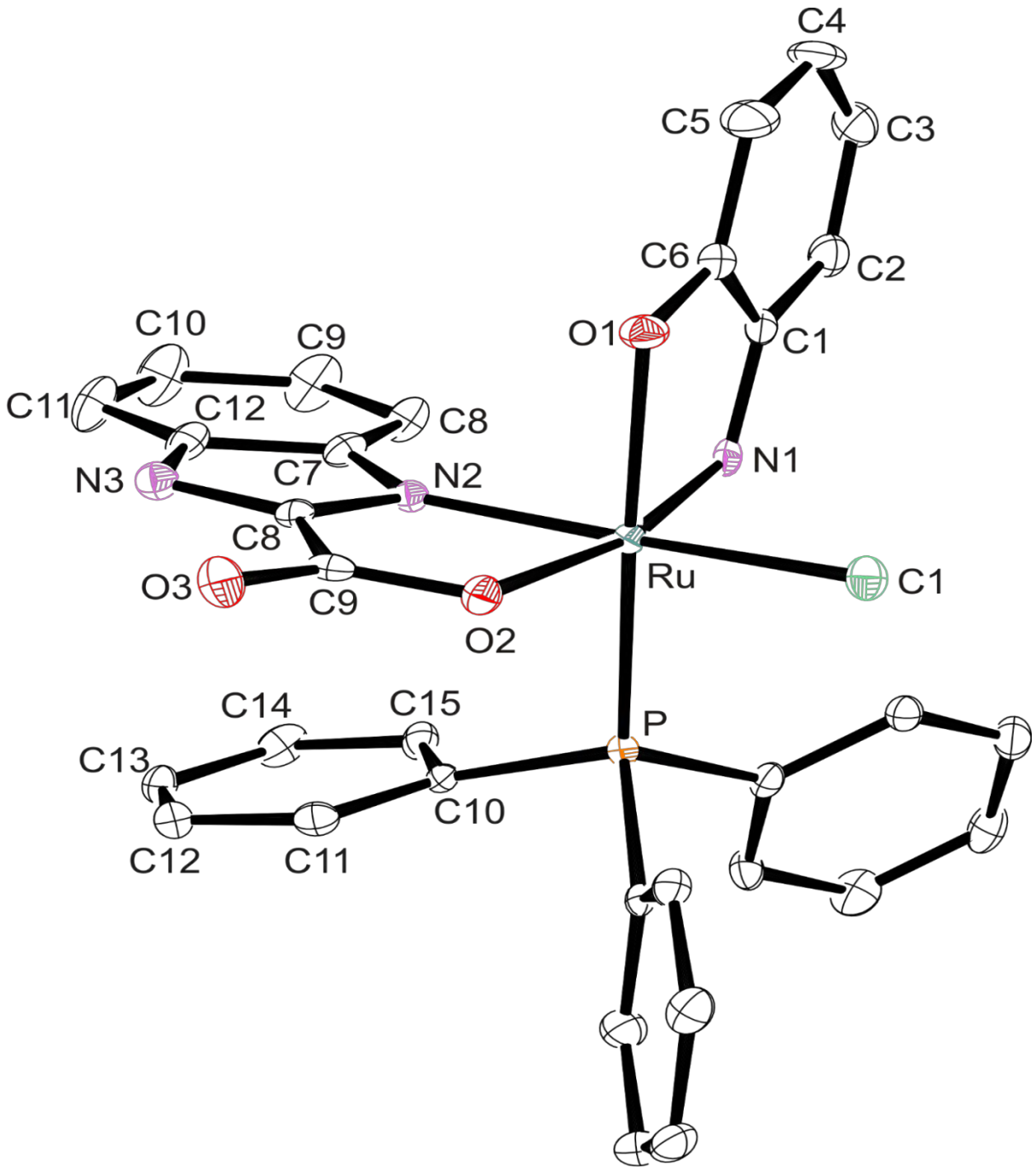

Figure 4.28: *An ORTEP view of complex **1** showing 50 % probability displacement ellipsoids and the atom labelling. The hydrogen atoms and ethanol molecule of recrystallization were omitted for clarity.*

In addition, re-enforcement is given by classical intermolecular (Cl···H26-O4 = 2.40(5) Å), (O4···H25A-N3A = 1.91(4) Å and O3···H24B-N1B = 2.09(3) Å) hydrogen bonding. Ultimately, these molecular interactions lead to columns of **1** running parallel to the [*b*]-axis.Compound **1** exhibits several intermolecular hydrogen bonds leading to a two-dimensional supramolecular structure transverse to the *ac*-plane (see Figure 4.29). The geometrical parameters for the hydrogen bonds supporting this structure are summarised in Table 4.2.

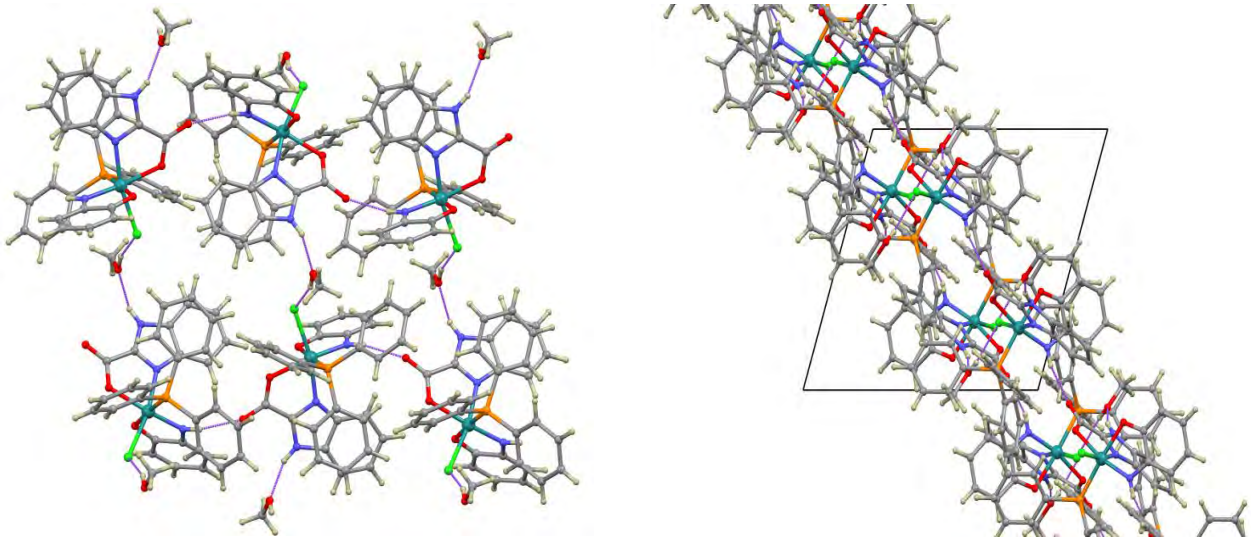

Figure 4.29: *[Left] Repeating unit of the two-dimensional hydrogen bond network of* ***1****. [Right] Supramolecular structure of* ***1*** *viewed down the b-axis showing the network to be transverse to the ac plane.*

Table 4.2: *Hydrogen bond lengths and bond angles for compound* ***1***.

Bond	D-H	H···A	D···A	D–H···A
N1B–H24B···O3	0.84(3)	2.09(3)	2.884(3)	158(3)
N3A–H25A···O4	0.85(4)	1.91(4)	2.706(4)	156(4)
O4–H26···Cl	0.83(5)	2.40(5)	3.187(3)	159(4)

In contrast to the nearly equidistant Ru-O bonds (Ru-O1 = 2.119(2) Å and Ru-O2 = 2.124(2) Å), the ruthenium to monoanionic amido nitrogen bond (Ru-N1 = 1.904(2) Å) and neutral benzimidazole (Ru-N2 = 2.058(3) Å) nitrogen bond differs as expected. In addition, the Ru-N1 coordination sphere bond length is comparable to the analogous amido bonds of the paramagnetic ruthenium(IV) complex, *trans-P, cis-Cl*-[$RuCl_2$(ddd)(PPh_3)$_2$] [**11**]. The carboxylate form of the bzca chelator is confirmed based on the C-O bond orders which can be readily distinguished by their respective bond distances (C9-O3 = 1.225(3) Å and C9-O2 = 1.283(4) Å).

*4.4.5.2 Crystal structure of cis-Cl, trans-P-[Ru^{II}(Hbhb)Cl_2(PPh_3)$_2$] (**2**)*

The molecular structure of **2** crystallizes out in a P-1 space group with two molecules occupying the triclinic unit cell. The bidentate coordination of the Hbhb chelator results in the formation of a constrained N1-Ru-O2 bite angle [85.71(7)˚] which pushes the chloro co-ligands (Cl1-Ru-Cl2 = 95.71(2)˚) more further apart from the ideal octahedral angle of 90˚ (see Figure 4.30). Furthermore, the influence of cyclometallation is clearly evident from the deviation from linearity of the *trans*-[Ru(PPh_3)$_2$] core (P1-Ru-P2 = 177.38(2)˚) and variable Ru-P bond lengths (Ru-P1 = 2.4229(7) Å and Ru-P2 = 2.3979(7) Å).

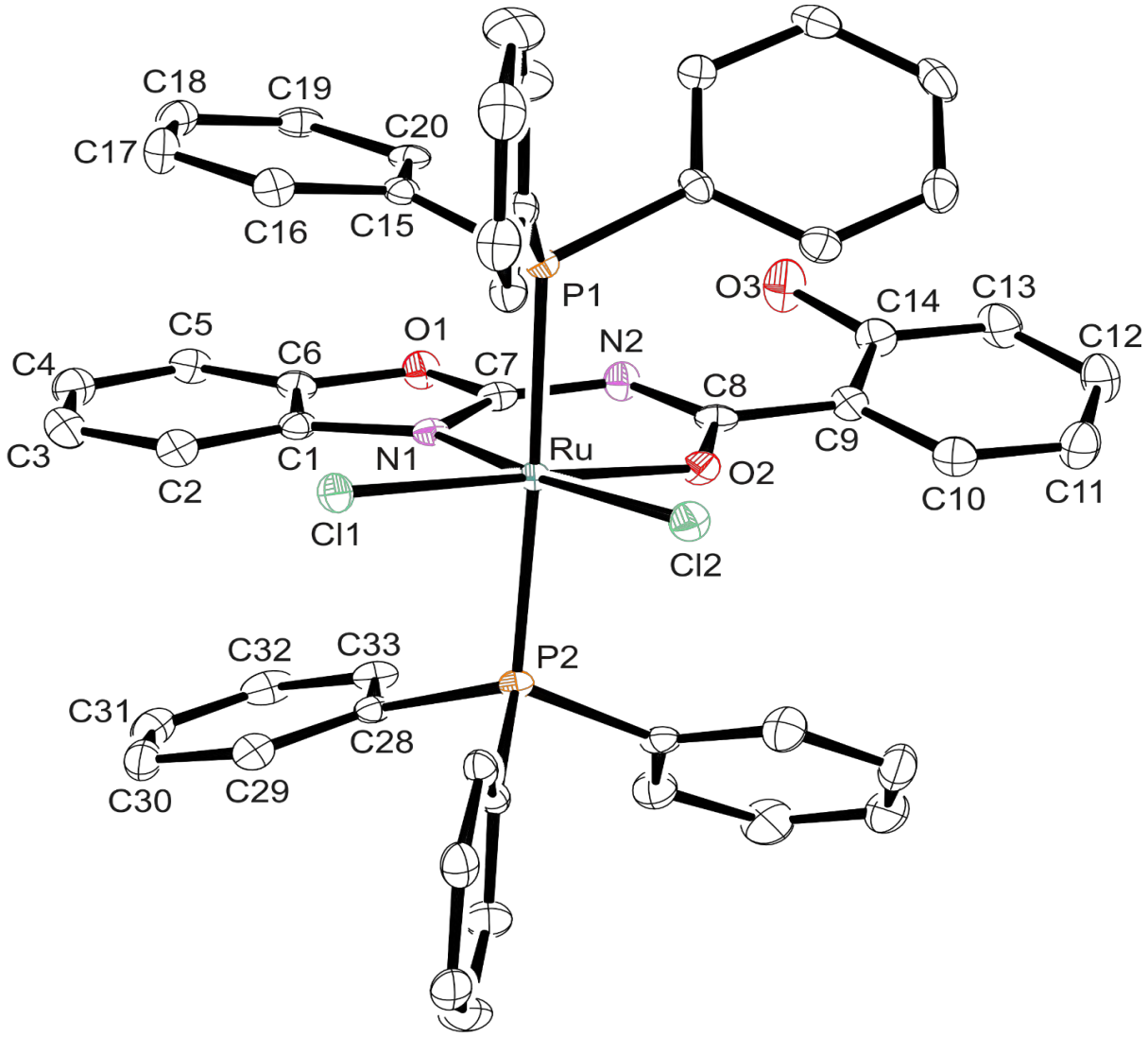

Figure 4.30: *An ORTEP view of complex* **2** *showing 50 % probability displacement ellipsoids and the atom labelling. The hydrogen atoms were omitted for clarity.*

Indicative to complex **1**, complex **2** has a series of intermolecular interactions. Hydrogen bonding interaction exists between the phenolic hydrogen and amide nitrogen atoms (O3-H39⋯N2 = 1.74(3) Å). This interaction is accompanied by interactions of the C1-C6 phenyl ring with the C15-C20 (3.598 Å) and C28-C33 (3.742 Å) phenyl rings. Subsequently, this leads to the benzoxazole moiety affording a dihedral angle of 17.58˚ with respect to the phenolic moiety and the molecules of **1** stacking in columns parallel to the *[b]*-axis. In addition to the weak C–H⋯Cl intramolecular interactions, compound **2** is linked by weak intermolecular C–H⋯O interactions into a dimeric supramolecular structure, refer to Figure 4.31.

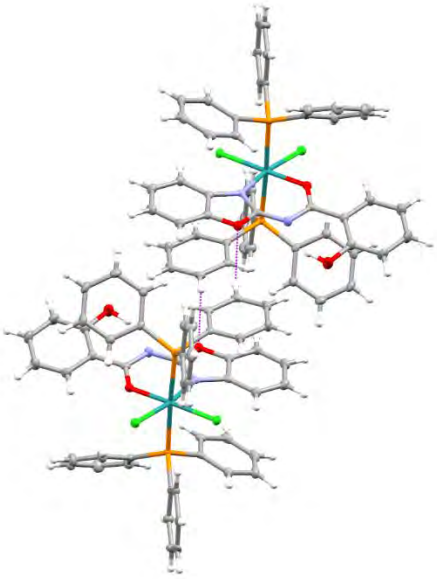

Figure 4.31: *Supramolecular dimeric structure of compound* **2** *viewed down the b-axis. The structure is supported by weak C–H⋯O interactions with geometrical parameters as follows: C18–H18 = 0.950 Å; H18⋯O1 = 2.489 Å; C18⋯O1 = 3.258(2) Å and C18–H18⋯O1 = 138˚.*

The *cis*-Ru-Cl coordination bonds (Ru-Cl1 = 2.3143(6) Å and Ru-Cl2 = 2.3462(6) Å) are different due to the difference in the *trans*-influences of the ketonic O2 and N1 benzoxazole atoms. However, these distances are shorter than the ruthenium halide

bond of **1** which is ascribed to the higher Lewis acid character of the metal centre of **1**. Interestingly, within the cyclometallated RuN1C7N2C8O2 ring, the deprotonation of the amide nitrogen resulted in a delocalized *pi*-conjugated system throughout the N1C7N2C8O2 moiety which can evidently be affirmed by the comparable C7-N1 (1.321(3) Å), C7-N2 (1.335(3) Å) and C8-N2 (1.343(3) Å) bond distances and the significant difference between the bond distances of C8-O2 (1.262(2) Å) from C14-O3 (1.360(3) Å).

The literature shows that numerous ruthenium benz(oxazole/imidazole) complexes with diverse structural features have been isolated. Among these complexes, is the mononuclear ruthenium (II) complex, *trans*-[$RuCl_2(Hbo)(PPh_3)_2$] (Hbo = 2-hydroxyphenylbenzoxazole) which has an identical Ru-$N_{benzoxazole}$ (2.120(2) Å) bond length as complex **2** (Ru-N1 = 2.120(2) Å) [**33**]. The Ru-$N_{benzimidazole}$ (2.058(3) Å) of complex **1** is comparable to the paramagnetic complex, *trans*-[$Ru^{III}Cl(bzp)(PPh_3)_2$] (Hbzp = *N*-(2-hydroxybenzylidene)benzimidazole) (Ru-$N_{benzimidazole}$ = 2.069(4) Å) [**23**]. Furthermore, as expected the Ru-O2 (2.124(2) Å) bond distance of **1** is shorter than the analogous bond distances of the ruthenium (II) complex, *cis*-[$Ru(bzca)_2(PPh_3)_2$] (Ru-$O_{carboxylate}$ = 2.133(4) Å and 2.117(4) Å) [**34**].

*4.4.5.3 Crystal structure of $(\mu\text{-}Cl)_2[RuCl(Hchpr)(PPh_3)]_2$ (**4**)*

Each molecule of **4** crystallizes out in a P-1 space group along with two toluene molecules of recrystallization. The bridging chloro-co-ligands affords a constrained 4-membered RuClRuCl ring with the opposing Cl1-Ru-Cl2 (84.94(2)˚) bond angles being equal (seeFigure 4.32). In addition, an inversion of symmetry occurs about these chloro-co-ligands (*viz.* Cl1 and Cl2) and hence the geometrical parameters around each metal centre are equivalent. Furthermore, the constrained 4-membered ring (RuClRuCl) and

bite angle (N2-Ru1-N1 = 87.93(7)˚) induces non-linearity in the P1-Ru1-Cl2 (178.75(2)˚), N2-Ru1-Cl1 (170.77(5)˚) and N1-Ru1-Cl3 (175.55(5)˚) bond angles.

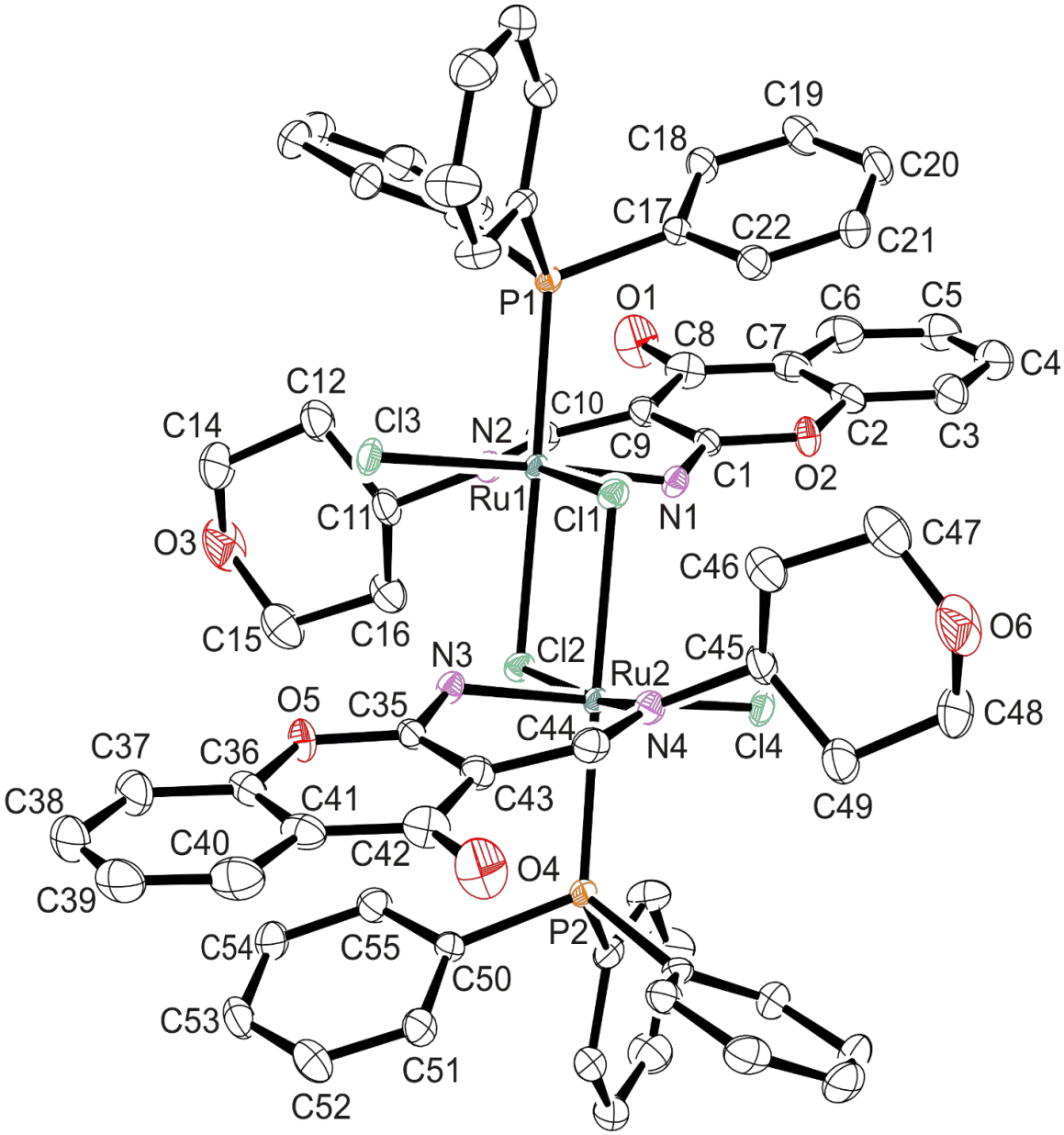

Figure 4.32: *An ORTEP view of compound* **4** *showing 50 % probability displacement ellipsoids and the atom labelling. The hydrogen atoms and toluene solvent molecules of recrystallization were omitted for clarity.*

The terminal Ru-Cl bonds (2.3744(7) Å) are significantly shorter than the bridging Ru-Cl bonds (Ru1-Cl1, Ru2-Cl2 = 2.4967(5) Å and Ru1-Cl2, Ru2-Cl1 = 2.4283(6) Å) and this trend is typical for chloro-bridged dinuclear ruthenium compounds. Intermolecular hydrogen-bonding is observed between the terminal chloro co-ligands and the amido hydrogen at 2.83(2) Å. Compound **4** exhibits a single classical intramolecular hydrogen bond (N1–H101···Cl2) with a relatively long D···A distance of 3.508(2) Å. In addition to this, it also shows a number of weak intramolecular and intermolecular C–H···Cl interactions in the solid state. The intermolecular interactions link the molecules into a one-dimensional network (see Figure 4.33) which is co-linear with the *b*-axis.

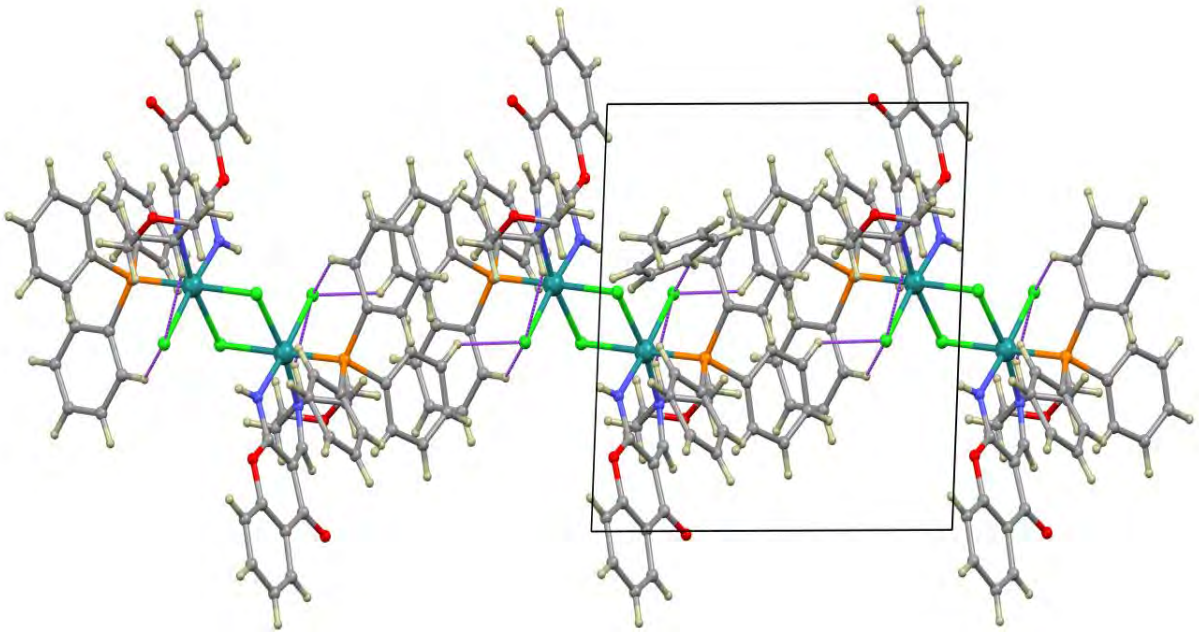

Figure 4.33: *Repeating unit of the three-dimensional supramolecular structure of compound* **4** *supported by C–H···Cl interactions (indicated as dashed purple tubes) viewed down the c-axis.*

The mononuclear complex **1** and dinuclear compound **4** share the same oxidation state and have comparable Ru-Cl (terminal for **4**) and Ru-P (2.3315(5) Å) bond lengths. The Ru-$N_{Schiff\ base}$ bond length of **4** (2.026(2) Å) is close to the lower limit of the 2.025(3) Å - 2.151(4) Å range found for other ruthenium(III) compounds with Schiff base chelates

[**11, 23, 35-38**]. In addition, the monoanionic charge donation of the amido nitrogen results in a shorter Ru-N_{amido} (1.972(2) Å) bond of **4** in comparison to its Ru-$N_{Schiff\ base}$ bond. The tetrahydropyran (THP) moiety adopts a chair conformation which is common to many transition metal complexes containing chelators incorporating the THP core [**39-43**].

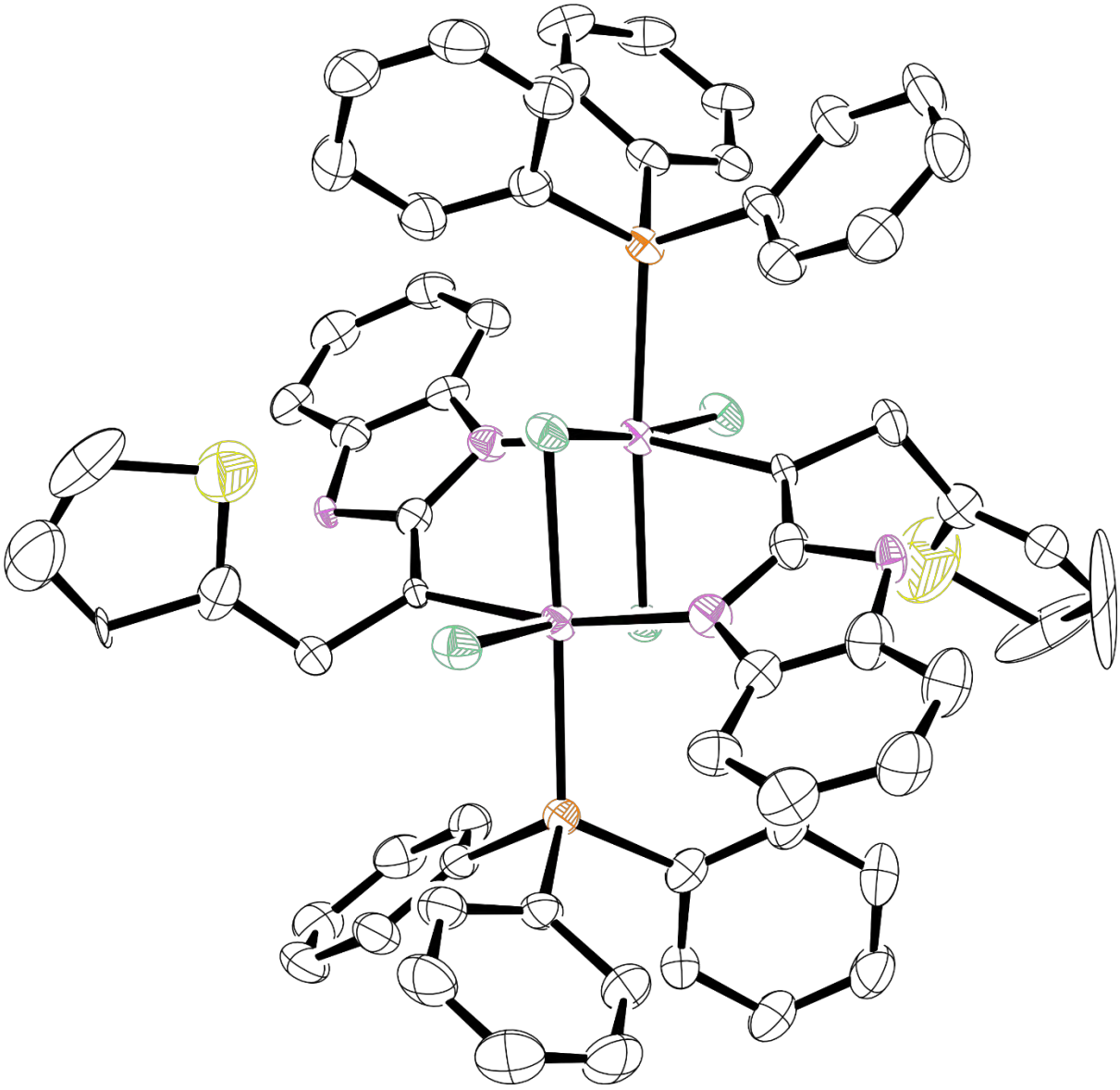

Figure 4.34: *Low resolution structure of compound* ***3.***

Table 4.3: *Crystal data and structure refinement data.*

	1·CH_3CH_2OH	**2**	**4**·2(C_7H_8)
Chemical formula	$C_{33}H_{29}ClN_3O_4PRu$	$C_{50}H_{39}Cl_2N_2O_3P_2Ru$	$C_{80}H_{76}Cl_4N_4O_6P_2Ru_2$
Formula weight	699.08	949.74	1595.33
Temperature (K)	100(2)	296(2)	100(2)
Crystal system	Monoclinic	Triclinic	Triclinic
Space group	$P2_1/n$	P-1	P-1
Unit cell dimensions (Å, °)	a= 12.5002(6)	a= 12.8703(7)	a= 12.8091(5)
	b= 19.6974(8)	b= 12.8876(7)	b= 12.9652(6)
	c= 12.6428(5)	c= 14.8744(8)	c= 13.7695(6)
	α =90	α =85.899(2)	α =68.311(2)
	β= 107.511(2)	β = 70.720(2)	β = 76.094(2)
	γ = 90	γ = 65.173(2)	γ = 82.489(2)
Crystal size (mm)	0.29 x 0.18 x 0.03	0.21 x 0.04 x 0.02	0.60 x 0.09 x 0.04
V(Å^3)	2968.7(2)	2107.1(2)	2060.34(15)
Z	4	2	1
Density (calc.) (Mg/m^3)	1.564	1.497	1.286
Absorption coefficient (mm^{-1})	0.716	0.622	0.585
F(000)	1424	970	818
θ range for data collection (deg)	1.98; 26.03	1.75; 26.16	1.63; 26.11
Index ranges	-14 ≤ h ≤ 15 -20 ≤ k < 24 -11 ≤ ℓ ≤ 15	-15 ≤ h ≤ 15 -15 ≤ k < 15 -18 ≤ ℓ ≤ 182	-15 ≤ h ≤ 15 -12 ≤ k < 15 -17 ≤ ℓ ≤ 17
Reflections measured	16731	35691	33857
Observed reflections [I>2σ(I)]	5837	8256	7981
Independent reflections	4698	7043	7260
Data/Restraints/parameters	4698/0/401	7043/1/545	7260/0/447
Goodness of fit on F^2	1.028	1.026	1.045
Observed R, wR^2	0.0363, 0.0767	0.0280, 0.0603	0.0282, 0.0726
R_{int}	0.040	0.034	0.022

Table 4.4: *Selected bond lengths [Å] and bond angles [°] for* ***1****.*

Ru-O1	2.119(2)
Ru-O2	2.124(2)
Ru-N1	1.904(2)
Ru-N2	2.058(3)
C9-O3	1.225(3)
C9-O2	1.283(4)
O1-Ru-N1	79.5(1)
O2-Ru-N2	76.94(9)

Table 4.5: *Selected bond lengths [Å] and bond angles [°] for* **2***.*

Ru-P1	2.4229(7)
Ru-P2	2.3979(7)
Ru-Cl1	2.3143(6)
Ru-Cl2	2.3462(6)
Ru-N1	2.120(2)
Ru-O2	2.042(2)
C7-N1	1.321(3)
C7-N2	1.335(3)
C8-N 2	1.343(3)
C8-O2	1.262(2)
C14-O3	1.360(3)
N1-Ru-O2	85.71(7)
Cl1-Ru-Cl2	95.71(2)
P1-Ru-P2	177.38(2)

Table 4.6: *Selected bond lengths [Å] and bond angles [°] for* ***4****.*

Ru-$Cl_{terminal}$	2.3744(7)
Ru1-Cl1	2.4967(5)
Ru2-Cl2	2.4967(5)
Ru1-Cl2	2.4283(6)
Ru2-Cl1	2.4283(6)
Ru-P	2.3315(5)
Ru-$N_{Schiff\ base}$	2.026(2)
Ru-N_{amido}	1.972(2)
Cl1-Ru1-Cl2	84.94(2)
Cl1-Ru1-Cl3	89.73(2)
N2-Ru1-N1	87.93(7)
P1-Ru1-Cl2	178.75(2)
N2-Ru1-Cl1	170.77(5)
N1-Ru1-Cl3	175.55(5)

4.5 References

1. J.B. Aitken, S. Antony, C.M. Weekley, B. Lai, L. Spiccia, H.H. Harris, *Metallomics*, 2012, **4**, 1051.
2. S. Medici, M. Peana, V.M. Nurchi, J.I. Lachowicz, G. Crisponi, M.A. Zoroddua, *Coord. Chem. Rev*., 2015, **284**, 329.
3. G. Gupta, G. Sharma, B. Koch, S. Park, S.S. Lee, J. Kim, *New J. Chem*., 2013, **37**, 2573.
4. J. Novales, N. Jonkhoff, J.H. Acquaye, *Polyhedron*, 2013, **62**, 148.
5. L. Oehninger, M. Stefanopoulou, H. Alborzinia, J. Schur, S. Ludewig, K. Namikawa, A. Muñoz-Castro, R.W. Köster, K. Baumann, S. Wölfl, W.S. Sheldrick, I. Ott, *Dalton. Trans.*, 2013, **42**, 1657.
6. M. Parveen, A.M. Malla, Z. Yaseen, A. Ali, M. Alam, *J. Photochem. Photobiol. B*, 2014, **130**, 179.
7. Y. Li, Z. Yang, J. Wu, *Eur. J. Med. Chem*., 2010, **45**, 5692.
8. F. Arjmand, I. Yousuf, *J. Organomet. Chem*., 2013, **743**, 55.
9. B. Wang, Z. Yang, M. Lü, J. Hai, Q. Wang, Z. Chen, *J. Organomet. Chem*., 2009, **694**, 4069.
10. M. Morais, S. Subramanian, U. Pandey, G. Samuel, M. Venkatesh, M. Martins, S. Pereira, J.D. Correia, I. Santos, *Mol. Pharm*., 2011, **8**, 609.
11. I.N. Booysen, S. Maikoo, M.P. Akerman, B. Xulu, O.Q. Munro, *J. Coord. Chem*., 2013, **66**, 3673.
12. P. Krishnamoorthy, P. Sathyadevi, K. Senthilkumar, P. Thomas Muthiah, R. Ramesh, N. Dharmaraj, *Inorg. Chem. Commun*., 2011, **14**, 1318.
13. A.L. Spek, *Acta Crystallogr.,Sect. D: Biol. Crystallogr.,* 2009, **D65**, 148.

14. Bruker APEX2, SAINT and SADABS. Bruker AXS Inc., 2010, Madison, Wisconsin, USA.
15. R.H. Blessing, *Acta Crystallogr.,Sect. A: Found. Crystallogr.,* 1995, **A51**, 33.
16. G.M. Sheldrick, *Acta Crystallogr.,Sect. A: Found. Crystallogr.,* 2008, **A64**, 112.
17. L.J. Farrugia, *J. Appl. Cryst.,* 2012, **45**, 849.
18. N.G. Tsierkezos, A.I. Philippopoulos, *Inorg. Chim. Acta*, 2009, **362**, 3079.
19. S.E. Diamond, F. Mares, B.S. Tovrog, 1980, *US Patent 4207305A*.
20. Z. Dong, P.J. Scammels, *J. Org. Chem.*, 2007, **72**, 9881.
21. F. Shia, M.K. Tsea, M. Beller, *J. Mol. Cat*., 2007, **270**, 68.
22. C.M. Che, W.P. Yip, W.Y. Yu, *Chem. Asian J*., 2006, **18**, 453.
23. I.N. Booysen, A. Adebisi, O.Q. Munro, B. Xulu, *Polyhedron*, 2014, **73**, 1.
24. L. Bennett, *J. Exp. Clin. Med*., 2012, **4**, 215.
25. S. Li, G. Chen, C. Zhang, M. Wu, S. Wu, Q. Liu, *Food Science and Human Wellness*, 2014, **3**, 110.
26. P. Ragendran, *Clin. Chim. Acta*, 2014, **436**, 332.
27. T.S. Kamatchi, N. Chitrapriya, S.K. Kim, F.R. Fronczek, K. Natarajan, *Eur. J. Med. Chem.*, 2013, **59**, 253.
28. T. Bal-Demirci, M. Şahin, E. Kondakçı, M. Özyürek, B. Ülküseven, R. Apak, *Spectrochim. Acta A*, 2015,**138**, 866.
29. Y.S. El-Sayed, M. Gaber, *Spectrochim. Acta A*, 2015, **137**, 423.
30. R. Ramachandran, P. Viswanathamurthi, *Spectrochim. Acta A*, 2013, **103**, 53.
31. G. Prakash, R. Manikandan, P. Viswanathamurthi, K. Velmurugan, R. Nandhakumar, *J. Photochem. Photobiol., B*, 2014, **138**, 63.
32. P. Anitha, N. Chitrapriya, Y.J. Jang, P. Viswanathamurthi, *J. Photochem. Photobiol. B*, 2013, **129**, 17.
33. J.G. Małecki, *Polyhedron*, 2012, **31**, 159.

34. J.G. Małecki, A. Maron, *Polyhedron*, 2012, **40**, 125.

35. R. Raveendran, S. Pal, *J. Organomet. Chem*., 2007, **692**, 824.

36. K. Nagaraja, S. Pal, *J. Organomet. Chem*., 2013, **745-746**, 404.

37. K. Nagaraja, S. Pal, *J. Organomet. Chem.,* 2013, **737**, 7.

38. S. Mandal, V. Kundi, D.K. Seth, K. Srikanth, P. Gupta, *Polyhedron*, 2014, **80**, 290.

39. D.T. Hill, B.M. Sutton, *Cryst. Struct. Commun*., 1980, **9**, 679.

40. P. Leibnitz, G. Reck, H.-J. Pietzsch, H. Spies, *Forschungszent Rossendorf (ber)*, 2001, **311**, 102.

41. D. Schwidom, M. Volkmann, A. Wolter, J. Heck, *Carbohydr. Res*., 2013, **365**, 26.

42. M. Sternberg, J. Rust, C.W. Lehmann, F. Mohr, *Helv. Chim. Acta*, 2013, **96**, 280.

43. Y. Mikata, Y. Sugai, M. Obata, M. Harada, S. Yano, *Inorg. Chem*., 2006, **45**, 280.

Chapter 5

Coordination modes of Di- and Triimines towards Ruthenium(II) and -(III) centres: Structural, Electrochemical and Radical Scavenging studies

5.1 Introduction

The discovery of NAMI-A, *trans*-[$Ru^{III}Cl_4$(DMSO)(Im)](ImH) (ImH = protonated imidazole)as a potential ruthenium metallopharmaceutical has led to a resurgence of interest in the coordination chemistry of ruthenium in medicinal inorganic chemistry [**1-4**]. Meticulous ligand design by utilizing chelators with neutral nitrogen donor atoms (*e.g.* $[Ru(bpy)_3]^{2+}$) has proven favourable in the stabilization of ruthenium in both high and low oxidation states [**4-6**]. In addition, the high metal-binding affinity of this class of ligands makes them excellent candidates as bifunctional chelators of ruthenium centres and scaffolds incorporating biologically relevant moieties [**7-8**]. The inclusion of biologically relevant ligands in coordination compounds of ruthenium is geared towards improving the biodistribution patterns of the metal complexes, thereby potentially minimizing side-effects with respect to healthy cells [**9-10**]. Literature have shown the exploration of coordination susceptibility of Schiff bases derived from biologically relevant moieties towards the ruthenium(II) and –(III) cores [**11-14**].

Like in the case of the coordination reactions of *trans*-[$RuCl_2(PPh_3)_3$] with the diimine ligands 2,6-*bis*-((6-amino-1,3-dimethyluracilimino)methylene)pyridine (H_4ucp) and 2,6-*bis*-((antipyrine-imino)methylene)pyridine (bpap) which readily afforded the metal complexes, [Ru^{II}(H_3ucp)Cl(PPh_3)] and *cis*-[$Ru^{II}Cl_2$(bpap)(PPh_3)], respectively [**11**]. The dinuclear ruthenium compound, (μ-Cl)$_2$[Ru^{III}Cl(Hchpr)(PPh_3)]$_2$ (H_2chpr = 2-amino-3-((tetrahydro-2*H*-pyran-4-ylimino)methyl)-4*H*-chromen-4-one) exhibits optimal redox properties governed by the well-defined Ru(II/III) and Ru(III/IV) redox couples observed within its cyclic

voltammogram. In turn, these optimal redox properties induced significantly higher DPPH radical scavenging activity than the corresponding free-ligand, H_2chpr and the natural antioxidant, vitamin C [**13**].

In this chapter, we investigate the coordination modes of di- and triimines towards the ruthenium(II) and –(III) cores. More specifically, the diamagnetic ruthenium(II) complex, *cis*-[$RuCl_2$(thppy)(PPh_3)] (**1**), the paramagnetic ruthenium(III) compounds, (μ-chb)[*mer*-$RuCl_3(PPh_3)]_2$ (**2**) and [Ru(pym)] (**3**) were isolated from the 1:1 molar coordination reactions of *trans*-[$Ru^{II}Cl_2(PPh_3)_3$] with 2,6-*bis*-((tetrahydropyranimino)methyl)pyridine (thppy), N^1,N^2-*bis*((chromone)methylene)benzene-1,2-diamine (chb) and *tris*-((1*H*-pyrrol-2-ylmethylene)ethane)amine (H_3pym), respectively. To evaluate the antioxidant potential of ruthenium compounds, radical scavenging studies were conducted with the DPPH and NO radicals. Notably, the biologically significant components of the present compounds (*viz.* pyrrole, chromone and tetrahydropyran) and their derivatives are known to exhibit both antioxidant and anticancer activities [**13**, **15**, **16**]; hence the inclusion of these moieties in metal complexes could potentially promote target-specific *in vivo* biodistribution patterns to malignant tumours.

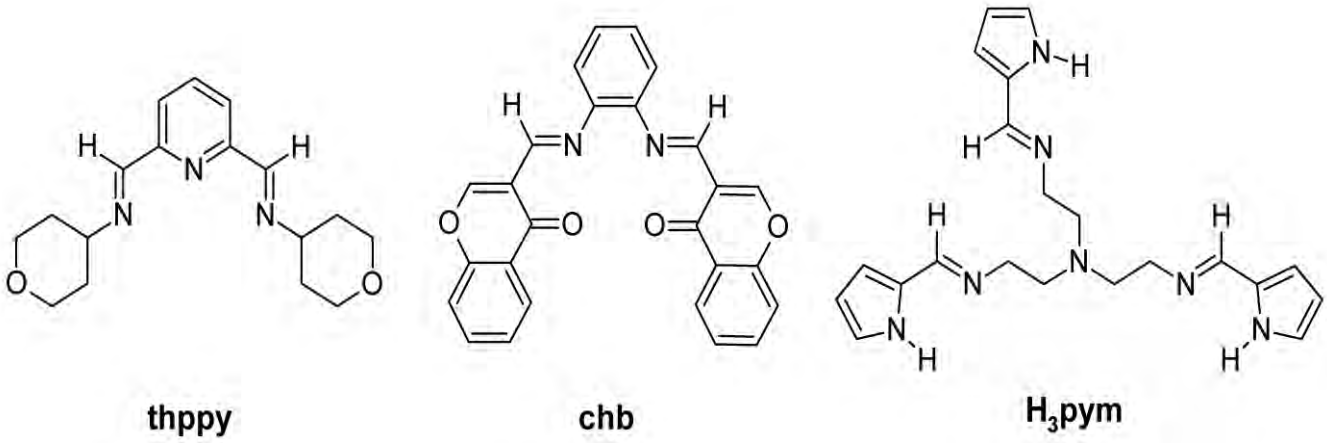

Figure 5.1: *Structures and abbreviations of the di- and triimines ligands.*

5.2 Experimental

5.2.1 Synthesis of ligands:

5.2.1.1 2,6-bis-((4-tetrahydropyranimino)methyl)pyridine (thppy)

A reaction mixture of 2,6-pyridinedicarboxaldehyde (0.20 g; 1.48 mmol), tetrahydro-2*H*-pyran-4-amine (0.31 cm^3; 2.96 mmol) and a catalyst, piperidine (3 drops) was heated at reflux temperature in methanol (20 cm^3). After four hrs, the resultant solution was left to stand for two days at room temperature. Then a cream white precipitate was filtered and washed with petroleum ether. M.P. = 133 – 135 ˚C; Yield = 92 %; IR (ν_{max}/cm^{-1}): υ(C=N) 1643 (s), υ(O-C-O)$_{thp}$ 1134, 1081 (vs);^{1}H NMR (295K/ppm): 8.44 (s, 2H, *H6*, *H12*), 8.03–7.92 (m, 3H, *H8*, *H9*, *H10*), 3.99–3.89 (m, 4H, *H5*, *H5*□, *H18*, *H18*□), 3.84–3.75 (m, 2H, *H1*, *H13*), 3.68–3.57 (m, 2H, *H1*□, *H13*□), 3.52–3.89 (m, 4H, *H4*, *H4*□, *H17*, *H17*□), 2.77–2.63 (m, 2H, *H2*, *H14*), 1.45–1.29 (m, 2H, *H2*□, *H14*□), 1.27–1.13 (m, 2H, *H3*, *H16*); UV-vis (DCM, (λ_{max} (ε, $M^{-1}cm^{-1}$))): 254 nm (8232); 278 nm (sh, 6137); 291 nm (7090); 298 nm (sh, 5259).

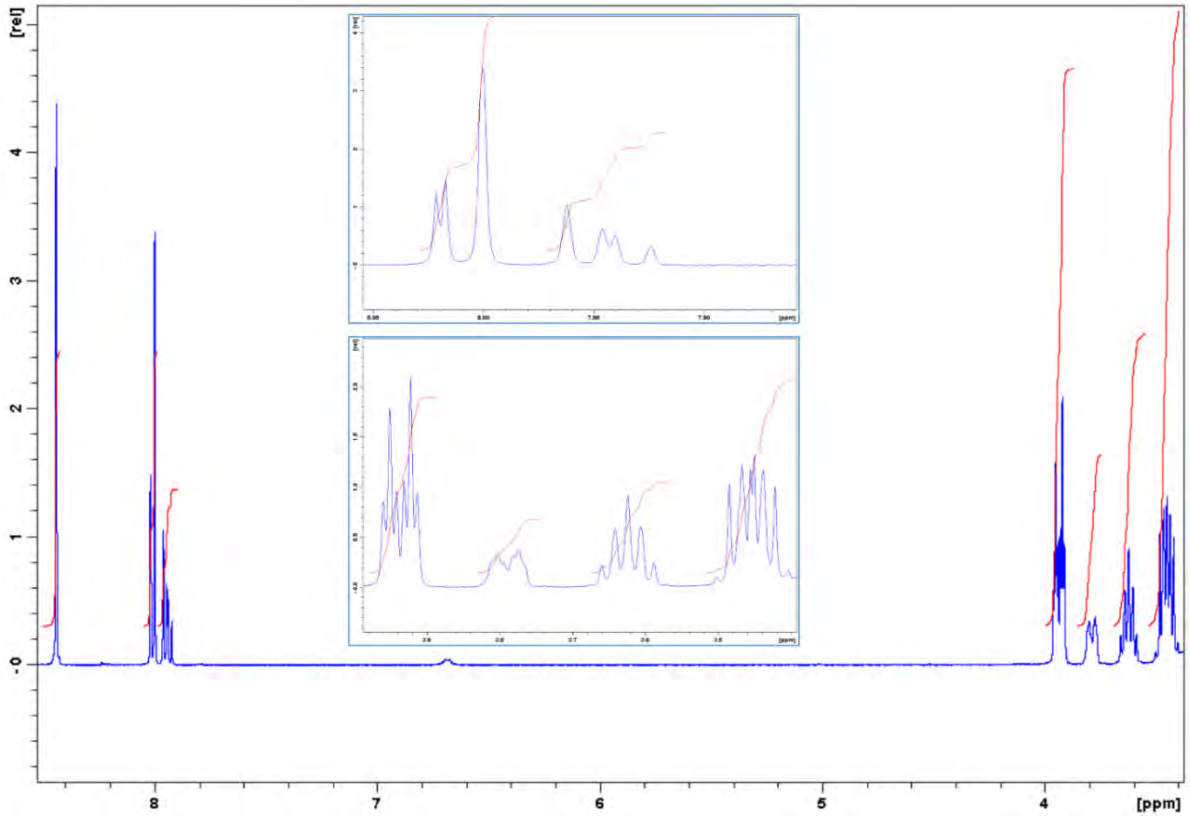

Figure 5.2: *^{1}H NMR spectrum of thppy.*

5.2.1.2 N^1,N^2-bis((3-chromone)methylene)benzene-1,2-diamine (chb)

3-Formylchromone (0.50 g; 2.88 mmol) and 1,2-diaminobenzene (0.15 g; 1.44 mmol) were heated at reflux temperature for five hrs in dry toluene. The reaction mixture was allowed to cool to room temperature and a red precipitate formed which was filtered and washed with cold toluene as well as petroleum ether. M.P. = 238 – 240 ˚C; Yield=90 %; IR (υ_{max}/cm^{-1}): υ(C=O) 1633 (s), υ(C=N) 1635 (sh, m),υ(O-C-O)$_{thp}$ 1131 (br, vs); ^{1}H NMR (295K/ppm): 14.27 (br, s, 2H, *H6*, *H23*); 10.19 (br, s, 2H, *H10*, *H17*); 8.56 (d, 2H, *H1*, *H18*); 7.41 – 7.29 (m, 4H, *H3, H12, H15, H20*); 7.21 – 7.13 (m, 4H, *H2, H13, H14, H19*); 7.00 – 6.91 (m, 2H, *H4*, *H21*); UV-vis (DCM, (λ_{max} (ε, M^{-1}cm^{-1}))): 263 nm (25843); 359 nm (47325); 383 nm (33619); 482 nm (sh, 1862).

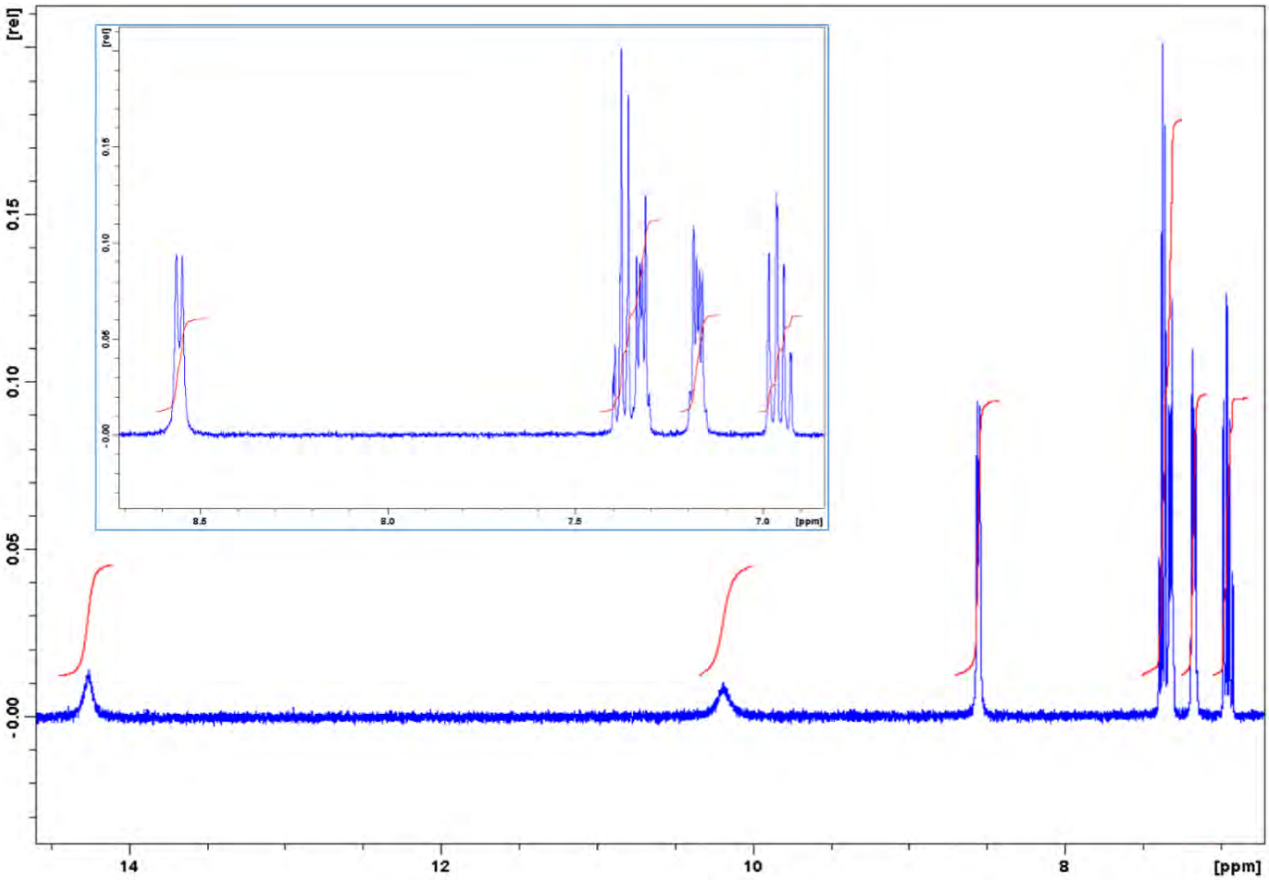

Figure 5.3: *^{1}H NMR spectrum of chb.*

5.2.1.3 *Tris-((1H-pyrrol-2-ylmethylene)ethane)amine (H_3pym)*

This compound was prepared using a method similar to those previously reported [**17**]. To a solution of *tris*-(2-aminoethyl) amine (1 cm^3; 6.84 mmol) in absolute ethanol (20 cm^3), pyrrole-2-carboxaldehyde (1.95 g; 20.52 mmol) was added with constant stirring. The resulting reaction mixture was heated until reflux for three hrs and cooled. Orange red crystalline material was obtained from the slow evaporation of ethanol/acetonitrile mixture (1:1, *v/v*). M.P = 138 – 140 ˚C; Yield= 80 %; IR (ν_{max}/cm^{-1}): υ(N-H) 3122, 3061 (m), υ(C=N)$_{imine}$ 1644 (vs), υ(C=N)$_{heterocyclic}$ 1555 (sh, m);^{1}H NMR (295K/ppm): 11.30 (br, s, 3H, *NH*), 7.97 (s, 3H, *H5*, *H12*, *H19*), 7.99 – 7.93 (m, 3H, *H3*, *H10*, *H17*), 6.35 – 6.32 (m, 3H, *H1*, *H8*, *H15*), 6.08 (t, 3H, *H2*, *H9*, *H16*), 3.33 (br, s, 12H, *H6, H6′, H7, H7′, H13, H13′, H14, H14′, H20, H20′, H21, H21′*). UV-vis (DCM/CH_3CN, (λ_{max} (ε, $M^{-1}cm^{-1}$))): 283 nm (46720); 346 nm (1423).

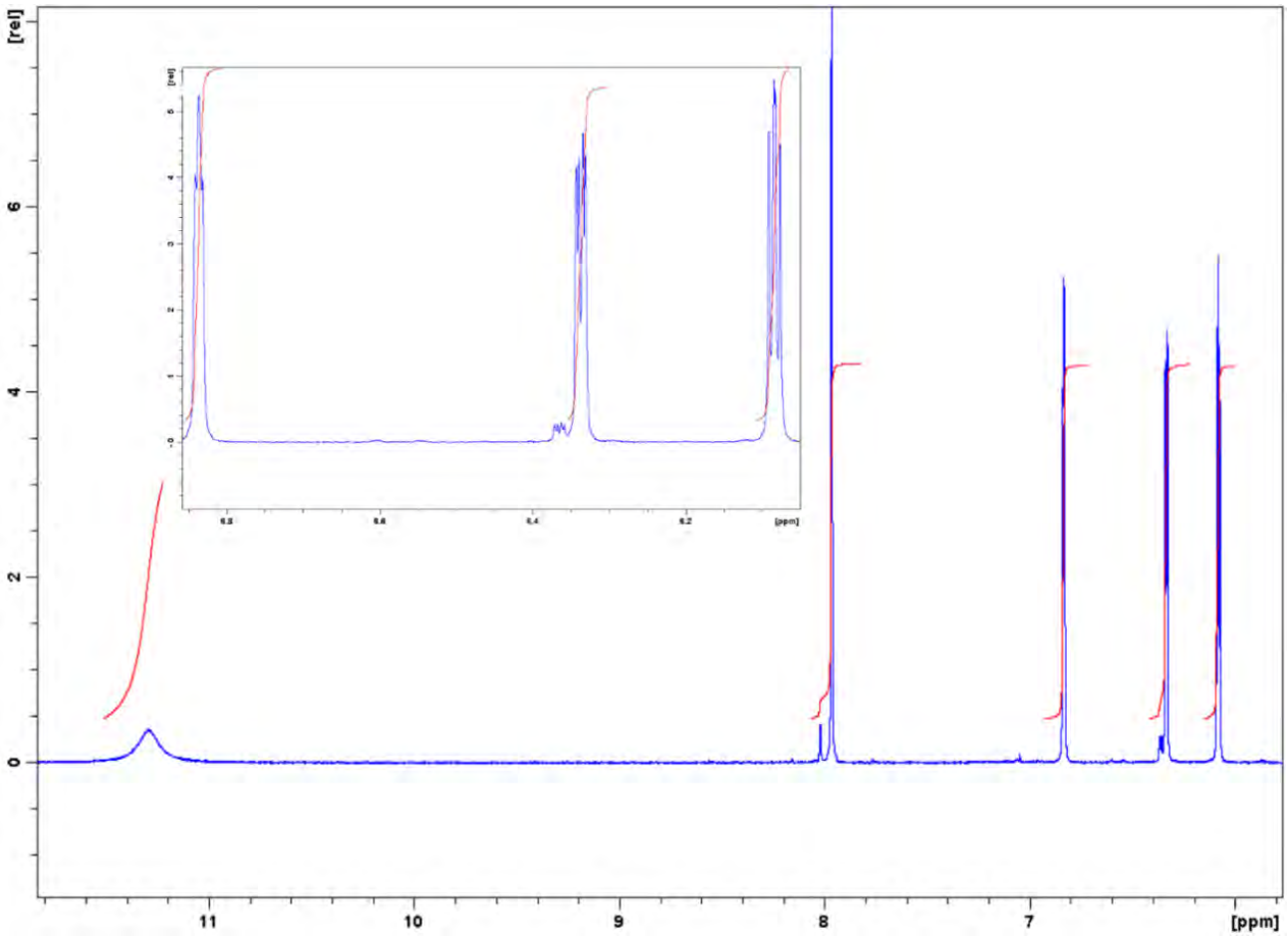

Figure 5.4: *^{1}H NMR spectrum of H_3pym.*

5.2.2 *Synthesis of metal complexes*

5.2.2.1 *cis-[$RuCl_2$(thppy)(PPh_3)] (**1**)*

A 1:1 molar reaction mixture of thppy (0.0314 g; 104 µmol) and *trans*-[$RuCl_2(PPh_3)_3$] (0.100 g; 104 µmol) was heated under reflux in toluene (20 cm^3) for six hrs. From the resulting dark purple solution, a maroon precipitate was attained. This precipitate was dissolved in dichloromethane and layered with hexane. XRD quality dark crystals were obtained from the layered solution after several days. M.P. > 350˚C; Yield = 80% (based on Ru);IR (ν_{max}/cm^{-1}): υ(C=N) 1635 (w), υ(O-C-O)$_{thp}$ 1134, 1081 (vs), υ(Ru-PPh_3) 698, υ(Ru-N) 525;^{1}H NMR (295K/ppm): 8.28 (s, 2H, *H6*, *H12*), 7.70 – 7.12 (m, 18H, *H8*, *H9*, *H10*, P*Ph*$_3$), 4.34 (t, 2H, *H5*, *H18*), 3.95 – 3.86 (m, 2H, *H5*□, *H18*□), 3.80 – 3.71 (m, 2H, *H1*, *H13*), 3.15 (t, 2H, *H1*□, *H13*□), 2.72 (t, 2H, *H4*, *H17*), 2.40 – 2.19 (m, 2H, *H4*□, *H17*□), 1.99 – 1.74 (m, 2H, *H2*, *H14*), 1.31 – 1.21 (m, 2H, *H2*□, *H14*□), 0.61 (d, 2H, *H3*, *H16*); ^{31}P NMR (295K/ppm): 30.58;Conductivity (DCM, 10^{-3}M): 12.5 ohm.cm^2.mol^{-1}; UV-vis (DCM, λ_{max} (ε, M^{-1} cm^{-1})): 239 nm (52195); 297 nm (sh, 6644); 317 nm (sh, 5137); 332 nm (sh, 3356); 461 nm (5848); 571 nm (2522); 688 nm (sh, 469).

5.2.2.2 *cis-Cl, (µ-chb)[$RuCl_3(PPh_3)]_2$ (**2**)*

A mixture of chb (0.0276 g; 104 µmol) and *trans*-[$RuCl_2(PPh_3)_3$] (0.100 g; 104 µmol) in toluene (20 cm^3) and one drop of 32% hydrochloric acid was heated under reflux for six hrs. A dark brown precipitate was filtered and washed with toluene as well as diethyl ether. Upon addition of 10 cm^3 acetonitrile to the filtrate, the slow evaporation of the resultant mixture afforded brown crystals suitable for X-ray analysis. M.P. > 350˚C; Yield = 77% (based on Ru); IR (ν_{max}/cm^{-1}): υ(N-H) 2950, 2938, 2846 (m), υ(C=N)$_{imine}$ 1615 (s), υ(O-C-O) 1159, 1143 (m), υ(Ru-PPh_3) 692 (vs), υ(Ru-N) 526 (vs), υ(Ru-O) 455 (w); Conductivity (DCM, 10^{-3} M): 12.66 ohm.cm^2.mol^{-1}; UV-vis (DCM, λ_{max} (ε, M^{-1} cm^{-1})): 263 nm (sh, 19164); 360 nm (13173); 454 nm (sh, 8522); 723 nm (sh, 1465).

5.2.2.3 *[Ru(pym)] (**3**)*

Equimolar quantities of H_3pym (0.0394 g; 104 µmol) and *trans*-[$RuCl_2(PPh_3)_3$] (0.100 g; 0.104 mmol) were heated at reflux temperature for eight hrs in toluene (20 cm^3). A dark

precipitate was filtered and washed with toluene, MeOH, CH_3CN, DCM and diethyl ether. Slow evaporation of the filtrate gave dark brown crystals. M.P. > 350˚C; Yield = 91% (based on Ru); IR (ν_{max}/cm^{-1}): $\upsilon(C=N)_{imine}$ 1605 (sh, s), $\upsilon(C=N)_{heterocyclic}$ 1573 (vs), υ(Ru-N) 524, 513 (vs);Conductivity (DMSO/CH_3CN (1:1, *v:v*), 10^{-3} M): 16.95 ohm.cm^2.mol^{-1}; UV-vis (DMSO/CH_3CN, λ_{max} (ε, $M^{-1}\,cm^{-1}$)): 291 nm (17531); 361 nm (sh, 10891).

5.3 X-ray diffraction

The X-ray data for the metal complexes were recorded on a Bruker Apex Duo equippedwith an Oxford Instruments Cryojet operating at 100(2) K and an Incoatec microsource operating at 30W power. Crystal and structure refinement data are given in Table 5.2. Selected bond lengths and angles are given in Tables 5.3, 5.4 and 5.5 for **1**.H_2O, **2**.CH_3CN and **3**, respectively. In all three cases the data were collected with Mo Kα (λ = 0.71073 Å) radiation at a crystal-to-detector distance of 50 mm. The following conditions were used for data collection: omega and phi scans with exposures taken at 30 W X-ray power and 0.50^o frame widths using APEX2 [**18**]. The data were reduced with the program SAINT [**18**] using outlier rejection, scan speed scaling, as well as standard Lorentz and polarization correction factors. A SADABS semi-empirical multi-scan absorption correction [**19**] was applied to the data. Direct methods, SHELX-2014 [**20**] and WinGX [**21**] were used to solve all three structures. All non-hydrogen atoms were located in the difference density map and refined anisotropically with SHELX-2014 [**20**]. All hydrogen atoms were included as idealised contributors in the least squares process. Their positions were calculated using a standard riding model with C-$H_{aromatic}$ distances of 0.93 Å and U_{iso} = 1.2 U_{eq}, C-$H_{methylene}$ distances of 0.99 Å and U_{iso} = 1.2 U_{eq} and C–H_{methyl}distances of 0.98 Å and U_{iso} = 1.5 U_{eq}. The O-H bonds of the water molecule for **1** were located in the difference density map and refined isotropically.

5.4 Results and Discussion

5.4.1 Synthesis and spectral characterization

The isolated ruthenium compounds **1** - **3** were formulated from the equimolar coordination reactions of *trans*-[$RuCl_2(PPh_3)_3$] with the respective Schiff bases: thppy, chb and H_3pym. In **1**, the thppy moiety acts as a neutral tridentate chelator through its $(NN)_{imino}N_{py}$ donor set while for **2**, the neutral chb moiety bridges the two *cis*-[$Ru^{III}Cl_3$] cores *via* its ketonic oxygen and imino nitrogen atoms. In the formation of the dinuclear compound **2**, initially the hydrochloric acid dissociates into its constituent ions followed by the oxidation of the metal centres by H^+ cations and in the process diatomic hydrogen gas forms from the reaction mixture [**22**, **23**]. Lastly, the coordination of chloro anions and the chelator to the respective metal atoms resulted in the isolation of **2**. Interestingly, the triimine pym chelator displaced all the co-ligands of the metal precursor leading to octahedral saturation through its three imino nitrogens and three deprotonated pyrrolidine nitrogen atoms. In fact, this phenomenon has been observed in the coordination reactions of *trans*-[$RuCl_2(PPh_3)_3$] with analogous tripodal triimine ligands derived from *tris*-(2-aminoethyl)amine [**24**]. However, the rigid ruthenium(II) arene cores remained intact for the organometallic ruthenium(II) complexes, [Ru(Ar)Cl(sal_3tr)] (sal_3tr = *tris*-2-(salicylaldimine ethyl)amine) and [Ru(Ar)Cl(py_3tr)] (py_3tr = *tris*-2-(2-pyridylimine ethyl)amine) where the arene (Ar) core can be hexamethylbenzene, *para*-cymene or hydroxyethoxybenzene [**25**].

Compounds **1** and **2** are highly soluble in high boiling point aprotic and chlorinated solvents while complex **3** is only partially soluble in a 1:1 (*v:v*) mixture of dimethylsulphoxide and acetonitrile. The low molar conductivity values of the formulated metal complexes affirm that they are non-electrolytes [**11**, **26**]. Only low resolution EPR spectra could be obtained for the metal complexes **2** and **3** which are typical of ruthenium(III) complexes with distorted octahedral geometries[**27**, **28**], see Figure 5.5. The ^{1}H NMR spectrum of **1** shows that the imino protons appear as a sharp singlet (at 8.28 ppm) which is more downfield in comparison to the analogous signal of its free ligand, thppy, at 8.44 ppm, see Figure 5.6. In the aromatic region of 7.70 – 7.12 ppm, a multiplet

integrates to 18 protons ascribed to the pyridyl moiety and triphenylphosphine co-ligand. The uncoordinated tetrahydropyran (thp) moieties are characterized by the expected up-field multiplet signals in the NMR spectrum between 3 and 4 ppm. Both thp moieties exhibit chair conformations in solution as evidenced by the lack of signals from boat conformers of the 6-membered rings (this is consistent with the X-ray data for **1**, *vide infra*). As expected, only one signal is observed in the ^{31}P NMR spectrum of **1** due to itstriphenylphosphine co-ligand, see Figure 5.7.

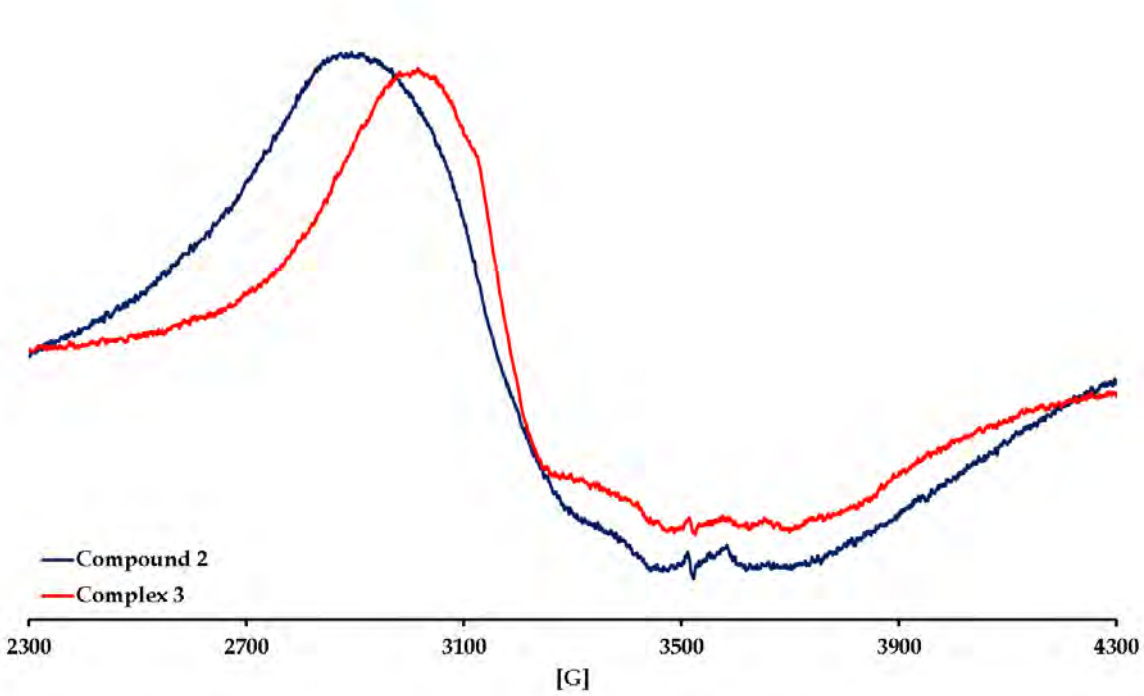

Figure 5.5: *EPR spectra of the solid samples of* **2** *and* **3** *at room temperature.*

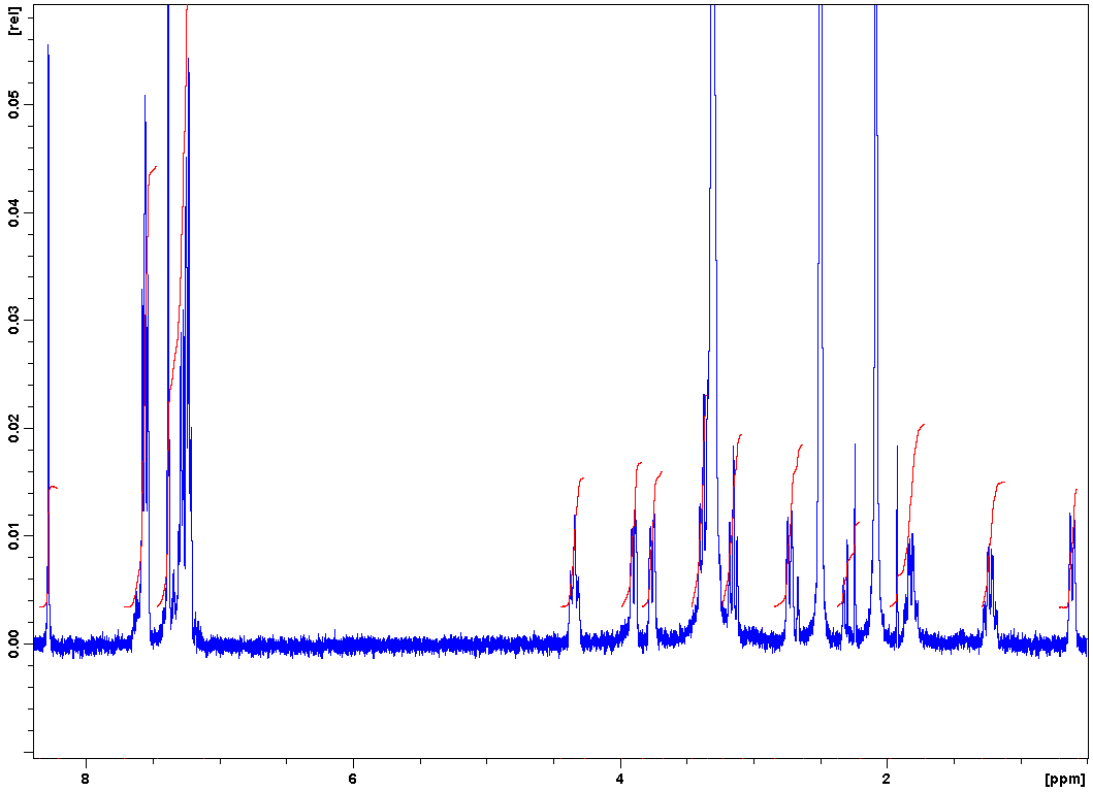

Figure 5.6: *^{1}H NMR spectrum of complex **1**.*

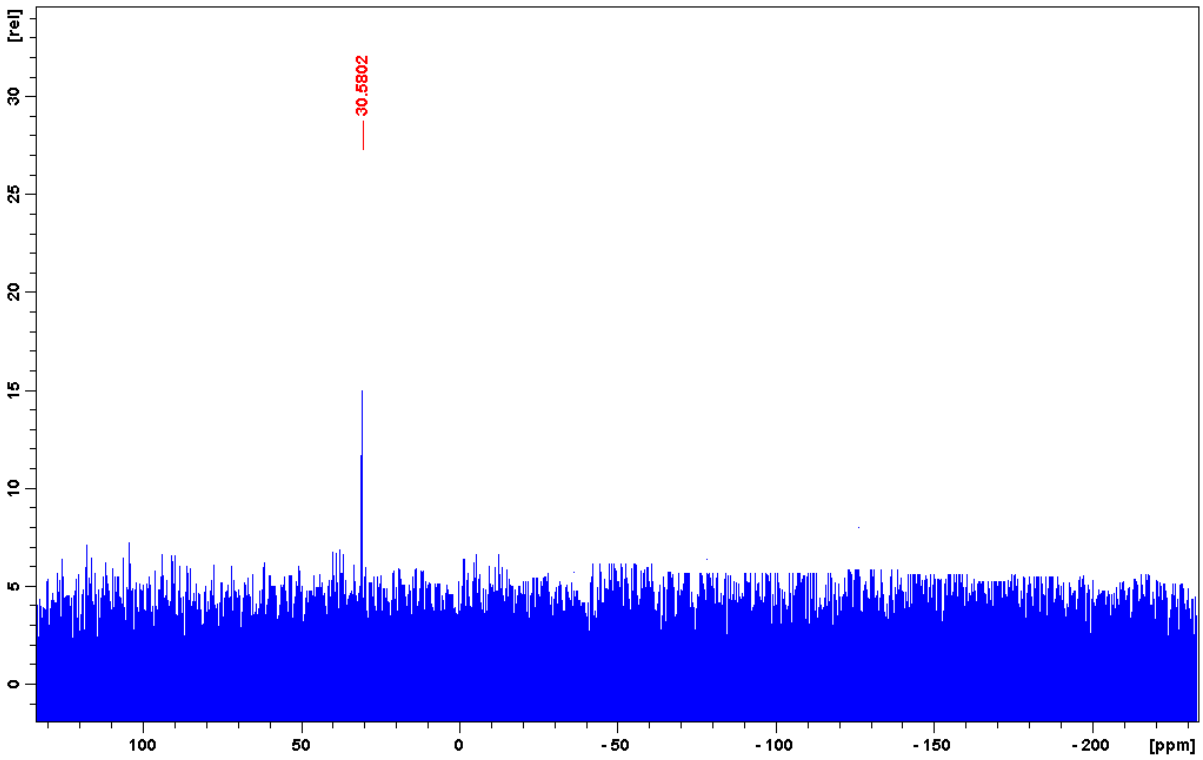

Figure 5.7: *^{31}P NMR spectrum of complex **1**.*

The IR spectra of the free ligands contain strong vibrations that are readily assigned to the imine C=N groups at 1643 cm^{-1} (for thppy), 1635 cm^{-1} (for chb) and 1644 cm^{-1} (for H_3pym), see Figures 5.8–5.10. Noticeably, these vibrations are found at significantly lower frequencies in the IR spectra of the respective metal complexes, *viz.* 1635 cm^{-1} for **1**, 1615 cm^{-1} for **2** and 1605 cm^{-1} for **3**, consistent with metal-to-ligand back-donation of electron density into π* molecular orbitals involving the C=N groups, which partly reduces the C=N bond order and thus stretching frequency of the C=N group relative to the free ligand. The intense stretching modes of the Ru–P bonds, υ(Ru-PPh_3) for **1** and **2** are found at 698 cm^{-1} and 692 cm^{-1}, respectively. Interestingly in **1**, the C–O–C ether group vibrations of the uncoordinated thp moieties vibrate at identical frequencies to those of the free ligand, thppy [ν(O-C-O) = 1081 cm^{-1} and 1134 cm^{-1}]. This reflects the fact that no interaction between the thp groups and metal atom exists. In contrast for **2**, the broad C–O–C ether group vibration (1131 cm^{-1}) of the free ligand, chb appears as a medium-intensity split vibration [at 1159 cm^{-1} and 1143 cm^{-1}] in the IR spectrum of the metal complex. The absence of the pyrrole N-H vibrations in the IR spectrum of **3** reflects deprotonation of the pyrrole rings and their coordination to the ruthenium(III) centre. For the remaining coordination sphere bonds, the Ru-N vibrational modes of the metal complexes are comparable with one another while the Ru-O vibrational mode of **3** appears at a frequency of 455 cm^{-1}.

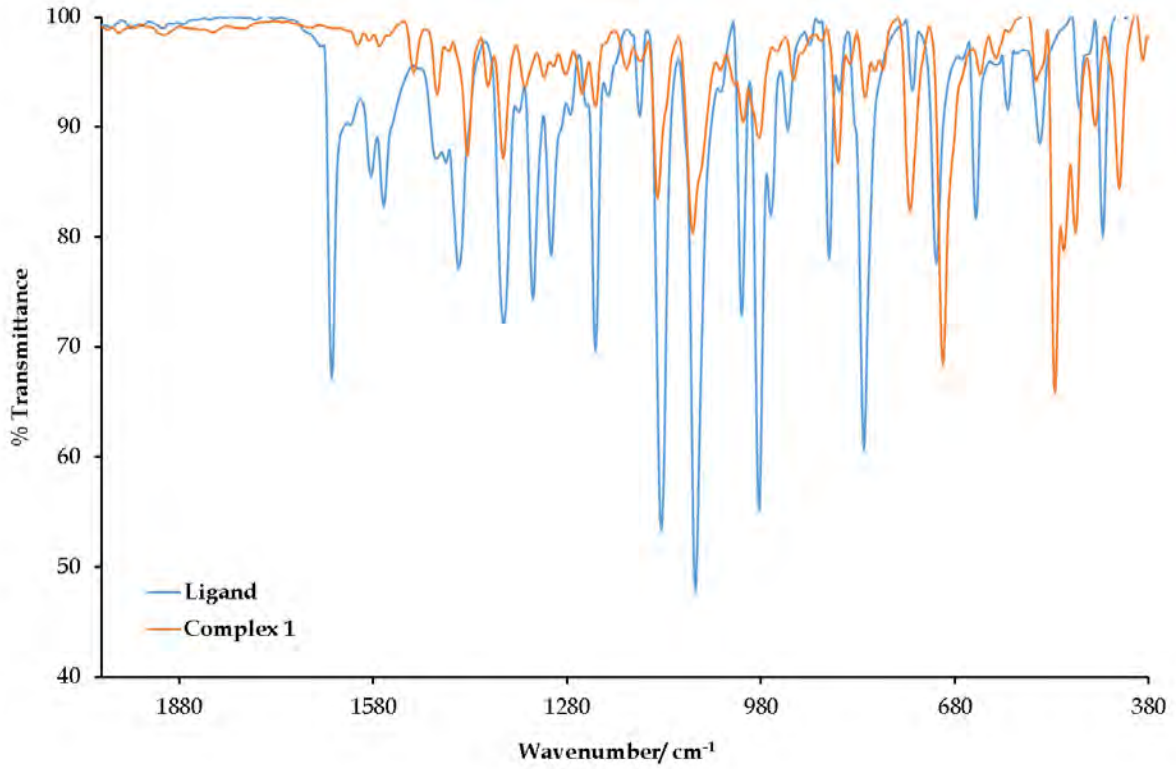

Figure 5.8: *Overlay IR spectra of complex **1** and its free-ligand, thppy.*

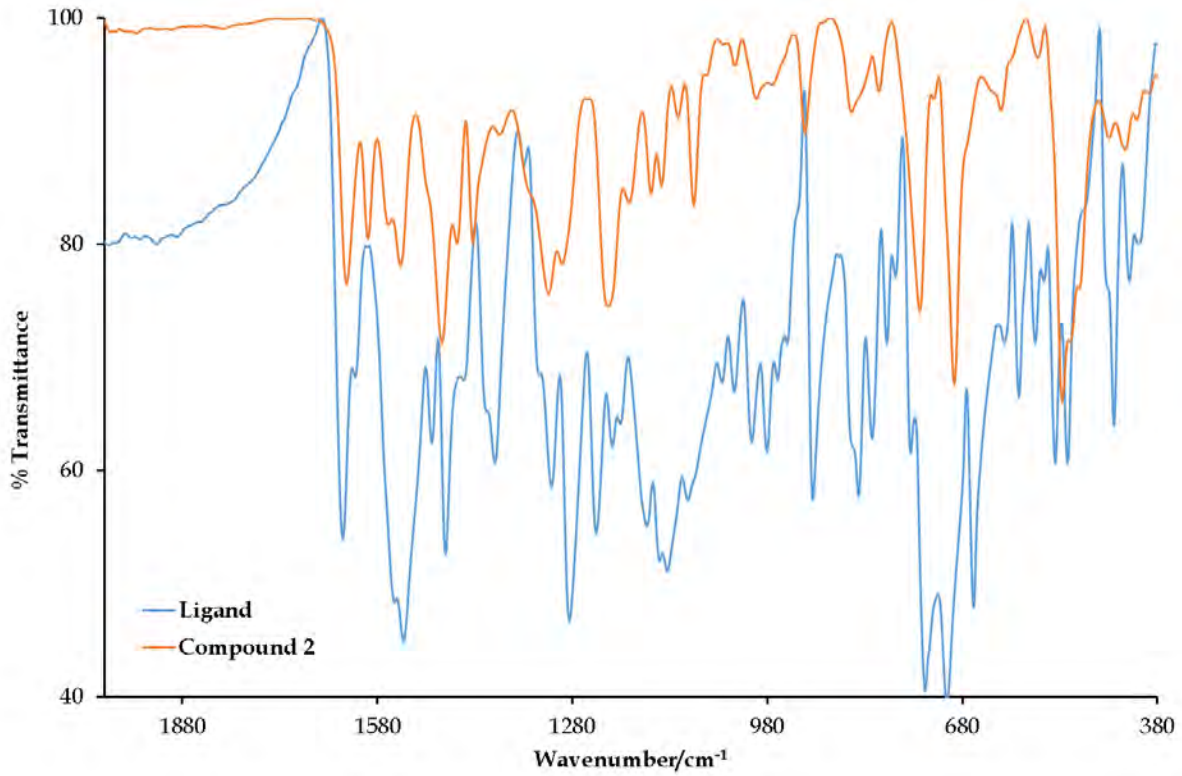

Figure 5.9: *Overlay IR spectra of compound **2** and its free-ligand, chb.*

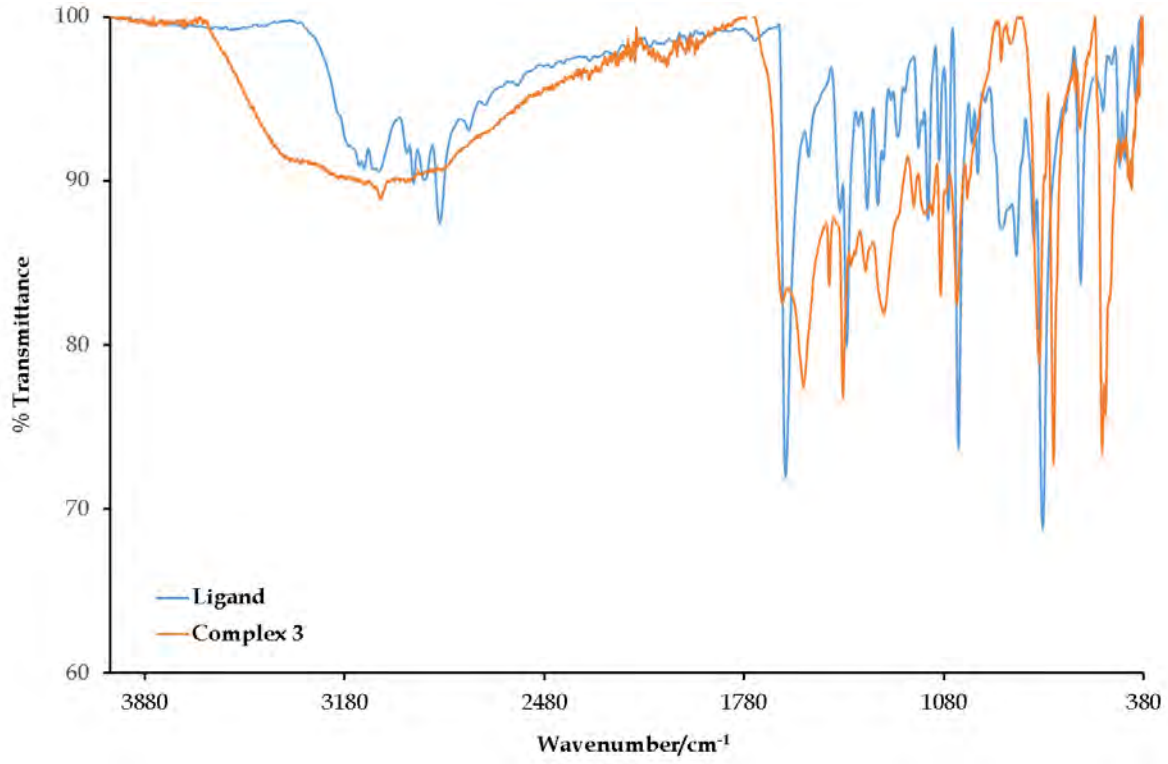

Figure 5.10: *Overlay IR spectra of complex* ***3*** *and its free-ligand, H_3pym.*

The UV-Vis spectral analysis reveals that several common intraligand π-π^* electronic transitions are shared among the free ligands and their respective metal complexes, see Figures 5.11–5.13. Furthermore, metal-to-ligand charge transfer (MLCT) bands at 461 nm and 571 nm for **1** are observed and despite its d^6 low-spin electron configuration, a metal-based (at 688 nm) electronic transition with a low extinction coefficient is observed. However, for the paramagnetic ruthenium(III) compounds, only a weak *d-d* transition for **2** is observed at 723 nm. The absence of the metal-based electronic transition of **3** is ascribed to a higher band-gap energy, whereas in **1**, a narrow band-gap energy makes the *d-d* electronic transition favourable [**29**].

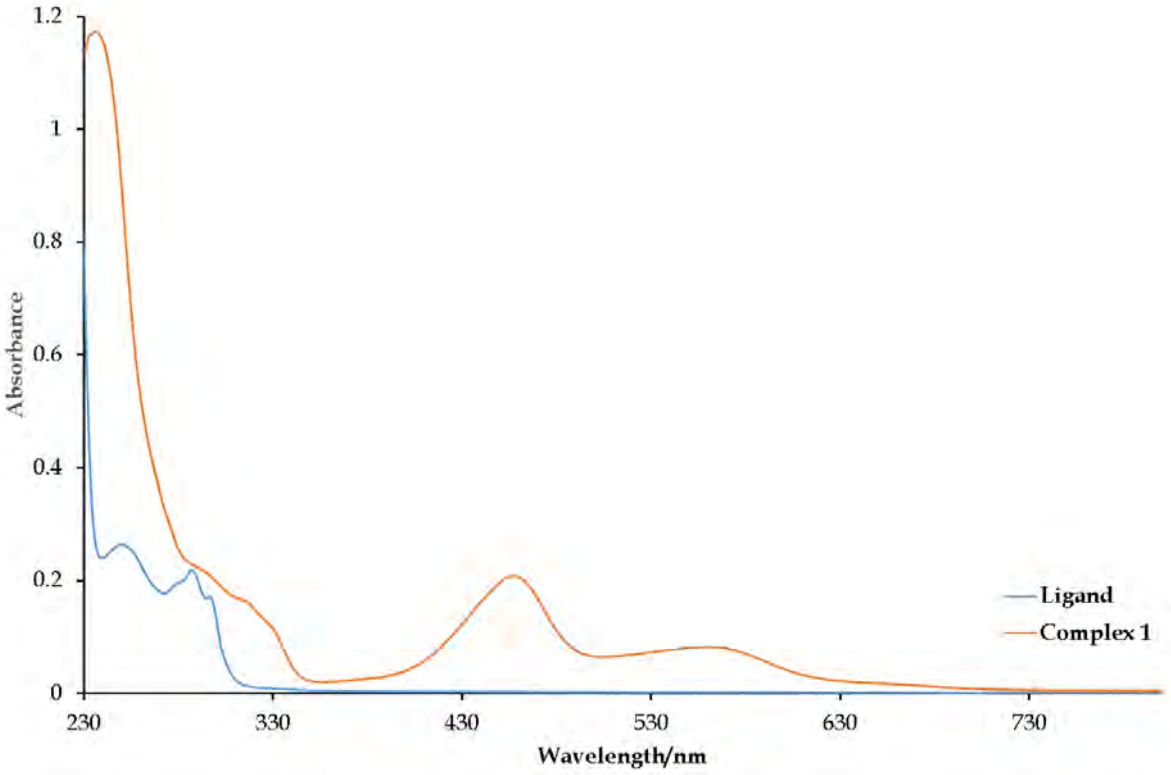

Figure 5.11: *Overlay UV-Vis spectra of complex* ***1*** *and its free-ligand, thppy.*

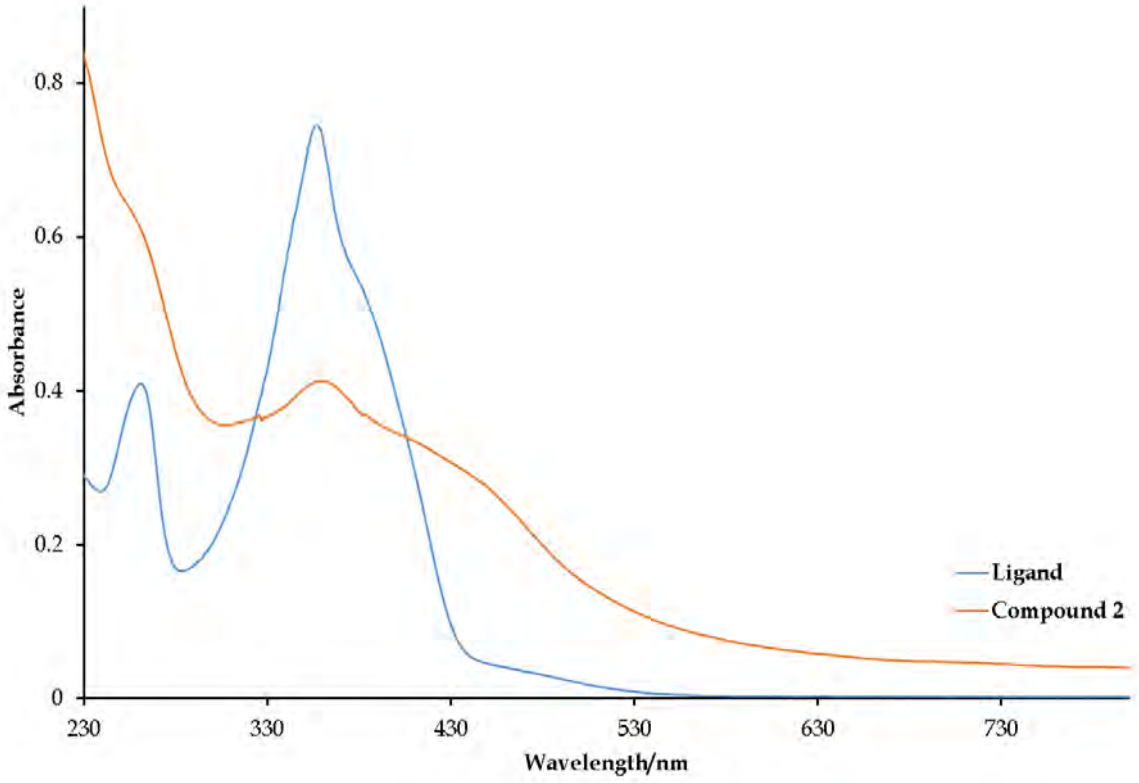

Figure 5.12: *Overlay UV-Vis spectra of compound* **2** *and its free-ligand, chb.*

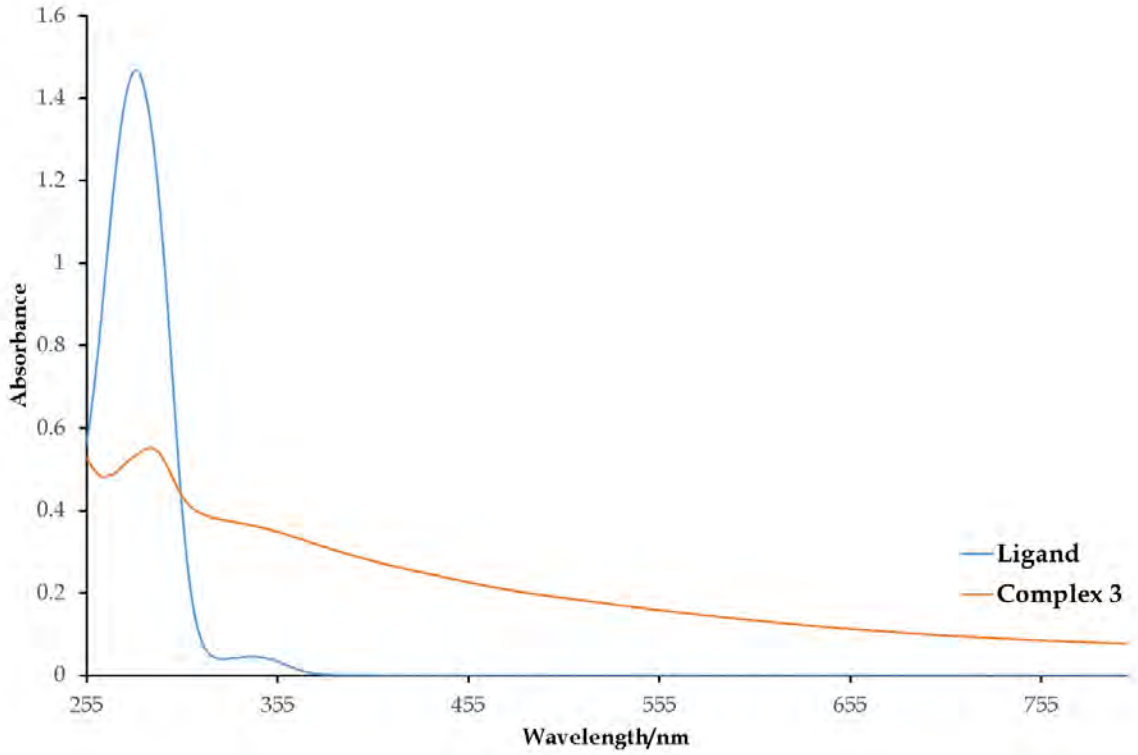

Figure 5.13: *Overlay UV-Vis spectra of complex* ***3*** *and its free-ligand, H_3pym.*

5.4.2 Voltammetry Analysis

Firstly, the voltammetric analysis of **3** was conducted in a 1:1 (*v:v*) solvent mixture of DMSO and CH_3CN since this complex is insoluble in DCM. Noteworthy for **3**, the use of coordinative solvents can potentially influence the redox behaviour of **3** as solvents such as DMF and DMSO typically induces axial coordination of metallophthalocyanines and in the process renders metal-based redox processes during voltammetry analysis [**30**]. The redox behaviours of **1** and **2** in the non-coordinating solvent, DCM shows one and two redox couples in their cyclic voltammograms (CVs), respectively (see Figures 5.14 and 5.15). All these redox couples are quasi-reversible as their peak-to-peak separations (ΔE) are different [ΔE(**1**) = 150 mV, ΔE(**2-A**) = 81 mV and ΔE(**2-B**) = 80 mV] to that of the ferrocene standard [ΔE(ferrocene-DCM) = 90 mV *vs* Ag|AgCl] under the same experimental conditions. The redox couples exhibits diffusion-controlled behaviour at increasing scan rates and have peak current ratios approaching one which suggests that each redox process correspond to

a one electron redox process. The single quasi-reversible redox couples observed in the CVs of **1** and **3** [ΔE(**3**) = 110 mV against the ΔE(ferrocene-mixture)= 100 mV] are consistent with the Ru(II/III) redox process as the halfwave potentials [$E_{½}$(**1**) = 0.625 V and $E_{½}$(**3**) = -0.755 V *vs* Ag|AgCl] compare favourably with other ruthenium(II) and –(III) complexes where the voltammetric studies have been conducted in either coordinating or non-coordinating solvents [**11**, **29**, **31**]. Compound **2** mimics the redox behaviour of the dinuclear (μ-Cl)$_2$[Ru^{III}Cl(Hchpr)(PPh$_3$)]$_2$ (H_2chpr = 2-amino-3-((tetrahydro-2*H*-pyran-4-ylimino)methyl)-4*H*-chromen-4-one) with the Ru(II/III) [$E_{½}$ = -0.143 V *vs* Ag|AgCl] and Ru(III/IV) [$E_{½}$ = 0.158 V *vs* Ag|AgCl] redox couples denoted as **A** and **B** in Figure 5.15[**13**].

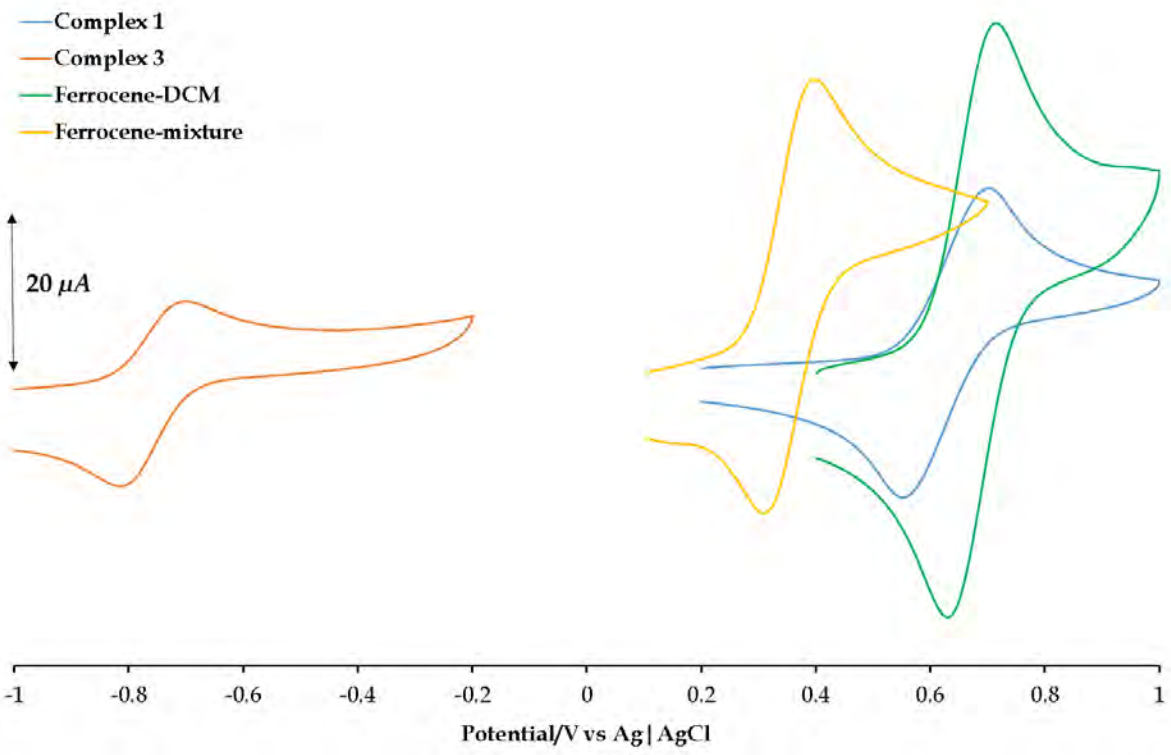

Figure 5.14: *Cyclic voltammograms (CVs) of **1** and **3** as well as their corresponding ferrocence standards at a scan rate of 100 mV/s conducted in DCM (viz. Ferrocene-DCM) and the DMSO:CH_3CN mixture (viz. Ferrocene-mixture).*

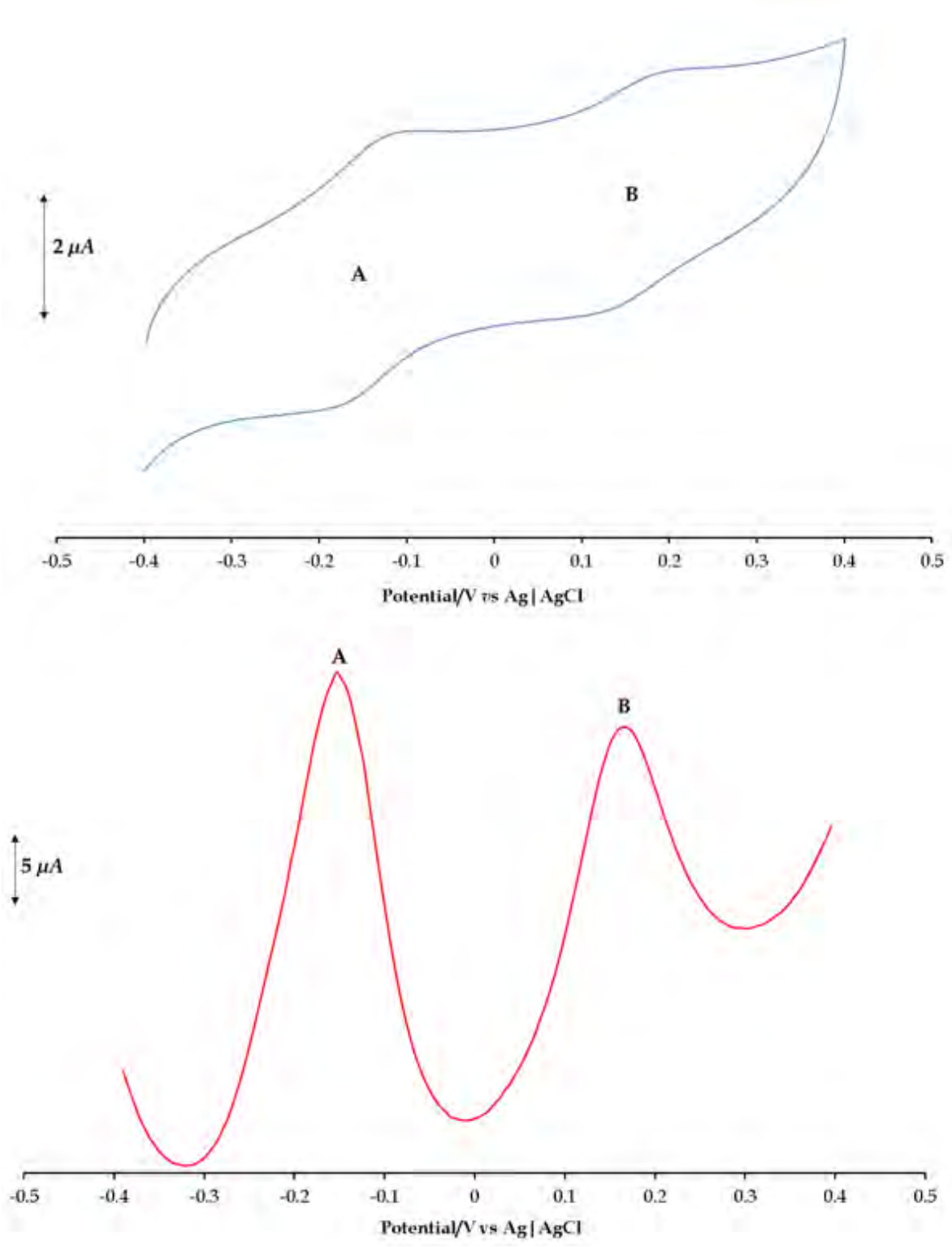

Figure 5.15: *CV (Top) at 200 mV/s and SWV (Bottom) of the dinuclear compound* **2**.

5.4.3 *Radical Scavenging Studies*

Abnormally high concentrations of free radicals in the human body are associated with oxidative stress and nitrosamination processes which can potentially lead to an array of cancers, Alzheimer's disease and cardiovascular ailments [**32-34**]. Current trends entail exploring the radical scavenging capabilities of ruthenium compounds as an alternative to the natural antioxidant, vitamin C and organic-based synthetic radical scavengers (*e.g.* butylated hydroxyl toluene (BHT)). The attractive attribute of these metal-based compounds is the easily interconverted oxidation states of ruthenium which makes them effective scavengers of free radicals. More specifically, the radical scavenging capabilities of ruthenium complexes can be induced either by the donation of an electron or a hydrogen from hydrocarbon co-ligands of the ruthenium complexes [**35-37**]. Furthermore, as the biologically significant components (*viz.* tetrahydropyran in **1**, chromone in **2** and pyrrole in **3**) are known antioxidants, the presence of these moeities can potentially enhance the radical scavenging capabilities of the formulated metallic compounds **1** - **3**.

The influence of the redox active metal centre is clearly noted with an increase in the radical scavenging activity of the metal complexes in comparison to the free ligand. Most notabaly is the NO radical scavenging activity of compound **2** [IC_{50}(NO) = 143 μM] versus thppy [IC_{50}(NO) = 308 μM], refer to Table 5.1. Furthermore, predominately all the metal complexes have lower IC_{50} values than the natural antioxidant, vitamin C [IC_{50}(NO) = 210 μM and IC_{50}(DPPH) = 147 μM], with the exception of **1** (for NO) and **3** (for DPPH) [**38**, **39**]. As mentioned before, the dinuclear compound, $(\mu\text{-Cl})_2[Ru^{III}Cl(Hchpr)(PPh_3)]_2$ exhibits similar redox behaviour as metal complex **2** and their resemblance is also reflected in their similar radical scavenging capabilities towards the DPPH radical [**13**]. In addition, the chromone-derived Schiff base neutralizes the NO and DPPH radicals more effectively compared with vitamin C while the thppy free-ligand has comparable DPPH radical scavenging capabilities to vitamin C.

Table 5.1: *IC_{50} values (in μM) of the metal complexes and their free-ligands. Each IC_{50} value has a standard deviation less than 8% with respect to its mean value.*

	NO	**DPPH**
1	231	44
2	143	87
3	151	194
thppy	527	54
chb	199	118
H_3pym	308	289

5.4.4 Crystallographic studies

Complex **1** co-crystallizes with a water molecule of recrystallization in the space group $P2_1/n$. Each monoclinic unit cell contains four molecules of **1**·H_2O and the crystal lattice is stabilized by a network of hydrogen-bonding occurring between **1**·H_2O dimers in which the water molecules bridge the complexes by hydrogen bonds involving the coordinated chloride ions, see Figure 5.16. Within each dimer, these hydrogen-bonding interactions induce the formation of an intermolecular 4-membered ring [Cl2···H1S-O3/ Cl2A···H1SA-O3A = 2.25(3) Å and Cl2A···H2S-O3/ Cl2···H2SA-O3A = 2.30(3) Å]. Furthermore, an intramolecular ring···ring π-type interaction occurs between the nearly co-planar pyridyl moiety and the C19-C24 phenyl ring of the PPh_3 co-ligand (centroid···centroid distance, 3.511 Å, see Figure 5.17).

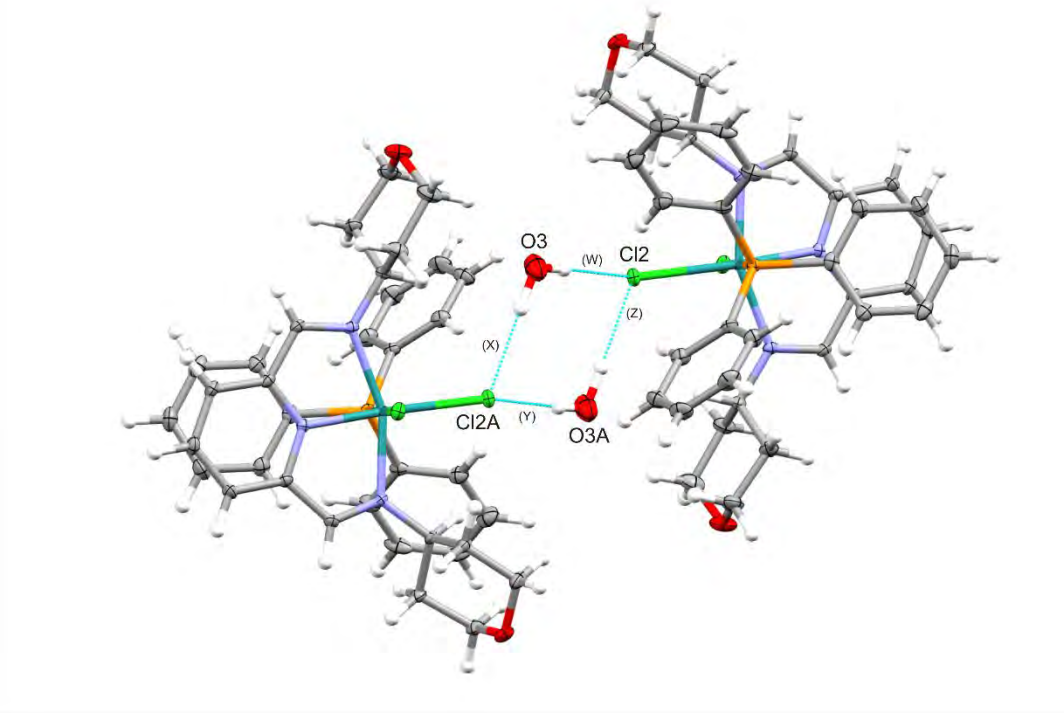

Figure 5.16: *A perspective view of the dimer of* ***1***.H_2O *formed by a series of hydrogen bonding interactions: Cl2···H1S-O3* ***(W)****/ Cl2A···H1SA-O3A* ***(Y)*** *= 2.25(3) Å and Cl2A···H2S-O3* ***(X)****/ Cl2···H2SA-O3A* ***(Z)*** *= 2.30(3) Å.*

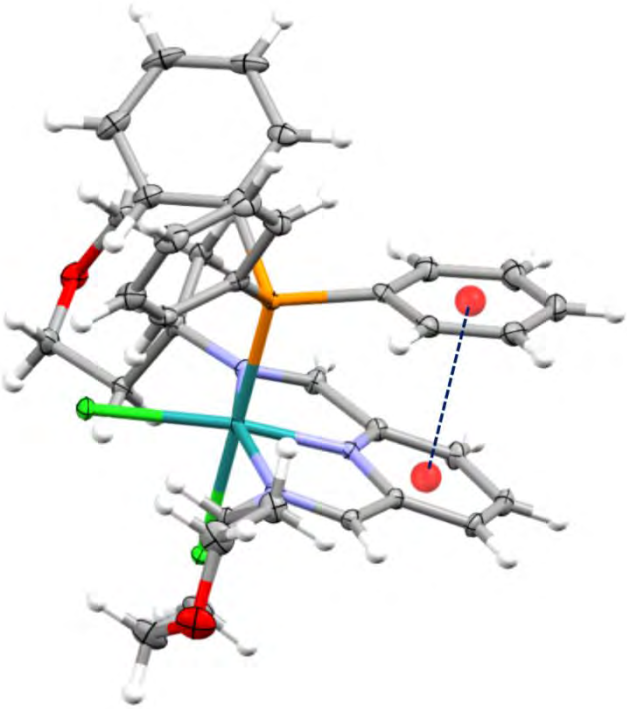

Figure 5.17: *A perspective view of* ***1*** *showing the nearly co-planar pyridyl moiety and the C19-C24 phenyl ring of the* PPh_3 *co-ligand.*

The crystal lattice of **2** is made up of concentric columns of **2** which run parallel both to the [*a*]- and [*b*]-axes. This arrangement of the molecules is conferred *via* intermolecular interactions between co-planar phenyl rings of the PPh_3 co-ligands and the annealed phenyl rings of the chromone with a distance of 3.798 Å, see Figure 5.18. An example is the interaction of the C45-C50 phenyl ring of the $P(2)Ph_3$ of **2** with respect to the C1-C5C9 ring of a chromone moiety of an adjacent molecule and the interaction between the C27-C32 phenyl ring of the triphenylphosphine co-ligand and the C18-C22C26 ring of the chromone moiety of a neighbouring molecule. The larger unit cell dimension of 3 allows sixteen molecules of **3** to pack in its cubic unit cell.

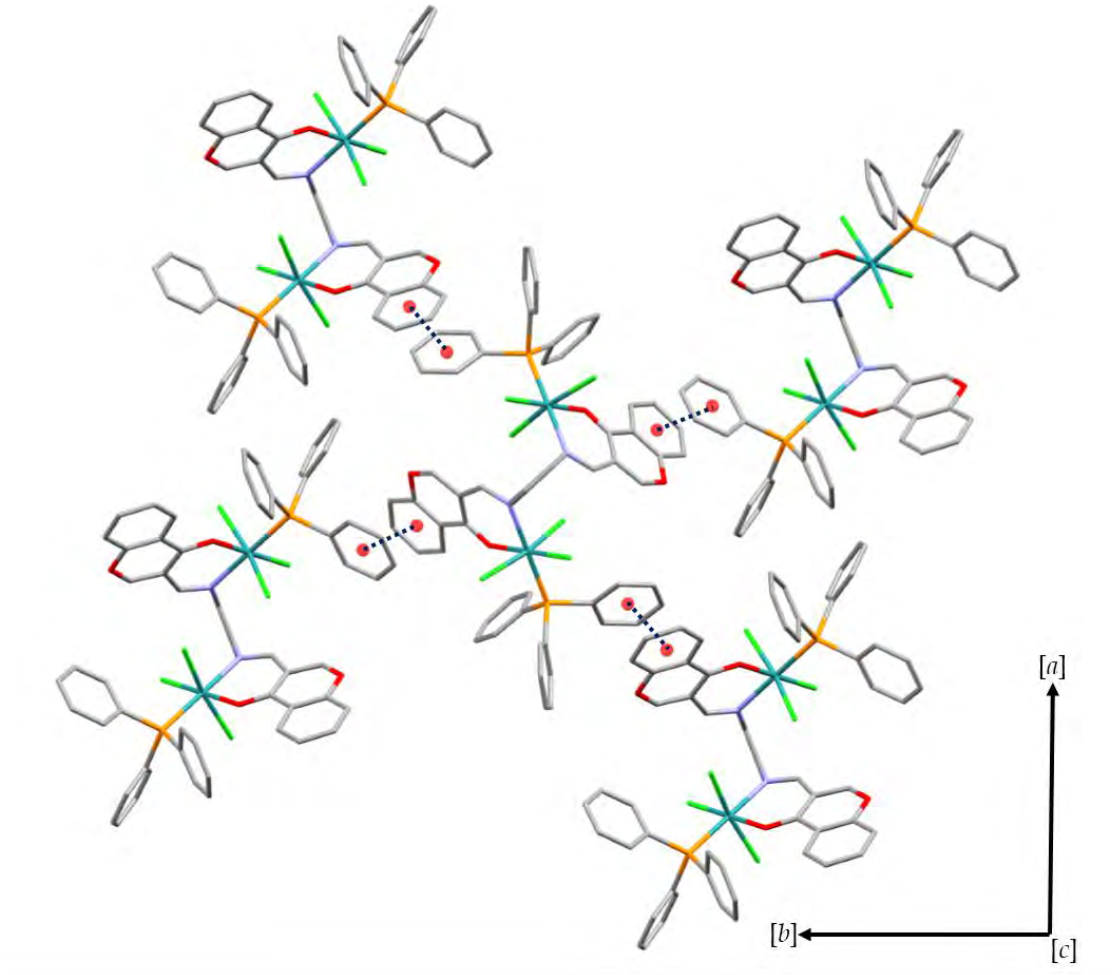

Figure 5.18: *A perspective view of* **2** *along the [a] and [b] axes illustrating the intramolecular interactions between the adjacent molecules.*

Although the bridging phenyl moiety (of the chb chelator in **2**) lies out of the planes of the chromone moieties by 88.20˚ and these moieties also form a dihedral angle of 65.31˚, the geometrical parameters around each metal centre in **2** are identical. Thus, the bond angles around the Ru1 atom will only be discussed. The octahedral coordination sphere of the metallic compounds are distorted as evidenced by the non-perpendicular bite angles [N1-Ru-N2 = 78.71(6)˚ and N2-Ru-N3 = 78.73(6)˚ for **1**, O1-Ru1-N1 = 89.5(1)˚ for **2** and $N_{pyrrole}$-Ru-N_{imino} = 77.94(8)˚ and N_{imino}-Ru-N_{imino} = 100.32(9)˚ for **3**] (see Figures 5.19 – 5.21). This deviation from octahedral coordination is emphasized further by the deviation from linearity of the equatorial bond angles for **1** [N2-Ru-Cl2 = 170.09(4)˚ and N1-Ru-N3 = 157.42(6)˚], the axial bond angle for **2** [Cl2-Ru1-Cl3 = 167.60(5)˚] as well as the $N_{pyrrole}$-Ru-N_{imino} bond angles of 172.37(9)˚ for **3**.

Surprisingly in **1**,the Ru-N_{imino} bond distances [Ru-N1 = 2.061(2) Å and Ru-N3 = 2.090(2) Å] are not equidistant; this is accompanied by commensurate differences for the opposing C=N-C bond angles [C6-N1-C3 = 121.2(1)˚ and C12-N3-C16 = 118.5(1)˚]. The anomalies in the above geometrical parameters probably reflect minor differences in the positions of the thppy moieties in three dimensional space. The Ru-N_{imino} bond length is considerably longer in the paramagnetic ruthenium compound **2** [Ru-N_{imino} =2.159(4) Å] due to their higher Lewis acid character of its metal atom compared to the diamagnetic character of **1**. As expected, the same trend is found when comparing the Ru-P [2.3099(5) Å for **1** and Ru1-P1 = 2.330(1) Å for **2**] and Ru-Cl [Ru-Cl1 = 2.4324(5) Å and Ru-Cl2 = 2.4707(5) Å for **1**; Ru1-Cl1 = 2.324(1) Å, Ru1-Cl2 = 2.332(1) Å and Ru1-Cl3 = 2.355(1) Å for **2**] coordination sphere bonds.The variable *trans*-influences of the N2 and P atoms effective on the chloro co-ligands accounts for the differences in the Ru-Cl bond distances of **1** whereasthe meridonally-arranged chloro co-ligands in **2** have comparable bond lengths to other metallic compounds containing the *mer*-$[RuCl_3]^{3+}$ core [**40-42**].However in **3**, due to the presence of the non-delocalized bridging aliphatic amine moiety, its Ru-N_{imino} bond distances of 2.070(2) Å are shorter than those of **2**. Also, the identical Ru-$N_{pyrrole}$ [2.049(2) Å] bond lengths of **3** were in the range [2.037(6)-2.082(9) Å] found for other ruthenium to monoanionic pyrrole nitrogen bonds [**43-46**].

The bond orders of the carbonyl-like C8-O1/C25-O3 double bonds of **2** are clearly established based on their shorter bond distances [1.251(5) Å] in comparison with the ether-type C–O bonds [O2-C6/O4-C23 = 1.333(7) Å and O2-C5/O4-C22 = 1.373(6) Å]; in effect, these bonds are in their ketonic forms. In support of the aforementioned deduction, the Ru-$O_{ketonic}$ bond distance [2.083(3) Å] differs clearly from the literature-based Ru^{III}-$O_{phenolate}$bond distances as seenin *trans*-[Ru(L)Cl(PPh_3)$_2$] [1.9906(15) Å] (H_2L = 2-hydroxy-1-naphthaldehyde-benzoylhydrazone), [Ru(pyhz)$_2$]ClO_4 [1.971(2)Å] (Hpyhz = 2-((2-(pyridin-2-yl)hydrazono)methyl)phenol) and [Ru(pzpo)(acac)] (H_2pzpo = 1,2-*bis*(2-(1-methyl-1*H*-pyrazol-3-yl)phenol)benzene) [1.983(3) Å and 2.008(3) Å] [**47-49**].

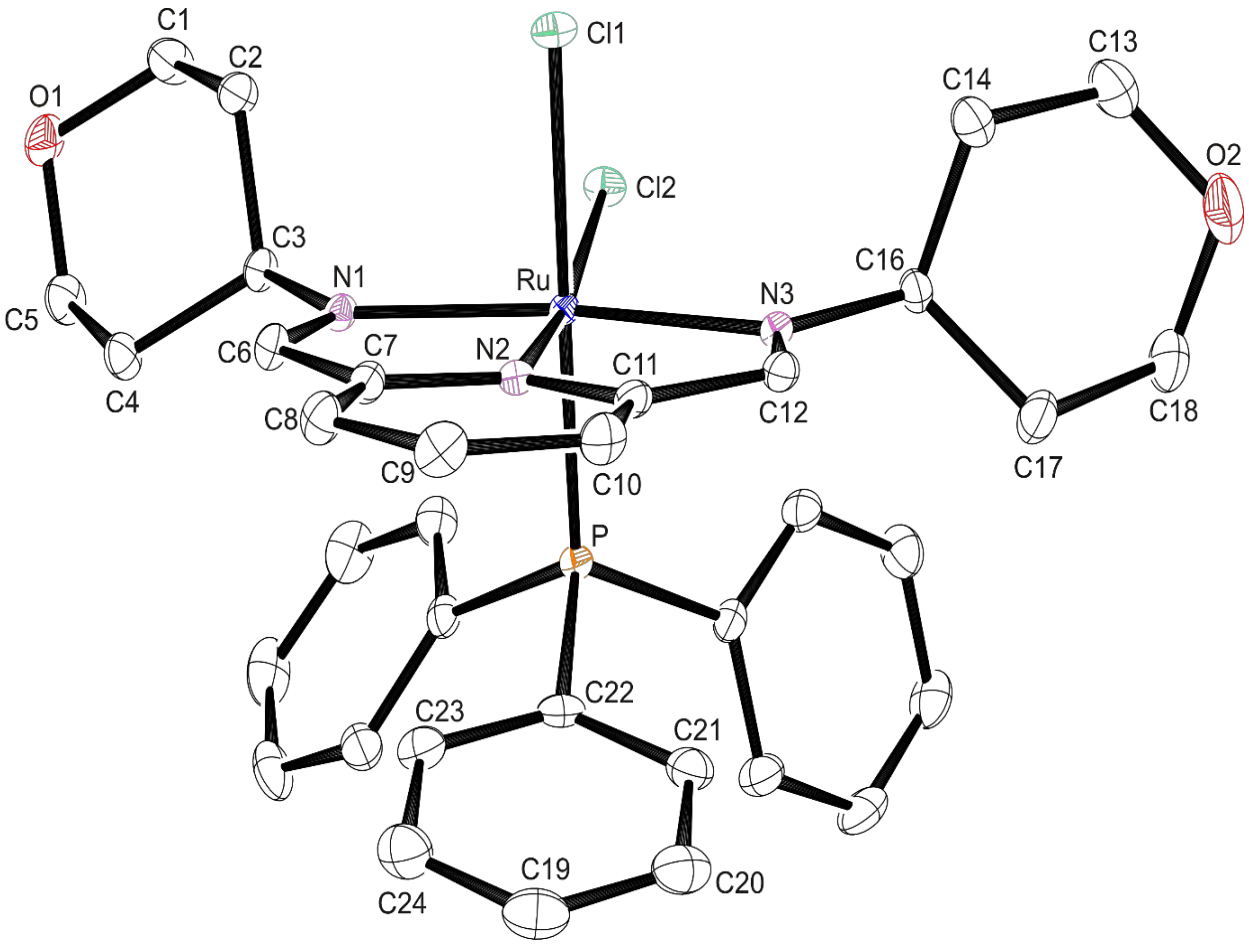

Figure 5.19: *An ORTEP view of complex* ***1*** *showing 50 % probability displacement ellipsoids and the atom labelling. The hydrogen atoms and water molecule of crystallization were omitted for clarity.*

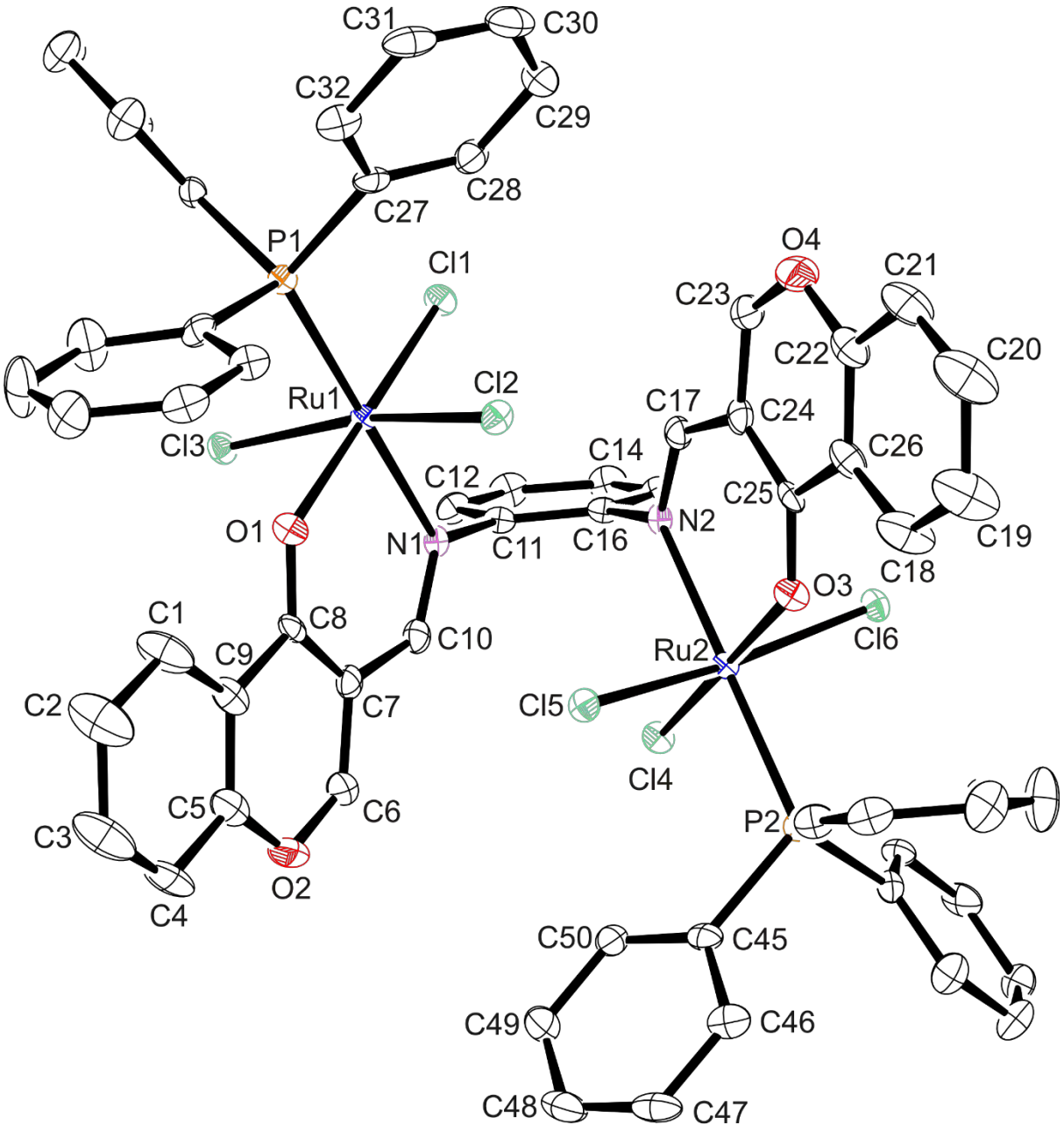

Figure 5.20: *An ORTEP view of compound* **2** *showing 50 % probability displacement ellipsoids and the atom labelling. The hydrogen atoms and ethanol molecule of crystallization were omitted for clarity.*

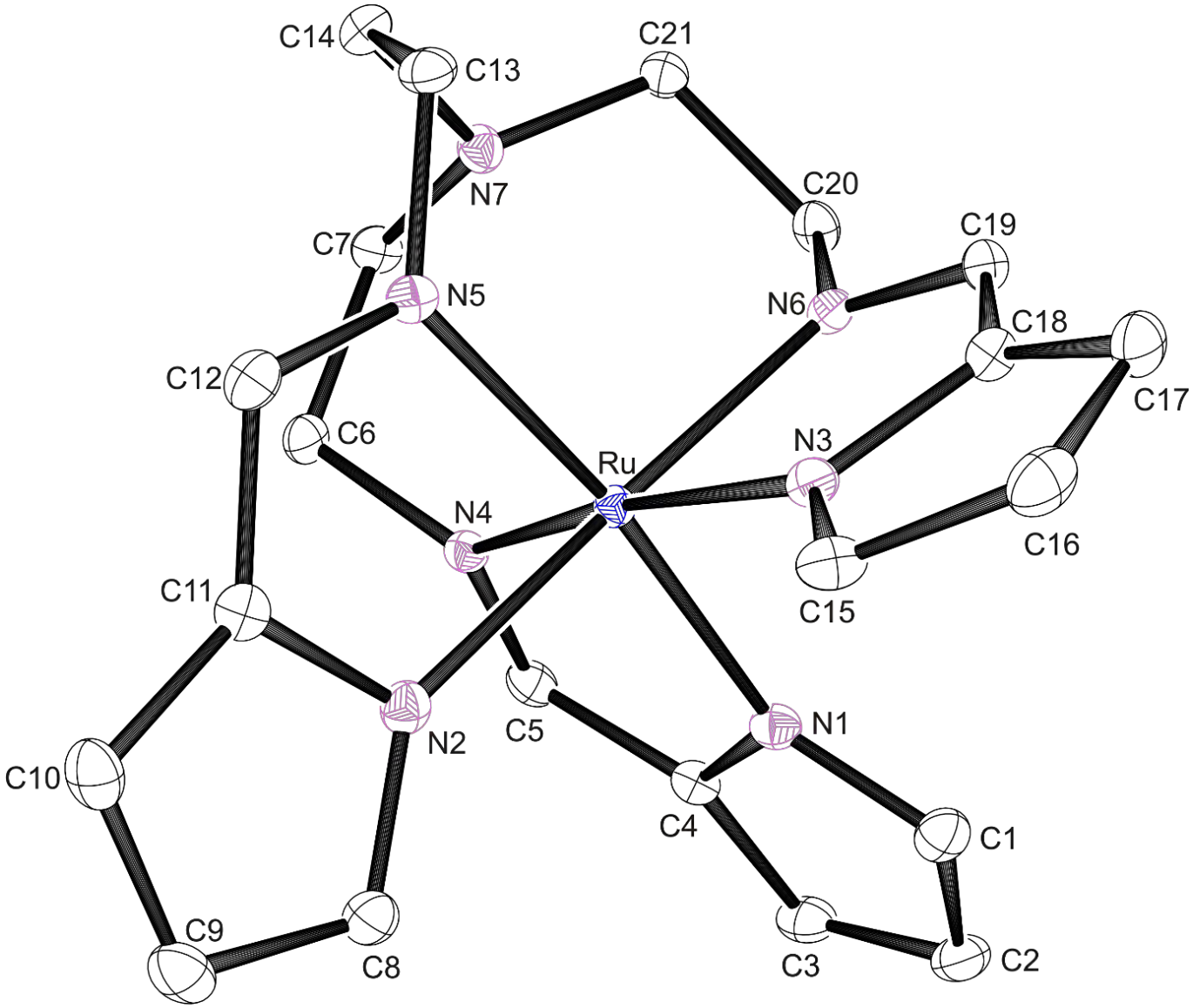

Figure 5.21: *An ORTEP view of complex* ***3*** *showing 50 % probability displacement ellipsoids and the atom labelling. The hydrogen atoms were omitted for clarity.*

Table 5.2: *Crystal data and structure refinement data.*

	1.H_2O	**2**.CH_3CN	**3**
Chemical formula	$C_{35}H_{40}Cl_2N_3O_3PRu$	$C_{66}H_{52}Cl_6N_4O_4P_2Ru_2$	$C_{21}H_{24}N_7Ru$
Formula weight	753.64	1441.92	475.54
Temperature (K)	100(2)	100(2)	100(2)
Crystal system	Monoclinic	Orthorhombic	Cubic
Space group	$P2_1/n$	$P2_12_12$	$I\text{-}43d$
Unit cell dimensions (Å, °)	a = 15.1098(5)	a = 16.168(1)	a = 19.9699(7)
	b = 13.5262(5)	b = 20.6678(13)	b = 19.9699(7)
	c = 16.6804(6)	c = 9.2012(6)	c = 19.9699(7)
	α = 90	α = 90	α = 90
	β = 97.080(2)	β = 90	β = 90
	γ = 90	γ = 90	γ = 90
V(Å^3)	3383.1(2)	3074.6(3)	7963.9(8)
Z	4	2	16
Density (calc.) (Mg/m^3)	1.480	1.577	1.586
Absorption coefficient (mm^{-1})	0.708	0.857	0.810
F(000)	1522	1456	3888
θ range for data collection (deg)	1.7; 27.1	1.60; 26.00	2.50; 30.01
Reflections measured	22561	11872	13549
Observed reflections [I>2σ(I)]	6565	5479	1804
Independent reflections	7443	5863	1913
Data/Restraints/parameters	7443/2/414	5863/1/384	1913/0/88
Goodness of fit on F^2	1.022	1.091	1.061
Observed R, wR^2	0.025; 0.060	0.031; 0.076	0.024; 0.0487
R_{int}	0.026	0.022	0.043

Table 5.3: *Selected bond lengths [Å] and bond angles [°] for* ***1****.*

N1-Ru-N2	78.71(6)
N2-Ru-N3	78.73(6)
N2-Ru-Cl2	170.09(4)
N1-Ru-N3	157.42(6)
C6-N1-C3	121.2(1)
C12-N3-C16	118.5(1)
Ru-N1	2.061(2)
Ru-N3	2.090(2)
Ru-P1	2.3099(5)
Ru-Cl1	2.4324(5)
Ru-Cl2	2.4707(5)

Table 5.4: *Selected bond lengths [Å] and bond angles [°] for* ***2****.*

O1-Ru1-N1	89.5(1)
Cl2-Ru1-Cl3	167.60(5)
Ru1-N1	2.159(4)
Ru1-P1	2.330(1)
Ru1-Cl1	2.324(1)
Ru1-Cl2	2.332(1)
Ru1-Cl3	2.355(1)
Ru1-O1	2.083(3)
C8-O1/C25-O3	1.251(5)
C6-O2/C25-O4	1.333(7)
C5-O2/C22-O4	1.373(6)

Table 5.5: *Selected bond lengths [Å] and bond angles [°] for* ***3****.*

*$N_{pyrrole}$-Ru-N_{imino}	77.94(8)
N_{imino}-Ru-N_{imino}	100.32(9)
$N_{pyrrole}$-Ru-N_{imino}	172.37(9)
Ru-N_{imino}	2.070(2)
Ru-$N_{pyrrole}$	2.049(2)

bite angles

5.5 References

[1] D. Gambino, L. Otero, *Inorg. Chim. Acta*, 2012, **393**, 103.

[2] A.K. Singh, D.S. Pandey, Q. Xua, P. Braunstein, *Coord. Chem. Rev*., 2014, **270–271**, 31.

[3] A. Bergamo, C. Gaiddon, J.H.M. Schellens, J.H. Beijnen, G. Sava, *J. Inorg. Biochem*., 2012, **106**, 90.

[4] F. Li, J.G. Collins, F.R. Keene, *Chem. Soc. Rev*., 2015, **44**, 2529.

[5] T. Rawling, A. McDonagh, *Coord. Chem. Rev*., 2007, **251**, 1128.

[6] Q. Sun, S. Mosquera-Vazquez, Y. Suffren, J. Hankache, N. Amstutz, L.M.L. Daku, E. Vauthey, A. Hauser, *Coord. Chem. Rev*., 2015, **282–283**, 87.

[7] K. Ypsilantis, S. Karkabounas, E. Georgiou, I. Zelovitis, A. Garoufis, *Inorg. Chim. Acta*, 2014, **421**, 152.

[8] S.M. Cloonan, R.B.P. Elmes, M.L. Erby, S.A. Bright, F.E. Poynton, D.E. Nolan, S.J. Quinn, T. Gunnlaugsson, D.C. Williams, *J. Med. Chem*., 2015, **58**, 4494.

[9] D. Sun, Y. Liu, Q. Yu, D. Liu, Y. Zhou, J. Liu, *J. Inorg. Biochem.*, 2015, http://dx.doi.org/10.1016/j.jinorgbio.2015.04.003.

[10] S. Wanninger, V. Lorenz, A. Subhan, F.T. Edelmann, *Chem. Soc. Rev*., 2015, **44**, 4986.

[11] I.N. Booysen, S. Maikoo, M.P. Akerman, B. Xulu, *Polyhedron*, 2014,**79**, 250.

[12] I.N. Booysen, A. Adebisi, O.Q. Munro, B. Xulu, *Polyhedron*, 2014,**73**, 1.

[13] I.N. Booysen, A. Adebisi, M.P. Akerman, *Inorg. Chim. Acta*, 2015, **433**, 13.

[14] I.N. Booysen, S. Maikoo, M.P. Akerman, B. Xulu, O. Munro, *J. Coord. Chem*., 2013, **66**, 3673.

[15] N. Phosrithong, J. Ungwitayatorn, *Bioorg. Chem*., 2013, **49**, 9.

[16] M.N. Narule, M.K. Gaidhane, P.K. Gaidhane, *J. Pharm. Res.*, 2013, **6**, 626.

[17] Y. Wang, T. Liang, J. Yao, T.Zhai, H. Fu, *Acta Crystallogr.,Sect. E: Struct. Rep. Online,* 2008, **E64**, 629.

[18] Bruker APEX2, SAINT and SADABS. Bruker AXS Inc., 2010, Madison, Wisconsin, USA.

[19] R.H. Blessing, *Acta Crystallogr.,Sect. A: Found. Crystallogr.,* 1995, **A51**, 33.

[20] G.M. Sheldrick, *Acta Crystallogr.,Sect. A: Found. Crystallogr.,* 2008, **A64**, 112.

[21] L.J. Farrugia, *J. Appl. Cryst.,*2012, **45**, 849.

[22] C. Tan, J. Liu, H. Li, W. Zheng, S. Shi, L. Chen, L. Ji, *J. Inorg. Biochem.*, 2008, **102**, 347.

[23] M.B. Cingi, M. Lanfranchi, M.A. Pellinghelli, M. Tegoni, *Eur. J. Inorg. Chem*., 2008, 703.

[24] S. Mandala, D.K. Seth, P. Gupta, *Polyhedron*, 2012, **31**, 167.

[25] B.C.E. Makhubela, M. Meyer, G.S. Smith, *J. Organomet. Chem.,* 2014, **772–773**, 229.

[26] N.G. Tsierkezos, A.I. Philippopoulos, *Inorg. Chim. Acta*, 2009, **362**, 3079.

[27] C.P. Matos, A. Valente, F. Marques, P. Adao, M.P. Robalo, R.F.M. de Almeida, J.C. Pessoa, I. Santos, M.H. Garcia, A.I. Tomaz, *Inorg. Chim. Acta,* 2013, **394**, 616.

[28] M.M. Subarkhan, R. Ramesh, *Spectrochim. Acta A,* 2015, **138**, 264.

[29] I.N. Booysen, S. Maikoo, M.P. Akerman, B. Xulu, *Trans. Met. Chem.*, 2015, **40**, 397.

[30] J.H. Zagal, F. Bedioui, J.P. Dodelet (Eds.). *N_4-Macrocyclic Metal Complexes*, Springer, New York (2006).

[31] P. Byabartta, S.K. Jasimuddin, G. Mostafa, T.-H. Lu, C. Sinha,*Polyhedron*, 2003, **22,** 849.

[32] G. Zengin, C. Sarikurkcu, A. Aktumsek, R. Ceylan, O. Ceylan, *Ind. Crop. Prod.*, 2014, **53**, 244.

[33] P. Anitha, N. Chitrapriya, Y. Jung Jang, P. Viswanathamurthi,*J. Photochem. Photobiol. B*, 2013, **129**, 17.

[34] M.C.F. Simoes, J.J.S. Sousa, A.A.C.C. Pais, *Cancer Lett.*, 2015, **357**, 8.

[35] T.S. Kamatchi, N. Chitrapriya, S.K. Kim, F.R. Fronczek, K. Natarajan, *Eur. J. Med. Chem.*, 2013, **59**, 253.

[36] T.S. Kamatchi, N. Chitrapriya, V.S. Jamal Ahamed, S. Moon, F.R. Fronczek, K. Natarajan, *Inorg. Chim. Acta*, 2013, **404**, 58.

[37] G. Prakash, R. Manikandan, P. Viswanathamurthi, K. Velmurugan, R. Nandhakumar, *J. Photochem. Photobiol. B*, 2014, **138**, 63.

[38] P. Krishnamoorthy, P. Sathyadevi, K. Senthilkumar, P. Thomas Muthiah, R. Ramesh, N. Dharmaraj, *Inorg. Chem. Commun.,* 2011, **14**, 1318.

[39] R. Ramachandran, P. Viswanathamurthi, *Spectrochim. Acta Part A*, 2013, **103**, 53.

[40] J.P. da Silva, F.R. Caetano, D.A. Cavarzan, F.D. Fagundes, L.L. Romualdo, J. Ellena, M. Jaworska, P. Lodowski, A. Barison, M.P. de Araujo,*Inorg. Chim. Acta*, 2011, **373**, 8.

[41] G. Tamasi, R. Cini,*J. Mol. Struct*., 2013, **1048**, 27.

[42] I. Turel, M. Pecanac, A. Golobic, E. Alessio, B. Serli, A. Bergamo, G. Sava, *J. Inorg. Biochem.*, 2004, **98**, 393.

[43] H. Brunner, T. Neuhierl, B. Nuber, *J. Organomet. Chem.,* 1998, **563**,173.

[44] H. Brunner, T. Neuhierl, B. Nuber, *Eur. J. Inorg. Chem.,* 1988, 1877.

[45] S.K. Patra, N. Sadhukhan, J.K. Bera, *Inorg. Chem.,* 2006, **45**, 4007.

[46] H. Brunner, R. Oeschey, B. Nuber, *Organometallics*, 1996, **15**, 3616.

[47] A. Kanchanadevi, R. Ramesh, N. Bhuvanesh, *J. Organomet. Chem.*, 2015, **788**, 49.

[48] K. Nagaraju, R. Raveendran, S. Pal, S. Pal, *Polyhedron*, 2012, **33**, 52.

[49] G.D. Frey, Z.R. Bell, J.C. Jeffery, M.D. Ward,*Polyhedron*, 2001, **20**, 3231.

Chapter 6

The isolation of new Ruthenium complexes with Lumazine derivatives: Structural, Electrochemical, Computational and Radical Scavenging Studies

6.1 Introduction

The exploration of ruthenium in medicinal inorganic chemistry is largely due to the discovery of NAMI-A, *trans*-[$RuCl_4$(DMSO)(Im)](ImH) {ImH = protonated imidazole} and KP1019 (*trans*-tetrachlorobis(indazole)ruthenate(III)) as potential metal-based anticancer drugs [**1**, **2**]. Their high cytoxicity towards metastatic tumours are accounted to the fact that ruthenium is a group congener of the essential element, iron and these first generation ruthenium chemotheraputic drugs share similar biodistribution patterns as iron [**3**, **4**]. However, more innovative drug design strategies are required to negate the common side effects associated with chemotherapy [**5**].

A current design strategy entails the use of scaffolds encompassing biologically significant moeities within the coordination sphere of ruthenium complexes [**6**]. These biologically significant moeities may promote the physiological biocompatability of the ruthenium complex and can also facilitate a target specific biodistribution towards tumours [**7**]. Hence the design of new target-specific ruthenium chemotherapeutic drugs provides scope for exploring the fundamental coordination chemistry of ruthenium towards biologically relevant ligand systems.

A plausible candidate as a biologically active moeity is lumazine which is a derivative of the enzyme, Lumazine synthase [**8**]. Lumazine synthase plays a pivotal role in the body through catalyzing the formation of Riboflavin (Vitamin B2) [**9**]. Deficiency of

riboflavin has been found to be associated with high tendencies of breast and cervical cancer occurences [**10**]. Moreover, one of the annealed ring systems of lumazine is a uracil which is a constituent of well-established chemotherapeutic drugs, uramustine and 5-fluoro-uracil [**11**]. In fact, demonstration of the coordination susceptibility of Schiff bases derived from 5, 6-diamino-1, 3-dimethyluracil towards ruthenium have been reported recently [**12**, **13**].

In this chapter, the isolation of new ruthenium complexes containing ligands derived from 6-acetyl-1,3,7-trimethyllumazine (almz) are reported. The coordination reactions using *trans*-[$RuCl_2(PPh_3)_3$] as the metal precursor yielded the diamagnetic ruthenium(II) complex, *cis*-[$RuCl_2$(bzlmz)(PPh_3)] (**1**) and paramagnetic ruthenium(III) complexes, *cis*-[$RuCl_2$(olmz)(PPh_3)] (**2**). The resultant metal complexes were spectroscopically characterized and structurally elucidated with single crystal X-ray analysis**.** In addition,the potentialantioxidant capabilities of these metal complexes were evaluated by means of radical scavenging studies with DPPH and NO radicals.

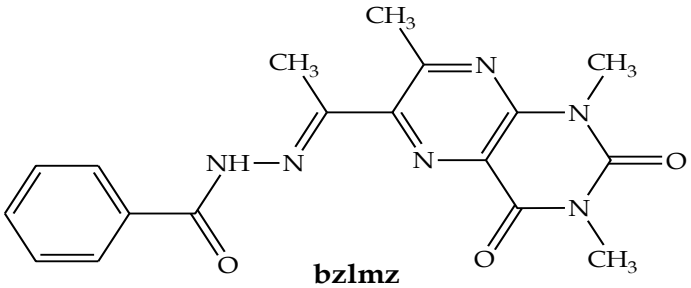

bzlmz

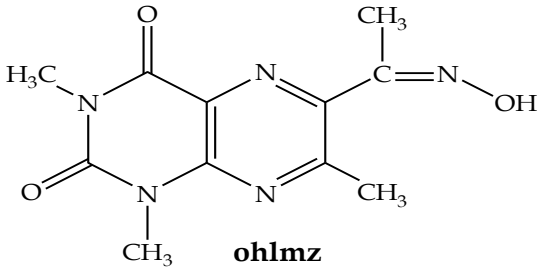

ohlmz

Figure 6.1: *Structures and abbreviations of the lumazine derivatives.*

6.2 Experimental

6.2.1 Synthesis of ligands:

6.2.1.1 6-acetyl-1,3,7-trimethyllumazine (almz)

The titled pro-ligandwas obtained from the reaction of 6-amino-1,3-dimethyl-5-nitrosouracil with acetylacetone as adapted from an experimental procedure attained from the literature [**14**].

6.2.1.2 N-1-[1,3,7-trimethyllumazine]benzohydride (bzlmz)

The synthetic procedure of the title compound was adopted and modified from a method previously reported [**15**]. The condensation reaction of benzohydrazide (0.11 g; 0.81 mmol) and 6-acetyl-1,3,7-trimethyllumazine(almz) (0.20 g; 0.81 mmol) was conducted in ethanol (20 cm^3). The resultant reaction mixture was heated until reflux for 6 hrs in the presence of a few drops of glacial acetic acid. A pale yellow solid formed which was filtered and washed with diethyl ether. Yield = 78%; M.P. = 258 - 260˚C; IR (ν_{max}/cm^{-1}): ν(N-H)$_{amide}$3226 (w), υ(C=O)$_{lumazine}$ 1694 (br, s), υ(C=O)$_{amide}$ 1652 (br, s), υ(C=N)$_{lumazine}$ 1547 (m), ν(C-N)$_{amide}$1268 (m); ^{1}H NMR (295K/ppm): 11.00 (s, 1H, *N6-H*), 9.36 (br, s, 2H, *H14, H18*), 7.72 – 7.40 (m, 3H, *H15*, *H16*, *H17*), 3.57 (s, 3H, *C8-H$_3$*), 2.82 (s, 3H, *N1-CH$_3$*), 2.65 (s, 3H, *N2-CH$_3$*),2.09 (s, 3H, *C11-H$_3$*); UV-Vis (DCM, (λ_{max} (ε, $M^{-1}cm^{-1}$))): 309 nm (17700); 351 nm (14400).

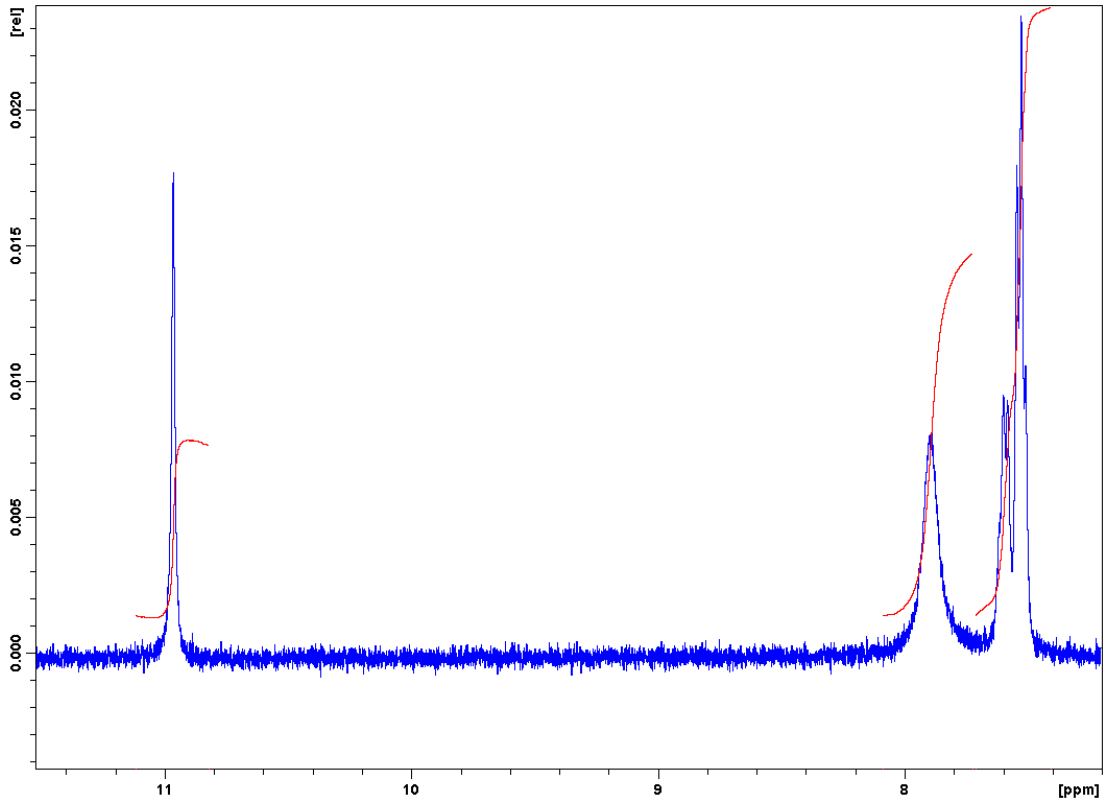

Figure 6.2: *^{1}H NMR spectrum of the free-ligand bzlmz in the region of 7.21 and 11.52 ppm.*

6.2.1.3 6-(hydroxyimino)ethyl)-1,3,7-trimethyllumazine (ohlmz)

The reaction of hydroxylamine hydrochloride (0.07 g; 1.01 mmol) and 6-acetyl-1, 3, 7-trimethyllumazine(almz) (0.20 g; 0.81 mmol) was carried out in 20 cm^{3} of ethanol under reflux for 6 hrs in the presence of a few drops of glacial acetic acid from a method previously reported [**16**]. Slow evaporation of the solution gave a pale purple crystalline material. Yield = 81%; M.P. = 240 - 242˚C; IR (ν_{max}/cm^{-1}): ν(N-H) 3440 (m), ν(O-H) 2901 (br, m), ν(C=O)$_{lumazine}$ 1707 (s), 1648 (vs, sh), ν(C=O)$_{amide}$ 1640 (br, s), ν(C=N)$_{lumazine}$ 1549 (s);^{1}H NMR (295 K/ppm): 11.68 (s, 1H, *OH*), 3.55 (s, 3H, *C1-H$_3$*), 3.32 (d, 6H, *N3-CH$_3$*, *N4-CH$_3$*), 2.36 (s, 3H, *C10-H$_3$*); UV-Vis (DCM, (λ_{max} (ε, M^{-1}cm^{-1}))): 347 nm (8800).

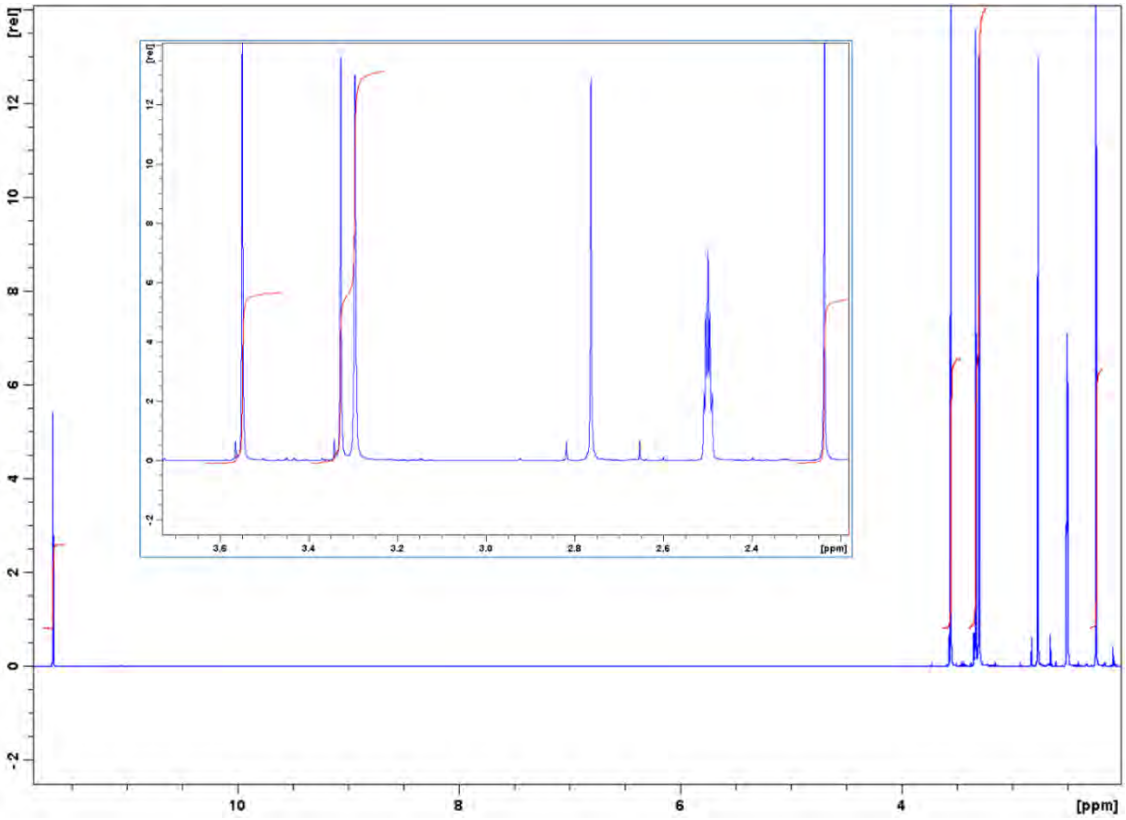

Figure 6.3: *^{1}H NMR spectrum of ohlmz. Inset: The methyl signals of ohlmz. The non-integrated signals are associated with deuterated dimethylsulphoxide.*

6.2.2 *Synthesis of metal complexes*

6.2.2.1 *cis-[RuCl$_2$(bzlmz)(PPh$_3$)] (**1**)*

A mixture of bzlmz (0.0382 g; 0.104 mmol) and *trans*-[RuCl$_2$(PPh$_3$)$_3$] (0.100 g; 0.104 mmol) was dissolved in 20 cm^3 of toluene. The resultant solution was heated until reflux for 6 hrs and filtered. Slow evaporation of the mother liquor gave dark brown crystals suitable for X-ray analysis. Yield = 68%; M.P. = 280 – 282 ˚C; IR (ν_{max}/cm^{-1}): ν(N-H)$_{amide}$3374 (w), υ(C=O)$_{lumazine}$ 1710, 1692 (s),υ(C=O)$_{amide}$ 1623 (s), υ(C=N)$_{lumazine}$ 1534 (s), ν(C-N)$_{amide}$1268 (m), ν(Ru-PPh$_3$) 695 (vs);^{1}H NMR (295K/ppm): 10.97 (s, 1H, *N6*), 9.36 (s, *toluene*), 8.16 (d, 2H, *H14*, *H18*), 7.66 – 7.06 (m, 18H, *H15*, *H16*, *H17*, *PPh$_3$*), 3.60 (s, 3H, *C8-H$_3$*), 2.73 (d, 6H, *N1-CH$_3$, N2-CH$_3$*), 2.11 (s, 3H, *C11-H$_3$*); ^{31}P NMR (295K/ppm): 25.55; UV-Vis (DCM, (λ_{max} (ε, M^{-1}cm^{-1}))): 300 nm (19139); 366 nm (10931); 447 nm (7392); 677

nm (474); Conductivity (DCM, 10^{-3} M): 9.20 ohm^{-1}cm^{-2}mol^{-1}; Anal. Calc. for $C_{43}H_{40}Cl_2N_6O_3PRu$ (%): C, 57.91; H, 4.52; N, 9.42. Found: C, 57.97; H, 4.18; N, 8.99;TOF-MS (*m/z*): Calcd: 909.14 [M]; Found: 799.06 [M-H_2O-C_7H_8].

*6.2.2.2 cis-[$RuCl_2$(olmz)(PPh_3)] (**2**)*

The title compound was formed from the 1:1 molar ratio reaction of ohlmz (0.0275 g; 0.104 mmol) with *trans*-[$RuCl_2(PPh_3)_3$] (0.100 g, 0.104 mmol) in 20 cm^3 of toluene after 6 hrs of heating at reflux temperature. A maroon precipitate was filtered and recrystallized from the slow diffusion of dichloromethane into *n*-hexane [1:1 (*v:v*)] which resulted in the formation of brown XRD quality crystals. Yield = 63%; M.P.> 350 ˚C; IR (ν_{max}/cm^{-1}): ν(C=O) 1688, 1620 (vs), ν(C=N) 1559 (m), ν(Ru-PPh_3) 696 (s); UV-Vis (DCM, (λ_{max} (ε, M^{-1}cm^{-1}))): 350 nm (6502); 461 nm (6646); 707 nm (550); Conductivity (DCM, 10^{-3}M): 15.00 ohm^{-1}cm^{-2}mol^{-1}; Anal. Calc. for $C_{28}H_{27}Cl_2N_5O_3PRu$ (%): C, 49.13; H, 3.98; N, 10.23. Found: C, 49.05; H, 3.96; N, 9.91; TOF-MS (*m/z*): Calcd: 684.03 [M]; Found: 684.02 [M].

6.3 X-ray diffraction

Crystal and structure refinement data are given in Table 6.2. Selected bond lengths and angles are given in Tables 6.3 and 6.4 for **1**.C_7H_8.H_2O and **2**, respectively. In both cases, the data were collected with Mo Kα (λ = 0.71073 Å) radiation at a crystal-to-detector distance of 50 mm. The following conditions were used for data collection: omega and phi scans with exposures taken at 30 W X-ray power and 0.50^o frame widths using APEX2 [**17**]. The data were reduced with the programme SAINT [**17**] using outlier rejection, scan speed scaling, as well as standard Lorentz and polarization correction factors. A SADABS semi-empirical multi-scan absorption correction [**18**] was applied to the data. Direct methods, SHELX-2014 [**19**] and WinGX [**20**] were used to solve all three

structures. All non-hydrogen atoms were located in the difference density map and refined anisotropically with SHELX-2014 [**19**]. All hydrogen atoms were included as idealised contributors in the least squares process. Their positions were calculated using a standard riding model with C-$H_{aromatic}$ distances of 0.93 Å and U_{iso} = 1.2 U_{eq}, C-$H_{methylene}$ distances of 0.99 Å and U_{iso} = 1.2 U_{eq} and C–H_{methyl}distances of 0.98 Å and U_{iso} = 1.5 U_{eq}. The O-H bonds of water molecule for **1** were located in the difference density map and refined isotropically.

6.4 Computational details

Computational calculations were conducted with GAUSSIAN 09W [**21**]. Geometry optimization of the ruthenium complex **1** was achieved through a DFT calculation using the B3LYP functional, with an accompanying hybrid basis set *viz*. the 6-311G^{++} (*d, p*) basis set was applied to all the C, H, N, O, Cl and P atoms and the LANL2DZ basis set, which makes use of effective core potentials, applied to the metal centre [**22**]. Prior to the calculation, the solvent molecules of recrystallization for **1** were omitted from the crystal structure and the resultant structure was used as the starting conformer. Good agreement was found between the optimized and geometrical parameters (refer to Table 2) with the minor deviations attributed to the fact that gas phase optimized structure do not account for non-classical hydrogen bonding interactions or any short distance contacts. Using the optimized structure of the metal complex, the lack of any negative Eigen values in the frequency calculations confirmed that the structure is at a global minimum on the potential energy surface [**23**].

6.5 Results and Discussion

6.5.1 Synthesis, spectral characterization and computational studies

The ruthenium(II) and –(III) complexes **1** and **2** were formulated from the 1:1 molar coordination reactions between *trans*-[$RuCl_2(PPh_3)_3$] and their respective free-ligands,

bzlmz and olmz, respectively. In **1** and **2**, the bzlmz and ohlmz coordinates *via* their respective tridentate $N_{imino}N_{pyrazine}O_{ketonic}$and $O_{ketonic}N_{pyrazine}O_{nitroso}$ donor sets, (see section 6.5.4, Figures6.15 and 6.18).

Interestingly, a fascinating transformation is observed from the free-ligand, ohlmz to the olmz chelator, see Scheme 6.1. This instrinsic molecular transformation of ohlmz is inititiated by Beckmann rearrangement of the oxime ohlmz (refer to Step **A**) [**24**]. In step **B**, the resultant intermediate undergoes deacetylation which is accompanied by a reaction between the acetate group and acetic acid. In addition, ruthenium catalyzed demethylation of the diketonic aliphatic compound occurs [**25**]. Thereafter, the amido nitrogen undergoes ruthenium catalyzed oxidation to form a nitroso group, see Step **C** [**26**]. Subsequently, the nitroso oxygen is protonated and the methyl group bonds covalently to the aliphatic nitrogen, see Step **D**. The compounds exhibit excellent solubility in alcoholic media and virtually all other polar solvents. The low conductivity values recorded for **1** and **2** confirm that both complexes are non-electrolytes in DCM.

The IR spectra of bzlmz and its complex (Figure 6.4) show numerous vibrations between 1200 cm^{-1} to 1800 cm^{-1} which are poorly resolved due to the extended π-conjugation within bzlmz. However, frequency calculations aided in the interpretation of these vibrations. More specifically, the simulated spectrum of **1** indicated a distinctive difference between coordinated ketonic and uncoordinated vibrations at 1669 cm^{-1} and 1776 cm^{-1}, respectively. In the overlay IR spectra of **1** and its free-ligand, an intense broad vibrational band at 1694 cm^{-1} (for the free-ligand, bzlmz) splits it into two vibrational bands at 1692 cm^{-1} (coordinated) and 1710 cm^{-1} (uncoordinated).

The $\nu(C{=}O)_{amide}$ is observed at 1740 cm^{-1} in the simulated spectrum of **1** while in the experimental spectra of **1** and its free-ligand, the amide C=O vibrations [1623 cm^{-1} for **1** and 1652 cm^{-1} for bzlmz free ligand] are found below the ketonic lumazine vibrations.

The simulated amide C-N (1265 cm^{-1}) and C=N (1561 cm^{-1}) compare well with the corresponding wavenumbers found for the peaks in the experimental spectra of **1** [ν(C=N) at 1534 cm^{-1} and ν(C-N) at 1268 cm^{-1}] and its free-ligand [ν(C=N) at 1547 cm^{-1} and ν(C-N) at 1268 cm^{-1}]. For **1**, the N-H bond vibrates essentially at the same positions at 3374 and 3377 cm^{-1} in the experimental – and simulated IR spectra, respectively. In both the experimental IR spectra of **1** and **2**, an intense characteristic ruthenium to triphenylphosphine signal is observed as 695 and 696 cm^{-1}, respectively [**27**].

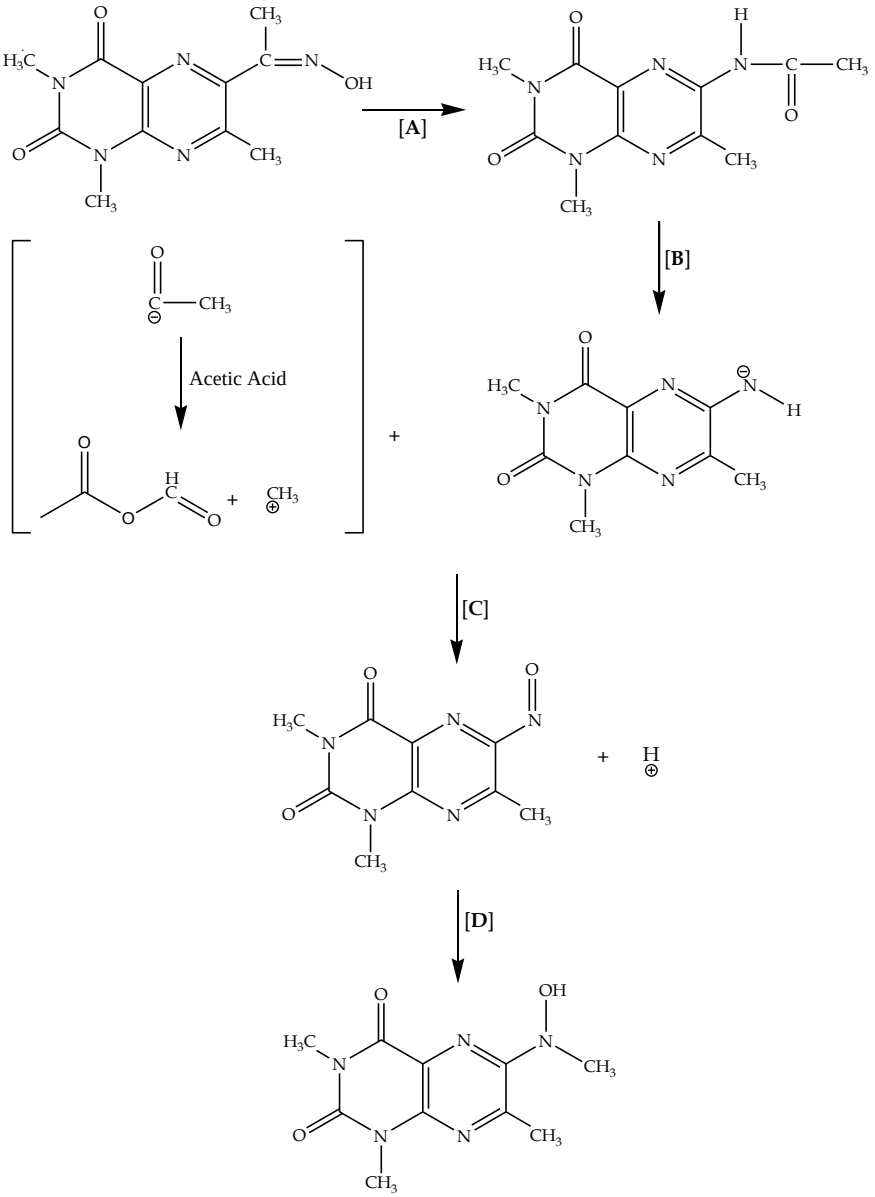

Scheme 6.1: *A proposed synthetic route for Holmz.*

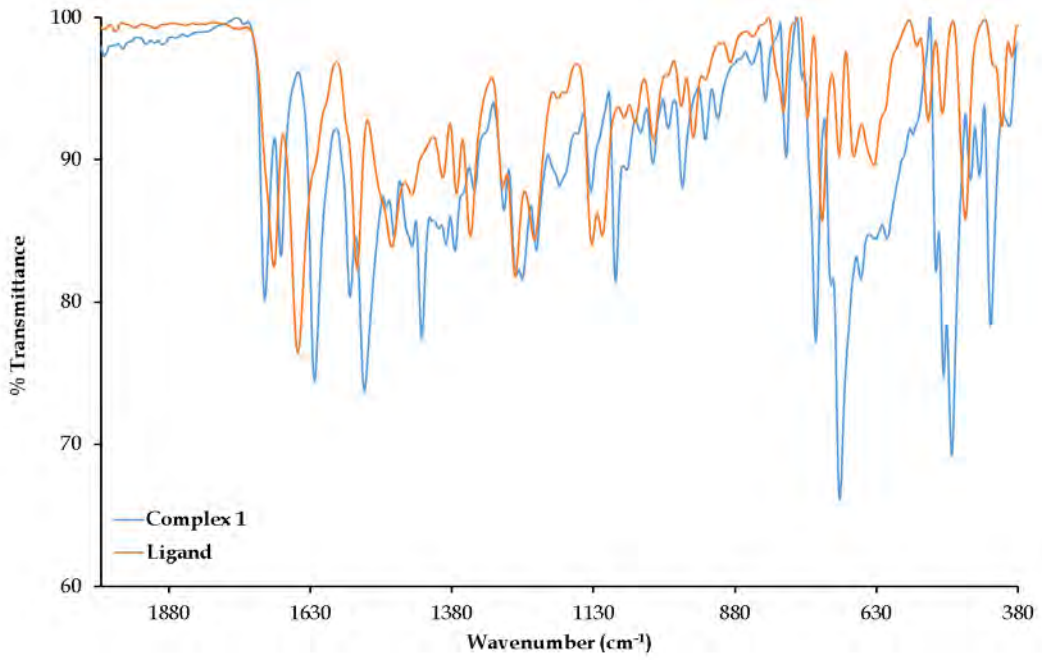

Figure 6.4: *Overlay IR spectra of complex* ***1*** *and its free-ligand, bzlmz in the region of 380 to 2000 cm-1.*

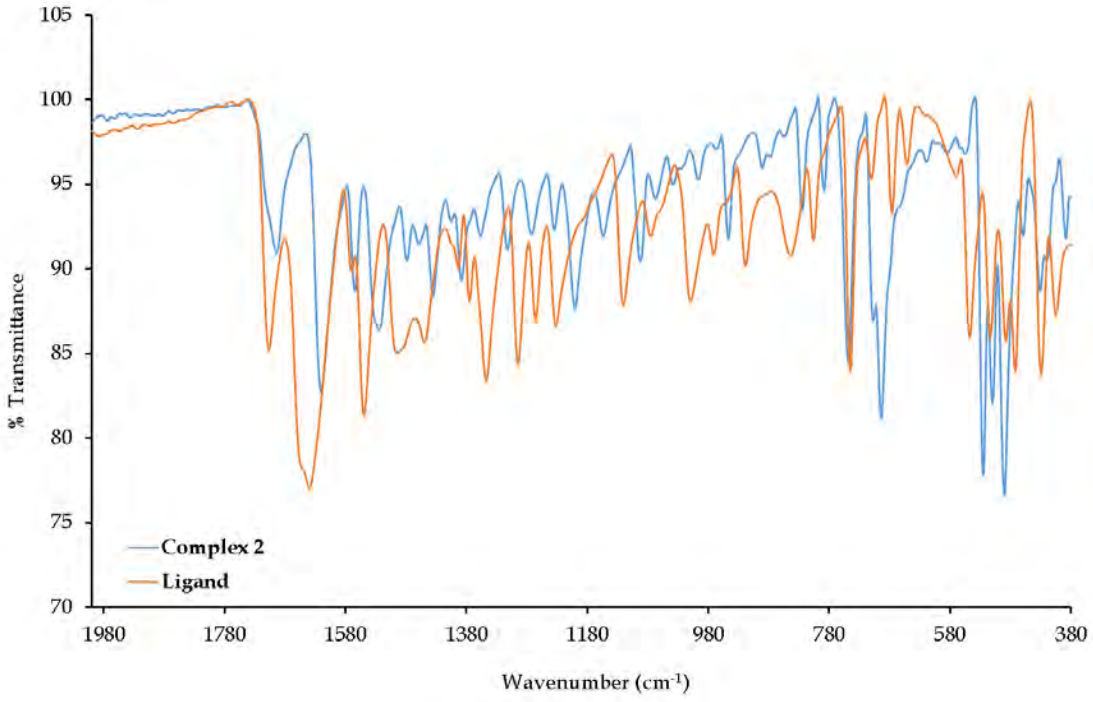

Figure 6.5: *Overlay IR spectra of complex* **2** *and its free-ligand, ohlmz in the region of 380 and 2000 cm-1.*

The ^{1}H NMR spectrum of **1** is dominated by an intense multiplet attributed to the signals of the triphenylphosphine co-ligand and selected phenylic protons of the bzlmz chelator (see Figure 6.6). The remaining aromatic signal resonates as a doublet at 8.16 ppm. The amide and methyl signals of the bzlmz chelator in **1** are found essentially at the same positions to analogous signals found within the proton spectrum of the corresponding free-ligand bzlmz. As expected, only one signal is observed in the ^{31}P NMR spectrum of **1** for its triphenylphosphine co-ligand (see Figure 6.7).

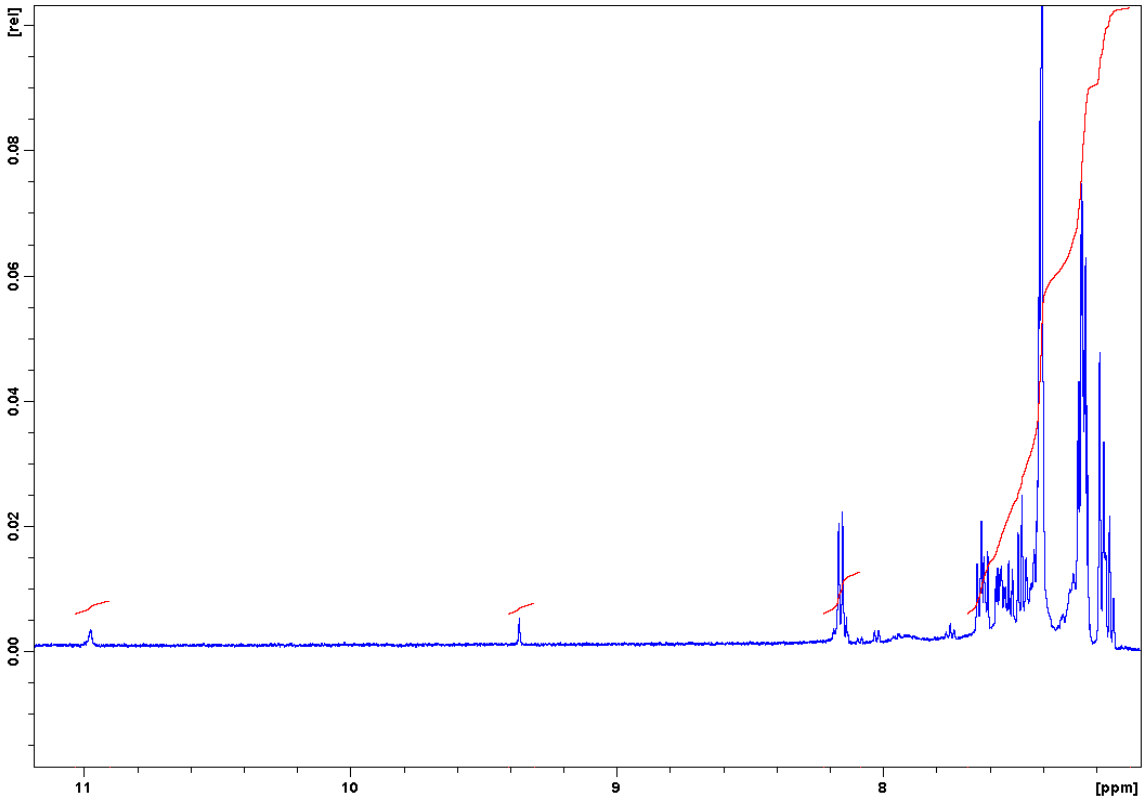

Figure 6.6: *^{1}H NMR spectrum of complex **1** in the region of 6.99 and 11.14 ppm.*

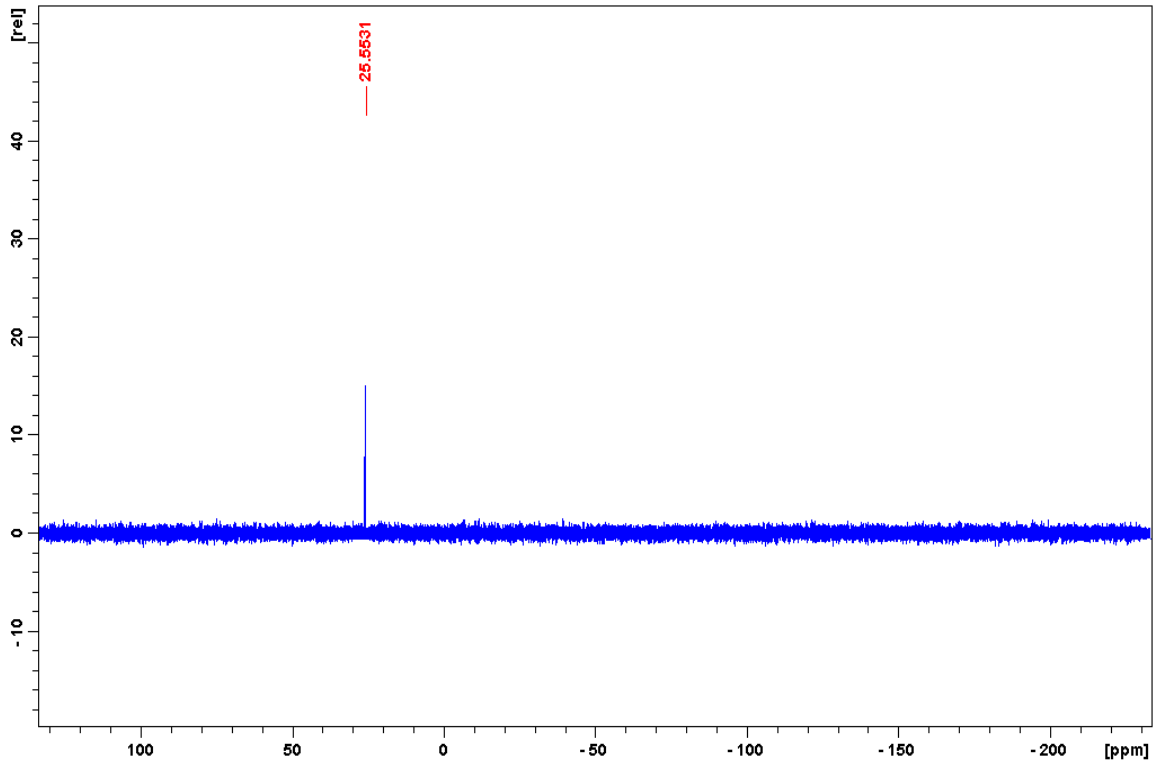

Figure 6.7: *^{31}P NMR spectrum of complex **1**.*

The UV-Vis spectra of the metal complexes show both intense π-π^* intraligand transitions below 400 nm associated with the conjugated bzlmz (in **1**) and olmz (in **2**) chelators (see Figures 6.8 and 6.9). In the region (between 400 nm and 600 nm), distinctive charge transfer bands appears; Metal-to-Ligand-Charge Transfer band at 477 nm and Ligand-to-Metal-Charge Transfer band at 461 nm for **1** and **2**, respectively. Despite complex **1** having a low-spin d^6 electron configuration, it also has a metal-based *d-d* electronic transition such as observed for the paramagnetic complex **2** [677 nm for **1** and 707 nm for **2**]. The presence of the metal-based electronic transition of **1** is ascribed to a computed low band-gap energy (2.685 eV) which makes the *d-d* electronic transition favourable. This finding concurs with our previous report where comparable band-gap energies were attained for the optimized structures of the ruthenium(II) complex cation, $[RuCl(Hobz)_2(PPh_3)]^+$ (Hobz = 2-hydroxyphenylbenzimidazole) [band-gap energy = 3.189 eV] and the paramagnetic ruthenium complex, $[Ru^{III}Cl(obs)_2(PPh_3)]$

[band-gap energy = 3.236 eV]; this computational data explained why both these metallic compounds had distinctive *d-d* electronic transitions [**28**].

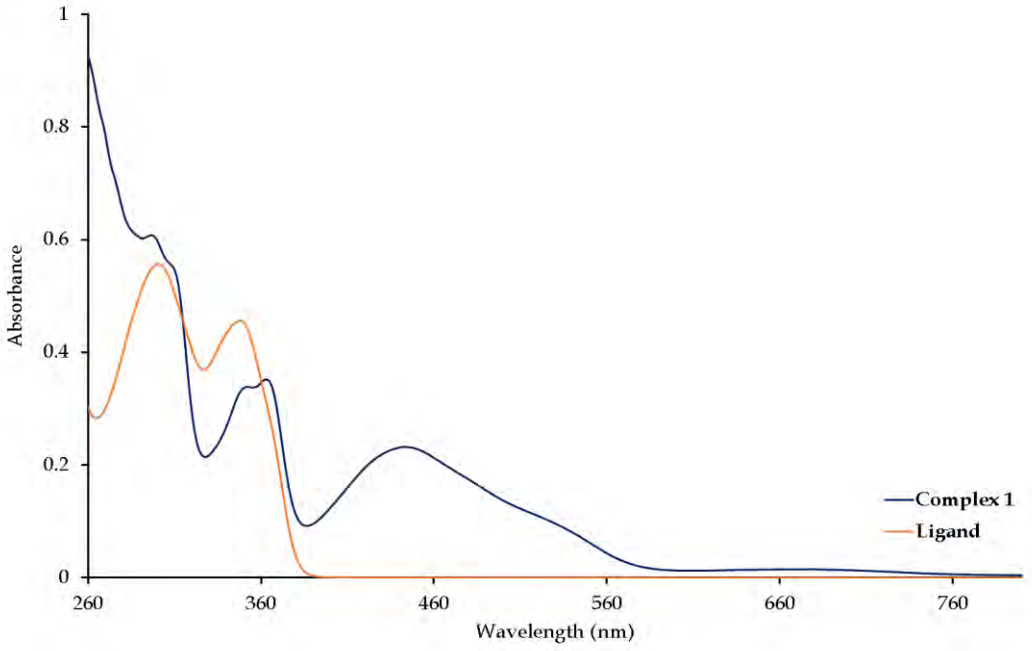

Figure 6.8: *Overlay UV-Vis spectra of complex* ***1*** *and its free-ligand, bzlmz.*

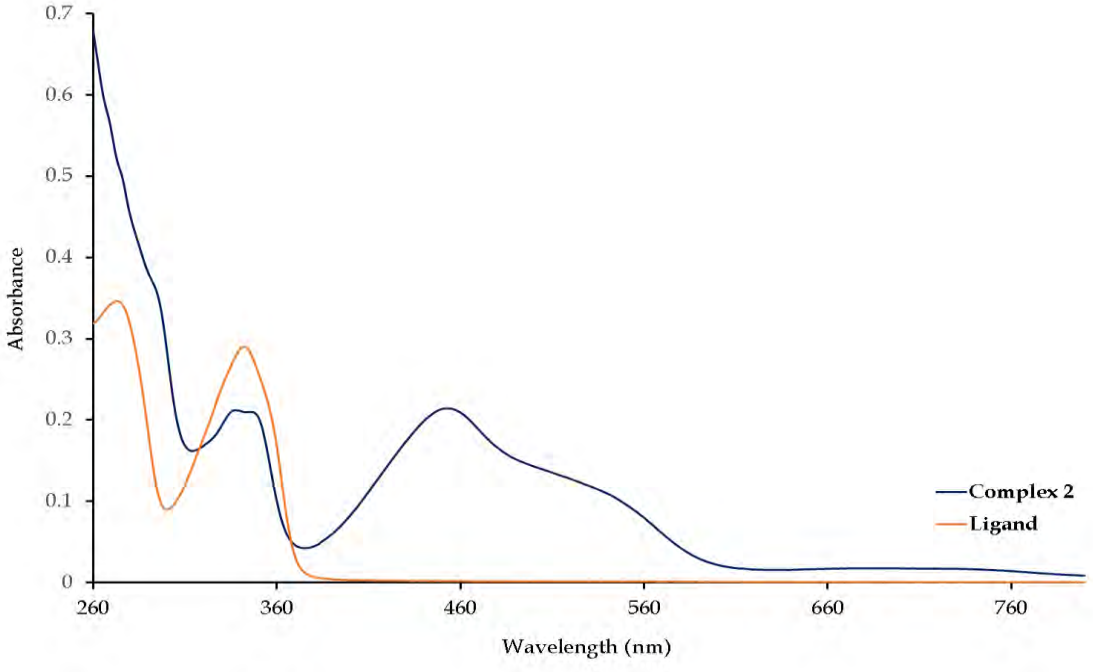

Figure 6.9: *Overlay UV-Vis spectra of complex* **2** *and its free-ligand, olmz.*

The EA data compare well with the calculated exact masses of the respective metal complexes while the low resolution mass spectra of **1** and **2** showed peaks corresponding to [M-H_2O-C_7H_8] at *m/z* 799.06 and [M] at *m/z* 684.02 (see Figures 6.10 and 6.11).

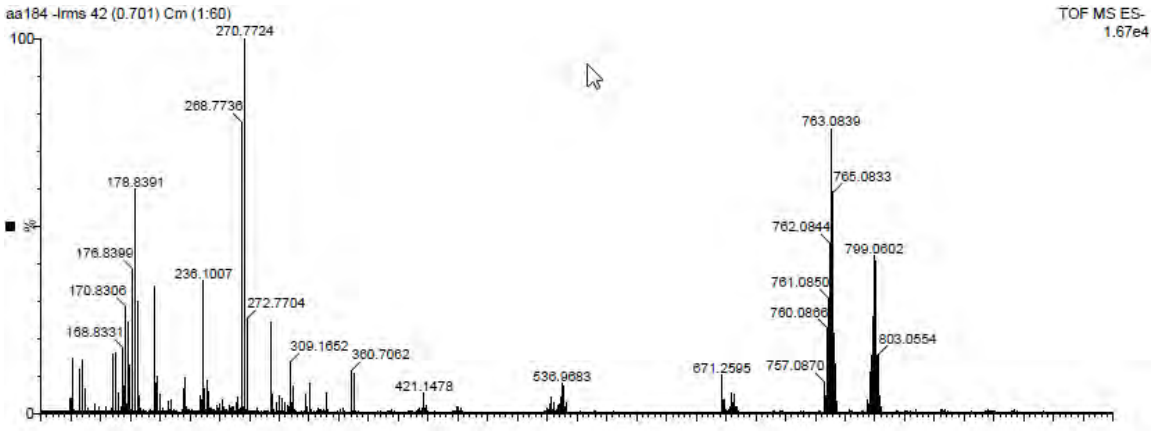

Figure 6.10: *Low resolution mass spectrum of complex **1**. The mass spectrum indicates that the compound is highly ionisable which leads to an intricate fragmentation pattern. The [M-H_2O-C_7H_8]$^+$ peak of **1** is observed at m/z 799.06.*

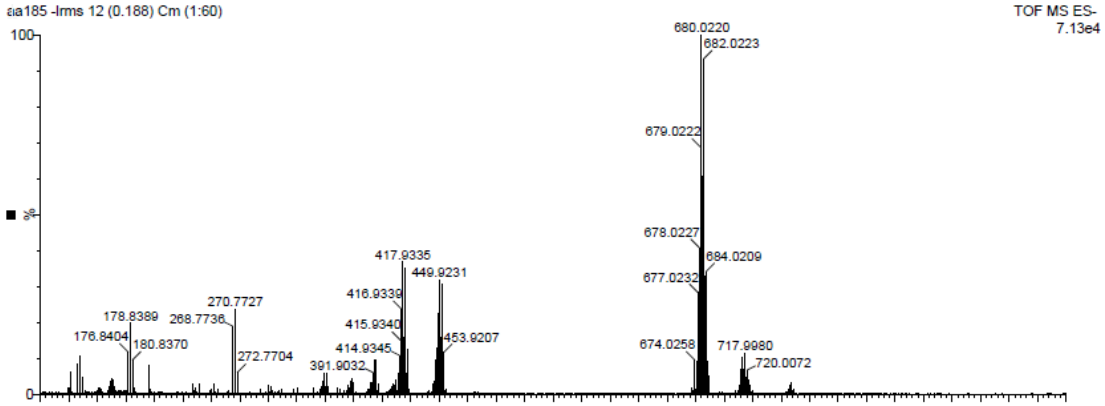

Figure 6.11: *Low resolution mass spectrum of complex **2**. The mass spectrum indicates that the compound is highly ionisable which leads to an intricate fragmentation pattern. The [M]$^+$ peak of **2** is observed at m/z 684.02.*

The EPR spectrum of **2** (see Figure 6.12) was obtained only in the solid state at room temperature. A low resolution singlet (*g*-value = 2.011) confirmed the presence of the paramagnetic metal centre of complex **2** in the solid state at 298 K. The nature of the EPR spectrum of **2** is characteristic of some low spin ruthenium(III) octahedral complexes [**29**].

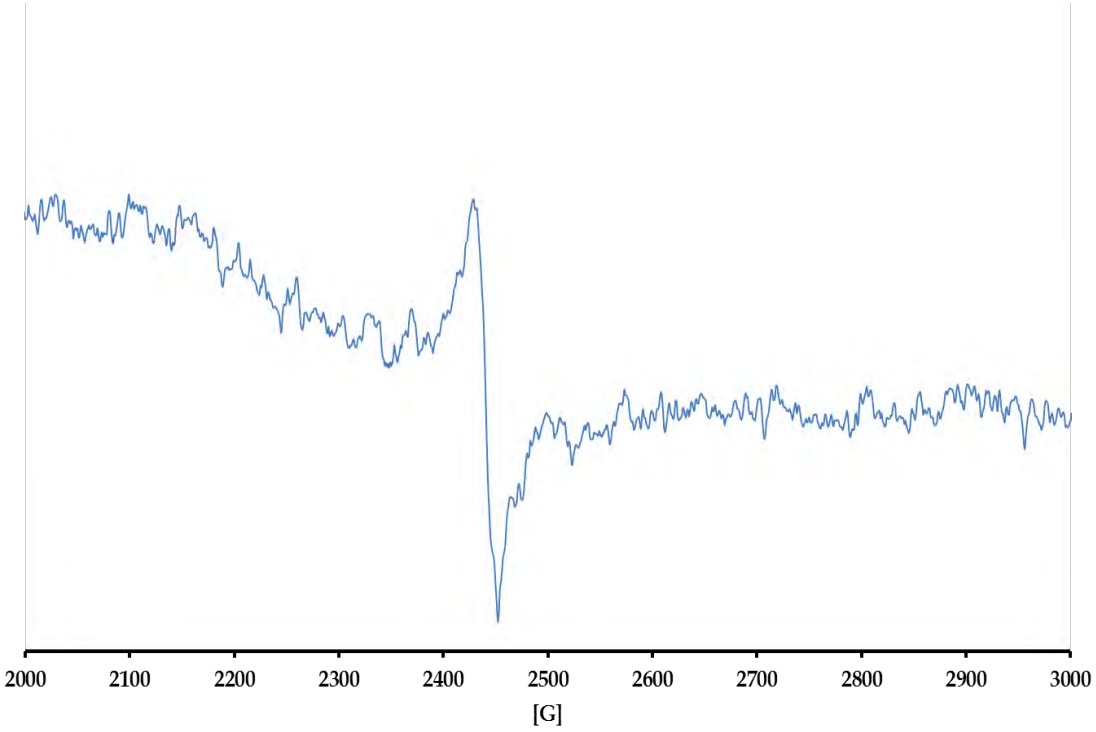

Figure 6.12: *Solid state EPR spectrum of complex* **2** *at 298K.*

6.5.2 Electrochemistry studies

The cyclic voltammograms (CVs) of **1** and **2** showed single redox couples attributed to the Ru(II)/Ru(III) redox couples as seen in Figure 6.13. The assignment is made based on the fact that their halfwave potentials [$E_{½}$ = 0.96 V (for **1**) and 0.83 V (for **2**) *vs* Ag|AgCl] resides in the potential window of -0.15 V and 0.96 V for halfwave potentials attained for mononuclear diamagnetic and paramagnetic ruthenium complexes under

the similar electrochemical conditions [**28**, **30**]. In addition, these redox couples corresponds to one electron redox processes governed by their peak to peak seperations (I_{pa}/I_{pc}) approaching 1. Furthermore, the redox couples are quasi-reversible as the peak to peak seperations of **1** (ΔE = 80 mV) and **2** (ΔE = 70 mV) are smaller than that of the standard ferrocene (90 *mV* at 100 *mV/s*)indicating faster electron transfer kinetics for the metal complexes. Also, the two redox couples displayed diffusion controlled behaviour with increasing scan rates. For instance, Figure6.14 shows overlay CVs of complex **2** for scan rates ranging from 25 mV/s to 200 mV/s, at increments of 25 mV/s.

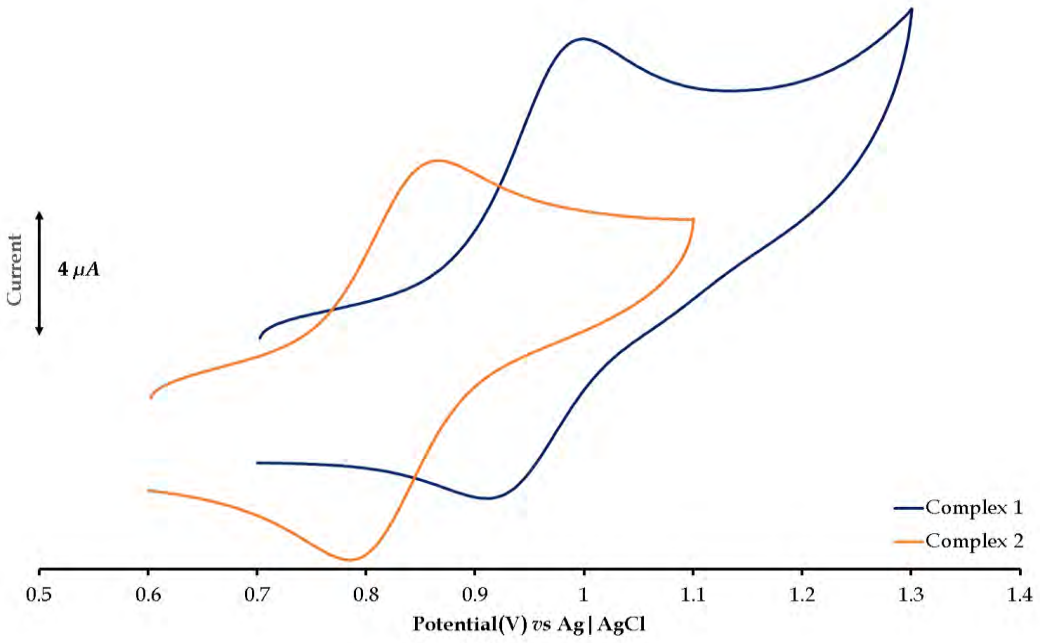

Figure 6.13: *Overlay cyclic voltammograms of complexes **1** and **2** at 100 mV/s.*

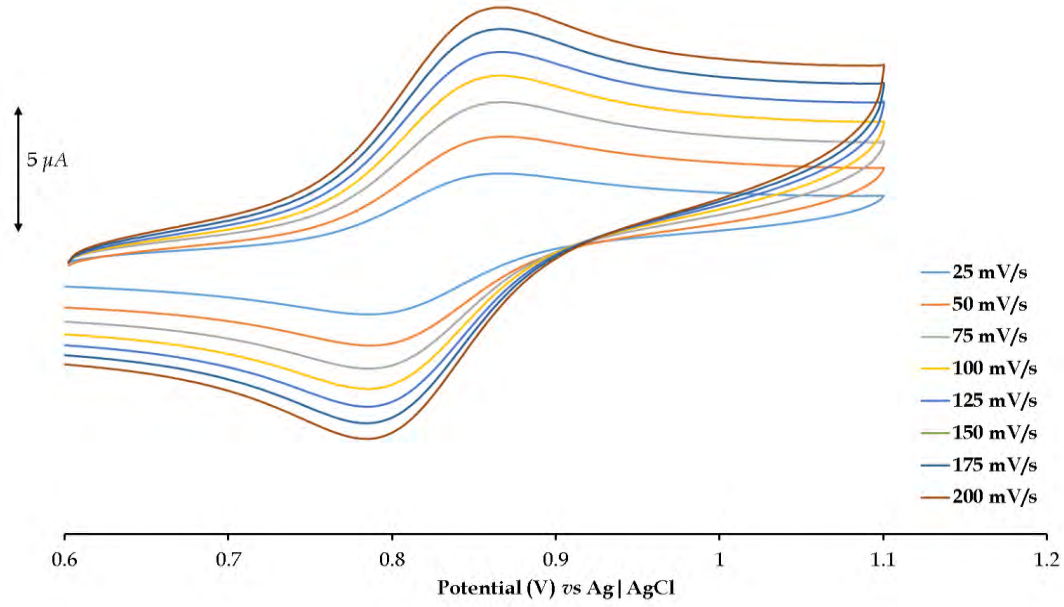

Figure 6.14: *Overlay CVs of complex* **2** *at incrementing scan ratesillustrating the diffusion-controlled behaviour of its redox couple.*

6.5.3 Radical Scavenging studies

The mutation of healthy cells by free radicals is reported to be a common cause of cancer, Alzheimer's disease and cardiovascular diseases [**31**, **32**]. To deter the negative effects of these free radicals, more effective radical scavengers are required other than the natural antioxidant, vitamin C. Previous studies have illustrated that ruthenium compounds have shown to be effective radical scavengers, largely owing to their optimal redox properties [**33**]. Indicative to these previous studies, the formulated ruthenium compounds **1** and **2** with lumazine moeities have shown to have significantly higher DPPH and NO radical scavenging activities in comparison to vitamin C [IC_{50}(NO) = 210 μM and IC_{50}(DPPH) = 147 μM], see Table 6.1 [**34, 35, 36**]. Furthermore, the metallic compounds have lower IC_{50} values than their corresponding ligands which emphasize the influence of the metal atoms in **1** and **2**.

In fact, the influence of the bzlmz chelator on the radical scavenging capability of **1** can be regarded as negligible. This deduction is based on the high IC_{50} values of the free-ligand, bzlmz when used for the scavenging of the DPPH and NO radicals, respectively. In contrast to metal-centred radical scavenging activity of **1**, the IC_{50} values of the free-ligand, ohlmz suggested that there could be a synergetistic mechanistic effect of radical activity induced by the redox activity of the metal centre and the donation of hydrogen by the olmz chelator of (**2**).

Table 6.1: *IC_{50} values (in µM) of the metallic compounds and their free-ligands. Each IC_{50} value has a standard deviation less than 3% with respect to its mean value.*

	NO	**DPPH**
1	36	46
2	34	63
bzlmz	1002	392
ohlmz	125	109

6.5.4 Crystallographic studies

Complex **1** co-crystallize with a water and a toluene molecule of recrystallization (see Figure 6.15). Molecules of **1** affords chains parallel to the [a]-axis induced by hydrogen-bonding between the water molecule and adjecent molecules of **1** (O4-HB⋯N3 = 2.17(7) Å and O4-HA⋯Cl2 = 2.22(5) Å), see Figure 6.16. The crystal lattice of **1** is further stabilized by classical *pi-pi* interactions between the C19-C24 phenyl ring (of the triphenylphosphine co-ligand) and the C7C9N4C1C6N3 ring (of the bzlmz chelator) defined by the centroid to centroid distance of 3.371 Å. Intermolecular interactions are also observed between the nearly co-planar toluene molecule and C6C1C2N1C4N2 ring (of the bzlmz chelator) with an interplanar spacing of 3.770 Å, see Figure 6.17. The aforementioned intermolecular interactions induced the molecules of **1** to stack in

columns aligned with the [b]-axis. Complex **2** crystallize out in a *C2/c*space-group with each monoclinic cell occupying 8 molecules of **2** (see Figure 6.18). Indicative to **1**, complex **2** exhibits *pi*-stacking intramolecular interactions (at 3.480 Å) between the C11-C16 phenyl ring (of the triphenylphosphine co-ligand) and N2C9C2N5C3C8 ring (of the bzlmz chelator), see Figure 6.19.

The constrained five-membered chelate rings within **1** [N5-Ru-N4 = 77.48(9)˚ and N4-Ru-O1 = 78.48(8)˚] and **2** [O1-Ru-N2 = 77.7(3)˚ and O2-Ru-N2 = 77.5(2)˚] afforded severe deviation in their respective octahedral given by the individual equotorial angles [N5-Ru-O1 =155.86(8)˚, Cl1-Ru-N4 = 173.42(7)˚ for **1** and O1-Ru-O2 = 155.1**(**2)˚, N2-Ru-Cl1 = 176.9(2)˚] all deviating from linearity. Furthermore, the lumazine moeity lies significantly out of the plane (by 87.32˚) of the C13-C18 phenyl ring which is accounts to the flexibility of the amide aliphatic group. The bond order of the C12-O3 [1.222(3) Å] bond is confirmed based on its similar distance in comparison to the ketonic C=O bonds within **1** [C2-O1 = 1.248(4) Å and C4-O2 =1.210(4) Å] and **2** [C7-O2 = 1.236(1) Å and C5-O3 =1.21(1) Å]. The presence of the paramagnetic metal (for **2**) is also confirmed based on the difference in the Ru-O [Ru-O1 = 1.993(8) Å and Ru-O2 = 2.335(5) Å] coordination bonds which affirms the olmz ligand acts as a tridentate monoanionic chelator. In fact, the ruthenium(III) complex, *trans*-[Ru(H_2npbh)Cl(PPh_3)$_2$] (H_2npbh = 2-hydroxy-1-naphthaldehyde-benzoylhydrazone) had comparable Ru-$O_{ketonic}$ [1.9906(15) Å] and Ru-$O_{phenolate}$ [2.0382(14) Å] bond lengths as **1** [**37**]. The lower Lewis acidic character of the diamagnetic ruthenium atom (in **1**) affords a shorter Ru-P [2.329(2) Å] coordination bond length in contrast to the analogous bond found within **2** [Ru-P = 2.329(2) Å]. However, despite the variable valency between **1** and **2**, the ruthenium to lumazine nitrogen coordination bonds of both metal complexes are nearly equidistant [1.904(2) Å for **1** and 1.900(6) Å for **2**]. In addition, the difference in the *cis*-orientated Ru-Cl bonds [Ru-Cl1 = 2.412(9) Å, Ru-Cl2 = 2.4527(9) Å for **1** and Ru-Cl1 = 2.411(2) Å, Ru-Cl2 =

2.427(2) Å for **2**] within the respective complexes are accounted to the difference influence imposed on the halides.

Although no ruthenium compounds (besides **1** and **2**) bearing lumazine moeities can be found in the Cambridge Crystallographic Data Centre (CCDC), several transition metal complexes with lumazine chelates have been isolated [**15**, **38**-**41**]. Among these transition metal complexes, the lumazine moeity and its multidentate chelators exhibits diverse coordination modes affording metal complexes with unique molecular geometries. In addition, several of these metal complexes exhibits unique anticancer activities while the presence of the lumazine moiety within the coordinates sphere of various *d*-block metals induces unique luminscent behaviours [**39**, **41**].

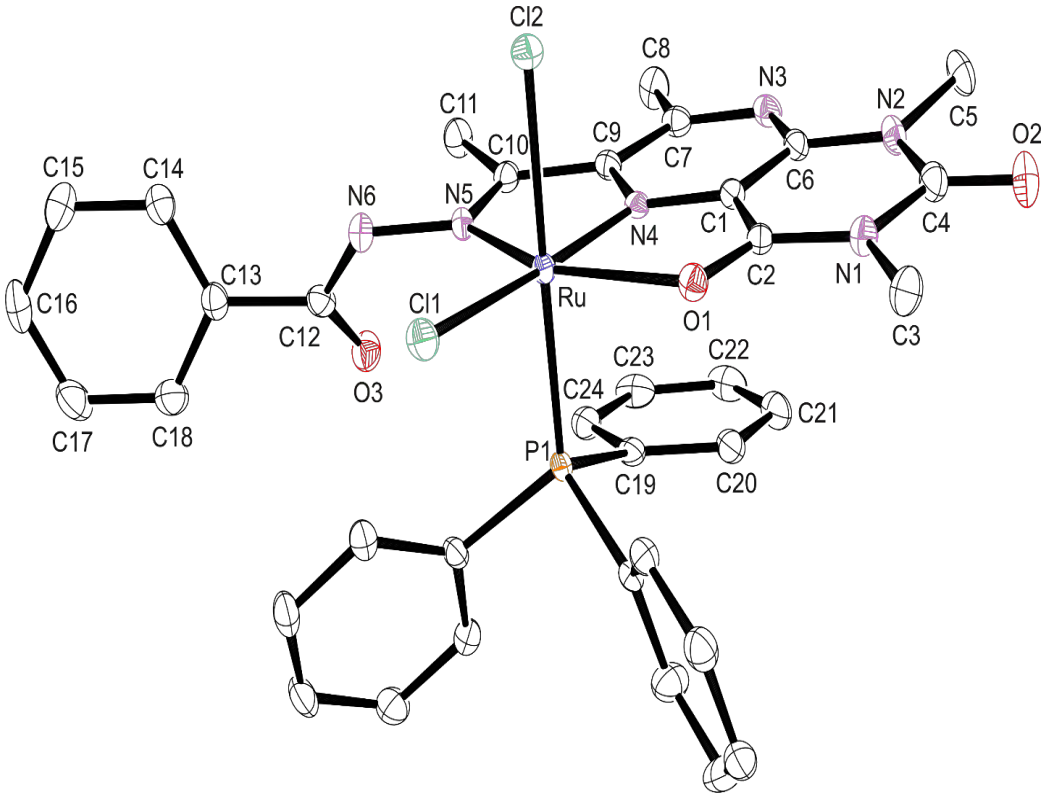

Figure 6.15: *An ORTEP view of compound* ***1*** *showing 50 % probability displacement ellipsoids and the atom labelling. The hydrogen atoms and toluene molecule of crystallization were omitted for clarity.*

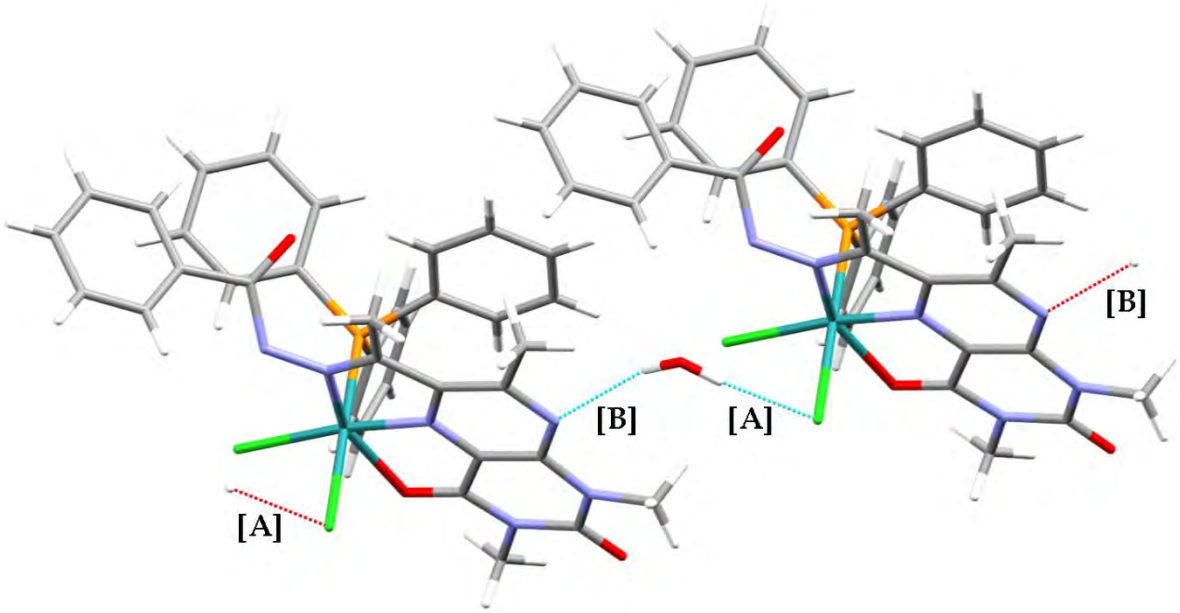

Figure 6.16: *A perspective view of the hydrogen-bonding occurring in* ***1;****O4-HA⋯Cl2 = 2.22(5) Å* ***[A]*** *and O4-HB⋯N3 = 2.17(7) Å* ***[B]****.*

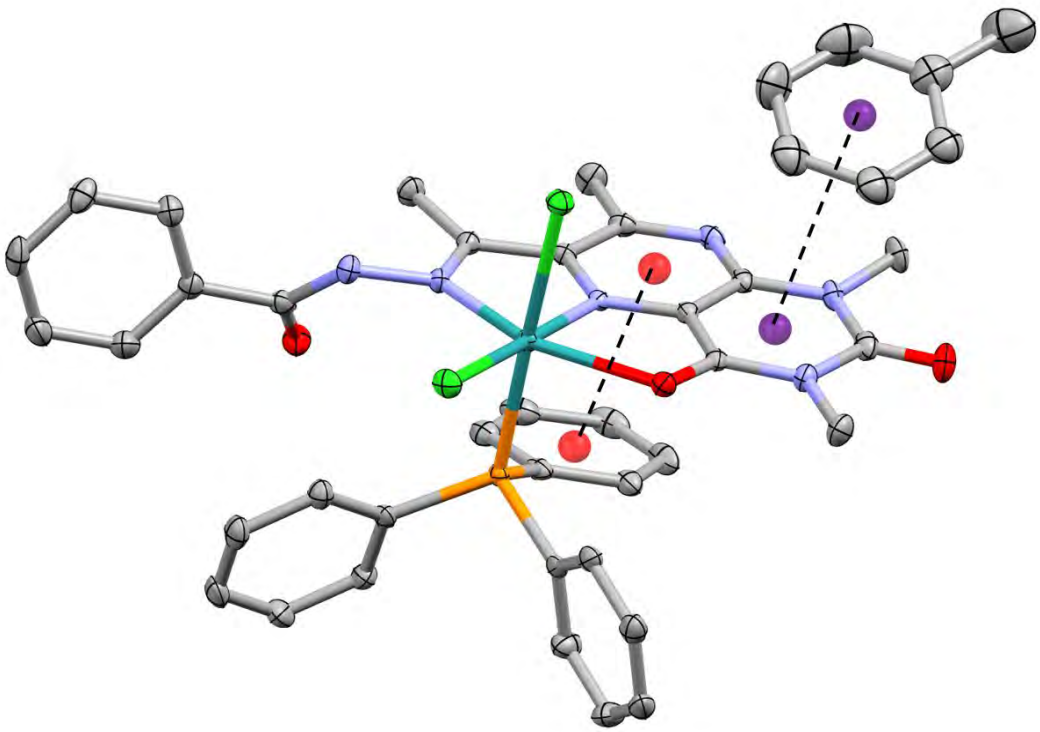

Figure 6.17: *A perspective view of inter- and intramolecular interactions stabilizing the crystal lattice of* ***1****.*

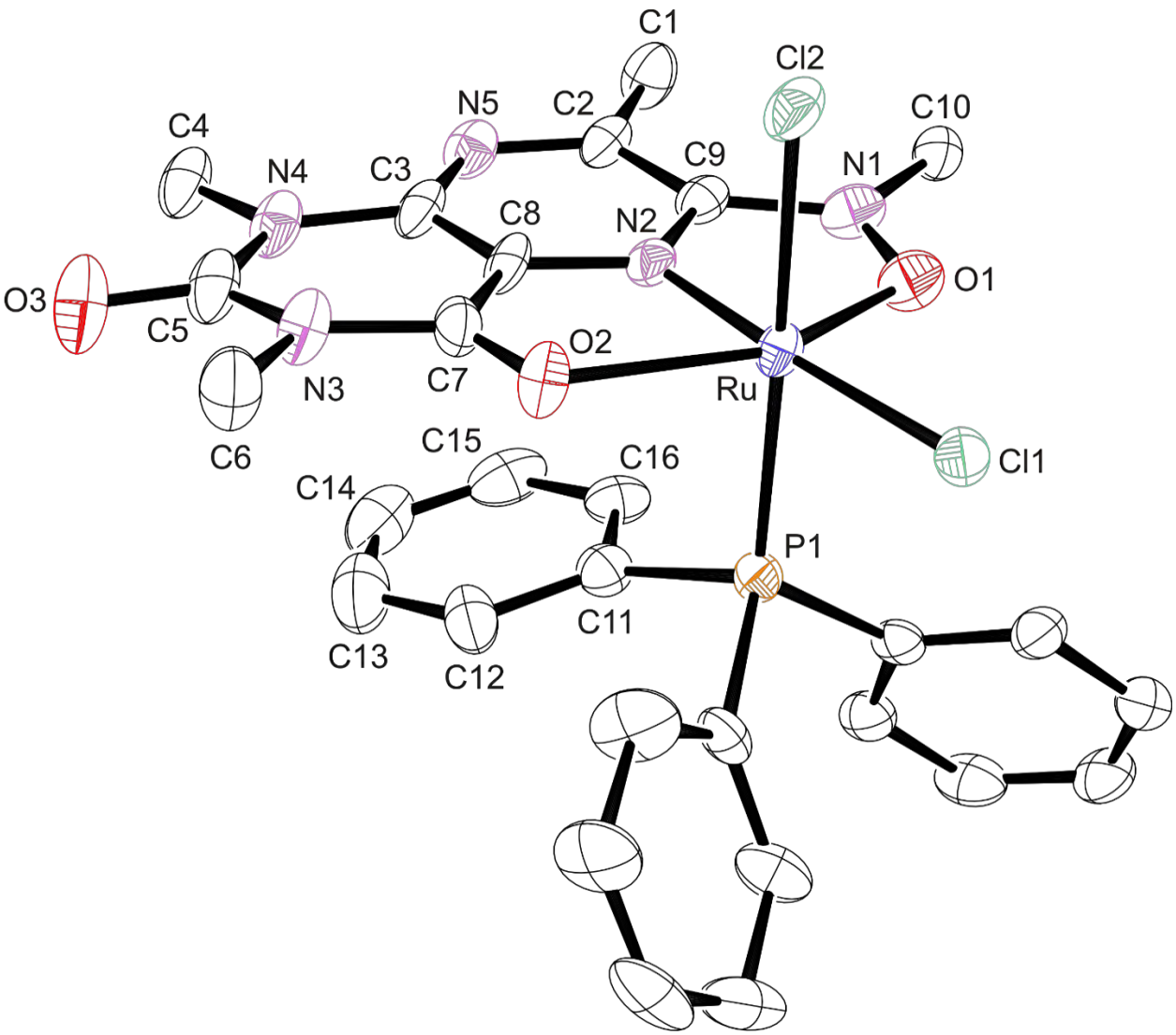

Figure 6.18: *An ORTEP view of compound* **2** *showing 50 % probability displacement ellipsoids and the atom labelling. The hydrogen atoms were omitted for clarity.*

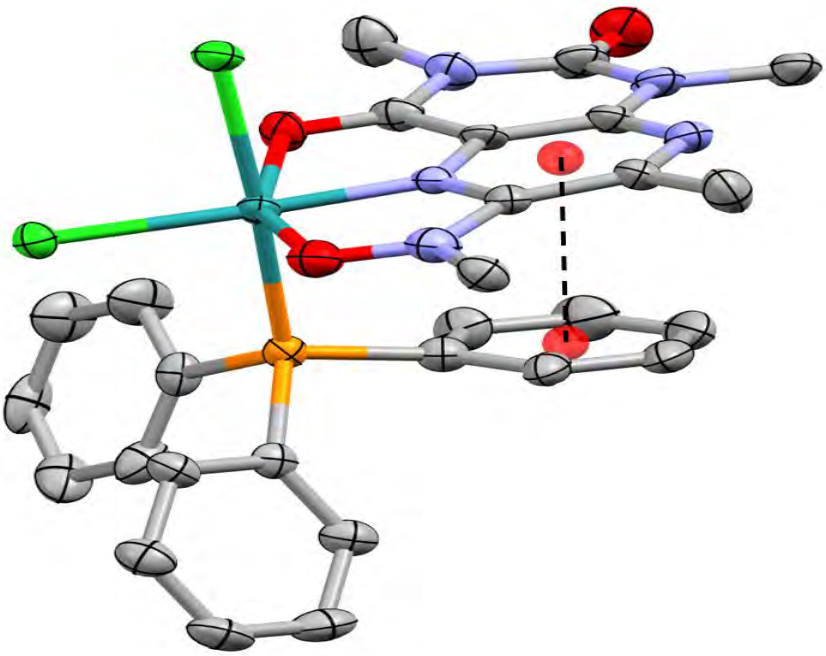

Figure 6.19: *A perspective view of the intramolecular interactions stabilizing the crystal lattice of* **2**.

Table 6.2: *Crystal data and structure refinement data.*

	1·H_2O·C_7H_8	**2**
Chemical formula	$C_{43}H_{42}Cl_2N_6O_4PRu$	$C_{28}H_{27}Cl_2N_5O_3PRu$
Formula weight	909.77	684.50
Temperature (K)	100(2)	100(2)
Crystal system	Triclinic	Monoclinic
Space group	P-1	C2/c
Unit cell dimensions (Å, °)	a = 10.162(5)	a = 22.7645(13)
	b = 13.587(5)	b = 17.5745(11)
	c = 16.268(5)	c = 17.3170(13)
	α = 105.202(5)	α = 90
	β = 106.096(5)	β = 110.728(3)
	γ = 103.762(5)	γ = 90
Crystal size (mm)	0.19 × 0.18 × 0.12 mm	0.32 × 0.11 × 0.04 mm
V(Å^3)	1962.2 (13)	6479.6 (7)
Z	2	8
Density (calc.) (Mg/m^3)	1.540	1.403
Absorption coefficient (mm^{-1})	0.629	0.733
F(000)	934	2776
θ range for data collection (deg)	1.39; 26.05	1.50; 26.20
Reflections measured	31830	23551
Observed reflections [I>2σ(I)]	7117	5084
Independent reflections	7653	6162
Data/Restraints/parameters	7653/1/527	6162/0/365
Goodness of fit on F^2	1.085	1.047
Observed R, wR^2	0.0341; 0.0858	0.0792; 0.2074
R_{int}	0.026	0.036

Table 6.3: *Selected bond lengths [Å] and bond angles [°] for* ***1****.*

	Experimental	**Optimized**
Ru-P	2.329(2)	2.4066
Ru-N4	1.904(2)	1.9525
Ru-N5	2.003(3)	2.0056
Ru-Cl1	2.412(9)	2.4821
Ru-Cl2	2.4527(9)	2.4481
C12-O3	1.222(3)	1.2175
C2-O1	1.248(4)	1.2357
C4-O2	1.210(4)	1.2109
N5-Ru-N4	77.48(9)	78.291
N4-Ru-O1	78.48(8)	78.887
N5-Ru-O1	155.86(8)	153.174
Cl1-Ru-N4	173.42(7)	171.196

Table 6.4: *Selected bond lengths [Å] and bond angles [°] for* ***2****.*

	Experimental
Ru-O1	1.993(8)
Ru-O2	2.335(5)
Ru-P	2.329(2)
Ru-Cl1	2.411(2)
Ru-Cl2	2.427(2)
Ru-N2	1.900(6)
C7-O2	1.236(1)
C5-O3	1.21(1)
O1-Ru-N2	77.7(3)
O2-Ru-N2	77.5(2)
O1-Ru-O2	155.1(2)
N2-Ru-Cl1	176.9(2)

6.6 References

1. B.S. Murray, M.V. Babak, C.G. Hartinger, P.J. Dyson, *Coord. Chem. Rev*., 2016, **306**, 86.
2. K.D. Mjos, C. Orvig, *Chem. Rev.,* 2014, **114**, 4540.
3. J.B. Aitken, S. Antony, C.M. Weekley, B. Lai, L. Spiccia, H.H. Harris, *Metallomics,* 2012, **4**, 1051.
4. R.K. Koiri, A. Mehrotra, S.K. Trigun, *Med. Hypotheses*, 2013, **80**, 841.
5. A.D. Oprea, R.R. Russell, K.S Russell, M. Abu-Khalaf, *J. Cardiothorac. Vasc. Anesth.*, 2015, http://dx.doi.org/10.1053/j.jvca.2015.06.020.
6. S. David, R.S. Perkins, F.R. Fronczek, S. Kasiri, S.S. Mandal, R.S. Srivastava, *J. Inorg. Biochem*., 2012, **111**, 33.
7. Z. Wang, H. Qian, S.Yiu, J. Sun, G. Zhu, *J. Inorg. Biochem*., 2014, **131**, 47.
8. M. Fischer, A. Bacher, *Arch. Biochem. Biophys*., 2008, **474**, 252.
9. A. Bacher, S. Eberhardt, W. Eisenreich, M. Fischer, S. Herz, B. Illarionov, K. Kis, G. Richter, *Vitam. Horm*., 2001, **61**, 1.
10. V.G. Premkumar, S. Yuvaraj, S. Sathish, P. Shanthi, P. Sachdanandam, *Vascul. Pharmacol*., 2008, **48**,191.
11. G.S. Khan, A. Shah, Z. Rehman, D. Barker, *J. Photochem. Photobiol. B*, 2012, **115**, 105.
12. I.N. Booysen, S. Maikoo, M.P. Akerman, B. Xulu, *Polyhedron*, 2014, **79**, 250.
13. I.N. Booysen, S. Maikoo, M.P. Akerman, B. Xulu, O. Munro, *J. Coord. Chem*., 2013, **66**, 3673.
14. Y. Kim, J. Kim, Y. Kang, *J. Korean Chem. Soc*., 1999, **43**, 535.

15. S.B. Jiménez-Pulido, F.M. Linares-Ordóñez, J.M. Martínez-Martos, M.N. Moreno-Carretero, M. Quirós-Olozábal, M.J. Ramírez-Expósito, *J. Inorg. Biochem.*, 2008, **102**, 1677.

16. S.B. Jiménez-Pulido, F. Hueso-Ureña, M.P. Fernández-Liencres, M. Fernández-Gómez, M.N. Moreno-Carretero, *Dalton Trans.*, 2013, **42**, 530.

17. Bruker APEX2, SAINT and SADABS. *Bruker AXS Inc.* (2010) Madison, Wisconsin, USA.

18. R.H. Blessing, *Acta Crystallogr.,Sect. A: Found. Crystallogr.,* 1995, **A51**, 33.

19. G.M. Sheldrick, *Acta Crystallogr.,Sect. A: Found. Crystallogr.,* 2008, **A64**, 112.

20. L.J. Farrugia, *J. Appl. Cryst.,*2012, **45**, 849.

21. M.J. Frisch, G.W. Trucks, H.B. Schlegel, G.E. Scuseria, M.A. Robb, J.R. Cheeseman, G. Scalmani, V. Barone, B. Mennucci, G.A. Petersson, H. Nakatsuji, M. Caricato, X. Li, H.P. Hratchian, A.F. Izmaylov, J. Bloino, G. Zheng, J.L. Sonnenberg, M. Hada, M. Ehara, K. Toyota, R. Fukuda, J. Hasegawa, M. Ishida, T. Nakajima, Y. Honda, O. Kitao, H. Nakai, T. Vreven, J.A. Montgomery Jr., J.E. Peralta, F. Ogliaro, M. Bearpark, J.J. Heyd, E. Brothers, K.N. Kudin, V.N. Staroverov, R. Kobayashi, J. Normand, K. Raghavachari, A. Rendell, J.C. Burant, S.S. Iyengar, J. Tomasi, M. Cossi, N. Rega, J.M. Millam, M. Klene, J.E. Knox, J.B. Cross, V. Bakken, C. Adamo, J. Jaramillo, R. Gomperts, R.E. Stratmann, O. Yazyev, A.J. Austin, R. Cammi, C. Pomelli, J.W. Ochterski, R.L. Martin, K. Morokuma, V.G. Zakrzewski, G.A. Voth, P. Salvador, J.J. Dannenberg, S. Dapprich, A.D. Daniels, O. Farkas, J.B. Foresman, J.V. Ortiz, J. Cioslowski, D.J. Fox, GAUSSIAN 09 (Revision A.01), Gaussian Inc., Wallingford, CT, 2009.

22. I.N. Booysen, M.B. Ismail, M.P. Akerman, *J. Coord. Chem.*, 2013, **66**, 4371.

23. M. Al-Noaimi, M.I. El-Baighouthi, O.S. Abdel-Rahman, S.F. Haddad, *Polyhedron*, 2011, **30**, 1884.

24. N.A. Owston, A.J. Parker, J.M.J. Williams, *Org. Lett.*, 2007, **9**, 3599.

25. R.A. Leising, J.S. Ohman, J.H. Acquaye, K.J. Takeuchi, *J. Chem. Soc., Chem. Commun.*, 1989, 905; C.M. Older, J.M. Stryker, *Organometallics*, 1998, **17**, 5596.

26. S.L. Jain, B. Sain, *Chem. Commun.*, 2002, 1040.

27. M. Muthu Tamizh, K. Mereiter, K. Kirchner, R. Karvembu, *J. Organomet. Chem.*, 2012, **700**, 194.

28. I.N. Booysen, S. Maikoo, M.P. Akerman, B. Xulu, *Trans. Met. Chem.*, 2015, **40**, 397.

29. M.M. Subarkhan, R. Ramesh, *Spectrochim. Acta A,* 2015, **138**, 264.

30. I.N. Booysen, A. Adebisi, O.Q. Munro, B. Xulu, *Polyhedron*, 2014,**73**, 1.

31. I. Assayag, S. Goldstein, A. Samuni, N. Berkman, *Free Radic. Biol. Med.*, 2015, **87**,148.

32. V.I. Lushchak, *Chem. Biol. Interact*., 2014, **224**, 164.

33. I.N. Booysen, A. Adebisi, M.P. Akerman, *Inorg. Chim. Acta*, 2015, **433**, 13.

34. R. Ramachandran, P. Viswanathamurthi, *Spectrochim. Acta Part A*, 2013, **103**, 53.

35. P. Anitha, N. Chitrapriya, Y. Jung Jang, P. Viswanathamurthi, *J. Photochem. Photobio. B*, 2013, **129**, 17.

36. G. Prakash, R. Manikandan, P. Viswanathamurthi, K. Velmurugan, R. Nandhakumar, *J. Photochem. Photobio. B*, 2014, **138**, 63.

37. A. Kanchanadevi, R. Ramesh, N. Bhuvanesh, *J. Organomet. Chem*., 2015, **788**, 49.

38. S.B. Jimenez-Pulido, N.A. Illan-Cabeza, F. Hueso-Urena, M.N. Moreno-Carretero, *Polyhedron,* 2013, **50,** 10.

39. I. Picon-Ferrer, F. Hueso-Urena, N.A. Illan-Cabeza, S.B. Jimenez-Pulido, J.M. Martinez-Martos, M.J. Ramirez-Exposito, M.N. Moreno-Carretero, *J. Inorg. Biochem.,* 2009, **103,** 94.

40. F. Hueso-Urena, S.B. Jimenez-Pulido, M.P. Fernandez-Liencres, M. Fernandez- Gomez, N. Moreno-Carretero, *Dalton Trans*., 2008, 6461.

41. F. Hueso-Urena, S.B. Jimenez-Pulido, M.N. Moreno-Carretero, M. Quiros-Olozabal, J.M. Salas-Peregrin, *Inorg. Chim. Acta,* 1998, **277**, 103.

Chapter 7

Conclusion and Future Work

Novel ruthenium complexes with multidentate N, X-donor (X = O, N, S) ligands encompassing various biologically relevant moieties were designed, synthesized and characterized. In addition, the optimal redox properties of these ruthenium complexes enable these metallic compounds to be radical scavengers. Furthermore, these multidentate chelators stabilized the metal centres in their respective oxidation states of +II, +III and +IV while conferring unique coordination modes.

The isolation of ruthenium complexes with Schiff base chelates containing benz(imidazole/othiazole/oxazole) moieties are described in chapter 3. Despite the structural similarities of the ligands, ruthenium(II) and -(III) complexes with unique structural features were obtained. The voltammetric assignments of the formulated metallic complexes were corroborated by UV-Vis spectroelectrochemistry experiments. ESR studies of the paramagnetic metal complexes confirmed their rhombic nature.

Chapter 4 reports the formation of ruthenium compounds bearing N-X donor (X = O, N) heterocyclic chelators. These chelators include benzoxazole-amide, benzimidazole-amines and chromone-derived Schiff base ligands. X-ray analysis revealed that the metal atoms in the mononuclear ([RuCl(pho)(bzca)(PPh_3)] (**1**) and *cis-Cl*, *trans-P*-[Ru^{III}(Hbhb)Cl_2(PPh_3)$_2$] (**2**)) and dinuclear ((μ-Htba,Cl)$_2$[Ru^{II}Cl(PPh_3)]$_2$ (**3**) and (μ-Cl)$_2$[Ru^{III}Cl(Hchpr)(PPh_3)]$_2$ (**4**)) metallic compounds are within centres of distorted octahedrons which are largely induced by the influence of chelating co-ligands. The crystal lattices of the respective complexes are stabilized by classical

hydrogen bonding supported by weak intermolecular bonding which results in diverse supramolecular structures. A proposed formation route of compound **1** supported by the literature provided insight into the unique molecular transformation of Hbzap into the pho and bzca bidentate chelators. Furthermore, the redox properties of these metallic compounds are comparable to other ruthenium compounds found within the literature. In addition, the metallic compounds had significantly higher radical scavenging capabilities than their corresponding free-ligands and the natural antioxidant, Vitamin C.

In chapter 5, the coordination behaviours of the diimines (*viz.* 2,6-bis-((4-tetrahydropyranimino)methyl)pyridine(thppy) and N^1,N^2-bis((3-chromone)methylene)benzene-1,2-diamine(chb)) and the triimine (*viz.*tris-((1H-pyrrol-2-ylmethylene)ethane)amine (H_3pym)) towards the *trans*-$[Ru(PPh_3)_2]^{2+}$ core afforded novel coordination compounds with diverse structural features: *cis*-$[RuCl_2(thppy)(PPh_3)]$ (**1**), (μ-chb)[*mer*-$RuCl_3(PPh_3)]_2$ (**2**) and [Ru(pym)] (**3**). The thppy chelator of **1** acts as a neutral tridentate ligand through its $(NN)_{imino}N_{py}$ donor set while the neutral chb ligand of **2** bridges the two *cis*-$[Ru^{III}Cl_3]$ cores *via* its ketonic oxygen and imino nitrogen atoms. In addition, the triimine ligand pym displaces all of the co-ligands of the metal precursor affording the hexa-coordinate *tris*(pyrrolide-imine) chelate of Ru(III), complex **3**. All the metal complexes have lower IC_{50} values in comparison to their corresponding free ligands while predominately all metallic compounds were more effective scavengers than the natural antioxidant, vitamin C.

Chapter 6 presents the formulation and spectroscopic characterization of ruthenium complexes with scaffolds incorporating lumazine moieties. Computational calculations at the DFT level aided in the interpretation of the experimental spectra of the metal complexes. X-ray analysis affirms the structural elucidation indicating that the metal atoms are in the centres of distorted octahedrons which are induced by their respective constrained equatorial bite angles.

The abovementioned results provide scope for investigating the anticancer, antimicrobial and antimalarial activities of the formulated metallic compounds. However, before the anticancer studies will be conducted, we envisage exploring the interactions of these metal complexes towards Calf Thymus (CT)-DNA and confirming the mode of interactions using Gel Electrophoresis. The aforementioned experiments are motivated by the fact that recent studies have shown that ruthenium(II) complexes with bulky triphenylphosphine co-ligands exhibit optimal DNA binding and protein interaction capabilities which was accompanied with lower cell toxicity [**1**]. Furthermore, there is an upsurge in the radiochemistry of ruthenium for development of new therapeutic ruthenium radiopharmaceuticals ascribed to the optimal half-life (371.8 days) and β-max energy of the 106-ruthenium radionuclide [**2**].

References

1. R. Sáez, J. Lorenzo, M.J. Prieto, M. Font-Bardia, T. Calvet, N. Omeñaca, M. Vilaseca, V. Moreno, *J. Inorg. Biochem.*, 2014, **136**, 1.

2. V. Takiar, D.S. Gombos, F. Mourtada, L.A. Rechner, A.A. Lawyer, W.H. Morrison, A.S. Garden, B.M. Beadle, *Pract. Radiat. Oncol.*, 2014, **4**, 189.